AFRL-VA-WP-TR-2003-3072

SURVIVABILITY OF AFFORDABLE AIRCRAFT COMPOSITE STRUCTURES

Volume 2: High Strain Rate Characterization of Affordable Woven Carbon/Epoxy Composites

Dr. Mahesh V. Hosur and Dr. Shaik Jeelani

Tuskegee University
Center for Advanced Materials
Tuskegee, AL 36088

Dr. Uday K. Vaidya
The University of Alabama in Birmingham

Dr. Sylvanus Nwosu
University of Pittsburgh

APRIL 2003

Final Report for 01 October 1999 – 01 March 2003

Approved for public release; distribution is unlimited.

STINFO FINAL REPORT

AIR VEHICLES DIRECTORATE
AIR FORCE RESEARCH LABORATORY
AIR FORCE MATERIEL COMMAND
WRIGHT-PATTERSON AIR FORCE BASE, OH 45433-7542

NOTICE

USING GOVERNMENT DRAWINGS, SPECIFICATIONS, OR OTHER DATA INCLUDED IN THIS DOCUMENT FOR ANY PURPOSE OTHER THAN GOVERNMENT PROCUREMENT DOES NOT IN ANY WAY OBLIGATE THE U.S. GOVERNMENT. THE FACT THAT THE GOVERNMENT FORMULATED OR SUPPLIED THE DRAWINGS, SPECIFICATIONS, OR OTHER DATA DOES NOT LICENSE THE HOLDER OR ANY OTHER PERSON OR CORPORATION; OR CONVEY AND RIGHTS OR PERMISSION TO MANUFACTURE, USE, OR SELL ANY PATENTED INVENTION THAT MAY RELATE TO THEM.

THIS REPORT HAS BEEN REVIEWED BY THE OFFICE OF PUBLIC AFFAIRS (ASC/PA) AND IS RELEASABLE TO THE NATIONAL TECHNICAL INFORMATION SERVICE (NTIS). AT NTIS, IT WILL BE AVAILABLE TO THE GENERAL PUBLIC, INCLUDING FOREIGN NATIONS.

THIS TECHNICAL REPORT HAS BEEN REVIEWED AND IS APPROVED FOR PUBLICATION.

/s/

ARNOLD H. MAYER
Project Engineer
Design and Analysis Methods Branch
Structures Division

/s/

MICHAEL L. ZEIGLER, Chief
Design and Analysis Methods Branch
Structures Division

/s/

DAVID M. PRATT, PhD
Technical Advisor
Structures Division

COPIES OF THIS REPORT SHOULD NOT BE RETURNED UNLESS RETURN IS REQUIRED BY SECURITY CONSIDERATIONS, CONTRACTUAL OBLIGATIONS, OR NOTICE ON A SPECIFIC DOCUMENT.

REPORT DOCUMENTATION PAGE

Form Approved
OMB No. 0704-0188

The public reporting burden for this collection of information is estimated to average 1 hour per response, including the time for reviewing instructions, searching existing data sources, searching existing data sources, gathering and maintaining the data needed, and completing and reviewing the collection of information. Send comments regarding this burden estimate or any other aspect of this collection of information, including suggestions for reducing this burden, to Department of Defense, Washington Headquarters Services, Directorate for Information Operations and Reports (0704-0188), 1215 Jefferson Davis Highway, Suite 1204, Arlington, VA 22202-4302. Respondents should be aware that notwithstanding any other provision of law, no person shall be subject to any penalty for failing to comply with a collection of information if it does not display a currently valid OMB control number. **PLEASE DO NOT RETURN YOUR FORM TO THE ABOVE ADDRESS**.

1. REPORT DATE *(DD-MM-YY)*	2. REPORT TYPE	3. DATES COVERED *(From - To)*
April 2003	Final	10/01/1999 – 03/01/2003

4. TITLE AND SUBTITLE
SURVIVABILITY OF AFFORDABLE AIRCRAFT COMPOSITE STRUCTURES
Volume 2: High Strain Rate Characterization of Affordable Woven Carbon/Epoxy Composites

5a. CONTRACT NUMBER
F33615-99-C-3608

5b. GRANT NUMBER

5c. PROGRAM ELEMENT NUMBER
62201F

6. AUTHOR(S)
Dr. Mahesh V. Hosur and Dr. Shaik Jeelani (Tuskegee University)
Dr. Uday K. Vaidya (The University of Alabama in Birmingham)
Dr. Sylvanus Nwosu (University of Pittsburgh)

5d. PROJECT NUMBER
2402

5e. TASK NUMBER
SA

5f. WORK UNIT NUMBER
AC

7. PERFORMING ORGANIZATION NAME(S) AND ADDRESS(ES)
Tuskegee University
Center for Advanced Materials
Tuskegee, AL 36088
The University of Alabama in Birmingham
University of Pittsburgh

8. PERFORMING ORGANIZATION REPORT NUMBER

9. SPONSORING/MONITORING AGENCY NAME(S) AND ADDRESS(ES)
Air Vehicles Directorate
Air Force Research Laboratory
Air Force Materiel Command
Wright-Patterson Air Force Base, OH 45433-7542

10. SPONSORING/MONITORING AGENCY ACRONYM(S)
AFRL/VASD

11. SPONSORING/MONITORING AGENCY REPORT NUMBER(S)
AFRL-VA-WP-TR-2003-3072

12. DISTRIBUTION/AVAILABILITY STATEMENT
Approved for public release; distribution is unlimited.

13. SUPPLEMENTARY NOTES This is volume 2 of three. See also AFRL-VA-WP-TR-2003-3071 and AFRL-VA-WP-TR-2003-3073. This report contains color.

14. ABSTRACT ***(Maximum 200 Words)***
Studies on the high strain rate impact tests performed on conventional unidirectional and affordable woven carbon/epoxy composites using the Split Hopkinson's Pressure Bar (SHPB) setup are presented in the this report. Stitched and unstitched samples made of plain and satin weave carbon/epoxy composites were subjected to high strain rate compression loading at strain rates varying from 320/s to 1149/s using a modified SHPB setup. Further unstitched samples were subjected to inplane off-axes loading at high strain rates at various angles. Failure modes were characterized through optical and scanning electron microscopy. Results of the test indicated that the peak stress increased with increase in strain rate. Under off-axes loading, the peak stress decreased with increase in off-axes angle. Stitching helped in preventing splitting damage.
Studies on carbon/epoxy plates using penetrating SHPB indicate that the strain rate, ultimate strain, and energy released increased nonlinearly, particle velocity and displacement increased linearly with impact energy and the dynamic modules seems to decrease nonlinearly with impact velocity, energy released, strain rate and strain. Penetration limit (PL) increased with increase in the thickness of the laminate. Damage modes include perforation and plugging above PL.

15. SUBJECT TERMS High Strain Rate, Hopkins Pressure Bar, Stitching, Woven Composites, Penetration Limit

16. SECURITY CLASSIFICATION OF:			17. LIMITATION OF ABSTRACT:	18. NUMBER OF PAGES	19a. NAME OF RESPONSIBLE PERSON (Monitor)
a. REPORT	b. ABSTRACT	c. THIS PAGE	SAR	152	Arnold Mayer
Unclassified	Unclassified	Unclassified			19b. TELEPHONE NUMBER *(Include Area Code)* (937) 255-5232

Standard Form 298 (Rev. 8-98)
Prescribed by ANSI Std. Z39-18

Table of Contents

Section **Page**

List of Figures.....v

List of Tables.....x

1. High Strain Rate Studies on Woven Stitched/Unstitched Carbon/Epoxy Composites.....1
1.1 Introduction.....1
1.2 Experimental Work.....2
1.2.1 Fabrication of Sample.....2
1.2.2 Static Compression Testing.....3
1.2.3 High Strain Rate Testing.....3
1.2.3.1 Data Analysis.....6
1.3 Results and Discussion.....8
1.3.1 Plain Weave Laminates.....9
1.3.1.1 Unstitched Plain Weave Carbon/Epoxy Laminates.....9
1.3.1.2 Stitched Plain Weave Carbon/Epoxy Laminates.....12
1.3.2 Satin Weave Carbon/Epoxy Laminates.....15
1.3.2.1 Unstitched Satin Weave Carbon/Epoxy Laminates.....15
1.3.2.1.1 In-plane Loading (0^0/Warp Direction).....15
1.3.2.1.2 In-plane Loading (90^0/Fill Direction).....17
1.3.2.2 Stitched Satin Weave Carbon/Epoxy Laminates.....20
1.3.2.2.1 Inplane Loading (0^0/Warp Direction).....20
1.3.2.2.2 Inplane loading (90^0/Fill Direction).....22
1.3.3 Comparison of Different Sample Configurations.....25
1.4 Conclusions.....26

2. Off-Axis High Strain Rate Characterization of Woven Fabric Composites.....27
2.1 Introduction.....27
2.2 Experimental Studies.....27
2.2.1 Material Selection and Specimen Fabrication.....27
2.2.2 Static and High Strain Rate Compression Testing.....28
2.3 Results and Discussion.....28
2.3.1 Plain Weave Carbon/Epoxy Laminates.....28
2.3.2 Satin Weave Carbon/Epoxy Laminates.....36
2.4 Summary and Conclusions.....50

3. High-Energy Penetration/Perforation Mechanics of Composite Plates.....52
3.1 Project Report Summary.....52
3.2 Introduction.....53
3.3 Experimental.....53
3.3.1. Installation and Calibration of the Hopkinson Impact System at the University of Pittsburgh School of Engineering.....53
3.3.2 Description of the Dynamic Optical Imaging System.....54
3.3.2.1 Ultra High-Speed Continuous Access Framing Camera.....54
3.3.2.2 Rotating Mirror Assembly.....56
3.2.2.3 Remove Fire Unit.....57
3.3.2.4. Camera Control.....57
3.3.2.5 Light Source (Cordin Model 607).....57
3.3.2.6 Gas Control System (Cordin Model 476/480).....57

3.2.2.7 Two-Channel Delay Generator (Cordin Model 450)…….....58
3.2.2.8 Two High-Speed CCD Video Camera system Ultra-High Speed Intensified Camera System (Cordin Dual Model 181)……58
3.4 Theoretical Formulation and Data Reduction Methods……59
3.4.1 Review of Classical SHPB analysis for Composite Penetration Mechanics……...59
3.4.1.1 Stress, Particle Velocity, and Force Measurements……...62
3.4.1.2 Energy Measurements…...……64
3.5 Experimental Design and Results……66
3.5.1 Experimental Considerations……...66
3.5.2 Experimental Results……...67
3.5.2.1 System Calibration……67
3.5.2.2 Characterization of the Wave Forms……70
3.5.2.3 Sample Responses to the High Strain Rate Perforation Damage……73
3.5.2.3.1 Energy Absorbed by the Composite Plate……73
5.5.2.3.2 Strain Rate Sensitivity……..73
3.5.2.3.3 Force and Energy Absorption Variations with Displacement……..77
3.5.2.4 Interaction and Effect of Incident Stress and Fiber Orientation on the Measurement of Energy Released……81
3.5.3 Measurements of Penetration Limit Velocities……...83
3.5.3.1 Penetration Limit Velocities of Laminated Composites……...83
3.5.3.2 Determination of Penetration Limit for Woven and Laminated Composites……89
3.5.3.3 Strain Rate Sensitivity and Measurement Near Perforation Threshold (Penetration Limit) energies for Woven composites...……94
3.5.4 Crack Propagation and High Speed Imaging Data……106
3.5.4.1 Calibration and Magnification of The High Speed Camera ……...106
3.5.4.2. Experimental Results Using Dynamic Optical Imaging of High-Speed Digital Video Camera……107
3.6 Quantitative Analysis of Perforated Carbon-Epoxy Plates by Micro-Raman Spectroscopy..120
3.6.1 Introduction……...120
3.6.2 Experimentation……121
3.6.3 Experimental Procedure...……122
3.6.4 Raman Experimental Results……123
3.7 Conclusions……129
3.8 Further Research and Recommendations……130

4. References……131

List of Acronyms……135

List of Figures

Figure **Page**

1. Conventional Compression Split Hopkinson Pressure Bar……3
2. Schematic of Compression Split Hopkinson Pressure Bar Setup……..4
3. Stress Reversal Using Modified Compression SHPB……...……5
4. Typical Dynamic Responses From Strain Gages Mounted on the Incident and Transmission Bars……..8
5. Dynamic Stress-Strain Response Of Unstitched Plain Weave Carbon/Epoxy Laminate for Inplane Loading……9
6. Optical Micrographs Of Unstitched Plain Weave Sample for In-plane Loading: Static, 369/s, 637/s and 1053/s……11
7. Optical and Scanning Electron Micrographs of Unstitched Plain Weave Samples for Inplane Loading At Strain Rate of 637/s……11
8. Optical and Scanning Electron Micrographs of Unstitched Plain Weave Samples for Inplane Loading At Strain Rate of 1053/s…..……12
9. Dynamic Stress-Strain Response of Stitched Plain Weave Carbon/Epoxy laminate for In-plane Loading……..13
10. Optical Micrographs of Stitched Plain Weave Sample for Inplane Loading: Static, 381/s, 613/s and 1038/s……...14
11. Optical and Scanning Electron Micrographs of Plain Weave Stitch Sample for In-plane Loading at Strain Rate of 613/s……14
12. Optical and Scanning Electron Micrographs of Plain Weave Stitch Sample for In-plane Loading at Strain Rate of 1038/s ……14
13. Dynamic Stress-Strain Response of Unstitched Satin Weave Carbon/Epoxy Laminate for Inplane Loading Along Warp Direction……...15
14. Optical Micrographs of Unstitched Satin Weave Sample for Warp Loading: Static, 350/s 648/s and 1021/s……...16
15. Optical and Scanning Electron Micrographs of Unstitched Satin Weave Samples for Warp Loading at Strain Rate of 648/s……...17
16. Optical and Scanning Electron Micrographs of Unstitched Satin Weave Samples for Warp Loading at Strain Rate of 1021/s……..17
17. Dynamic Stress-Strain Response of Unstitched Satin Weave Carbon/Epoxy Laminate for In-plane Loading along Fill Direction……18
18. Optical Micrographs of Satin Weave Un-Stitch Sample for Fill Loading: Static, 391/s, 617/s and 1045/s……...18
19. Optical and Scanning Electron Micrographs of Satin Weave Unstitch Samples for Fill Loading at Strain Rate of 617/s……19
20. Optical and Scanning Electron Micrographs of Satin Weave Unstitch Samples for Fill Loading at Strain Rate of 1045/s..……19
21. Dynamic Stress-Strain Response of Stitched Satin Weave Carbon/Epoxy Laminate Loaded in Warp Direction……21
22. Optical Micrographs of Satin Weave Stitch Sample for Warp Loading: Static, 360/s, 601/s and 1110/s……...21
23. Optical and Scanning Electron Micrographs of Stitched Satin Weave Samples for Warp Loading at Strain Rate of 601/s……22
24. Optical and Scanning Electron Micrographs of Stitched Satin Weave Samples for Warp Loading at Strain Rate of 1061/s..……22
25. Dynamic Stress-Strain Response of Stitched Satin Weave Carbon/Epoxy Laminate Loaded in Fill Direction….……..23

26. Optical Micrographs of Stitched Satin Weave Laminate Loaded in Fill Direction at: Static, 391/s, 617/s and 1045/s……24
27. Optical and Scanning Electron Micrographs of Satin Weave Stitch Samples for Fill Loading at Strain Rate Range of 617/s……24
28. Optical and Scanning Electron Micrographs of Satin Weave Stitch Samples for Fill Loading at Strain Rate Range of 1045/s……...24
29. Variation of Peak Stress with Strain Rate……25
30. Variation of Modulus with Strain Rate…….....25
31. Stress-Strain curves at Different Orientation Under Static Loading……29
32. Dynamic Compressive Stress-Strain Plots For The Samples Loaded Along Warp (0°) Direction at Different Strain Rates……...31
33. Dynamic Compressive Stress-Strain Plots for the Samples Loaded Along 15° Direction at Different Strain Rates……...32
34. Dynamic Compressive Stress-Strain Plots for the Samples Loaded Along 30° Direction at Different Strain Rates……...32
35. Dynamic Compressive Stress-Strain Plots for the Samples Loaded Along 45° Direction at Different Strain Rates……...33
36. Comparison of Dynamic Stress-Strain Response of Samples Tested at Different On- and Off- Axes Angles at Strain Rate of ~1400/s……33
37. Comparison of Dynamic Stress-Strain Response of Samples Tested at Different On- and Off- Axes Angles at Strain Rate of ~1800/s……34
38. Micrographs of the Samples Tested Under High Strain Rate Compression Loading Along Warp (0°) direction at (a) 1187/s, (b) 1285/s, (c) 1474/s, (d) 1773/s, and (e) 2289/s……..35
39. Micrographs of the Samples Tested Under High Strain Rate Compression Loading Along 15° Orientation (a) 387/s, (b) 1474/s, (c) 1692/s, (d) 1893/s and (e) 1900/s……...35
40. Micrographs of the Samples Tested Under High Strain Rate Compression Loading Along 30° Orientation (a) 1345/s, (b) 1546/s, (c) 1747/s, (d) 1853/s and (e) 2001/s...……..36
41. Micrographs of the Samples Tested Under High Strain Rate Compression Loading Along 45° Orientation (a) 1457/s, (b) 1670/s, (c) 1830/s, (d) 1981/s and (e) 2162/s…...……..36
42. Compressive Stress-Strain Response of Satin Weave Carbon/Epoxy Laminates Under On- and Off-Axes Loading……..38
43. Dynamic Compressive Stress-Strain Response of Satin Weave Carbon/Epoxy Laminates Loaded Along 0° (Warp)……..39
44. Optical Micrographs of Samples Tested Along 0° at (a) 1342/s, (b) 1526/s, (c) 1694/s, (d) 1877/s, and (e) 2215/s……40
45. Dynamic Compressive Stress-Strain Response of Satin Weave Carbon/Epoxy Laminates Loaded Along 15° Direction……40
46. Optical Micrographs of Samples Tested Along 15^0 Direction at (a) 1414/s, (b) 1508/s, (c) 1748/s, (d) 1902/s, and (e) 2135/s…….……41
47. Dynamic Compressive Stress-Strain Response of Satin Weave Carbon/Epoxy Laminates Loaded Along 30° Direction…….....42
48. Optical Micrographs of Samples Tested Along 30^0 Direction at (a) 1417/s, (b) 1582/s, (c) 1718/s, (d) 1918/s, and (e) 2125/s…….....43
49. Dynamic Compressive Stress-Strain Response of Satin Weave Carbon/Epoxy Laminates Loaded Along 45° Direction……44
50. Optical Micrographs of Samples Tested Along 45° Direction at (a) 1325/s, (b) 1481/s, (c) 1699/s, (d) 1915/s, and (e) 2134/s……...44
51. Dynamic Compressive Stress-Strain Response of Satin Weave Carbon/Epoxy Laminates Loaded Along 60° Direction……45
52. Optical Micrographs of Samples Tested Along 60^0 Direction at (a) 1402/s, (b) 1602/s, (c) 1716/s, (d) 1823/s, and (e) 2114/s……...46

53. Dynamic Compressive Stress-Strain Response of Satin Weave Carbon/Epoxy Laminates Loaded Along 75° Direction……47
54. Optical Micrographs of Samples Tested Along 75^0 Direction at (a) 1320/s, (b) 1488/s, c) 1665/s, (d) 1717/s, and (e) 1886/s……47
55. Dynamic Compressive Stress-Strain Response of Satin Weave Carbon/Epoxy Laminates Loaded Along 90° (Weft/Fill)……..48
56. Optical Micrographs of Samples Tested Along 90° Direction (Weft/Fill) at (a) 1390/s, (b) 1491/s, (c) 1670/s, (d) 1845/s, and (e) 2149/s……49
57. Dynamic Compressive Stress-Strain Response of Satin Weave Carbon/Epoxy Laminates Loaded Along Different Orientations at a Strain Rate of ~1400/s……...49
58. Dynamic Compressive Stress-Strain Response of Satin Weave Carbon/Epoxy Laminates Loaded Along Different Orientations at a Strain Rate of ~1900/s……..……50
59. System configuration showing a) High-Speed Continuous Access Camera and Two High-Speed Video cameras b) High speed Camera Looking Into Sample Holder Illuminated by 5kV Flash Unit Via Fiber Optical Cables……55
60. System Instrumentation Control Room b) Nicolet Data Acquisition System with Display of Typical Strain Wave……...56
61. Integrated Operational Layout Of The Penetrating Split Hopkinson Pressure Bar (P-SHPB) system……..59
62. A Schematic Diagram Of The Penetrating Hopkinson Bar System Showing (top) Perforation Sample Holder Fixture and (bottom)) System Configuration and Instrumentation……60
63. Different Types of Penetrators Used in Current Tests……68
64. a) Variation of Striker Impact and Penetrator Velocities with Compressor Air Pressure (MPa) and (b) Variation of Incident Bar Penetration Energy with Striker Velocity ($V_{pb}=0.0665V_i, R^2 = 0.92, E_{pb}=0.0271E_i, R^2=1.0$)……...69
65. Typical Strain Wave Pulses for a) 68 J (30 psi) and b) 246 J (75 psi)……71
66. Time Variations of a) Total Energy Absorbed Showing Peak Energy and Energy Absorbed by Specimen b) Particle Velocity for Varying Striker Impact Energies……..72
67. Time Variations of a) Sample Stress and b) Loading Force for Varying Striker Impact Energies……74
68. Variations of Sample Stress with a) Strain Rate and b) Strain for Varying Striker Impact Energies……75
69. Variations of Strain Rate with a) Strain and b) Sample Stress Using Conical Hemispherical Penetrator for Varying Striker Impact Energies……...76
70. Variations of a) total energy absorbed b) loading force with displacement for Varying Striker Impact Energies……77
71. Effects of Impact Velocity on a) Ultimate Strain b) Ultimate Strength…….……..78
72. Effects of Striker Impact Velocity on a) Total Peak Energy Absorbed in Penetration/Perforation Event b) Peak Particle Velocity and Displacement……...……78
73. Effects of a) Strain and b) Displacement on Materials Responses……...79
74. Effects of a) Total Energy Absorbed in the Penetration/Perforation Event, b) Impact Energy, c) Strain, and d) Strain Rate on Dynamic Modulus……80
75. Photographs Showing Rear Surface Damage Pattern for a) 8-Layer Weaved Carbon Fiber at 39 J, 68 J, 120 J, and 159 J b) 16-Ply $[\pm45/0/90]_{2s}$ Graphite/Epoxy Laminates at 68, 80, 148, 152 J Using (c) 3/16-inch Conical Hemispherical Penetrator……..87
76. Variation of a) Residual Velocity and b) Specimen Damage Height With Striker Impact Velocity for [±45/0/90] and [±45] Fiber Layups of Laminated Graphite-Epoxy Composite Using 1/4-inch Hemispherical-nosed Penetrator……..88
77. Relationship Between Critical Striker Velocity for Penetration of Laminated Graphite-Epoxy Composite Using 1/4-inch Hemispherical-nosed Penetrator…….89

78. Variation of a) Crack Height and b) Crack Length with Striker Impact Energy for Woven Graphite Epoxy Composite Using1/4-inch Spherical Nose Penetrator……...90
79. Variation Of Striker Bar Ballistic Limit Velocity With Sample Thickness for Three Penetrator Geometries (a and c) Protruding Spherical and b) Protruding Hemispherical and d) Conical Hemispherical……..91
80. Strain Rate Time History Using a) 3/16-, b) 1/4-inch Protruding Spherical Penetrators at 68 J for 12-, 16- and 24-Layer Woven Sample, c) Effect of Thickness on Strain Rate……..95
81. Variation of a-c) Sample Stress and d-f) Strain Rate Using 1/4 inch Hemispherically-
i. Nosed Penetrator for Three-Sample Thickness…..……...96
82. Comparison of Energy Absorption for 1/4-Inch Protruding Spherical and 1/4-inch Conical Hemispherical Penetrators for 12-, 16-, and 24-Layer Specimen……....98
83. Effect of Specimen Thickness on Energy Absorption for 1/4-inch Hemispherical Penetrator at 68 J……..99
84. Variations of Particle Velocity, Energy Released, Ultimate Strain, Ultimate Stress, Strain Rate and Loading Force BPL, at PL and APL……...100
85. Effect of Penetrator Size: Comparison of Variations Of Ultimate Strain And Energy Released, Strain Rate for 3/16-inch and 1/4-inch Spherical Penetrator near BPL, at (BL) and APL……..101
86. Effect of Penetrator Size: Comparison of Variations of Peak Loading Force and Strain Rate for 3/16- and 1/4-inch Spherical Penetrators Near BPL, at PL, and APL…….102
87. Variation of Energy Absorbed by Woven Composite Plate with Striker Impact Energy Penetrated with 3/16-, 7/52- and 1/4-inch Protruding Spherical Penetrators……124
88. Effect of Penetrator Geometries: Comparison of Variations of Strain Rate with Sample Thickness for 3/16- and 1/4-inch Protruding Spherical and Conical Hemispherical Penetrator Sizes in the Vicinity of Damage Threshold Regions (BPL, at PL, and APL)……...105
89. Penetration of Graphite-Epoxy Woven Specimens Using 1/4-inch a) Conical Hemispherical- nosed and b) Protruding Spherical-nosed penetrator……107
90. Crack Propagation for 12-Layered Woven Graphite-Epoxy Specimen BPL Velocity Using 1/4-Spherical Penetrator……108
91. Crack Propagation for 12-Layered Woven Graphite-Epoxy Specimen at PL Velocity Using 1/4-inch Spherical Penetrator at 68 J Above BL Impact Energy……..109
92. Crack Propagation for 16-Layered Woven Graphite-Epoxy Specimen BPL Velocity Using 1/4-Inch Spherical Penetrator at 68 J……...……110
93. Crack Propagation For 16-Layered Woven Graphite-Epoxy Specimen at PL Velocity Using 1/4-Inch Spherical Penetrator at 76 J……...111
94. Crack Propagation for 16-Layered Woven Graphite-Epoxy Specimen APL Velocity Using 1/4-Inch Conical HemiSpherical Penetrator At 85 J……112
95. Crack propagation for 24-Layered Woven Graphite-Epoxy Specimen BPL Velocity Using 1/4-Inch Conical Hemispherical Penetrator at 180 J……...113
96. Crack Propagation For 24-Layered Woven Graphite-Epoxy Specimen APL Velocity Using 1/4-Inch Conical Hemispherical Penetrator at 201 J……...114
97. Variations of Crack Length With Crack Extension Time From the High-Speed Images Around the PL Energies for a) 12 Layer, b) 16 Layer and c) 24 Layer Specimens……...115
98. Crack Propagations Using High-Speed Video CCD Camera And 1/4-inch Spherical-nosed Penetrator……116
99. Crack Propagations Using High-Speed Video CCD Camera And 1/4-inch Conical-nosed Penetrator……117
100. Variation of Crack Speed with a) Damage Energy Threshold and b) Sample Thickness Measured With High-Speed Camera at 100kFPS-12kFPS (BPL=54 J, PL=76 J, and APL=84 J)……...118

101. Comparison of Average Crack Speed Variation With a) Damage Threshold Levels around the PL Energies, and b) Striker Impact Energies for Conical Hemispherical and Protruding Spherical Penetrators……..119
102. Experimental Configuration for Obtaining Strain Intensity Profile From the a) Surface and b) Internal Transverse (In-plane) Surface of Damaged Specimen…..…….123
103. Comparison of Raman Spectrum for 16-Layer Sample a) Compression and Tension Sides at Center Location b) Compression Side Damage Compared to Undamaged Sample……...124
104. Comparison of Raman Spectrum of Undamaged and Damaged Samples for 16-Layer a) Tension Side at Center Location b) Tension Side Damage Compared to Undamaged Sample……..125
105. Strain Intensity Profile for 16-Layer Sample for a) Tension and b) Compression……...126
106. Strain Intensity Profile for a) Protruding Spherical, and b) Conical Hemispherical Penetrator at Varying Sample Strains (%)……127
107. Variation of Strain Induced Raman Shift Averaged Over all the Locations With Sample Average Strain……128

List of Tables

Table **Page**

1. Static and Dynamic Properties of Unstitched Plain Weave Carbon /Epoxy Laminates...…...10
2. Static and Dynamic Properties Of Stitched Plain Weave Carbon /Epoxy Laminates……..13
3. Static and Dynamic Properties of Unstitched Satin Weave Carbon /Epoxy Laminates Loaded in the Warp Direction……..……....16
4. Static and Dynamic Properties of Unstitched Satin Weave Carbon /Epoxy Laminates Loaded in the Fill Direction……..19
5. Static and Dynamic Properties of Stitched Satin Weave Carbon /Epoxy Laminates Loaded in the Warp Direction……...20
6. Static And Dynamic Properties of Stitched Satin Weave Carbon /Epoxy Laminates Loaded in the Fill Direction……..23
7. On- and Off-Axes Properties of Woven Composites Under Static Loading……....29
8. On- and Off-Axes Properties of Woven Composites Under Dynamic Loading……..…...30
9. Properties Of Eight-Harness Satin Weave Carbon/Epoxy Laminates Under Static Compression Loading At Different Orientations……...……..37
10. Properties of Eight-Harness Satin Weave Carbon/Epoxy Laminates Under High Strain Rate Compression Loading Along the 0° (Warp) Direction……....39
11. Properties f Eight-Harness Satin Weave Carbon/Epoxy Laminates Under High Strain Rate Compression Loading Along the 15° Direction…..…….……41
12. Properties of Eight-Harness Satin Weave Carbon/Epoxy Laminates Under High Strain Rate Compression Loading Along the 30° Direction……...42
13. Properties of Eight-Harness Satin Weave Carbon/Epoxy Laminates Under High Strain Rate Compression Loading Along 45° Direction…….……43
14. Properties of Eight-Harness Satin Weave Carbon/Epoxy Laminates Under High Strain Rate Compression Loading Along 60° Direction……45
15. Properties of Eight-Harness Satin Weave Carbon/Epoxy Laminates Under High Strain Rate Compression Loading Along 75° Direction……46
16. Properties of Eight-Harness Satin Weave Carbon/Epoxy Laminates Under High Strain Rate Compression Loading Along the 90° Direction (Weft/Fill)……48
17. Experimental Parameters……..68
18. Factorial Analysis……81
19. Results of Factorial Experiment……82
20. Analysis of Variance……82
21. Two Way Analysis of Variance……83
22. Penetration Test Data for 24-Ply Quasi-Isotropic Laminate $[+45/-45/0/90]_{3s}$……84
23. Penetration Test Data for 8-Ply Quasi-Isotropic Laminate $[+45/-45/0/90]_{s}$…..…..……84
24. Penetration Test Data for 4-Ply Quasi-Isotropic Laminate [+45/-45/0/90]….……85
25. Penetration Test Data for 16-Ply Laminate $[+45/-45]_{4s}$……...….85
26. Penetration Test Data for 8-Ply Laminate $[+45/-45]_{s}$……...….85
27. Penetration Test Data for 4-Ply Laminate [+45/-45]……...….85
28. Summary of Ballistics Velocities for Laminated Graphite/Epoxy……...89
29. Damage Initiation Energy/Layer for Graphite Epoxy Woven Specimen Using 3/16-Inch Protruding Spherical Penetrator……...92
30. Damage Initiation Energy/Layer for Graphite Epoxy Woven Specimen Using 7/32-Inch Protruding Spherical Penetrator……...92
31. Damage Initiation Energy/Layer for Graphite Epoxy Woven Specimen Using 1/4 -Inch Protruding Spherical Penetrator……93
32. Damage Initiation Energy/Layer for Graphite Epoxy Woven Specimen Using 3/16 -Inch Protruding Hemispherical Penetrator……..93

33. Damage Initiation Energy/Layer for Graphite Epoxy Woven Specimen Using
1/4 -Inch Conical Hemispherical Penetrator……94

1. High Strain Rate Studies on Woven Stitched/Unstitched Carbon/Epoxy Composites

In this study, experimental investigations on stitched and unstitched woven carbon/epoxy laminates under high strain rate compression loading are discussed. Stitched/unstitched laminates were fabricated with aerospace-grade plain and satin weave fabrics with room temperature curing SC-15 epoxy resin using affordable vacuum assisted resin infusion molding (VARIM) process. The samples were subjected to high strain rate loading using modified Compression Split Hopkinson's Pressure Bar (SHPB) at three different strain rates ranging from 320/s to 1149/s. Failure mechanisms were characterized through optical and scanning microscopy. Results are discussed in terms of unstitched/stitched configuration, fabric type, and loading directions. Dynamic compression properties are compared with those of static loading.

1.1 Introduction

In some practical cases, the loading on composite structures is dynamic. Examples include bird strikes on aircraft structures, underwater mine blasts on ship hulls, ballistic impact on civil structures, armored vehicles, and automobile accidents. Further, development of constitutive equations for the material used in structures subjected to dynamic loading requires knowledge of the variation in material strength with applied rate of loading and how stress and strain are related. Hence, it is essential to characterize the response of composite materials to high strain rate loading. Studies related to the testing of stitched composites at high strain rates are limited. Much of the previous research in the field of high strain rate loading has been performed on unstitched composites and ductile metallic materials. It is only in the recent past that significant efforts have been made to examine high strain rate properties of more brittle substances such as composites, ceramics, and certain geological materials. A SHPB is widely used to generate high strain rate response data of materials under tension, compression, and torsional loading as it gives the scope to test materials over a wide range of strain rates. In the last two decades, research on the high strain rate response of laminated fiber-reinforced composites has gained momentum as these materials are increasingly accepted as viable lightweight structural materials. Sierakowski has reviewed over 120 articles dealing with high strain rate behavior of filamentary composites materials [1]. In this article, various experimental techniques used for evaluating the dynamic performance of composites, as well as results obtained by researchers for various types of filamentary composites, are discussed. El-Habak studied the mechanical behavior of woven glass fiber-reinforced composites at failure strain rates ranging from 100/s to 1000/s [2]. He studied the effect of sizing of the fibers, and two different resin systems: epoxy and vinyl ester. He found that, while sizing did not influence the high strain rate behavior, composites made of vinyl ester matrix yielded higher strength.

Montiel et al. reported the dynamic behavior of AS4 graphite/polyether ether ketone (PEEK) cross-plied composite laminates at strain rate upto 8/s using a drop tower assembly [3]. Results from these studies indicate that at strain rates of the order of 8/s, the strength increased 42 percent over the static values, and strain to failure increased over 25 percent. Harding studied the effect of strain rate and specimen geometry on the compression strength of woven glass-reinforced epoxy laminates [4]. Two specimen designs were tested, one consisting of Permglass 22FE and HY750 resin with 48 layers (cylindrical test specimen), while strip specimens of E0glass type 11X2EC5 and ZD927 epoxy resin were used in the 44-layer strip specimens. Results show that the compression strength and failure strains are strongly dependent on the specimen geometry. However, the limitations of these conclusions arise from the fact that the material system for the two geometries of samples is different.

Researchers at the University of Delaware have studied the dynamic response of a large number of composite material systems up to strain rates of 1200/s and gathered data on the changes in yield stress,

yield strain, ultimate stress, modulus of elasticity. and total strain energy to failure [5-7]. Results of their study indicate considerable increase in strength and stiffness with the increase in strain rate. In general, the high strain response was found to be largely material dependent. Woldenbet and Vinson studied the effect of specimen geometry in high strain rate testing of graphite/epoxy laminates [7]. The experiments discussed show the effect of varying the length to diameter (L/D, or aspect ratio) of the specimen, as well as the effect of changing from more typical cylindrical to square/rectangular specimen geometry. The results of both studies were compared, and no statistically significant effect of either L/D or geometry could be found. Waas et al. have studied static and dynamic response of unidirectional glass/epoxy laminates with varying fiber volume fraction [8]. They found that dynamic strength and relative strain are 1.7 times higher than that of the static values. However, they conclude that there is only a marginal difference in the static and dynamic stiffness. Hsiao and Daniel have investigated the strain rate effects on transverse compression and shear behavior of unidirectional carbon/epoxy laminates and observed similar trends [9]. In contrast, Hosur et al. [10] and Vaidya et al. [11], in their studies on thick-section composites have observed that the dynamic strength and stiffness values increase with the increase in strain rate upto a certain limit. At higher strain rates, they report decrease in both strength and stiffness. Weeks et al. [12] and Ninan et al. [13] have reported that the stress-strain relation is linear only when the sample is loaded in the longitudinal direction. Shankar et al. [14] have investigated the dynamic compressive properties of a uniweave composite laminate with and without reinforcement stitching and have reported that there is a reduction in peak stress value due to stitching.

From the literature study, it is evident that work on high strain rate characterization of stitched composites is very limited. Stitching is being considered in the industry for improving the damage resistance/tolerance of composites [15-21]. In addition, most of the reported work is carried out using classical SHPB. In the classical SHPB, the specimen is subjected to repeated loading. In case the sample does not fail during first loading, then microstructural examination of the sample after loading cannot be correlated to the recorded stress-strain data. Nemat-Nasser et al. have proposed modifications to classical SHPB using which is it possible to subject the sample to a single controlled compression pulse [22]. Hence, in the current work, characterization of stitched woven carbon/epoxy composites under high strain rate compression rate loading was undertaken utilizing a modified SHPB. Two weave architectures plain and eight harness satin weaves–were considered. Both stitched and unstitched plain (17 layer) and satin weave (17 layer) carbon/epoxy laminates were fabricated using an affordable liquid molding process, VARIM. Samples that are 12.7 mm (width) by 12.7 mm (height) by (thickness) were prepared from the laminates. In cases of stitched laminates, samples were carefully cut so as to have a cross-stitch node exactly at the center. In the case of eight harness satin weave samples, the test matrix includes loading along two in-plane directions–warp and fill. The samples were tested at three different strain rate ranges (1) 320/s–391/s; (2) 613/s–645/s; and (3) 1001/s–1149/s. For each range of strain rate, three samples were tested. Peak stress, strain at peak stress, and modulus were tabulated and compared. Responses of samples to loading under static and high strain rate conditions were compared. Failure mechanisms were characterized through optical and scanning electron microscopy.

1.2 Experimental Work

1.2.1 Fabrication of Sample

For both stitched and unstitched configurations of plain and satin weave architecture, 17-layer carbon/epoxy laminates were manufactured using a VARIM process using Applied Polyremic low-viscosity SC-15 resin system. For the fabrication of stitched laminates, layers of dry fabric were stacked together and stitched using three-cord Kevlar thread in a lockstitch pattern with a stitch pitch of 6 mm. An orthogonal grid pattern of stitch was employed. Samples of size 12.7 mm (width) by 12.7 mm (height) by

(thickness) were cut for high strain rate testing. In the case of stitched panels, samples were cut so as to have a cross-stitch node exactly at the center of the sample using a low-speed diamond saw. Subsequently, specimens were polished using a sanding rotor equipped with fine sandpaper (grit # 800) to ensure parallel loading edges.

1. 2.2 Static Compression Testing

To determine the static strength, a quasi-static test was carried out on different types of samples used in the study in a Material Testing System (MTS) machine in displacement control mode with a constant crosshead speed of 1.27 mm/min. The load and crosshead displacement response for each test was recorded by the data acquisition system. The data was corrected for machine compliance. For this, a test was carried out without any sample by loading platens in compression and recording resulting load-displacement response. From this response, the slope of displacement-load was determined, which gives combined compliance of the testing machine and loading platens. Load data for each sample was multiplied by the compliance value, giving displacement of the machine and loading platens. The displacement value so determined was deducted from the test data of samples, which gives actual displacement of the samples.

1.2.3 High Strain Rate Testing

For high strain rate testing, a modified SHPB test system was used on cube samples of nominal size–6 mm. The classical compression SHPB consists of a gas chamber, striker bar, incident bar and the transmission bar. Figure 1 illustrates a schematic representation of a conventional SHPB setup for a compression test. The dynamic stress-strain response in the sample is obtained by sandwiching the sample between the incident and transmission bars of common cross-sectional area and elastic moduli. The impact on the specimen is induced through the release of a striker bar (by releasing the nitrogen gas in the gas chamber) that impacts the incident bar. Upon impact, a compressive stress wave is induced in the incident bar. When the wave reaches the interface between the incident bar and the specimen, a portion of the incident wave is reflected back in to the bar as a tensile pulse, and the remaining portion is transmitted in to the specimen as a compressive wave. The pulse that is transmitted in to the specimen propagates through its length and reaches the interface between the specimen and the transmission bar. A portion of the wave is reflected back in to the specimen, and the remaining portion is transmitted in to the transmission bar as a compressive pulse. The transmission bar is then displaced along its axis and rests when the other end of it reaches a dashpot. The stress wave in the specimen undergoes numerous internal reflections during the test. It is assumed that the stress distribution in the specimen is uniform in a given cross section, the bars remain elastic, and ends of both the incident and the transmission bars in contact with the specimen remain flat.

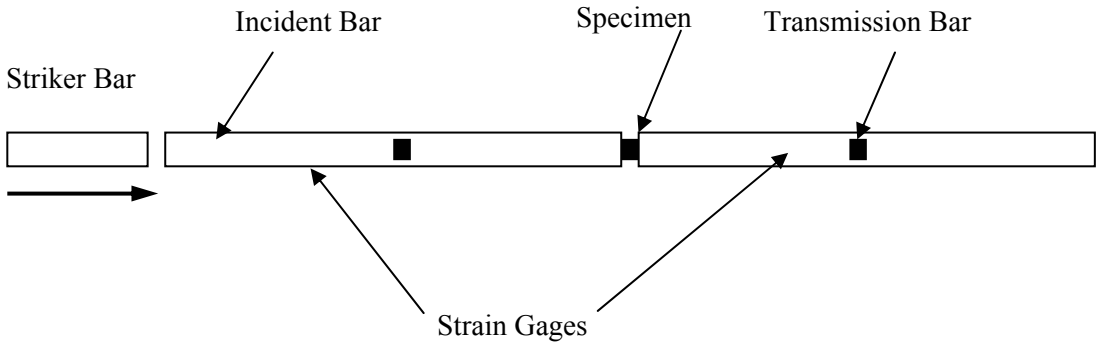

Figure 1. Conventional Compression SHPB

In the conventional SHPB technique, if the sample does not fail in the course of loading by the initial compressive pulse, the sample will be subjected to repeated loading by the elastic waves traveling back and forth in the incident bar. Thus, the technique is limited to obtaining dynamic stress-strain relation to failure. It does not easily allow recovery of the specimen at various levels of loading for microscopic analysis, which is necessary for understanding microstructural damage evolution associated with loading histories.

Using the modified SHPB, repeated loading of the sample is avoided by using an incident bar with a transfer flange at the loading end in combination with an incident tube and a reaction mass. Typical setup of modified SHPB is shown schematically in Figure 2. By modifying the loading end of the incident bar, a stress pulse consisting of a compression segment followed by a tension segment is generated in the incident bar. Figure 3 shows overall design of the stress reversal mechanism. The loading end of the incident bar begins with a transfer flange. The incident tube is a hollow circular cylinder having the same cross-sectional area as that of the incident and the striker bars, and made of the same material as the striker and the incident bars. Thus, the incident bar, the incident tube, and the striker bar have common impedance. The incident tube rests against the transfer flange at one end and at the other end against a reaction mass, which is a large rigid steel cylinder. The incident bar passes through the incident tube and the reaction mass.

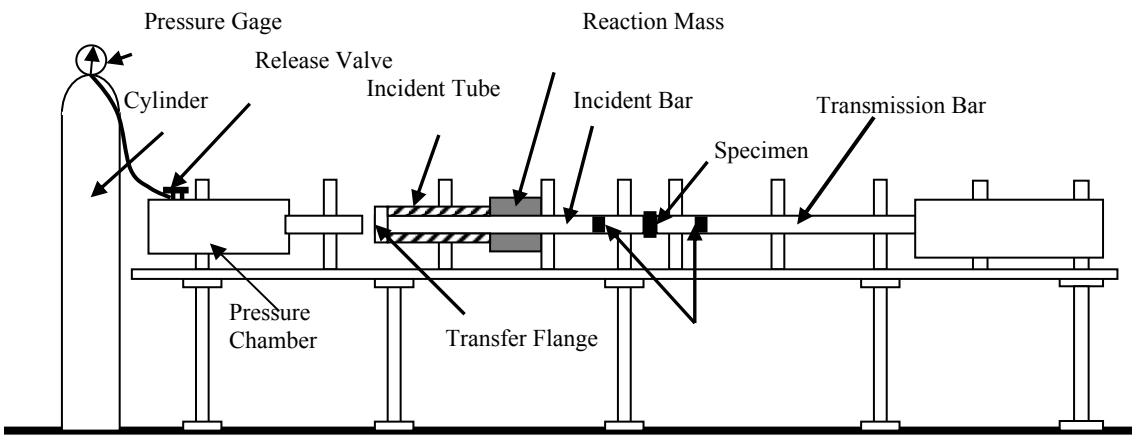

Figure 2. Schematic of Compression SHPB Setup

When the striker bar impacts the transfer flange of the incident bar, all the bars that include the striker bar, the incident bar and the incident tube will be loaded in compression with common axial strain. The compression pulse in the incident bar travels toward the specimen. The compression pulse in the striker bar reaches the transfer flange at its free end as a tension pulse. Since the combined cross section of the incident bar and the tube is twice that of the striker bar, having the same material properties, the striker bar begins to bounce away from the transfer flange. Meanwhile, the compression pulse in the incident tube reflects from the reaction mass as compression, since the rigid reaction mass gives fixed boundary condition to the incident tube (at fixed end, a compressive pulse reflects as compressive pulse and at free end as tensile pulse) and reaches the transfer flange and imparts a tensile pulse to the incident bar (after getting reflected from the transfer flange). This tensile pulse follows the initial compression pulse in the incident bar traveling toward the sample.

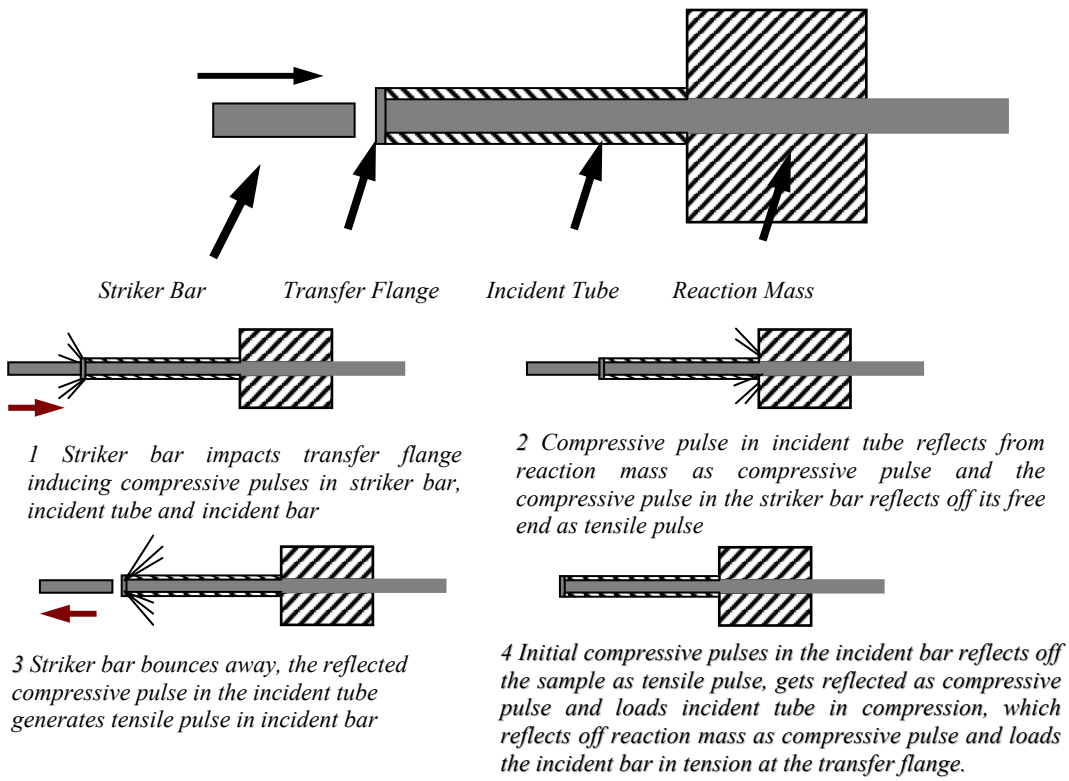

Figure 3. Stress Reversal Using Modified Compression SHPB

The initial compression pulse traveling in the incident bar is partly transmitted through the sample in to the transmission bar and is partly reflected off the sample in to the incident bar as a tension pulse. The reflected tension pulse in the incident bar is then transmitted in to the incident tube as compression pulse by the transfer flange-incident tube configuration. This compression pulse is then reflected back as compression pulse in the incident tube and then as tension pulse back in to the incident bar, through the transfer flange. Finally, the tensile pulse traveling in the incident bar is reflected off the sample as a compression pulse in to the incident bar. This compression pulse is then reflected back in the incident bar as a tensile pulse once it reaches the transfer flange. Hence, once the sample is loaded in compression by the initial compression pulse, it will remain intact to be recovered since all subsequent pulses that move toward the specimen are tensile.

The setup used in the current study consists of striker, incident, and transmission bars, and the incident tube made of 1045 maraging steel. The diameter of the striker, incident, and transmission bars is 19 mm each. The length of striker bar is 22.86 cm, while that of incident and transmission bars is each 1.524 m (60 inches). The incident tube is 38.1 cm long and has an inner diameter of 19 mm and outer diameter of 26.87 mm. The reaction mass has an inner diameter of 19 mm and an outer diameter of 104.14 mm, with a length of 15.24 cm. The specimen is sandwiched between the incident bar and the transmission bar. Petroleum jelly is applied at surfaces of the specimen that are in contact with the bars to reduce the effect of friction. Depending on the required strain rate, area of cross section, and length of the specimen, the pressure at which the striker bar is to be released is calculated. In using the SHPB, strain gage transducers mounted on the incident and the transmission bars at a distance of 76.2 cm (30 inches) from the specimen are used as signal monitors.

1.2.3.1 Data Analysis

The transient strain history is recorded from the strain gages mounted on the incident and the transmission bars. Two gages are mounted diametrically opposite to each other on each bar to record any bending strains. The data is acquired using a high-speed data acquisition card with Gagescope V2.92 software at a sampling rate of 2 MHz. The stress-strain relation is developed based on one-dimensional elastic bar-wave theory for a pulse propagating in a uniform bar, which is initially unstrained and at rest before the pulse arrives. The following assumptions are made in deriving the stress-strain relation for the Hopkinson Bar:

1. The incident, the transmission, and the striker bar must remain elastic. This is usually easy to satisfy from a practical point of view. High-strength steel such as maraging steel, which has a yield strength of about 2500 MPa, is the choice material for the incident, the transmission and the striker bars.
2. Wave propagation in the pressure bar is one dimensional. It is necessary to look in to the exact solution to see whether the assumption of one dimensional wave propagation is valid. An exact solution for wave propagations has been studied for an infinite cylinder bar. Upon impact of the striker bar on the incident bar, a step pressure pulse is set up at the end of the incident bar. The exact solution for a cylindrical bar contains infinite modes. The fundamental mode associated with the long wavelengths ($\lambda >> R$, where λ is the wavelength and R is the radius of the bar) propagates at the sonic wave speed C_0. Smaller wavelengths (($\lambda < R$) tend to propagate at much slower speed. However, most of the energy is contained in the longer wavelengths. Since the long wavelengths dominate the spectrum, the state of deformation is essentially one dimensional for sufficiently long bars. Further, the surface measurements are nearly equal to the axial displacements. For this assumption to hold good, the elastic bars should have a length to diameter (L/D) ratio of at least 20, where l and d are the length and the diameter of the elastic bars. In the current study, an L/D ratio of 80 is used.
3. The third assumption is that the specimen undergoes homogeneous deformation. When the stress wave enters the sample, particles undergo deformation both axially and radially. As the specimen length is short compared to the bar lengths, the initial stress wave in the specimen undergoes numerous internal reflections. Within a composite material specimen, there may be a difference in the wave speed in the fiber and matrix materials. Dee et al. [14] and Li et al. [23] have reported that if a minimum of three to four wave reflections within the length of the specimen are achieved prior to specimen failure, the stress distribution along the specimen length will smooth out, and the specimen is assumed to be in a uniform state of stress. For the samples tested in the current study, the wave speed was ultrasonically determined to be 4120 m/s. For the sample length of 6 mm, it requires 5.83 microseconds to achieve four transits within the sample. The total duration of the transmitted pulse is about 75 microseconds. Hence, if the initial portion of the pulse is neglected, over the major portion of the impact duration, the sample is in equilibrium state.

If ε_i, ε_r, ε_t, are respectively the incident, reflected, and transmitted pulses and subscript 1 and 2 are the two ends of the specimen, the displacements at the ends of the specimen are given by

$$u_1 = \int_0^t C_0 \varepsilon_1 dt \tag{1}$$

$$u_2 = \int_0^t C_0 \varepsilon_2 dt, \tag{2}$$

where, C_0 is the wave velocity in the Hopkinson bars. In terms of the incident, reflected and transmitted pulses,

$$u_1 = C_0 \int_0^t (\varepsilon_i - \varepsilon_r) dt \tag{3}$$

$$u_2 = C_0 \int_0^t \varepsilon_t dt, \tag{4}$$

where, stresses and strains are assumed positive in compression. The average strain in the specimen is

$$\varepsilon_s = \frac{u_1 - u_2}{L}. \tag{5}$$

or, in terms of the strain pulses,

$$\varepsilon_s = \frac{C_0}{L} \int_0^t (\varepsilon_i - \varepsilon_r - \varepsilon_t) dt, \tag{6}$$

where, L is the length of the specimen. The forces at the ends of the specimen are obtained from

$$P_1 = EA(\varepsilon_i + \varepsilon_r) \tag{7}$$

$$P_2 = EA\varepsilon_t, \tag{8}$$

where E and A are Young's modulus and the cross-sectional area of the Hopkinson bars. The average force is calculated from

$$P_{av} = \frac{EA}{2}(\varepsilon_i + \varepsilon_r + \varepsilon_t). \tag{9}$$

If it is assumed that $P_1 = P_2$, that is forces are equal at both the ends of the specimen, then from Equations (7) and (8)

$$(\varepsilon_i + \varepsilon_r) = \varepsilon_t$$

$$\text{or } \varepsilon_i = \varepsilon_t - \varepsilon_r \tag{10}$$

substituting Equation (10) in Equation (6) and Equation (9)

$$\varepsilon_s = \frac{C_0}{L} \int_0^t (\varepsilon_t - \varepsilon_r - \varepsilon_r - \varepsilon_t) dt$$

$$\text{or } \varepsilon_s = \frac{-2C_0}{L} \int_0^t \varepsilon_r dt \tag{11}$$

$$P_{av} = EA\varepsilon_t. \tag{12}$$

For the specimen of cross-sectional area A_s, the stress and the strain rate in the specimen become

$$\sigma_s = E\frac{A}{A_s}\varepsilon_t = K_1\varepsilon_t \tag{13}$$

$$\dot{\varepsilon}_s = \frac{-2C_0}{L}\varepsilon_r = K_2\varepsilon_r \tag{14}$$

K_1 and K_2 are the stress and the strain rate multiplying factors for a given specimen and the setup. Hence, only the transient strain data is required to be recorded. Utilizing this data and using Equations 13 and 14, the transient stress and strain rate can be calculated. Strain rate data is then integrated to get the strain versus time data. By superimposing with the stress versus time data, the transient stress-strain data is obtained. For this data analysis, VuPoint signal analysis software was used. Typical incident, transmitted and reflected signals are shown in Figure 4.

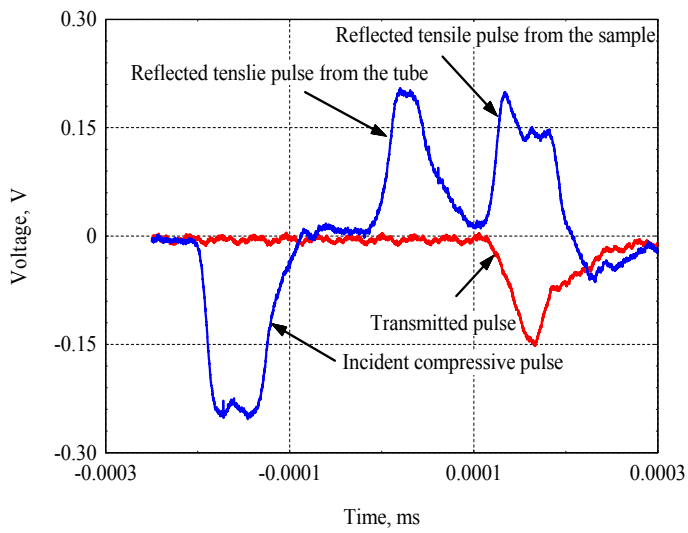

Figure 4. Typical Dynamic Responses from Strain Gages Mounted on the Incident and Transmission Bars

1.3 Results and Discussion

In the high strain rate testing, samples were tested along the in-plane direction. Based on the average strain rates, the samples were grouped in three strain rate ranges: (1) 320/s–391/s; (2) 613/s–645/s; (3) 1001/s–and 1149/s. The lower and higher numbers in each range indicate the limits that include all sample configurations. For individual configurations, these numbers vary slightly. For each range of strain rate, three samples were tested. The transient data for each sample tested under high strain rate data was recorded and stored. The dynamic stress-strain response of laminates was computed for each sample from responses measured using the strain gages mounted on the incident and transmission bars. The data acquisition system was triggered at the instant when the initial compressive pulse reaches the location of the strain gage on the incident bar. The strain rate versus time and stress versus time data were stored in separate files. To plot the dynamic stress-strain curve, it is important to synchronize the two pulses. The starting time was selected from the transmitted pulse at the instant when it started deviating from zero, and the ending time was selected at the time when the pulse flattened out. The portion of the reflected pulse was chosen for the corresponding time range and integrated to get the strain versus time data. Strain rate for each sample is obtained by the slope of strain versus time plot. Strain versus time and stress

versus time data were superimposed by choosing stress for the Y-axis and strain for the X-axis to obtain stress-strain curve. Quasi-static tests were conducted to compare with the high strain rate response.

1.3.1 Plain Weave Laminates

Plain weave fabric ensures the simplest form of interlacing of two sets of yarns in such a way that the yarns interlace each other at right angles. In this weave, fiber tows interlace in alternate order; i.e., the first warp tow overlaps the first fill tow and passes under the second fill tow, and the second warp tow passes under the first fill tow and overlaps the second one and so on. Plain weave gives equal numbers of warp and fill overlaps in unit of weave. Hence, under in-plane loading, the testing was carried out only in the warp direction as the fill direction response was expected to be the same (which was found to be the case in preliminary tests) for stitched and unstitched configurations.

1.3.1.1 Unstitched plain weave carbon/epoxy laminates

The data for static and dynamic tests is summarized in Table 1, which gives the values for peak stress and strain at peak stress and modulus for plain weave unstitched configuration. Figure 5 illustrates the stress-strain response of unstitched 17-layer plain weave carbon/epoxy laminate loaded in the in-plane direction for both static and dynamic loading. Here, each curve is a representative sample for static and high strain rate loading and is not the average of three samples tested for each case. The peak stress is higher for the dynamic loading case. Under dynamic loading, it can be noticed from the graph that peak stress and the slope of stress-strain response increase with strain rate. Average value of peak stress is 196 MPa for the quasi-static, and 333, 415, and 446 MPa, respectively, for the samples tested at three ranges of strain rates, namely 327/s–364/s; 618/s–642/s, and 1002/s–1060/s. As compared to static value, there is an increase of 30-60 percent. The strain at peak stress is much higher for static loading. The average value of strain at peak stress for dynamic loading was of the order of 30–50 percent of the static value. The dynamic modulus is about 2.5 to 4.5 times the static modulus. As the loading is in-plane of the laminate, it induces multiple delaminations. Since the sample size is small, any presence of cracks and porosities in the sample will critically influence the response of the sample. The observed trend in the increase in peak

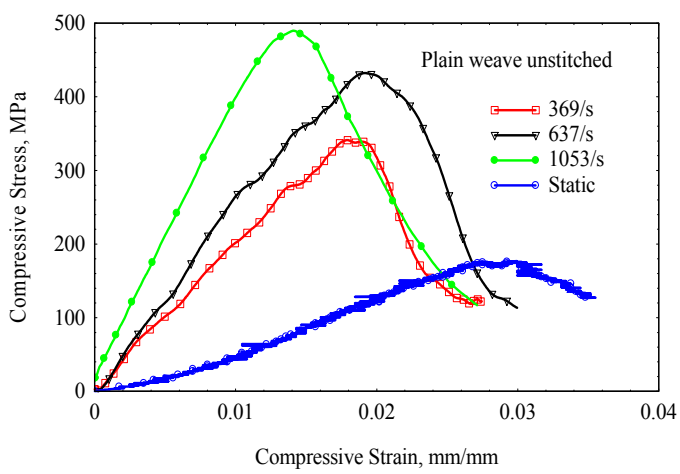

Figure 5. Dynamic Stress-Strain Response of Unstitched Plain Weave Carbon/Epoxy Laminate for Inplane Loading

stress and decreased strain at peak stress under dynamic loading is due to the combined effect of the viscoelastic nature of the polymeric matrix, the time dependent nature of the accumulating damage and considerable temperature rise in the sample. Li and Lambros [24] in their recent study have quantified the temperature rise using infrared detectors. They have observed a temperature increase of approximately 20 °C for a strain rate of 3000/s in high strain rate compression and as much as 100 °C in tension for a strain rate of 1500/s. They have attributed heating due to the global matrix failure (which is the dominant failure mode under compressive loading) as the temperature rises significantly at times when the specimens undergo multiple fragmentations. Palmese et al. [25] have shown that the glass transition temperature of the interface region surrounding a fiber of a polymeric composite is much lower than that of the bulk matrix material. Thus, the amount of heating as small as a few degrees Celsius during the failure process in polymeric matrix composites may have an adverse effect on the composite's continued integrity.

Table 1. Static and Dynamic Properties of Unstitched Plain Weave Carbon /Epoxy Laminates

Sample	Peak Stress, MPa	Strain at Peak Stress	Strain Rate, S^{-1}	Modulus MPa
01	195	0.038	Static	0.86 E4
02	202	0.040	Static	0.83 E4
03	191	0.039	Static	0.79 E4
Average	196	0.039	Static	0.83 E4
01	342	0.018	327	2.12 E4
02	338	0.022	369	1.96 E4
03	317	0.019	364	1.98 E4
Average	333	0.019	354	2.02 E4
04	381	0.024	618	1.89 E4
05	429	0.017	642	3.10 E4
06	433	0.019	637	2.35 E4
Average	415	0.020	633	2.45 E4
07	416	0.017	1060	3.31 E4
08	430	0.014	1002	3.25 E4
09	492	0.014	1053	4.02 E4
Average	446	0.015	1039	3.52 E4

The failure modes of the samples loaded in-plane at static and high strain rate loading at different strain rates are illustrated through optical micrographs in Figure 6. In the case of static loading, the failure is due to the combined effect of crushing on the loading face with global shearing and splitting of the laminate with the buckling of fibers along the shear plane. Under static loading, the laminate will have lot of time to distribute the load and undergo steady deformation. Hence, the strain for the static loading is higher as compared to the high strain rate loading. The failure modes under dynamic loading are distinctly different than the static case. At all strain rates, the samples showed delamination and shear fracture. At strain rates 327/s–369/s and 618/s– 642/s, multiple shear fracture zones were evident. Delamination becomes an additional failure mode with multiple shear fractures that coalesce in to longitudinal fracture. At strain rate range of 1002/s-1060/s, samples split in to two or more sublaminates. Figures 7 and 8 illustrate optical and scanning electron micrographs of samples loaded at strain rates of 637/s and 1053/s, respectively. The optical micrographs show the loading and the side face of samples. The scanning electron micrographs are chosen from selected locations on the sample to highlight the dominant failure modes, as shown on the optical micrographs. These figures illustrate clearly the failure modes through

delamination, shear fracture, and fiber microbuckling along the shear fracture plane. In addition, the crushing of loading face is quite evident on the micrograph of the sample loaded at 1053/s.

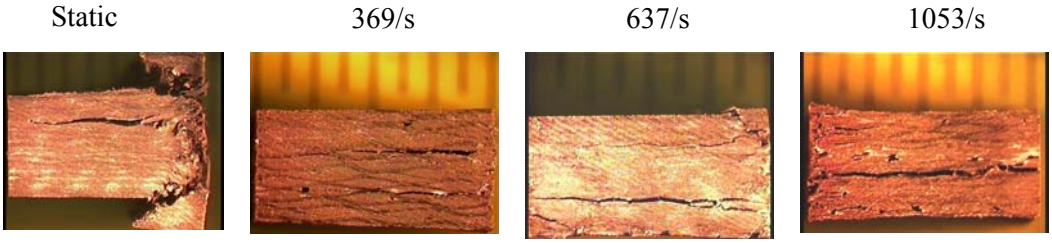

Figure 6. Optical Micrographs of Unstitched Plain Weave Sample for In-plane Loading Static, 369/s, 637/s and 1053/s

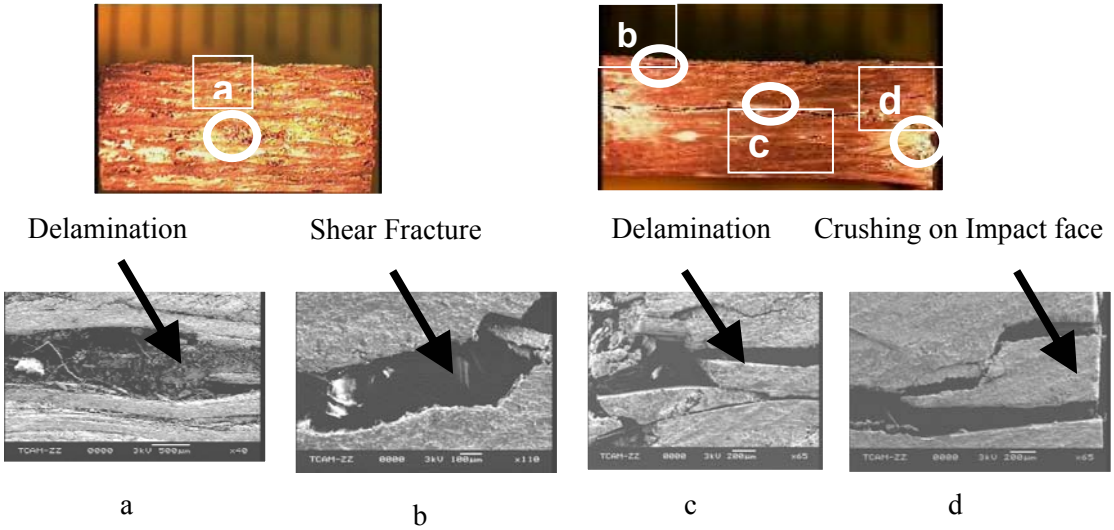

Figure 7. Optical and Scanning Electron Micrographs of Unstitched Plain Weave Samples for In-plane Loading at a Strain Rate of 637/s

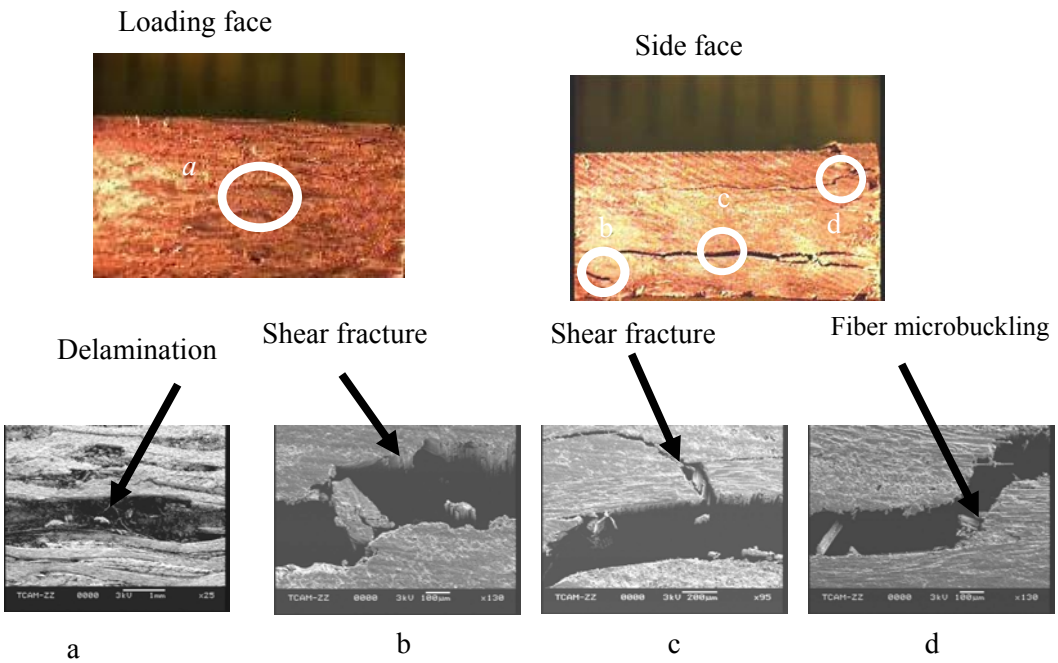

Figure 8. Optical and Scanning Electron Micrographs of Unstitched Plain Weave Samples for In-plane Loading at Strain Rate of 1053/s

1.3.1.2 Stitched Plain Weave Carbon/Epoxy Laminates

The data for static and dynamic properties for plain weave stitched configuration is summarized in Table 2, which gives peak stress, strain at peak stress, and modulus of the samples. Figure 9 illustrates dynamic response curves for the plain weave stitched samples tested in the in-plane direction for static and at different strain rates of loading. Average value of peak stress is 184 MPa for the quasi-static, and 247, 295, and 352 MPa, respectively, for the samples tested at three ranges of strain rates; namely, 322/s–381/s; 613/s–685/s and 1001/s–1077/s. The dynamic modulus was about 1.8 to 3 times higher as compared to static modulus. However, if the properties of stitched and unstitched samples are compared, the static properties would be affected slightly. However, the dynamic strength reduced considerably with modulus reducing slightly. The modes of failure are quite different. Due to the presence of stitch line at the center of the sample, the damage fronts that initiate at the loading face get arrested at the stitch location. The energy absorption takes place through buckling and brooming of the laminate above the stitch line under static loading. This is illustrated through the micrograph shown in Figure 10. However, under dynamic loading the failure is again different. At lower strain rate range of 322/s–381/s, there are few cracks that initiate through the length of the laminate. These cracks initiate at the loading face and get arrested by the stitch. At strain rate range of 613/s–685/s, the number of cracks increase and the shear mode becomes prominent. Optical and scanning electron micrographs in Figure 11 illustrate this trend. At the strain rate range of 1001/s–1077/s, the samples fail by crushing at the loading face and a major shear fracture that initiates from the loading surface and terminates at the stitch line (see Figure 11). Figure 12 illustrates the optical and scanning electron micrographs of the samples loaded at 1038/s. Scanning

electron micrographs illustrated through Figure 12 a-c show the termination of damage front at the stitch line. Figure 12-d illustrates the crushing at the impact surface along with the shear fracture zone.

Table 2. Static and Dynamic Properties of Stitched Plain Weave Carbon/Epoxy Laminates

Sample	Peak stress, MPa	Strain at Peak Stress	Strain Rate, S^{-1}	Modulus MPa
01	190	0.038	Static	0.98 E4
02	182	0.032	Static	1.02 E4
03	180	0.035	Static	1.00 E4
Average	184	0.035	Static	1.01 E4
01	228	0.013	381	2.10 E4
02	287	0.017	387	1.57 E4
03	225	0.015	322	1.72 E4
Average	247	0.015	363	1.79 E4
04	300	0.021	613	2.27 E4
05	292	0.015	685	2.41 E4
06	293	0.028	629	2.03 E4
Average	295	0.021	642	2.23 E4
07	341	0.014	1038	2.94 E4
08	393	0.016	1001	3.20 E4
09	321	0.014	1077	2.70 E4
Average	352	0.014	1039	2.95 E4

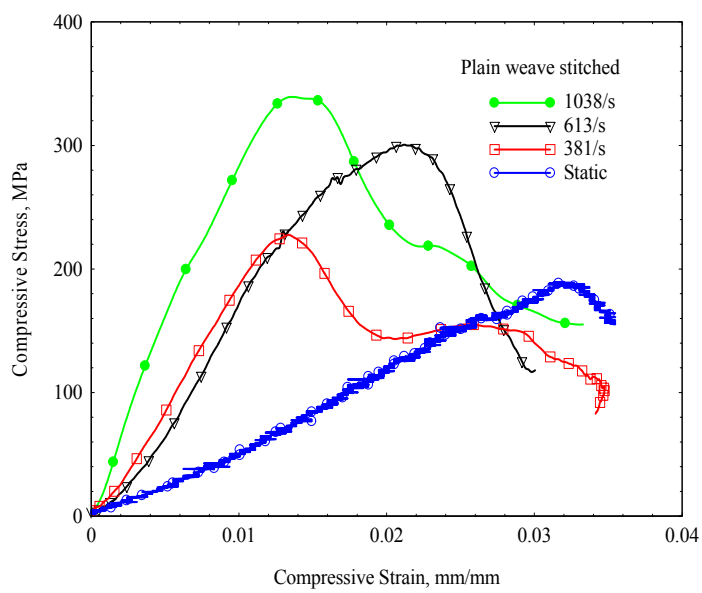

Figure 9. Dynamic Stress-Strain Response of Stitched Plain Weave Carbon/Epoxy Laminate for In-plane Loading

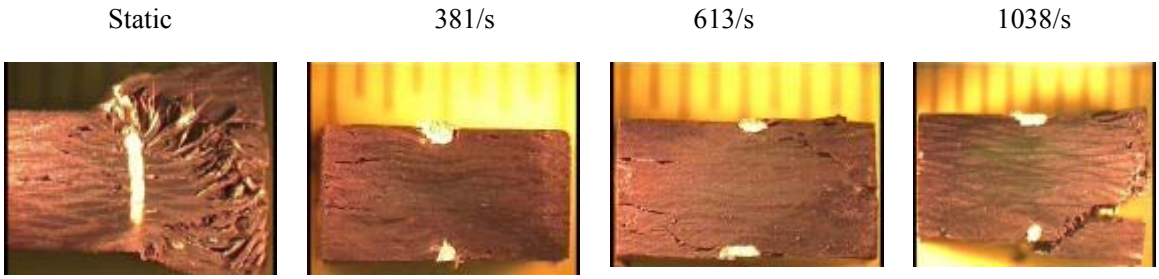

Figure 10. Optical Micrographs of Stitched Plain Weave Sample for In-plane loading Static, 381/s, 613/s and 1038/s

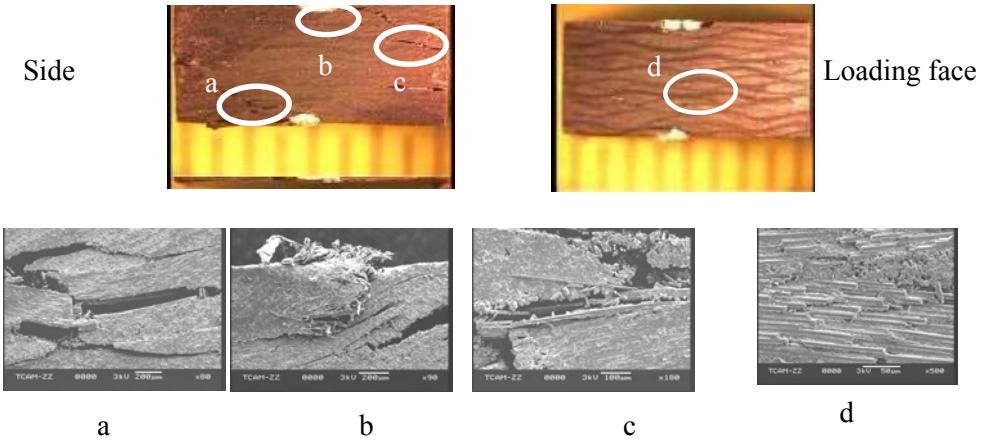

Figure 11. Optical and Scanning Electron Micrographs of Plain Weave Stitch Sample for In-plane Loading at Strain Rate of 613/s

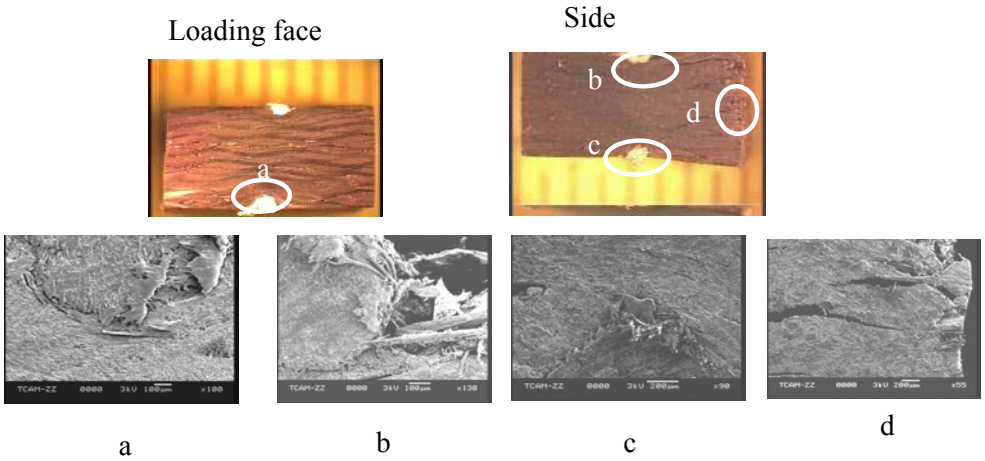

Figure 12. Optical and Scanning Electron Micrographs of Plain Weave Stitch Sample for In-plane Loading at Strain Rate of 1038/s

1.3.2 Satin Weave Carbon/Epoxy Laminates

In the case of eight harness satin weave, the surface of the cloth consists almost entirely of fill floats, as in the repeat of weave, each thread of fill passes over seven and under one threads of warp. This arrangement produces fabric with a maximum degree of smoothness without prominent weave features. The unit weave size is considerably larger in this case. Since the high strain rate sample dimensions are small, it can be reasonable to expect the response to be slightly different in the fill and warp directions. Hence, in the test matrix for satin weave samples, the loading along both fill and warp directions is considered.

1.3.2.1 Unstitched Satin Weave Carbon/Epoxy Laminates

1.3.2.1.1 In-plane Loading (0°/Warp Direction)

The data for static and dynamic tests is summarized in Table 3, which gives the values for peak stress, strain at peak stress, and modulus for unstitched satin weave laminates loaded in warp direction. Figure 13 illustrates the stress-strain response of 17-layer unstitched satin weave carbon/epoxy laminate loaded in the in-plane warp direction for both static and dynamic loading. The values of peak stress and the modulus are higher for the dynamic loading case and increase with increase in strain rate. Average value of peak stress is 227 MPa for the quasi-static, and 379, 446, and 525 MPa, respectively, for the samples tested at three ranges of strain rates, namely 344/s–375/s, 645/s–651/s, and 1021/s–1149/s. The average value of modulus for the corresponding loading rates is respectively 1.11E4, 2.19E4, 2.6E4, and 4.5E4 MPa. The strain at peak stress was higher for static loading. For the dynamic loading it was 50–59

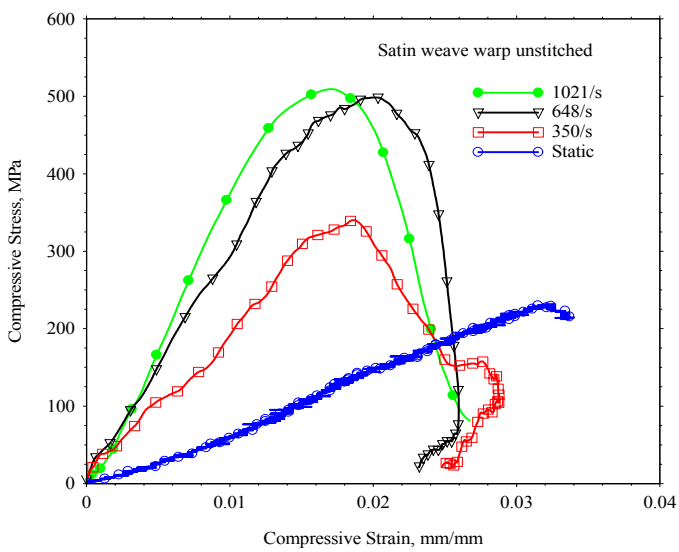

Figure 13. Dynamic Stress-Strain Response of Unstitched Satin Weave Carbon/Epoxy Laminate for Inplane Loading Along Warp Direction

percent of static value. Under dynamic loading, variation in the strain at peak stress with strain rate was marginal. The properties of satin weave samples showed relatively higher value as compared to plain weave laminates. This is attributed to the lower crimp angles in the satin weave laminates, which also influences the failure modes. The optical micrographs for the unstitched satin weave samples loaded in the in-plane warp direction for different ranges of strain rates are shown in Figure 14. In the case of static loading, the failure is due to the global shearing of the laminate with the microbuckling of fibers along the

shear plane. The predominant brooming effect that was seen in plain weave samples is not evident here. The major energy absorbing mechanism is fiber microbuckling. Optical micrographs of the samples indicated little damage for samples loaded at 350/s–375/s strain rate range and some indications of delamination and shear fracture at 645/s–651/s. The samples loaded in the range of 1021/s–1149/s, however, exhibited catastrophic failure through multiple delamination and shear fracture. Scanning electron micrographs of the loading face of the sample impacted at 646/s indicate initiation of splitting of the laminate, while the side faces show the indications of delamination and shear fracture (Figure 15). Figure 16, illustrate optical and scanning electron micrographs of the sample loaded at 1021/s. Figure 16-a illustrate the splitting damage at the loading face and Figure 16-b represents the longitudinal splitting of the laminate along with the shear fracture. These shear zones tend to coalesce and propagate further as longitudinal crack along the interface of the plies, thus splitting the sample in to two or more pieces.

Table 3. Static and Dynamic Properties of Unstitched Satin Weave Carbon /Epoxy Laminates Loaded in the Warp Direction

Sample	Peak stress, MPa	Strain at Peak Stress	Strain Rate, S^{-1}	Modulus, MPa
01	232	0.034	Static	1.20 E4
02	225	0.036	Static	1.15 E4
03	224	0.032	Static	1.00 E4
Average	227	0.034	Static	1.11 E4
01	411	0.019	344	2.16E4
02	384	0.018	350	1.98 E4
03	342	0.019	375	2.43 E4
Average	379	0.018	356	2.19 E4
04	501	0.020	648	3.20 E4
05	409	0.019	651	2.20 E4
06	430	0.020	645	2.41 E4
Average	446	0.019	648	2.60 E4
07	486	0.015	1021	4.64 E4
08	510	0.017	1106	4.46 E4
09	580	0.015	1149	4.42 E4
Average	525	0.015	1092	4.50 E4

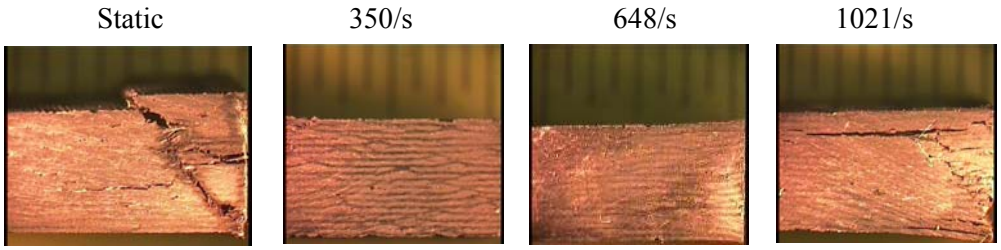

Figure 14. Optical Micrographs of Unstitched Satin Weave Sample for Warp Loading Static, 350/s, 648/s and 1021/s

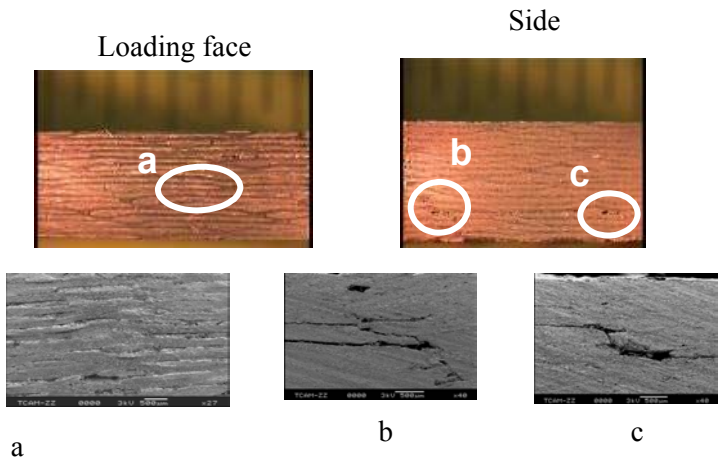

Figure 15. Optical and Scanning Electron Micrographs of Satin Weave Unstitch Samples for Warp Loading at Strain Rate of 648/s

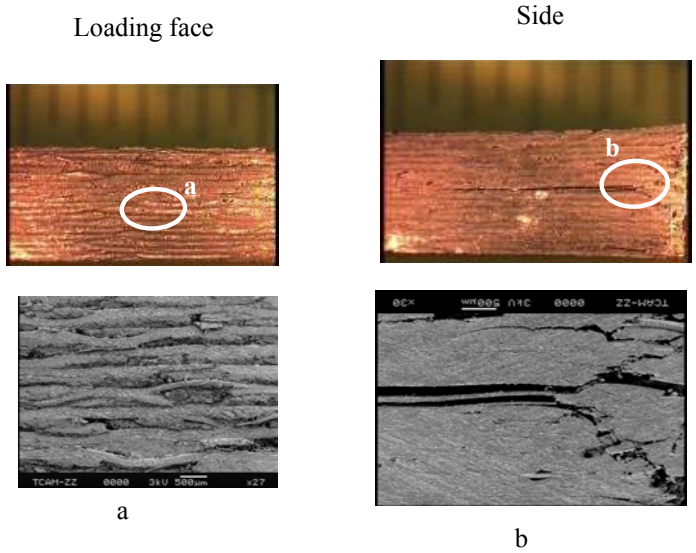

Figure 16. Optical and Scanning Electron Micrographs of Unstitched Satin Weave Samples for Warp Loading at Strain Rate of 1021/s

1.3.2.1.2 In-plane Loading (90°/Fill Direction)

Static and dynamic properties of the unstitched satin weave samples loaded in the fill direction are given in Table 4. Figure 17 illustrates stress-strain response for both static and dynamic loading. The average value of peak stress is 237 MPa for the quasi-static and 400, 493, and 561 MPa respectively, for the samples tested at three ranges of strain rates, namely 364/s–391/s; 558/s–675/s and 1045/s–1123/s. There was a 76–141 percent increase in peak stress under dynamic loading compared to static value. The strain

at peak stress was higher for static loading, the average strain value at peak stress under dynamic loading was 50–56 percent of the static value. The dynamic modulus was again higher by about 3.5 to 4.5 times as compared to the static value. As compared to warp direction values, all of the properties are higher for the fill direction loading. Optical micrographs for samples tested under static and dynamic loading in the fill direction are shown in Figure 18. The sample under static loading failed predominantly by shear fracture. The number of shear planes was more as compared to the sample loaded in the warp direction. Interestingly, the samples loaded under dynamic conditions illustrate more shear fracture zones that initiated from the loading surface. However, at the strain rate of 1045/s, the sample split right along the mid height with minimum shear fracture. Figures 19 and 20 illustrate the optical and scanning electron micrographs of the samples loaded at 617/s and 1045/s, respectively. It can be noticed that the failure mode is totally dominated by delamination and splitting with very little shear fracture. This is a considerable shift as compared to warp direction loading.

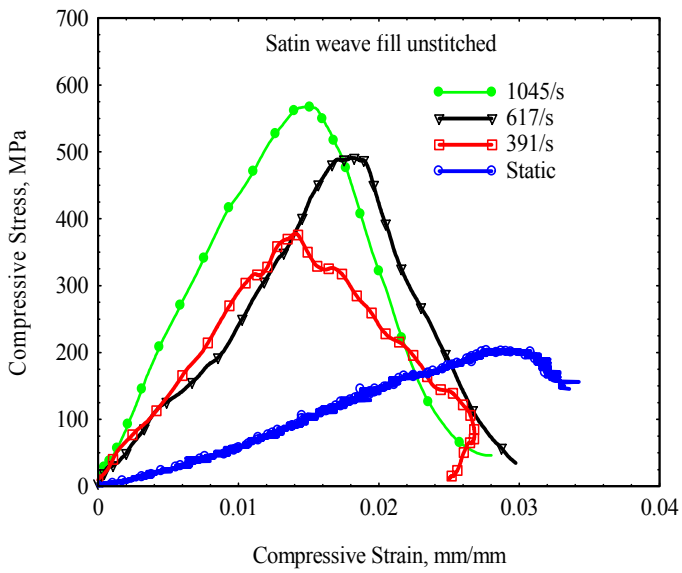

Figure 17. Dynamic Stress-Strain Response of Unstitched Satin Weave Carbon/Epoxy Laminate for In-plane Loading Along the Fill Direction

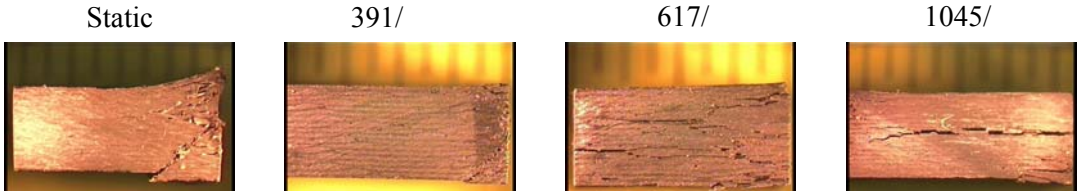

Figure 18. Optical Micrographs of Satin Weave Unstitched Sample for the Fill Loading Static, 391/s, 617/s and 1045/s

Table 4. Static and Dynamic Properties of Unstitched Satin Weave Carbon/Epoxy Laminates Loaded in the Fill Direction

Sample	Peak stress, MPa	Strain at Peak Stress	Strain Rate, S^{-1}	Modulus, MPa
01	225	0.032	Static	1.12 E4
02	242	0.030	Static	1.21 E4
03	244	0.029	Static	1.18 E4
Average	237	0.030	Static	1.17 E4
01	434	0.018	369	3.28 E4
02	380	0.014	391	3.61 E4
03	385	0.020	364	3.83 E4
Average	400	0.017	374	3.57 E4
01	462	0.018	558	4.29 E4
02	493	0.018	617	4.31 E4
03	526	0.017	675	3.71 E4
Average	493	0.017	617	4.10 E4
01	570	0.015	1045	5.02 E4
02	568	0.017	1070	4.25 E4
03	545	0.016	1123	4.69 E4
Average	561	0.016	1079	4.65 E4

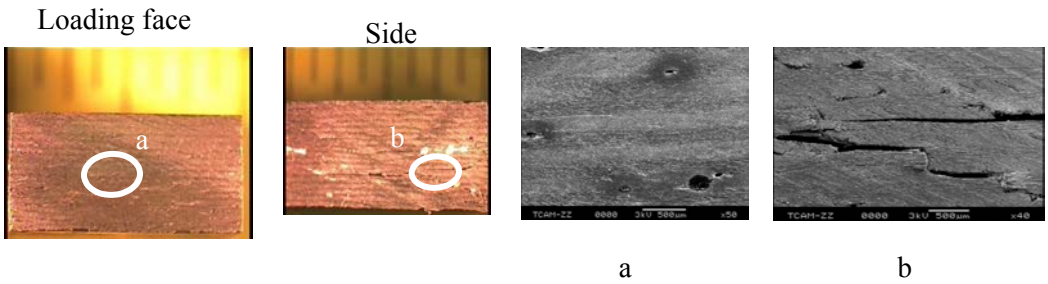

Figure 19. Optical and Scanning Electron Micrographs of Satin Weave Unstitched Samples for Fill Loading at Strain Rate of 617/s

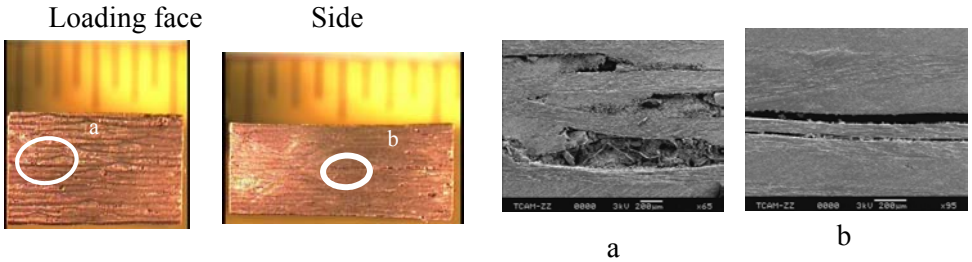

Figure 20. Optical and Scanning Electron Micrographs of Satin Weave Unstitched Samples for Fill Loading at Strain Rate of 1045/s

1.3.2.2 Stitched Satin Weave Carbon/Epoxy Laminates

In the case of stitched satin weave carbon/epoxy laminates, the samples are tested in two different directions; i.e. along warp and fill directions, data in terms of average values for peak stress and strain at peak stress for different stitched configurations are summarized. Results of the study are discussed in the following sections.

1.3.2.2.1 In-plane Loading (0°/Warp Direction)

Table 5 gives the values for peak stress, strain at peak stress and modulus for stitched satin weave laminates loaded under static and high strain rate compression in the warp direction. Figure 21 illustrates the stress-strain response for both static and dynamic loading. The average value of peak stress is 222 MPa for the quasi-static and 308, 361, and 400 MPa, respectively, for the samples tested at three ranges of strain rates; namely, 324/s–361/s, 601/s–621/s, and 1088/s–1110/s. The peak stress is higher for the dynamic loading case and increases with increase in strain rate. The strain at peak stress was higher for static loading. For the dynamic loading, it was 40–50 percent of static value. Under dynamic loading, variation in the strain at peak stress with strain rate was marginal. The dynamic modulus is about 2 to 4.5 times as compared to static loading. A comparison of stitched and unstitched samples (Table 3) loaded in the warp direction indicates that the static property is not affected much. Under dynamic loading, the peak stress reduces considerably, whereas the modulus is affected little except at the highest strain rate range.

Table 5. Static and Dynamic Properties of Stitched Satin Weave Carbon/Epoxy Laminates Loaded in the Warp Direction

Sample #	Peak stress, MPa	Strain at Peak Stress	Strain Rate, S^{-1}	Modulus, MPa
01	205	0.037	Static	0.78 E4
02	254	0.039	Static	0.81 E4
03	208	0.038	Static	0.85 E4
Average	222	0.038	Static	0.81 E4
01	281	0.020	324	1.91 E4
02	334	0.020	360	2.23 E4
03	308	0.018	361	2.60 E4
Average	308	0.019	349	2.24 E4
01	363	0.019	621	2.45 E4
02	339	0.020	615	2.62 E4
03	381	0.014	601	3.26 E4
Average	361	0.017	613	2.77 E4
01	352	0.015	1011	3.48 E4
02	423	0.016	1088	3.02 E4
03	424	0.018	1110	3.36 E4
Average	400	0.016	1069	3.28 E4

Optical micrographs for samples tested under static and dynamic loading conditions are shown in Figure 22. Under static loading, the fracture is dominated by shear. Shear fracture fronts initiate from the center of the sample and extend outward before terminating at the stitch line. However under dynamic loading, the damage is more through longitudinal cracks which extend as delaminations in few samples up to the strain rate of 645/s. However, at the strain rate range of 1088/s–1110/s, the predominant failure is due to

shear fracture and delamination splitting of the sheared portion of the laminate. Figure 23 illustrates optical and scanning electron micrographs of the stitched satin weave sample loaded along the warp direction at the strain rate of 601/s. The scanning electron micrograph (SEM) of the loaded face indicates clear delamination, whereas the SEM of the side face indicates the shear fracture which gets arrested at the stitch location. Figure 24 indicates the optical and scanning electron micrographs of the sample loaded at 1061/s. The damage on the loading face is more severe. The SEM of the side face shows severe damage in the sample, as the portion of it is clearly removed at the stitch location (Figure 24-b). Hence, under both static and dynamic loading, stitching prevents total fracture of the sample and facilitates higher energy absorption, which will be helpful in vehicle crash situations.

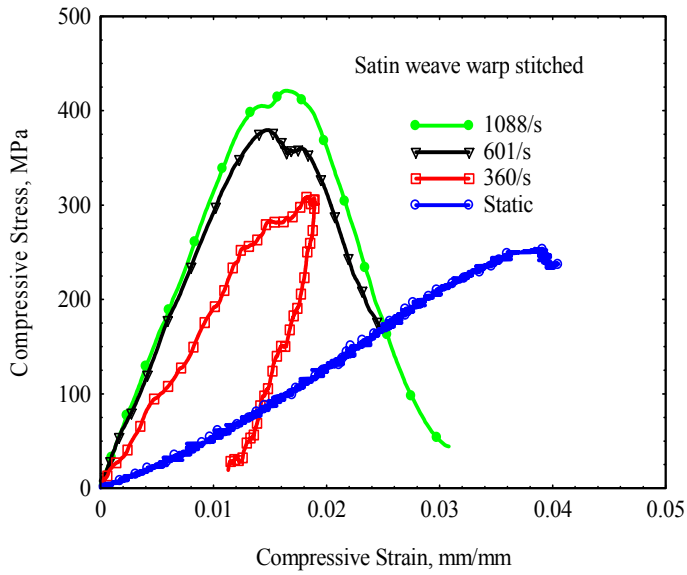

Figure 21. Dynamic Stress-Strain Response of Stitched Satin Weave Carbon/Epoxy Laminate Loaded in the Warp Direction

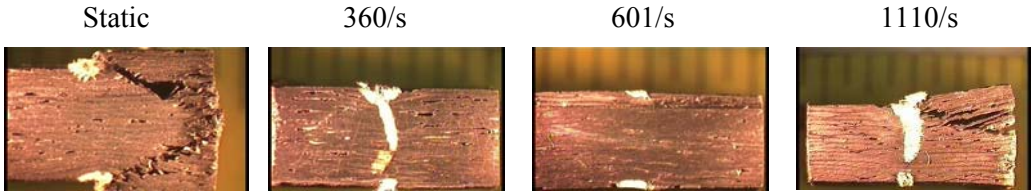

Figure 22. Optical Micrographs of Satin Weave Stitched Sample for the Warp Loading Static, 360/s, 601/s and 1110/s

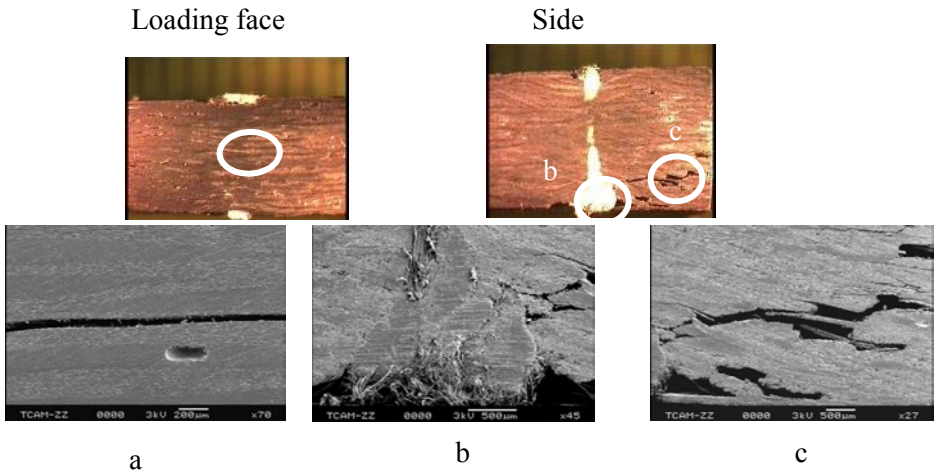

Figure 23. Optical and Scanning Electron Micrographs of Stitched Satin Weave Samples for the Warp Loading at Strain Rate of 601/s

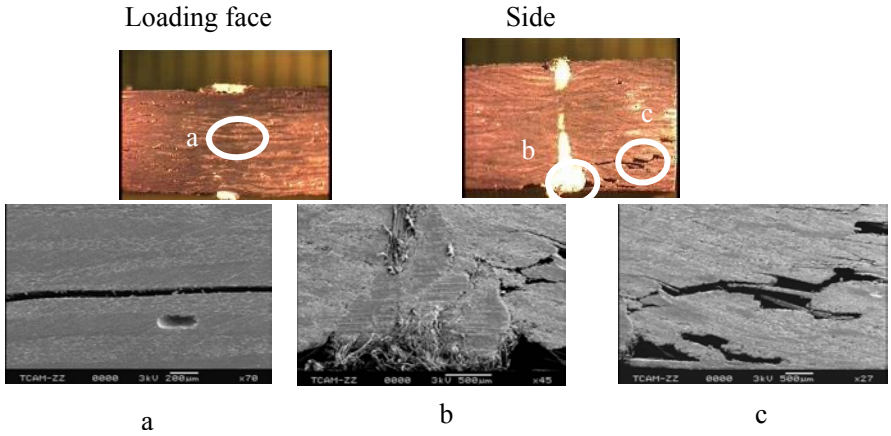

Figure 24. Optical and Scanning Electron Micrographs of Stitched Satin Weave Samples for the Warp Loading at Strain Rate of 1061/s

1.3.2.2.2 In-plane Loading (90°/Fill Direction)

Results of the static and dynamic tests on satin weave stitched samples loaded in the fill direction are presented in Table 6. Figure 25 illustrates stress-strain for both static and dynamic loading. Average value of peak stress is 204 MPa for the quasi-static, and 330, 370, and 394 MPa, respectively, for the samples tested at three ranges of strain rates, namely 320/s–385/s, 599/s–645/s and 1007/s–1118/s. There was a 55–90 percent increase in peak stress under dynamic loading compared to static value. The average strain value at peak stress under dynamic loading was 35–48 percent of the static value. The dynamic modulus was higher by 3.5 to 4.5 times as compared to static value. A comparison between the properties of the stitched samples loaded in fill (Table 6) and warp (Table 5) indicate very little difference in the properties. However, the trend of lower value of dynamic peak stress of stitched samples (Table 6) as compared to the unstitched samples (Table 4) is well maintained for the samples loaded in the fill direction. Optical micrographs for samples tested under static and dynamic loading conditions are shown

in Figure 26. The sample loaded under static compression exhibited shear failure, while the samples loaded dynamically indicated delaminations at lower strain rates (up to 645/s) and shear fracture with splitting at the strain rate range of 1007–1118/s. Figures 27 and 28 illustrate the scanning electron microscope study for key areas as indicated on the optical micrographs for two different strain rate ranges. Under static loading, the samples failed by shear failure up to the stitched line, and in the case of dynamic loading at the lowest strain rate range of 320/s–385/s, the samples showed no visible damage, and in the range of 608/s–645/s, the samples exhibited splitting delaminations up to the stitching intersection, and at the higher strain rate range of 1007/s–1118/s, the failure modes were shear fracture, multiple delamination, and global buckling of the sample.

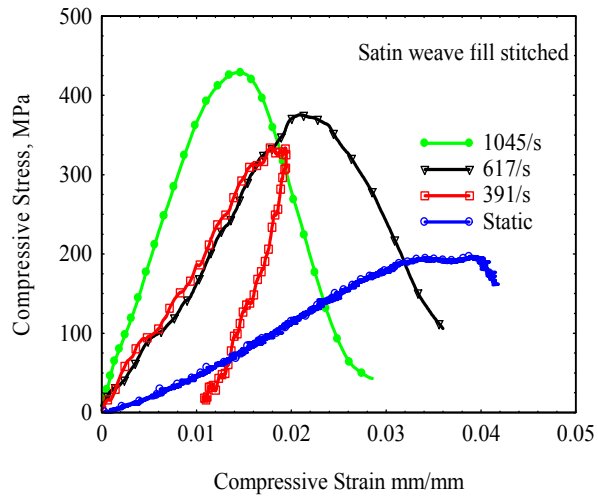

Figure 25. Dynamic Stress-Strain Response of Stitched Satin Weave Carbon/Epoxy Laminate Loaded in the Fill Direction

Table 6. Static and Dynamic Properties of Stitched Satin Weave Carbon/Epoxy Laminates Loaded in the Fill Direction

Sample	Peak stress, MPa	Strain at Peak Stress	Strain Rate, S^{-1}	Modulus, MPa
01	170	0.038	Static	0.68E4
02	198	0.039	Static	0.95E4
03	243	0.040	Static	0.75E4
Average	204	0.039	Static	0.80E4
01	352	0.019	320	2.91 E4
02	302	0.017	376	2.77 E4
03	335	0.018	385	3.00 E4
Average	330	0.018	360	2.89 E4
01	374	0.019	645	3.15 E4
02	375	0.020	608	3.24 E4
03	363	0.018	599	3.19 E4
Average	370	0.019	618	3.19 E4
01	384	0.015	1007	3.38 E4
02	367	0.015	1076	3.56 E4
03	429	0.014	1118	3.87 E4
Average	394	0.014	1067	3.60 E4

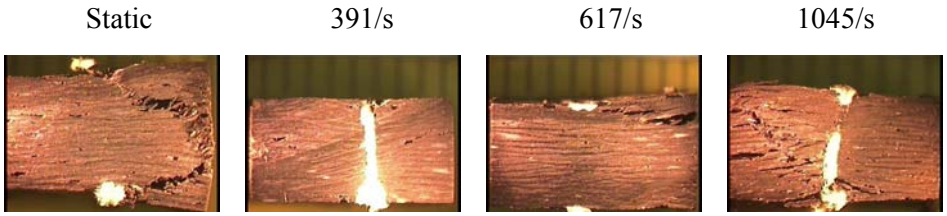

Figure 26. Optical Micrographs of Stitched Satin Weave Laminate Loaded in the Fill Direction at Static, 391/s, 617/s, and 1045/s

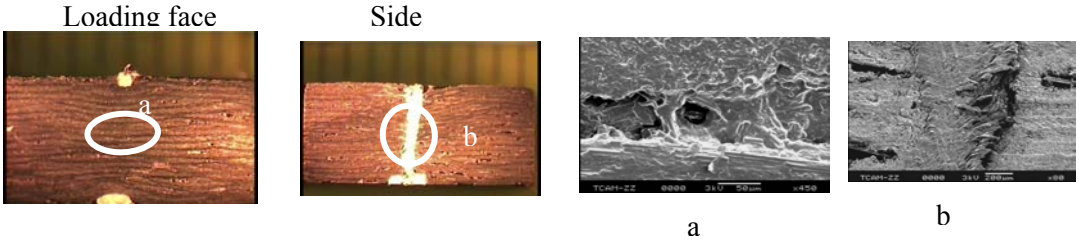

Figure 27. Optical and Scanning Electron Micrographs of Satin Weave Stitch Samples for the Fill Loading at Strain Rate Range of 617/s

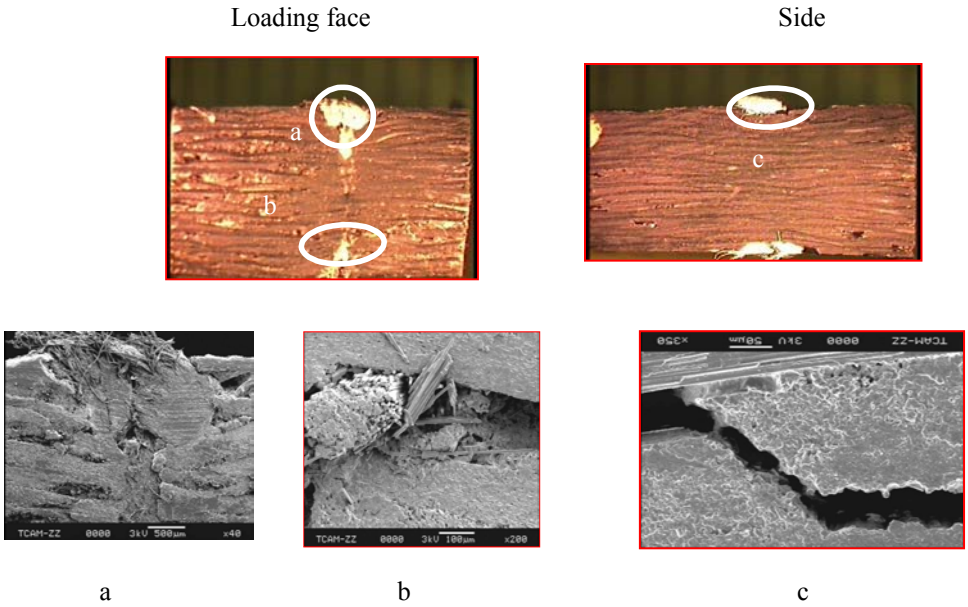

Figure 28. Optical and Scanning Electron Micrographs of Stitched Satin Weave Samples Loaded Along Fill Direction at Strain Rate Range of 1045/s

1.3.3 Comparison of Different Sample Configurations

It is worthwhile to compare the results of static and high strain rate tests for different sample configurations. The results of Tables 1 through 6 are plotted for the six sample configurations in figures 29 and 30, which illustrate the variation of peak stress and modulus as functions of the strain rate. For each sample configuration, the data is fitted with a linear curve. From these curves, it is clear that both peak stress and modulus values are higher for unstitched samples as compared to the corresponding stitched samples. Properties for satin weave samples were higher as compared to the plain weave samples. This is attributed to the straighter fabric architecture that resulted in lower crimp angle in satin weave fabric. Among the satin weave samples, the fill-direction-loaded samples exhibited higher static and dynamic behavior as compared to the warp-direction-loaded samples. Shear fracture was dominant for the samples which had higher crimp angles. Though stitching reduced the dynamic peak stress in the samples, it facilitated higher energy absorption. The damage front was arrested by the stitch line. This will be of particular importance in situations like vehicular crash.

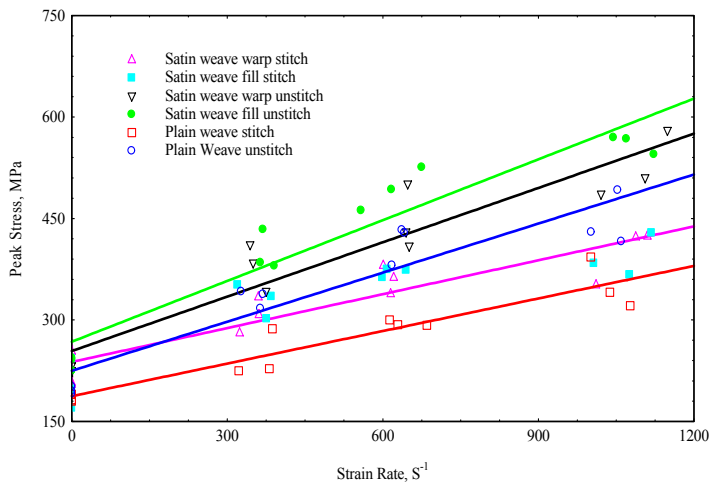

Figure 29. Variation of Peak Stress with Strain Rate

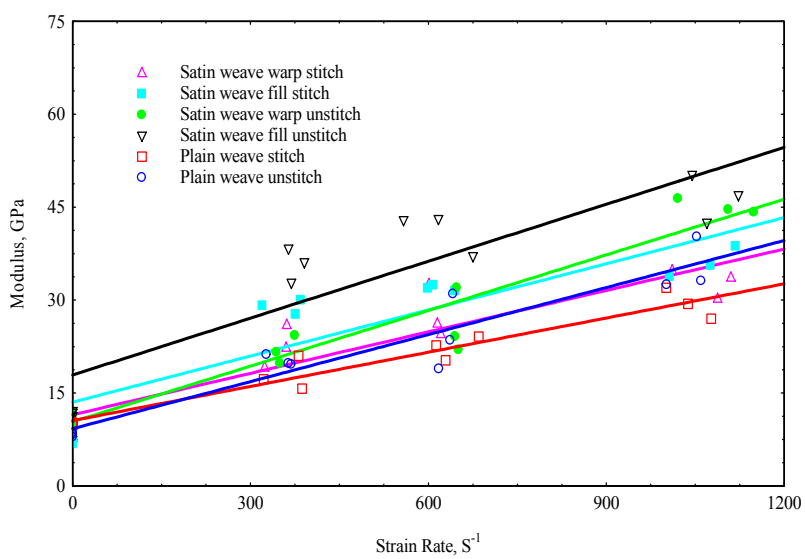

Figure 30. Variation of Modulus with Strain Rate

1.4 Conclusions

Investigations were carried out on 17-layer plain and satin weave unstitched and stitched carbon/epoxy laminates manufactured using affordable VARIM under high strain rate loading. The high strain rate tests were conducted using a modified compression SHPB. Using this setup, it is possible to subject the sample to single, controlled input pulse. Plain weave samples were subjected to impact loading in the in-plane warp direction; whereas, in the case of satin weave, impact was carried out in both in-plane warp as well as fill directions. The samples were tested in three different strain rate ranges (1) 320/s–391/s, (2) 613/s–645/s, (3) 1001/s–1149/s. For each range of strain rate, three samples were tested. Quasi-static tests were conducted to compare the results with high strain rate loading. Failure mechanisms were characterized through optical and scanning microscopy. The following conclusions were drawn from the study:

1. Peak stress and modulus were higher for dynamic loading when compared to static loading in case of both stitched and unstitched plain and satin weave samples.
2. As the sample has considerable time for deformation and load redistribution under static loading, the strains are higher. Strain at peak stress was found to be 2–3 times higher in the case of static loading as compared to dynamic loaded samples for all configurations.
3. The peak stress and modulus increases with increase in strain rate for both stitched and unstitched plain and satin weave samples.
4. Unstitched satin and plain weave laminates exhibited higher peak stress and modulus than stitched satin and plain weave laminates for both in-plane loading directions.
5. Satin weave samples exhibit higher peak stress and modulus as compared to plain weave samples. This is due to the straighter fabric architecture of satin weave, resulting in lower crimp angle.
6. For the satin weave samples (both stitched and unstitched), peak stress and dynamic modulus were higher when the samples were loaded in the fill as compared to the warp direction loading.
7. Failure modes were different for both stitched and unstitched samples and also for both satin and plain weave. Unstitched samples predominantly failed by splitting and delaminations, whereas in case of the stitched samples, the failure was by shear fracture, which was arrested by the stitched threads, which also facilitated in higher energy absorptions.

2. Off-Axis High Strain Rate Characterization of Woven Fabric Composites

2.1 Introduction

Studies on the dynamic characterization of advanced composite materials under off-axes loading have been limited. In a majority of structural applications, the composite component has its principal orthotropic material axes aligned with the structural loading axes, i.e., the 0° fiber ply direction is laid parallel to the major loading direction. This means that the component behaves symmetrically under in-plane loading conditions. The current application of composite materials does not utilize the full potential of the material capabilities. We can extend the application of composite materials by having the orthotropic axes of the laminate, off-axis to structural axes and, thus, achieve unique structural behavior, i.e., in-plane shear deformation under axial loading or out-of-plane twisting under axial bending. This off-axis configuration can be tailored to achieve specific deformation. Two research examples of this type of structural tailoring can be seen on the Rockwell highly maneuverable aircraft technology (HiMAT) Demonstrator and the Grumman X-29 forward swept wing (FSW) demonstrator aircraft where the material orthotropic axis is off-set by 36° to the bending axis [26]. Weeks et al. [27] characterized the rate-dependent behavior of AS4/PEEK thermoplastic composite over a wide strain rate range. Off-axis composite specimens were tested in simple tension using SHPB. Weeks et al. observed that the stress/strain curves showed little difference at different orientations, but when compared with quasi-static stress/strain curve, the effect of strain rate was evident. Ninan et al. [28, 29] attempted to characterize the high strain rate behavior of fiber composites using off-axis composite specimens and SHPB. Various factors affecting the SHPB analysis, such as specimen-bar interface friction and extension shear coupling, were numerically and experimentally investigated. Woldesenbet et al. conducted experimental investigations using a SHPB setup to study the effect of fiber orientation on the compressive dynamic properties of a unidirectional IM7/8551-7 graphite/epoxy and K49/3501-6 Kevlar/epoxy composites [30, 31]. They observed that changing the fiber orientation changes the values of ultimate strength and strain of the composite. Vinson et al. conducted experimental investigations on unidirectional IM7/8551-7 graphite/epoxy composites loaded under compression using SHPB at various off-axes angles over strain rates varying from 250-1100/s [32]. Based on the experimental results, they suggested a semi empirical equation correlating static and dynamic strengths with a function that accounts for the orientation and the strain rate. Another important aspect that needs to be addressed to employ composite structures is their cost. Conventionally fiber- reinforced composites are manufactured using prepregs with expensive autoclave molding method. High technology areas are looking for alternative affordable manufacturing methods that can be used with confidence to make structural components without compromising the performance. VARIM is one such simplified and environmentally responsible method of processing. If the industry has to use parts made using the VARIM process, then there is a need generate data for mechanical properties to assist the design. There is limited data available on the off-axis dynamic characterization of woven fabric carbon/epoxy composites manufactured using VARIM process. Hence, in the current effort, investigations are carried out to characterize advanced carbon/epoxy laminates under off-axes high strain rate compression loading using a modified SHPB. Experimental investigations were carried out to characterize plain and satin weave carbon epoxy laminates under dynamic compression loading at different off-axis directions. Response of the laminates was characterized and is discussed in terms of peak stress, strain at peak stress, modulus.

2.2 Experimental Studies

2.2.1 Material Selection and Specimen Fabrication

For fabricating the laminate, plain weave carbon fabric of style 4060-6 weighing 0.3389 kg/m^2 and satin weave fabric of style 5999, 0.336 kg/m^2 were used with SC-15 epoxy resin system using VARIM process.

Samples of size 6 (width) by 6 (height) by 12 (thickness) mm were cut from the panels using a low-speed diamond saw. Subsequently, specimens were polished using sanding rotor equipped with fine sandpaper (grit #800) to ensure parallel loading edges. For off-axis loading, samples were cut at the required angles (0°–45° for plain weave and 0°–90° for satin weave at 15° increments). All of the angles were measured with respect to the 0° (warp) direction of the laminates.

2.2.2 Static and High Strain Rate Compression Testing

To determine the static strength, quasi-static testing was carried out on different types of samples used in the study in an MTS machine in displacement control mode with a constant crosshead speed of 1.27 mm/min. The load and crosshead displacement response for each test was recorded by the data acquisition system. The data was corrected for machine compliance. For high strain rate testing, a modified SHPB test system described in Section 1 was used on different samples in this study.

2.3 Results and Discussion

2.3.1 Plain Weave Carbon/Epoxy Laminates

In the high strain rate testing, samples were tested both along the in-plane direction along 0°, 15°, 30°, and 45°. Samples were tested at strain rates ranging from 1187 to 2289/s. The transient data for each sample tested under high strain rate data was recorded and stored. The dynamic stress-strain response of laminates was computed for each sample from responses measured using the strain gages mounted on the incident and transmission bars. Quasi-static tests were conducted to compare with the high strain rate response. Table 7 gives the results of the static compression tests. Figure 31 represents the stress-strain plot of representative samples subjected to static compression loading for all orientations. The stress-strain curves for 0° samples remain linear till failure, whereas for other angles the relation is nonlinear. This is due to the coupling between axial and shear deformation. The higher the inclination of fibers is to the loading direction, the greater will be the influence of shear deformation. This results in the decrease in peak stress to failure as the orientation increases along with the increase in the strain to failure. Further, modulus also decreases sharply with increase in orientation.

Table 8 represents the dynamic compression properties for plain weave carbon/epoxy composites. For each orientation 10 samples were tested. Increasing the breach pressure increased the strain rate. In the current test, breach pressure was varied from 62–110 kilopascals (9–16 psi). The strain rate for a given pressure setting increased as the orientation of the sample to loading increased. As the orientation increased the peak stresses dropped for all of the strain rates. This is due to the coupling between the axial and shear deformation. Further, the trend of increasing strain at peak stress and decreasing modulus with orientation was well maintained under dynamic loading. In comparison with the static properties, dynamic peak stresses were considerably higher (about 200 percent for 0° and 15° and 150 percent for 30° and 45°). However, strain to failure for dynamic loading was about 50–60 percent as compared to the static value. The dynamic modulus is about 4–5 times the static modulus.

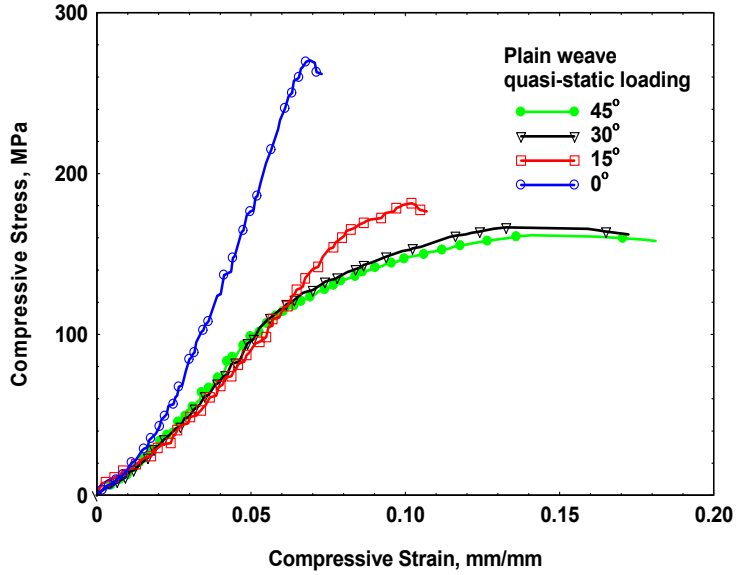

Figure 31. Stress-Strain Curves at Different Orientation under Static Loading

Table 7. On- and Off-Axes Properties of Woven Composites under Static Loading

Loading Angle	Sample	Peak Stress, (MPa)	Strain at Peak Stress	Modulus, (MPa)
0°	JSI01	295	0.058	4450
	JSI02	271	0.069	4319
	JSI04	262	0.080	4363
	Average	276	0.069	4377
15°	JS151	202	0.101	2135
	JS152	175	0.072	2352
	JS154	181	0.102	2366
	Average	186	0.092	2284
30°	JSI301	171	0.156	2161
	JSI303	165	0.146	2188
	JSI304	166	0.140	2178
	Average	167	0.147	2176
45°	JS452	161	0.147	2122
	JS453	163	0.182	1893
	JS455	149	0.139	2029
	Average	158	0.156	2015

Table 8. On- and Off-Axes Properties of Woven Composites under Dynamic Loading

Strain Rate (S^{-1})	Peak Stress, MPa	Strain at Peak Stress	Modulus, MPa
Loading along 0°			
1187	352	0.019	2.42E+04
1239	399	0.020	2.34 E+04
1285	430	0.019	2.79E+04
1374	512	0.021	2.98E+04
1474	416	0.022	2.25E+04
1550	499	0.021	2.76E+04
1773	442	0.023	2.40E+04
1822	466	0.022	2.47E+04
1903	346	0.024	1.88E+04
2289	352	0.045	1.11E+04
Loading along 15°			
1387	329	0.029	1.66 E+04
1474	326	0.027	1.57E+04
1522	330	0.030	1.59E+04
1579	299	0.034	1.43E+04
1692	308	0.025	1.68E+04
1770	340	0.024	1.94E+04
1801	307	0.038	1.24E+04
1840	295	0.027	1.46E+04
1893	293	0.029	1.36E+04
1900	326	0.028	1.46E+04
Loading along 30°			
1345	216	0.048	1.12E+04
1467	238	0.050	1.23E+04
1546	231	0.049	1.05E+04
1600	229	0.059	1.00E+04
1655	244	0.053	1.23E+04
1747	218	0.059	1.01E+04
1802	237	0.049	1.14E+04
1853	234	0.058	1.13E+04
1877	249	0.040	1.14E+04
2001	245	0.045	1.20E+04
Loading along 45°			
1457	226	0.059	1.11E+04
1508	227	0.057	1.21E+04
1618	221	0.063	1.08E+04
1670	236	0.052	1.18E+04
1744	232	0.062	1.17E+04
1830	224	0.071	8895
1920	232	0.063	1.29E+04
1981	236	0.068	1.11E+04
2064	236	0.076	9491
2162	237	0.070	1.16E+04

It is seen from Table 8 that as the strain rate is increased, peak stress and dynamic modulus increase up to a certain limit and then decrease with further increase in the strain rate for 0° samples. Dynamic stress-strain plots of some samples are given in Figure 32, which also give an indication of this effect. The

observed trend in the increase in peak stress and decreased strain at peak stress under dynamic loading is due to the combined effect of the viscoelastic nature of the polymeric matrix, the time-dependent nature of the accumulating damage, and considerable temperature rise in the sample. In the case of static loading, the failure is due to the global shearing of the laminate with the microbuckling of fibers along the shear plane. Laminate has more time to distribute the load and undergo steady deformation. Hence, the strain for the static loading is higher as compared to the high strain rate loading.

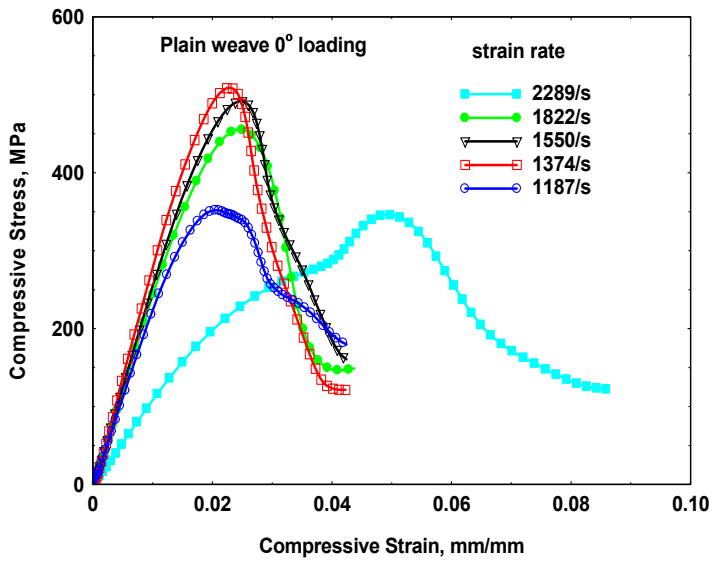

Figure 32. Dynamic Compressive Stress-Strain Plots for the Samples Loaded Along Warp (0°) Direction at Different Strain Rates

Dynamic stress-strain responses for off-axes loading are plotted and shown in Figures 33-35, which represent the responses of samples tested at 15°, 30° and 45° orientations, respectively. For the samples tested at 15° and 30° orientations, the stress-strain relations exhibit linear trend till about 70 percent of the peak stress, beyond which the trend becomes nonlinear with large strains. The effect of shear deformation becomes increasingly dominant as the orientation increases. This can be seen in the response over the non-linear region of samples loaded along 30° and over most of the region for the samples loaded along 45°. The ratio of linear strain to nonlinear strain increases rapidly and is about 3, 5, and 5–6.5 times for the samples tested at 15°, 30° and 45° orientations respectively. Again, this is attributed to the dominant shear deformation. The undulation of the fabric and the resulting crimp angle also contribute to the increased shear deformation. The effect of strain rates on samples tested at different orientations is shown in Figures 36 and 37. Figure 35 represents the stress-strain responses of samples tested at different orientation at strain rates around 1375/s-1450/s, whereas Figure 37 represents the stress-strain responses of samples tested at different orientations at strain rates around 1775/s–1800/s. From both of the figures, the difference in the dynamic response of samples tested along 0° and off-axes angles is very much evident.

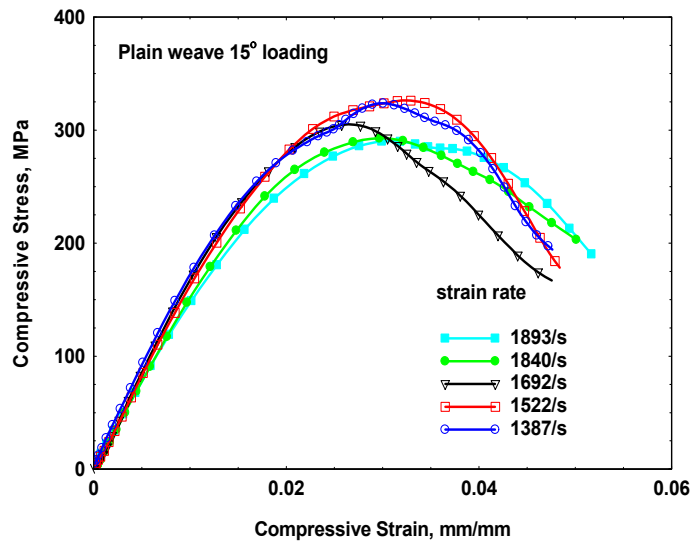

Figure 33. Dynamic Compressive Stress-Strain Plots for the Samples Loaded Along 15° Direction at Different Strain Rates

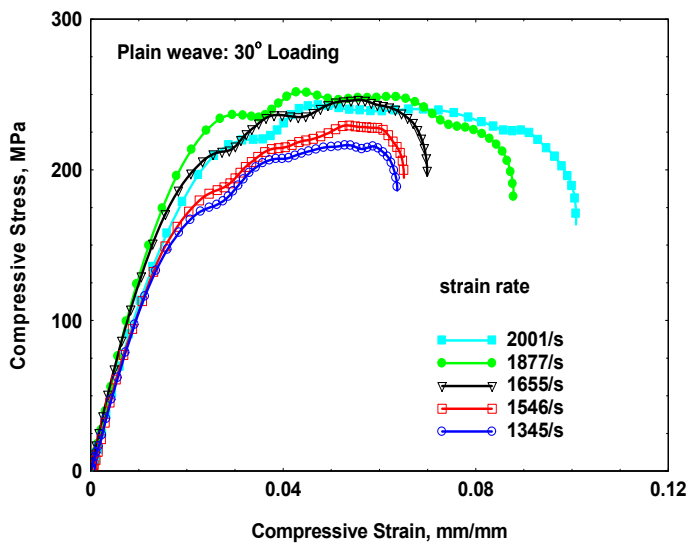

Figure 34. Dynamic Compressive Stress-Strain Plots for the Samples Loaded Along 30° Direction at Different Strain Rates

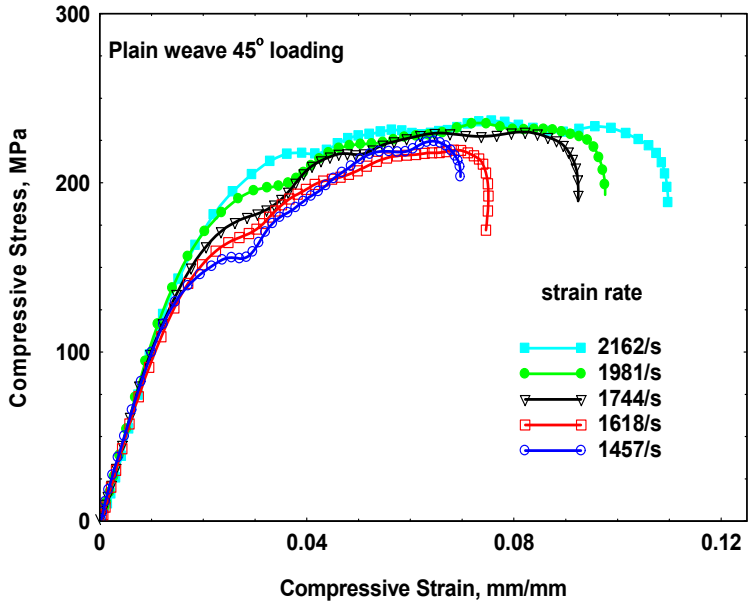

Figure 35. Dynamic Compressive Stress-Strain Plots for the Samples Loaded Along 45° Direction at Different Strain Rates

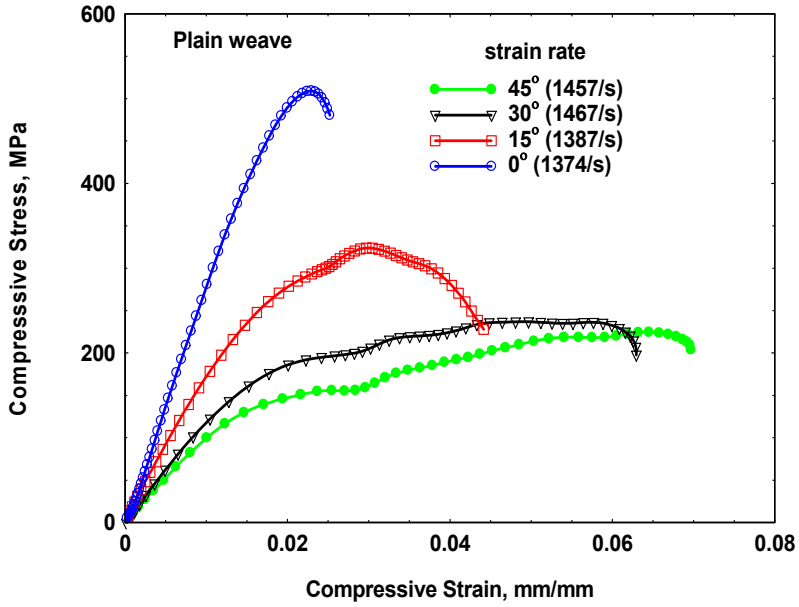

Figure 36. Comparison of Dynamic Stress-Strain Response of Samples Tested at Different On- and Off-Axes Angles at Strain Rate of ~1400/s

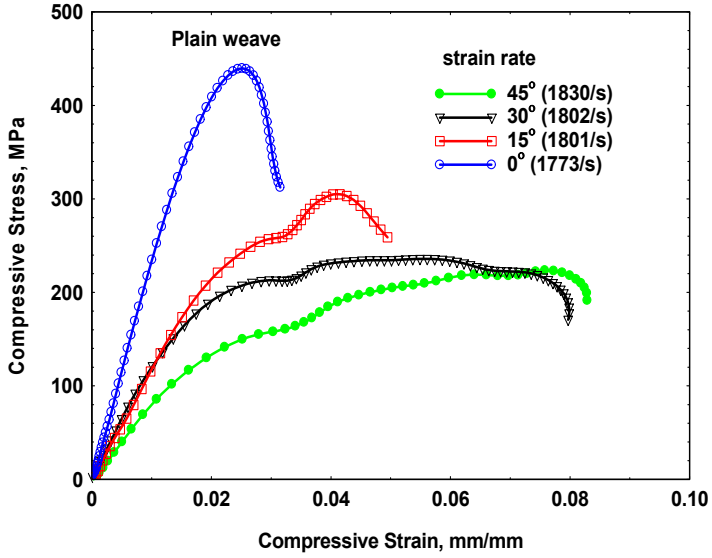

Figure 37. Comparison of Dynamic Stress-Strain Response of Samples Tested at Different On- and Off-Axes Angles at Strain Rate of ~1800/s

The failure modes of the samples loaded in-plane at different strain rates are illustrated through optical micrographs shown in Figures 38–41. Failure mechanisms are dominated by the orientation as well as the strain rate. The samples loaded along 0^0 showed delamination and shear fracture at all the strain rates (figure 37). At the strain rates of 1187/s and 1285/s, multiple shear fracture zones were evident. At the strain rates of 1474/s and above, the samples split into two or more sub laminates. Delamination becomes additional failure mode with multiple shear fractures that coalesce into longitudinal fracture. The failure behavior remains similar when the samples are tested at the orientation of 15^0 (figure 38). However, the total volume of cracks are considerably less Samples tested at strain rates of 1387 and 1474/s exhibit longitudinal cracks as the predominant failure modes. Shear cracks were seen to just start developing at 1474/s. With the increase in the strain rate (1692/s, 1801/s), the shear fracture becomes dominant failure mechanism. At 1692/s, multiple shear fracture is evident and at higher strain rates of 1893/s and 1900/s, the samples split into two pieces, delamination being the major cause of failure with multiple shear fractures that leads to longitudinal fracture. For the samples loaded along 30^0 at lower strain rates and for the samples loaded along 45^0 at all strain rates, there were no apparent indications of any damage (figures 40, 41). There were some indications of microcracks on the surface of the samples when loaded along 30^0 orientation at higher strain rates. However, the overall integrity of the samples remained intact. This was also reflected in the stress-strain responses. The samples seem to unload elastically after the peak load. Any permanent deformation is attributed to the combined effect of the viscoelastic nature of the polymeric matrix, the time dependent nature of the accumulating damage and considerable temperature rise in the sample.

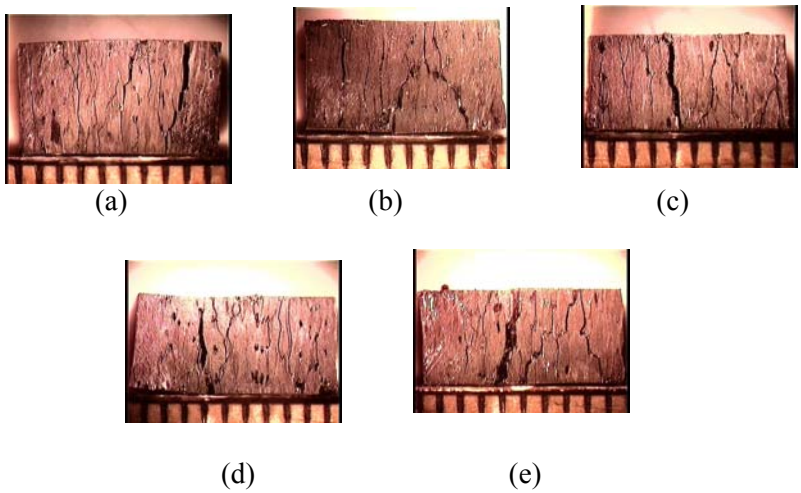

Figure 38. Micrographs of the Samples Tested Under High Strain Rate Compression Loading Along the Warp (0°) Direction at (a) 1187/s, (b) 1285/s, (c) 1474/s, (d) 1773/s, and (e) 2289/s

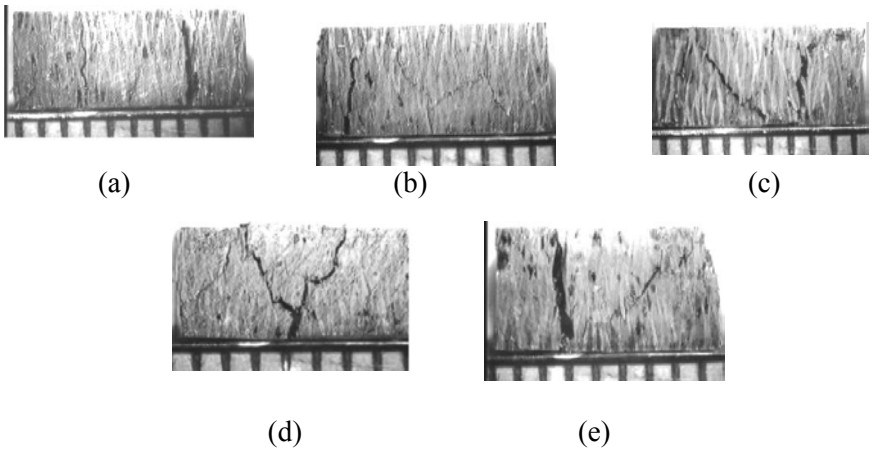

Figure 39. Optical Micrographs at Different Strain Rates for Off-Axis Loading Along the 15° Orientation (a) 387/s, (b) 1474/s, (c) 1692/s, (d) 1893/s, and (e) 1900/s

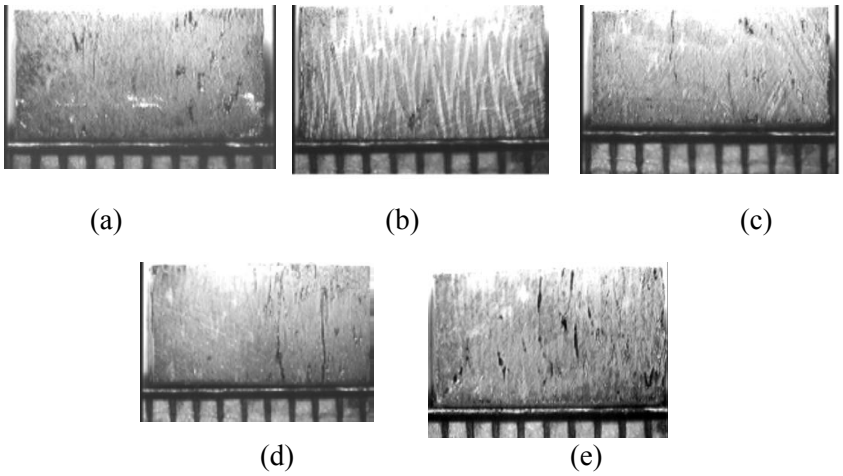

Figure 40. Optical Micrographs at Different Strain Rates for Off-Axis Loading Along the 30° Orientation (a) 1345/s, (b) 1546/s, (c) 1747/s, (d) 1853/s, and (e)2001/s

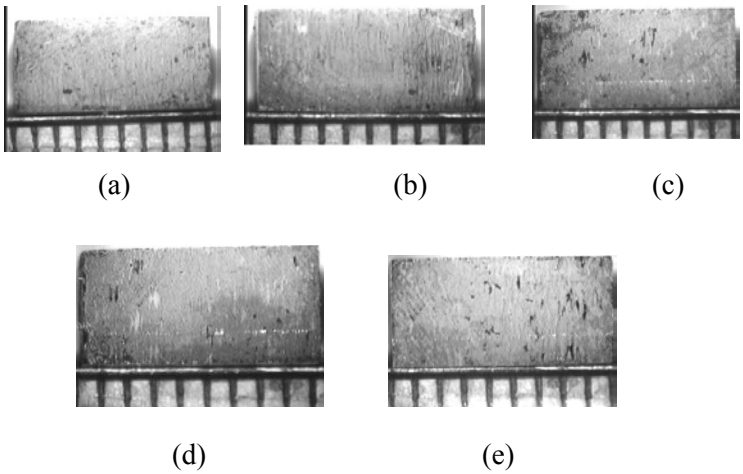

Figure 41. Optical Micrographs at Different Strain Rates for Off-Axis Loading Along the 45° Orientation (a) 1457/s, (b) 1670/s, (c) 1830/s, (d) 1981/s, and (e) 2162/s

2.3.2 Satin Weave Carbon/Epoxy Laminates

In this study, experimental investigations were carried out to test satin weave carbon/epoxy samples in the inplane direction under static and high strain rate compression loading. Under high strain rate loading, samples were tested in the in-plane direction along 0°, 15°, 30°, 45°, 60°, 75°, and 90°. The eight-harness satin weave fabric composite, due to specifics of the weaving and the sample dimensions used for high strain rate loading, exhibits different properties along the warp and fill directions. Under high strain rate loading, samples were tested at strain rates ranging from 1092/s to 2425/s. The transient data for each sample tested under high strain rate was recorded and stored. The dynamic stress-strain response of laminates was computed for each sample from responses measured using the strain gages mounted on the incident and transmission bars. Quasi-static tests were conducted to compare with the high strain rate

response. Table 9 gives the results of the static compression tests. It is noticeable from the table that static strength and modulus decrease with an increase in the orientation of the fiber tows up to 45° and then increase with further increase in the orientation. The strain to failure, however, increases with an increase in the orientation up to 45° and then decreases with further increase in the orientation. The properties of samples loaded along the fill direction are greater than those loaded along the warp direction. Figure 42 represents the stress-strain plot of representative samples subjected to static compression loading for all orientations, which illustrates this trend. The stress-strain curves for 0° and 90° samples remain linear till failure, whereas for other angles, the relationship is nonlinear, the non linearity increasing with the increase in off-axes angles from the primary warp or fill directions. This effect is attributed to coupling between axial and shear deformations. The higher the inclination of fibers is to the loading direction, the greater will be the influence of shear deformation. This results in the decrease in peak stress and modulus as well as an increase in the strain to failure as the orientation increases.

Table 9. Properties of Eight-Harness Satin Weave Carbon/Epoxy Laminates Under Static Compression Loading at Different Orientations

Orientation	Specimen	Peak stress, MPa	Strain at Peak Stress	Modulus, MPa
0°	JSI01	334	0.109	4122
0°	JSI02	290	0.087	5064
0°	JSI03	313	0.087	4926
AVERAGE		312	0.094	4704
15°	JS151	225	0.125	4114
15°	JS152	225	0.130	4153
15°	JS153	213	0.134	4016
AVERAGE		221	0.130	4094
30°	JS301	182	0.167	2468
30°	JS302	186	0.177	2554
30°	JS303	185	0.191	2439
AVERAGE		184	0.178	2487
45°	JS451	184	0.179	1965
45°	JS452	182	0.156	2023
45°	JS453	195	0.219	2439
AVERAGE		187	0.185	2142
60°	JSI601	191	0.202	1983
60°	JSI602	192	0.177	2090
60°	JSI603	191	0.156	2539
AVERAGE		191	0.178	2204
75°	JS751	238	0.086	4146
75°	JS752	235	0.092	3944
75°	JS753	231	0.080	4283
AVERAGE		235	0.086	4124
90°	JSI901	355	0.102	4338
90°	JSI902	356	0.117	4565
90°	JSI903	362	0.101	4702
AVERAGE		358	0.107	4868

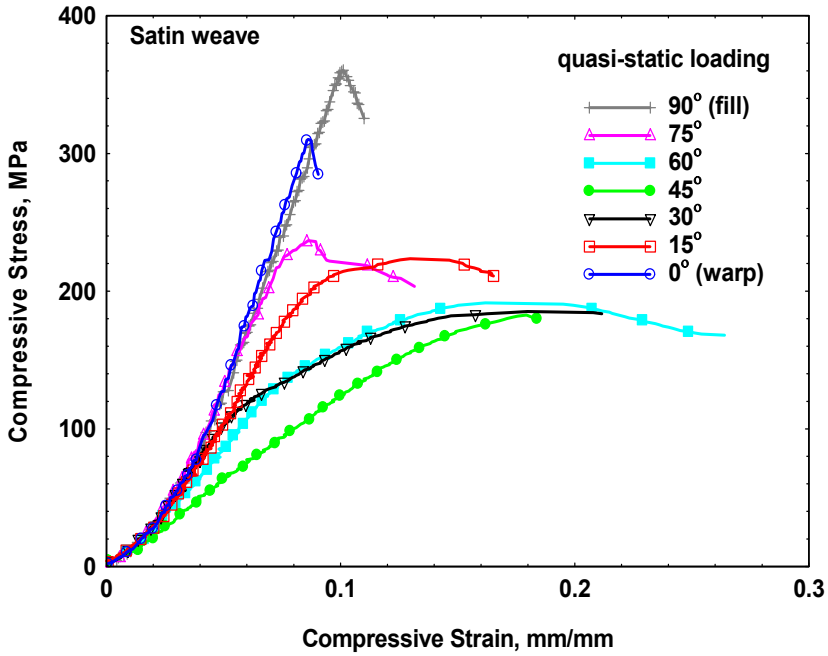

Figure 42. Compressive Stress-Strain Response of Satin Weave Carbon/Epoxy Laminates Under On- and Off-Axes Loading

Tables 10–16 represent the dynamic compression properties for satin weave carbon/epoxy composite samples loaded along different orientations at different strain rates. For each orientation, 10 samples were tested. Variation in the strain rate was obtained by changing the breach pressure. In the current test, breach pressure was varied from 62–110 kilopascals (9–16 psi). Table 10 gives the dynamic properties of samples tested along the 0° (warp) direction at strain rates ranging from 1092/s to 2425/s. The peak stress and modulus show an increasing trend with the increase in strain rate up to the strain rate of 1877/s, beyond which the trend reverses. Under dynamic loading, there is variation of about 150 percent in the peak stress value and about 200 percent variation in the dynamic modulus. However, variation in the strain at peak stress was within 20 percent in most cases. In comparison with the static properties, the dynamic peak stresses varied from 25 percent to 200 percent, whereas the dynamic modulus was 3 to 6 times higher. However, the strain at peak stress under dynamic loading was about one-third when compared with the corresponding strain under static loading. Figure 42 illustrates dynamic stress-strain plot of samples tested at five different strain rates. It can be seen from stress-strain plots that the dynamic peak stress and the slope of stress-strain plot (modulus) increase with an increase in strain rate up to the strain rate of 1877/s and then decrease considerably at the strain rate of 2215/s. The observed trend in the increase in peak stress and decreased strain at peak stress under dynamic loading is due to the combined effect of the viscoelastic nature of the polymeric matrix, the time-dependent nature of the accumulating damage and considerable temperature rise in the sample. While the samples exhibit a combination of shear fracture with longitudinal splitting at lower strain rates, the failure is largely through longitudinal splitting at high strain rates, as illustrated in Figure 43. In the case of static loading, the failure is due to the global shearing of the laminate, with the microbuckling of fibers along the shear plane. The sample has more to distribute the load and undergo steady deformation. Hence, the failure strain for the static loading is higher as compared to the high strain rate loading. These mechanisms are true for any high strain rate compression loading of composite materials. Hence, in the following sections, the discussion

will be based on the comparison of static and dynamic properties, and the variation of properties with the strain rate, and the failure modes.

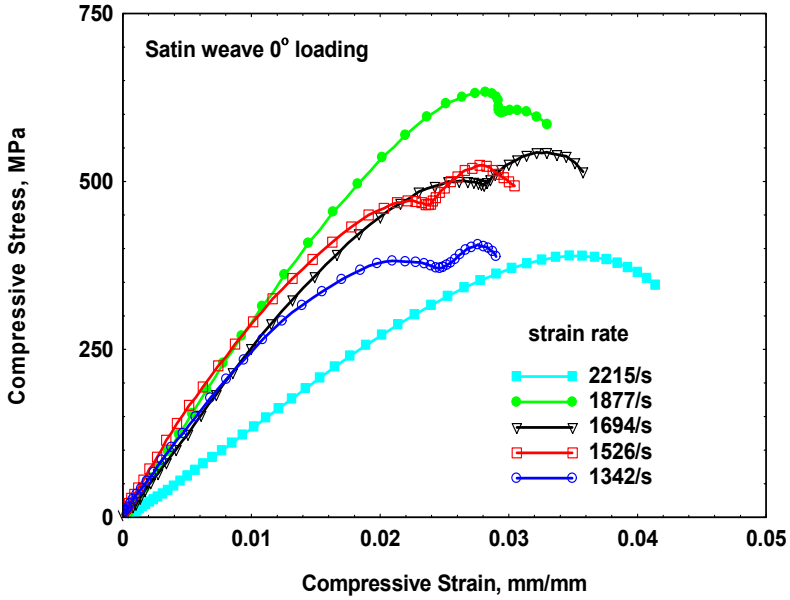

Figure 43. Dynamic Compressive Stress-Strain Response of Satin Weave Carbon/Epoxy Laminates Loaded Along 0° (Warp)

Table 10. Properties of the Eight-Harness Satin Weave Carbon/Epoxy Laminates Under High Strain Rate Compression Loading Along the 0° (Warp) Direction

Strain Rate	Peak Stress, MPa	Strain at Peak Stress	Modulus, MPa
1092	417	0.026	21800
1342	405	0.027	27500
1428	478	0.025	27500
1526	526	0.027	27100
1567	641	0.025	30700
1694	545	0.032	25400
1877	635	0.028	28900
1894	560	0.029	24500
2215	378	0.030	16900
2425	390	0.035	14200

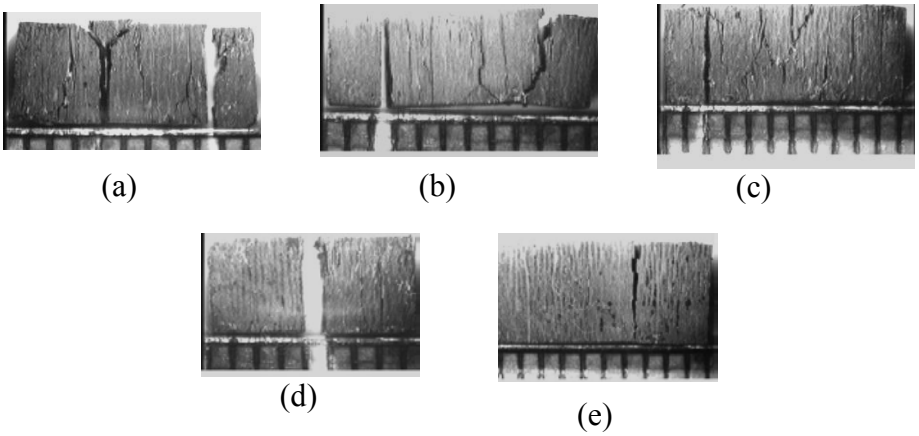

Figure 44. Optical Micrographs of Samples Tested Along 0° at (a) 1342/s, (b) 1526/s, (c) 1694/s, (d) 1877/s, and (e) 2215/s

Table 11 lists the dynamic properties of the samples tested along the 15° direction. The strain rates varied from 1411/s to 2132/s. The peak stress and modulus under dynamic loading were about 2 and 6–10 times higher respectively as compared to the corresponding values obtained under static loading. When compared with the properties of the samples tested at high strain rate loading along the 0°, the strain rates increased considerably for the same pressure setting. Further, there was a sharp drop in the peak stress and modulus and increase in the strain at peak stress. This is due to the coupling between the axial and shear deformation, which is further reflected in the dynamic stress-strain response, as shown in Figure 45. The linear portion in the

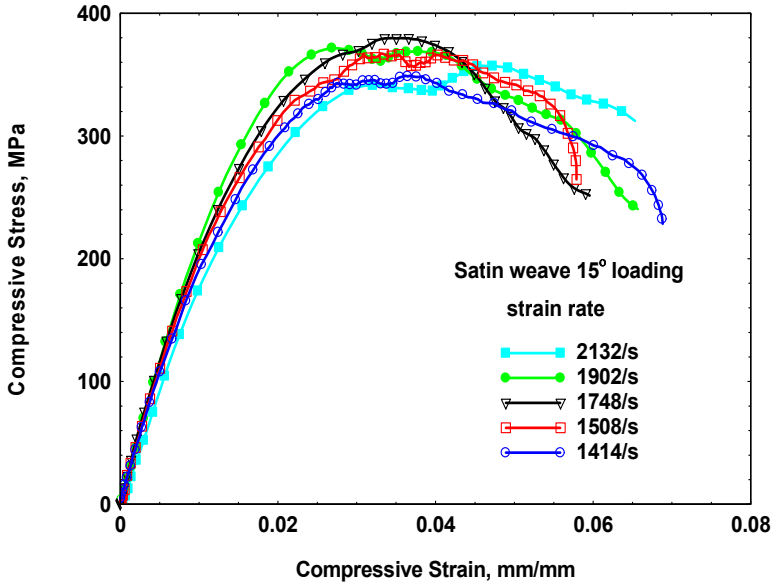

Figure 45. Dynamic Compressive Stress-Strain Response of Satin Weave Carbon/Epoxy Laminates Loaded Along the 15° Direction

stress-strain response is only about 14 percent, whereas the nonlinear response is very dominant. While the trend of increase in dynamic peak stress and modulus with increase in strain rate is well maintained,

the variations in peak stress and modulus, within the strain rates reported in this study, are within 10 percent and 25 percent respectively. The variation in the strain at peak stress was about 10 percent in most cases. As far as the failure modes are concerned, the samples did not exhibit any visible indications of damage up to a strain rate of 1508/s (Figure 46 a and b). There were several shear cracks at strain rates in the range of 1713/s–1950/s (fig. 46c and d). At the strain rate of 2132/s, there was catastrophic failure of the sample (Figure 46 e) indicated by large shear fractures.

Table 11. Properties of Eight-Harness Satin Weave Carbon/Epoxy Laminates Under High Strain Rate Compression Loading Along the 15° Direction

Strain Rate	Peak Stress, MPa	Strain at Peak Stress	Modulus, MPa
1411	349	0.036	19200
1508	368	0.033	20600
1603	355	0.032	20500
1713	376	0.034	20600
1748	381	0.035	19500
1799	354	0.039	19600
1902	366	0.044	15900
1950	359	0.037	18700
2097	388	0.029	19900
2132	358	0.046	17700

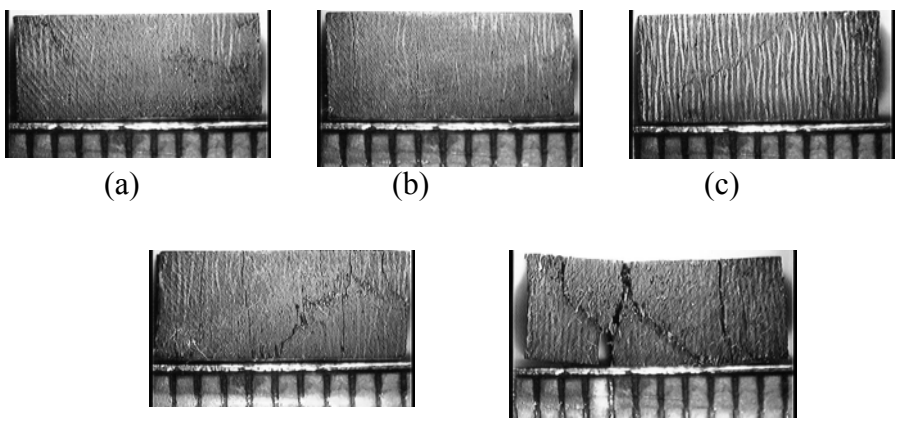

(a) (b) (c)

(d) (e)

Figure 46. Optical Micrographs of Samples Tested Along the 15° Direction at (a) 1414/s, (b) 1508/s, (c) 1748/s, (d) 1902/s, and (e) 2135/s

Table 12 lists the dynamic properties of satin weave carbon/epoxy samples loaded along the 30° direction. Here the strain rate ranged from 1417/s to 2125/s. The peak stress and the dynamic modulus did not exhibit much variation (Figure 47). However, the strain at peak stress indicated considerable variation. Here again the effect of shear-extension coupling is quite evident, with the shear deformation dominating the response. The ratio of linear to nonlinear response was in the range of 6–9. None of the samples tested along 30° exhibited any visible indications of damage (Figure 48 a-e). Hence, it may not

be appropriate to compare the response of static and dynamic properties, as the samples were loaded to failure under static loading. Even with this exception, it is noticeable that the dynamic peak stress and modulus were about 1.5 and 5 times higher as compared to the corresponding values under static loading.

Table 12. Properties of Eight-Harness Satin Weave Carbon/Epoxy Laminates Under High Strain Rate Compression Loading Along the 30° Direction

Strain Rate	Peak Stress, MPa	Strain at Peak Stress	Modulus, MPa
1417	248	0.054	12800
1482	246	0.049	14400
1582	241	0.045	13200
1718	259	0.054	14300
1796	245	0.039	13200
1861	253	0.057	14000
1918	260	0.048	14100
2013	251	0.058	13500
2097	256	0.063	13800
2125	256	0.064	13200

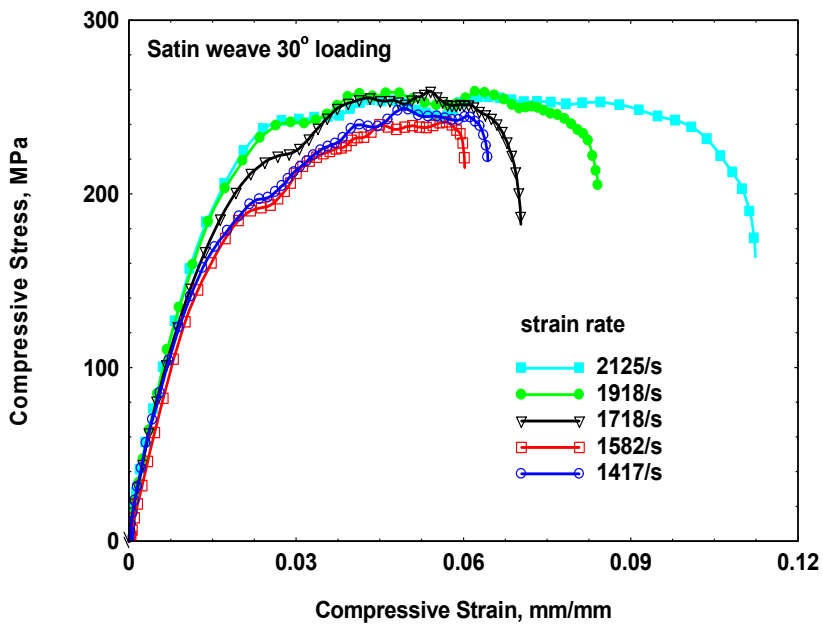

Figure 47. Dynamic Compressive Stress-Strain Response of Satin Weave Carbon/Epoxy Laminates Loaded Along the 30° Direction

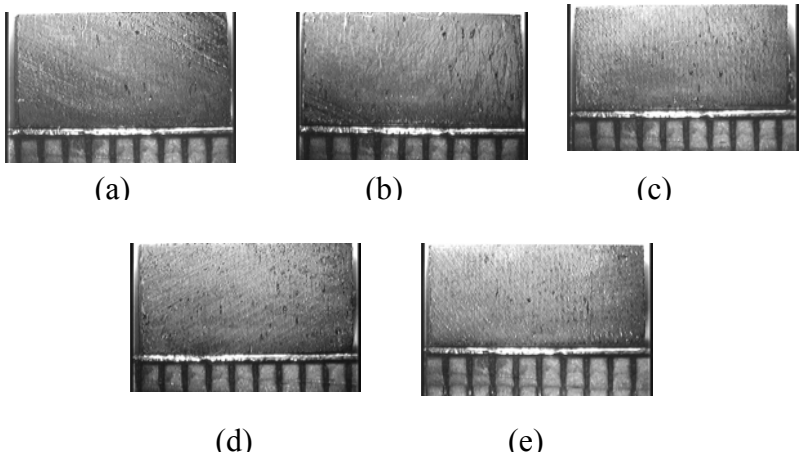

Figure 48. Optical Micrographs of Samples Tested Along the 30° Direction at (a) 1417/s, (b) 1582/s, (c) 1718/s, (d) 1918/s, and (e) 2125/s

Dynamic properties of the satin weave carbon/epoxy samples tested along the 45° direction are given in Table 13. Dynamic stress-strain plots of representative samples are shown in Figure 49, optical micrographs of which are shown in Figure 49 a-e. The strain rate obtained was in the range of 1237/s–2134/s. There was about 10 percent variation in the peak stress with very little variation in the dynamic modulus. The ratio of linear to nonlinear response was about 4:5. There is an increase in the peak stress by about 20–33 percent as compared to the static value. The dynamic modulus is about 5.5 times higher than the static modulus. The strain at peak stress under dynamic loading was about one-third as compared to the corresponding value under static loading. Here again, these values give a lower bound on the comparative values as the samples under dynamic loading did not fail.

Table 13. Properties of Eight-Harness Satin Weave Carbon/Epoxy Laminates Under High Strain Rate Compression Loading Along the 45° Direction

Strain Rate	Peak Stress, MPa	Strain at Peak Stress	Modulus, MPa
1237	221	0.052	11300
1325	211	0.051	10600
1481	227	0.057	11800
1531	220	0.055	11400
1618	212	0.057	10200
1699	235	0.060	11900
1784	236	0.065	11600
1915	241	0.069	11500
2017	247	0.076	10700
2134	240	0.066	11200

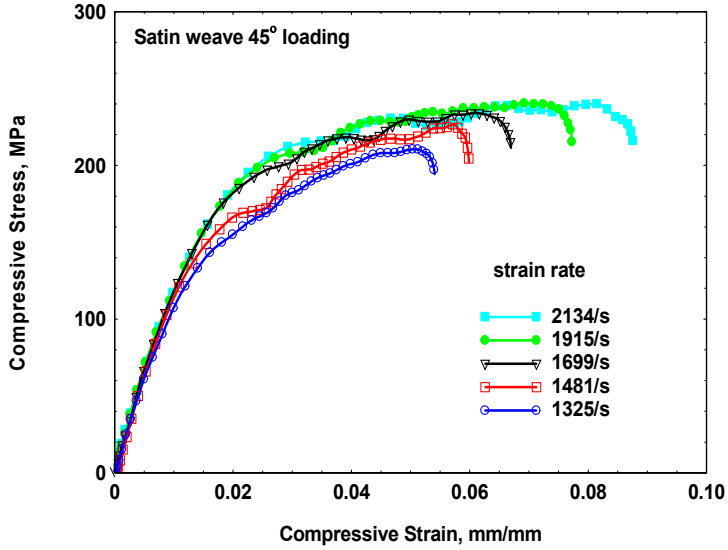

Figure 49. Dynamic Compressive Stress-Strain Response of Satin Weave Carbon/Epoxy Laminates Loaded Along the 45° Direction

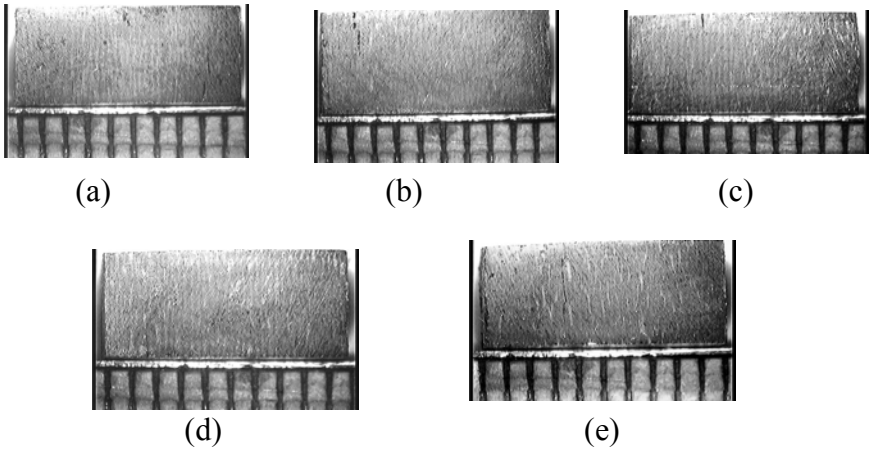

Figure 50. Optical Micrographs of Samples Tested Along the 45° Direction at (a) 1325/s, (b) 1481/s, (c) 1699/s, (d) 1915/s, and (e) 2134/s

Dynamic properties of samples tested along the 60° direction are listed in Table 14. Dynamic stress strain plots of representative samples are illustrated in Figure 50, optical micrographs of which are depicted in Figure 52 a-e. When compared with the static properties, dynamic properties were about 1.5 and 7 times higher for peak stress and modulus, respectively, and the strain at peak stress was about one-third. Within the range of strain rates obtained in the current study under dynamic loading, there was a variation of about 15 percent in peak stress and about 10 percent in the modulus value. These values increased with the increase in strain rate. Again, none of the samples exhibited any failure. The coupling between axial and shear deformation was well maintained, with large nonlinear response. The ratio of linear to nonlinear response was about 6:8.

Table 14. Properties of Eight-Harness Satin Weave Carbon/Epoxy Laminates Under High Strain Rate Compression Loading Along the 60° Direction

Strain Rate	Peak Stress, MPa	Strain at Peak Stress	Modulus, MPa
1244	240	0.046	13600
1402	269	0.047	15100
1506	260	0.043	15000
1602	267	0.046	14700
1716	268	0.040	15600
1765	268	0.063	15800
1823	274	0.061	15400
1902	265	0.062	14400
2110	277	0.061	13600
2114	270	0.046	13200

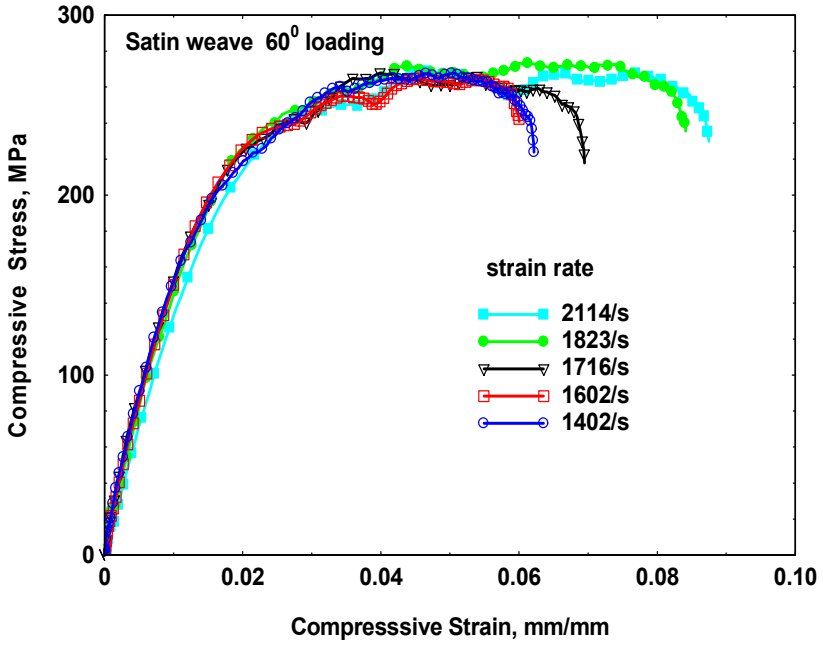

Figure 51. Dynamic Compressive Stress-Strain Response of Satin Weave Carbon/Epoxy Laminates Loaded Along the 60° Direction

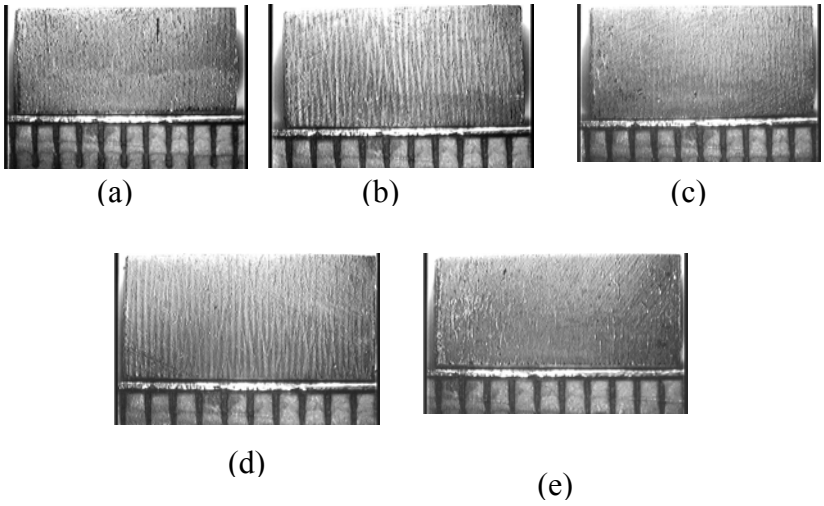

Figure 52. Optical Micrographs of Samples Tested Along the 60° Direction at (a) 1402/s, (b) 1602/s, (c) 1716/s, (d) 1823/s, and (e) 2114/s

The properties of satin weave samples under high strain rate loading at 75° direction are listed in Table 15. Dynamic stress-strain plots of some representative samples are illustrated in Figure 53. The optical micrographs of these samples are shown in Figure 54 a-e. When compared to the static properties, dynamic properties were higher by about 2 and 5–7 times for peak stress and modulus, respectively, and the strain at peak stress was about one-third. Within the strain rate range obtained (1270/s-1886/s), the peak stress varied by about 20 percent, the modulus varied by about 50 percent, and the strain at peak stress varied by about 20 percent, with the properties increasing with the increase in the strain rate. From the optical micrographs, it is seen that there was no visible indication of damage up to the strain rate of 1488/s. With a further increase in the strain rate, samples started exhibiting shear failure. The volume of fracture was higher at higher strain rate. The shear crack angle decreased with increases in the strain rate. The effect of shear deformation began to diminish, as can be seen from the ratio of linear to nonlinear response, which is about 1:2.5.

Table 15. Properties of 8-Harness Satin Weave Carbon/Epoxy Laminates Under High Strain Rate Compression Loading Along 75^0

Strain Rate	Peak Stress, MPa	Strain at Peak Stress	Modulus, MPa
1270	424	0.025	21900
1320	421	0.026	21900
1411	448	0.030	22300
1488	442	0.034	23300
1541	375	0.029	22200
1604	425	0.029	21600
1665	470	0.025	26400
1689	450	0.024	26800
1717	495	0.026	28400
1886	475	0.027	25600

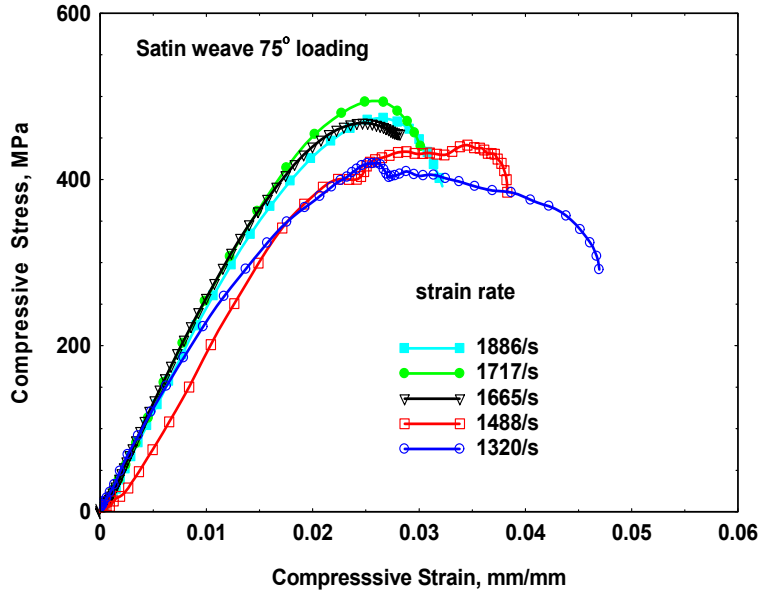

Figure 53. Dynamic Compressive Stress-Strain Response of Satin Weave Carbon/Epoxy Laminates Loaded Along the 75° Direction

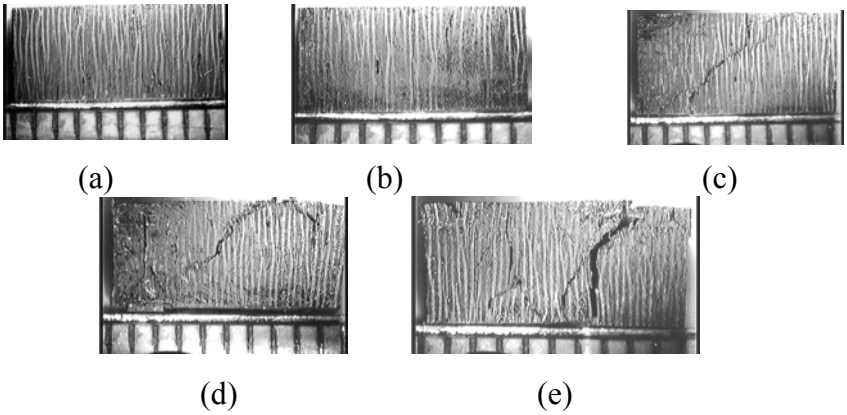

Figure 54. Optical Micrographs of Samples Tested Along the 75° Direction at (a) 1320/s, (b) 1488/s, (c) 1665/s, (d) 1717/s, and (e) 1886/s

Table 16 lists the dynamic properties of satin weave carbon/epoxy samples loaded along the 90° direction (weft/fill). Dynamic stress-strain plots of representative samples are drawn and shown in figure 55, the optical micrographs of which are depicted in Figure 56 a-e. When compared to static properties, dynamic properties exhibit an increase of 1.5–1.9 and 5.5–6.7 times for the peak stress and the modulus, respectively, and the strain at peak stress was about 25–32 percent. The stress-strain response was linear up to about 70 percent of the loading. The dynamic peak stress and slope of stress-strain plot (modulus) again exhibit the increasing trend with the increase in strain rate. The failure was predominantly by splitting of the sample into two or three sublaminates. There was no indication of any shear fracture. Though the fabric is woven in nature due to which one can expect certain shear fracture, it can be noted

that in the case of satin weave, the effect of weaving is very minimal with fiber tow maintaining straight portion over most of its length. Moreover, this effect is magnified due to small sample dimensions.

Table 16. Properties of Eight-Harness Satin Weave Carbon/Epoxy Laminates Under High Strain Rate Compression Loading Along the 90° Direction (Weft/Fill)

Strain Rate	Peak Stress, MPa	Strain at Peak Stress	Modulus, MPa
1390	523	0.025	27400
1491	604	0.032	28600
1564	623	0.026	28700
1670	638	0.025	31100
1749	684	0.026	31200
1845	685	0.027	32400
1971	654	0.028	29400
2090	682	0.031	27000
2149	679	0.030	29600

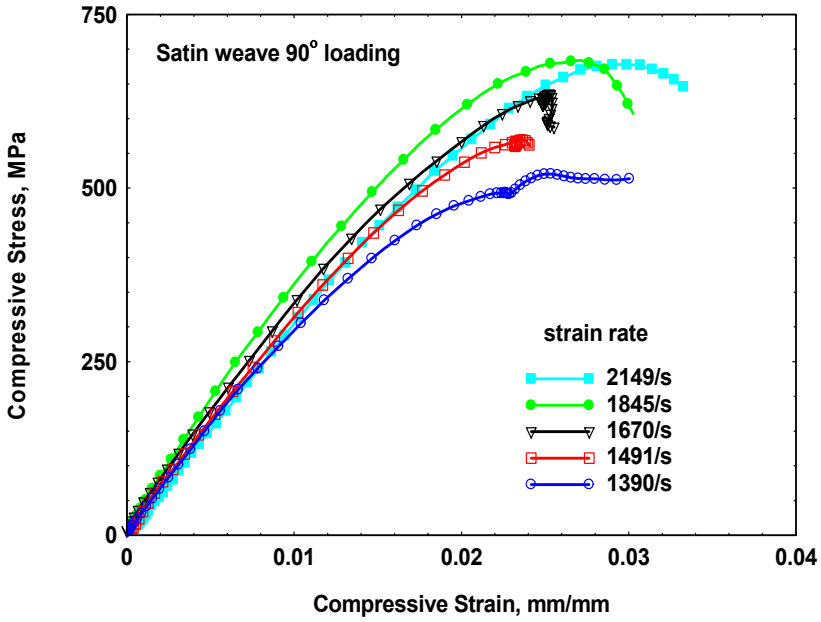

Figure 55. Dynamic Compressive Stress-Strain Response of Satin Weave Carbon/Epoxy Laminates Loaded Along the 90° Direction (Weft/Fill)

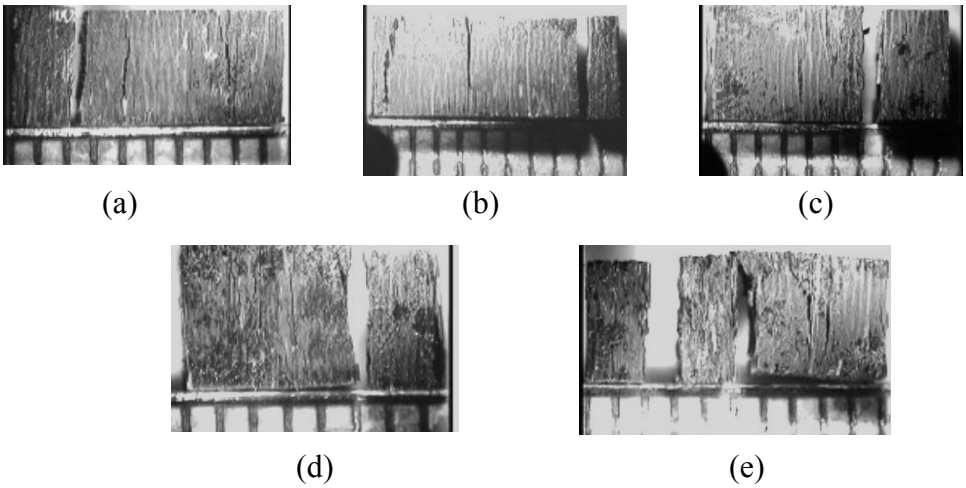

Figure 56. Optical Micrographs of Samples Tested Along the 90° Direction (Weft/Fill) at (a) 1390/s, (b) 1491/s, (c) 1670/s, (d) 1845/s, and (e) 2149/s

To highlight the dynamic response of samples tested along on and off-axes angles, stress-strain plots are plotted at two different strain rates, one around 1400/s and the other around 1900/s (see Figures 57 and 58). These two figures sum up the response of satin weave samples at different orientations. The properties of samples loaded along weft/fill are higher in comparison with those loaded along the warp direction. The response was largely linear along these two directions. Once the samples are loaded along off-axes angles, the response tends to become highly nonlinear due to the coupling of axial and shear deformation.

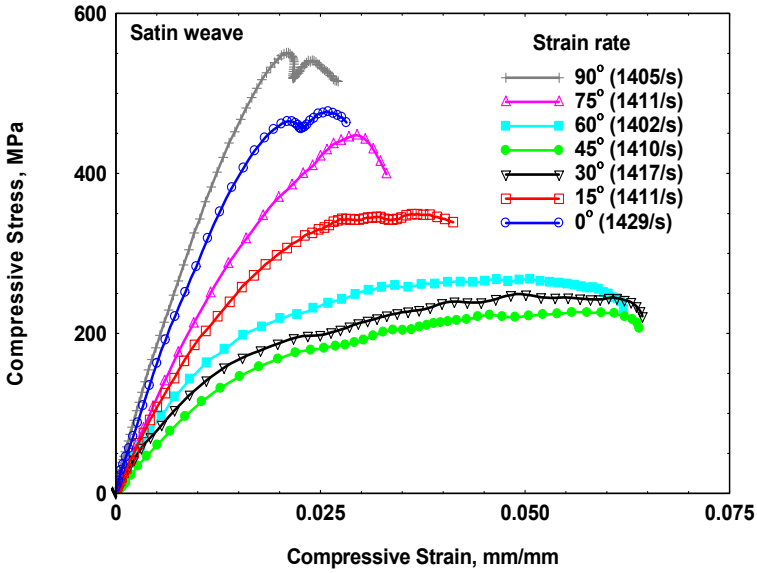

Figure 57. Dynamic Compressive Stress-Strain Response of Satin Weave Carbon/Epoxy Laminates Loaded Along Different Orientations at a Strain Rate of ~1400/S

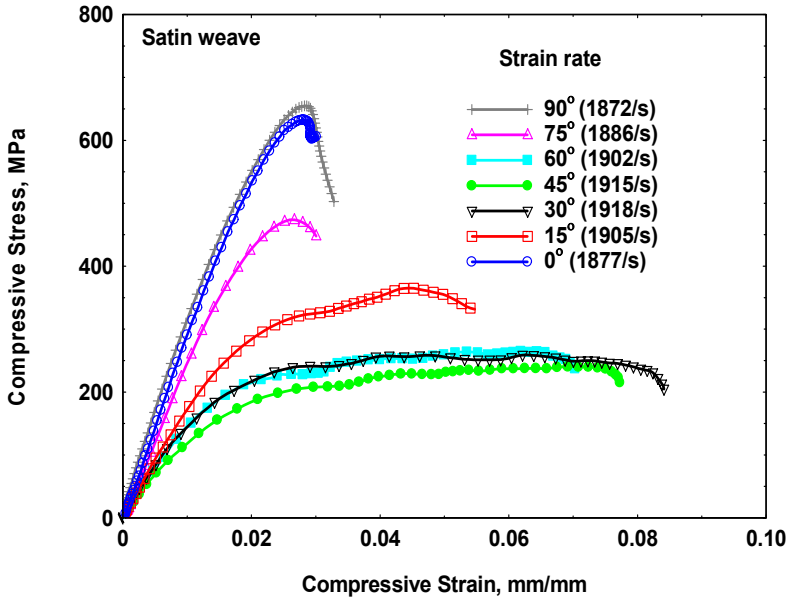

Figure 58. Dynamic Compressive Stress-Strain Response of Satin Weave Carbon/Epoxy Laminates Loaded Along Different Orientations at a Strain Rate of ~1900/S

2.4 Summary and Conclusions

Investigations were carried out on 37-layer plain and satin weave carbon/epoxy laminates manufactured using affordable VARIM under high strain rate loading. High strain rates tests were conducted using a modified compression SHPB. Using the setup, it is possible to subject samples to single controlled input pulses. Samples were subjected to impact loading in inplane direction along 0°, 15°, 30°, and 45° angles for plain weave fabric laminates and along 0°, 15°, 30°, 45°, 60°, 75°, and 90° angles for satin weave fabric laminates. Quasi-static tests were conducted to compare the results with high strain rate loading.

The following conclusions were drawn from the study:

1. In all of the cases, there was a considerable increase in the stiffness at high strain rate loading as compared to static loading. Peak stresses were higher for the high strain rate loading as compared to the static loading.
2. The ultimate strength and strain of the woven carbon/epoxy composites varied considerably with the orientation of the fibers to loading direction. Fabric architecture influenced the dynamic response. Fiber undulation and crimp angle influenced the nonlinear response of the samples loaded along off-axes orientations. The samples loaded along off-axes angles exhibited a large nonlinear response, which increased with increaser in orientation up to 45°.
3. There was a trend of increasing strength and stiffness with increasing strain rates up to certain strain rates beyond which the trend reverses for samples loaded along warp and weft/fill directions. This was due to the combined effect of the fiber direction, viscoelastic nature of the matrix, failure modes, response time for the development of failure surfaces, the volume of the failure surfaces generated, and the temperature rise.
4. As the properties are highly directional dependent, there was a need to generate a large database to include different layups and orientations used in general practice as well as to include other properties

like tension, shear, etc. Further, there is still a need to address the effects of temperature and moisture on the off-axis response of woven fabric composites, for which there is no data available in open literature.

3. High-Energy Penetration/Perforation Mechanics of Composite Plates

3.1 Project Report Summary

The objective of this research is to study the high-energy penetration/perforation mechanics of composite plates using an integrative split penetration Hopkinson pressure bar and high-speed optical imaging system. The project objectives and statement of work (SOW) were accomplished by the following tasks:

1. Installation and calibration of system at the University of the Pittsburgh School of Engineering.
2. Investigation of propagation of penetration head and surface crack damage in the vicinity perforation threshold velocity using dynamic optical imaging of an ultra high-speed continuous access camera.
3. Investigation of energy absorption profiling using dynamic optical imaging of a high-speed digital video camera.
4. Investigation of strain intensity profile and quantitative analysis of the perforation damage mode of carbon-epoxy plates.

The results show strain rate, ultimate strain and energy absorption increases with impact energy; particle velocity and displacement increase linearly with impact energy. Within the threshold (penetration) energy for perforation, energy absorption increases linearly with impact energy. Energy absorption and strain rate are sensitive to increases in strain, and increase non-linearly. The dynamic modulus (defined as ultimate strength relative to the ultimate strain) is shown to decrease non-linearly with impact velocity, energy absorption, strain rate and strain. The simple power law function of the form $y = ax^2$ was sufficient to predict the dependency. On the average, strain rate and loading forces increase with damage energy threshold levels, from below the penetration Limit to above penetration Limit. The result shows that there is a significant difference between the effects of penetrator size on a specimen strain rate. As the size of the penetrator is increased, the penetration and perforation thresholds increase significantly. Thus, for the same energy level, the smaller penetrator will deliver more energy to the target. The size of the nose contact area is more significant in energy delivery than the shape of the penetrator itself. Specimen energy absorption is strongly dependent on thickness, penetrator geometry and penetrator size. The results indicate that a conical hemispherical penetrator will defeat its target at a higher energy level than a spherical penetrator will.

Micro-Raman spectroscopy is shown to be a reliable quantitative means of characterizing residual strain in a damaged specimen. Raman shift is inversely proportional to the strain in tension and directly proportional to strain in compression and indicates a local minimum at the center of highest strain corresponding to the point of impact and therefore highest strain. The results show that in woven specimen, the crack also appears crossed and propagates in both directions probably due to the woven nature of the specimen. It is conceivable that the cracks first initiate at the point of intersections of the weave and move in both directions.

3.2 Introduction

It is well known that the failure of laminated composite materials depends on such factors as incident stress, penetrator geometry, impact energy, and material thickness and fiber orientation. A great deal of work has been done investigating the characteristics of composite fracture. In particular, the research and investigations of Nwosu and Czarnecki [33] and Zukas [34] examined the crack propagation and perforation of laminated graphite-epoxy samples. It is documented that a threshold energy exists above which a visible crack is initiated on the laminate's rear surface, and that the perforation energy that is dissipated in the composite laminate depends on the laminate's thickness and fiber layup as well as the impact parameters and incident stress. Some of these factors, investigated through the implementation of a factorial design in this research, were seen to experience a noninteraction with respect to energy absorption. Earlier work by Nwosu [35–37] reported statistical quantification of effects of incident stress, material thickness, and fiber orientation on energy absorption. Utilizing orthogonal arrays, it was shown that the effects of incident stress and fiber orientation were statistically significant. One of the objectives of the proposed study was to determine if the significant interactions and noninteractions found in prior studies were repeatable, and hence, conclusive. The findings of the second focus of this research, the determination of the penetration Limit, or critical-impact velocity defined as the velocity below which an object will fail to perforate a barrier, are supported by past research [34]. This can also be expressed in terms of bar perforation threshold velocity, although we maintain that the latter is better since the experimenter controls the striker impact velocity. The determination of a penetration limit is of significant importance since knowing penetration limit is critical to building, designing, and evaluating protective structures that undergo any penetration type of impact. Such structures must be designed above such threshold conditions.

This self-contained final report is presented in sections that directly relate to the SOW. Section 3.3 documents the work in the modification, installation, and calibration of the penetrating Hopkinson bar system. Section 3.4 outlines the classical data reduction method for general analysis of dynamic stress-strain data. The experimental results to accomplish the first two objectives of the SOW are reported in this section. Section 3.5 reports the critical experimental results of the application of high-speed imaging in dynamic failures behavior. This is further supported and documented in Section 3.6, through an exploratory laser -based quantitative method of characterizing the penetration type of damage. The report concludes with Section 3.7 which includes key project accomplishments and recommendations for further investigation.

3.3 Experimental

3.3.1 Installation and calibration of the Hopkinson impact system at the University of Pittsburgh School of Engineering

The installation of the Hopkinson bar started with the design and fabrication of a new and modified I-beam. Because the system is installed in a sub basement, the I-beam platform needed to be anchored in two separate pieces. No special anchoring of the bases was needed. The modified SHPB apparatus consists of incident, transmitter, and striker bars (300 maraging AMS 6414 steel), each being 25.4 mm (1 inch) in diameter. The incident and transmitter bars are 3.66 m (12-ft) in length, while the striker bar is 0.305 m (1-ft) long. The striker is housed inside a 0.610-m (2-ft) launch cylinder and is driven by compressed air of up to 1.72 MPa (250 psi). To

begin each test, the desired pressure is manually set using a gauge between the launch cylinder and the reservoir. A switch in the control room activates the opening of a quick-acting solenoid valve, allowing compressed air acceleration of the striker into the incident bar. The impact-end of the striker is spherically rounded with a 50.8 m (2-in) radius for a repeatable point of contact with the incident bar on a plane centrally normal to the longitudinal direction of the wave propagation. Proper axial alignment between the striker and incident bars is ensured to minimize flexure. The uniaxial waveform generated in the bar determines the rate at which energy is transferred from the bar to laminated plate. The geometrical shape of the striker and the impact velocity controls the shape of the waveform. The stress wave amplitude varies with impact velocity, while the stress profile changes with striker geometry. Incident and transmitter bars are guided through pillow blocks containing low-friction ball bearings. The bushings (mounted on a rigid steel channel which is backed up by an I-beam) support the bar shifts without restraining them. The support can be adjusted laterally and vertically for proper alignment. To minimize vibration, the unit is anchored to steel beams running through a 102-mm (4 inch) steel-reinforced concrete deck. A 6.35-mm (0.25-inch)-diameter rod is attached to one end of the striker and protrudes outside the cylinder as a means of adjusting the stroke length (and therefore striker velocity). Venting holes along the launch tube maintain a low-pressure zone in front of the striker and prevent the possibility of multiple impacts.

Figure 59a shows the new and modified version of the integrative Hopkinson bar system installed at the University of Pittsburgh Materials Dynamic Behavior lab. The lab is also designed as photographic processing lab to handle all film processing for the high-speed cameras. Figure 59b shows the fiber-optics attachment to the specimen holder that allows for illumination of the sample during a damage event. All the experiments are remotely controlled via an adjoining instrumentation room.

The data acquisition system shown in Figure 60 consists of two Nicolet Pro 42 high-speed digital oscilloscopes. Incident, reflected, and transmitted waves are recorded at a rate of 20 million samples per second and stored in a PC storage device. The system has 12-bit digitizer offering 0.025 percent resolution and a storage capability of 250,000 samples per channel with its 26 megabytes of RAM. The signal analysis could be completed using a Nicolet spectrum analyzer or by a special Lotus or Excel scheme developed for numerical integration.

3.3.2 Description of the Dynamic Optical Imaging System

The dynamic optical imaging system consists of (a) a ultra high-speed continuous access framing camera provided by a Cordin Model 333 camera and (b) two high-speed charge-coupled device (CCD) video camera systems. Each of these units and their associated components are described below [38].

3.3.2.1 Ultra High-Speed Continuous Access Framing Camera

The Cordin Model 330 is a continuous writing, simultaneous streak and framing camera. The continuous writing feature allows it to be used to photograph random events that are not possible

with the more common synchronous access cameras. The objective lens forms a primary image; this image is relayed to a combination beam splitter/slit and is optically reduced 2:1. The beam splitter/slit consists of two coated glass wedges between which is an aluminized surface with a 0.10-mm slit across its face. The glass wedges performs two functions: (1) they divide the light for the framing and the streak portion of the camera, and (2) they tilt the image plane of both the streak image and framing image to match the mechanical offset of the streak and framing film tracks. The image coming through the slit is relayed to the streak track with a single lens that magnifies the primary image two times. The primary image for the framing portion is relayed to a beam splitter with a lens pair at 1:1 magnification. Here the image is divided and relayed to the rotating mirror by two spherical mirrors, one for each path. These two paths are 180 degrees apart when the light is re-imaged onto the opposite sides of the rotating mirror. Two banks of spherical mirrors, 41 per bank, then relay the final images onto the framing tracks, with a magnification of 1:2. The first frame of each track is exposed simultaneously with the last frame of the previous track. This provides 80 unique frames. The film used on all three tracks is standard 35 mm size. Both streak and framing tracks utilize special cassettes that permit convenient loading and unloading.

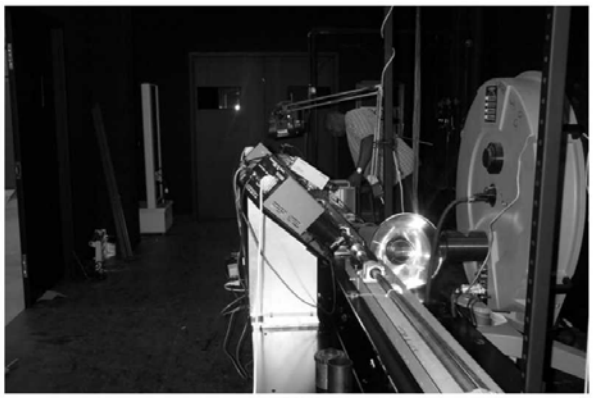

(a)

(b)

Figure 59. System Configuration Showing a) High-Speed Continuous Access Camera and Two High-Speed Video Camera, b) High-Speed Camera Looking into Sample Holder Illuminated by 5 kV Flash Unit Via Fiber Optical Cables

(a)

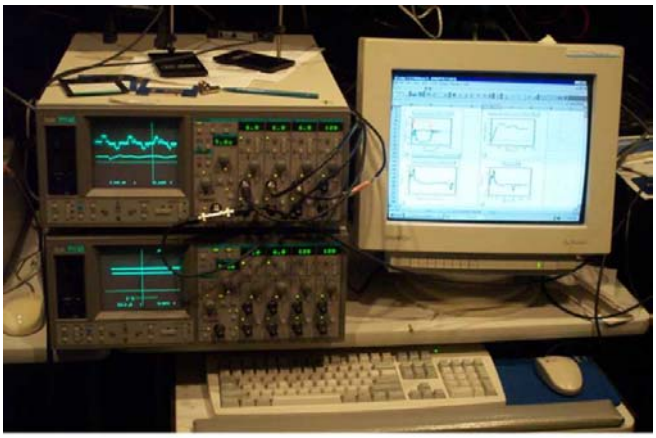

(b)

Figure 60. a) System Instrumentation Control Room b) Nicolet Data Acquisition System with Display of Typical Strain Wave

The rotating mirror is three sided and all three surfaces are aluminized. The mirror may be air driven up to 5000 revolutions per second (rps). From 5,000 rps to the top speed of 8,333 rps, it must be driven by helium, and the camera must be filled with helium. For the present investigation, only air is used. The control of the turbine speed, capping shutter, firing pulse delay, and turbine speed recording is done by a separate control unit (usually a Model 470).

3.3.2.2 Rotating Mirror Assembly

The Model 330-04 Rotating Mirror Assembly consists of a ball-bearing-suspended beryllium-rotating mirror powered by an air or helium driven turbine. The mirror has three faces, which are 0.66 by 1.25 inches. The assembly is capable of a top speed of 8,333 rps. Use of beryllium as a mirror material guarantees a minimum of mirror distortion at top speed. The beryllium is over-coated with aluminum and silicon monoxide to optimize reflectivity. The mirror and turbine

assembly is ball bearing suspended, thus reducing maintenance to a minimum. In addition, as a consequence, the assembly can be operated in any desired position. Mechanical resonance of the mirror is sufficiently suppressed to warrant safe operation at all desired frequencies up to its maximum safe speed of 8,333 rps. Other components of Model 330 are described in the following sections.

3.3.2.3 Remote Fire Unit

The Model 330 remote fire unit is used in conjunction with the Model 470 (camera control) to fire the camera control.

3.3.2.4 Camera Control

The camera control is a highly reliable solid-state digital system used to control the sequencing of events applicable to the operation of high-speed, rotating mirror cameras. One of the primary features of this model is the ability to preset the delay of the fire pulse that places the image from the rotating mirror onto the predetermined position of the cameras film track. The control receives a series of mirror signals from the camera electropak. The period of the pulse string is inversely proportional to the rotating mirror frequency. When the period of the pulse string is twice the preselected reference period (rotor at half speed), the camera shutter is opened. After the shutter is open, and the mirror period is equal to or less than the pre-selected reference period, the built-in time delay generator will begin its preset delay with the next mirror pulse. The output signal from the time delay is used to trigger the fire-pulse-generating circuitry. Once the fire pulse is generated, the shutter is closed and the drive gas to the rotor is shut off, and the mirror period at the time of firing the system is retained on the counter.

3.3.2.5 Light Source (Cordin Model 607)

The light source provides a single-shot-high-intensity flash in the normal mode whose duration can be varied between 40 and 625 microseconds. Energy from the high-voltage supply is stored in the capacitors of the pulse-forming network. A trigger signal from the impact of the striker bar causes the flash tube to conduct energy out of the network. A second trigger pulse delayed by the amount of time prescribed by the front panel thumb wheel switch triggers the quenching spark gap in the control assembly. The remaining energy stored in the capacitors of the pulse-forming network is dumped through the quenching spark gap to ground and the flash tube light output is extinguished. The impedance of this gap is a few milliohms, while the flash tube impedance is 5 ohms. The trigger also activates a relay that opens the input power line and drops a crowbar across the pulse-forming network, discharging the high voltage capacitors.

3.3.2.6 Gas Control System (Cordin Model 476/480)

The gas control system provides the interface between the camera control electronics and the gas-turbine-driven rotating mirrors. Two seconds after the DRIVE ON button is pressed on the Model

470, the solenoid valve in the Model 480 is opened, and the preset pressure is sent to the Model 476A slave regulator. The Model 476A gas control is normally located at the camera and acts as the slave in a master/slave pressure regulator system. It receives the drive gas through a 3/4-inch line, and sends it through a filter and then through the slave regulator.

3.3.2.7 Two-Channel Delay Generator (Cordin Model 450)

The delay generator provides simple delay functions through the user interface and logical placement of switches and controls on the front and rear panels. Two complete, independent output channels allow two different delays of up to 1 second in length to be programmed in 0.1 microsecond increments initiated by a common trigger input, also provided by the Hopkinson striker bar impact. Both outputs allow switch selectable output polarity providing positive (rising) or negative (falling) edge 5-volt logic level signals capable of 50-ohm drive. In addition, both outputs are protected from damaging transients or spikes with independent suppression networks connected between the output circuitry and output connectors.

3.3.2.8 Two High-Speed CCD Video Camera system Ultra High Speed Intensified Camera System (Cordin Dual Model 181)

The Dual Model 181 camera system can be used to record two short exposure frames at any predetermined time during an event. It can be operated using either front or back lighting. The two frames can be separated in time from 0 nanoseconds (ns) to 1 millisecond (ms) in 10 ns steps. The exposure time of each frame can be set to any value between 10 ns and 1,000,000 ns (1 ms) in steps of 10 ns. In addition, the intensifier gain can be independently set for each camera so that proper exposure can be achieved even when using different exposure times with each camera. The system combines the optical path of the two cameras so they both look at the same scene through a beam splitter. The optics has been selected to give a field of view of approximately 5 by 8 mm. Optionally, each or both cameras will accept a Pentax K mount lens for general high-speed photographic work.

The camera system consists of two models 181 intensified cameras, one dual camera power supply, a nine inch black and white monitor for focus mode, a computer for setup of the cameras and images recorded with them. The system includes a time-delay generator Model 9650A to time the pictures and to set the exposure time, and the cables to connect all of the components. Each camera contains an intensified CCD camera. The combined optical path makes it possible to view and photograph the same scene with both cameras. Both cameras are focused to the same image plane. The image magnification of each camera is individually calibrated in the setup. Because each of the objective lenses has a slightly different focal length, the magnifiers used with each camera will have a slightly different magnification, thus there will be a slight difference in magnification between the two cameras. The system is synchronized with the event to be recorded using a time-delay generator, which sets both the time delay and exposure time for each camera by means of a general purpose interface bus (GPIB) interface to the computer.

Figure 61 shows the layout of the integration of the penetrating split Hopkinson's pressure bar (P-SHPB), with the continuous rotating high-speed camera, high-speed video CCD cameras and the peripheral instrumentation. The entire integrative system is operated by a single trigger activated by the impact of the P-SHPB striker bar.

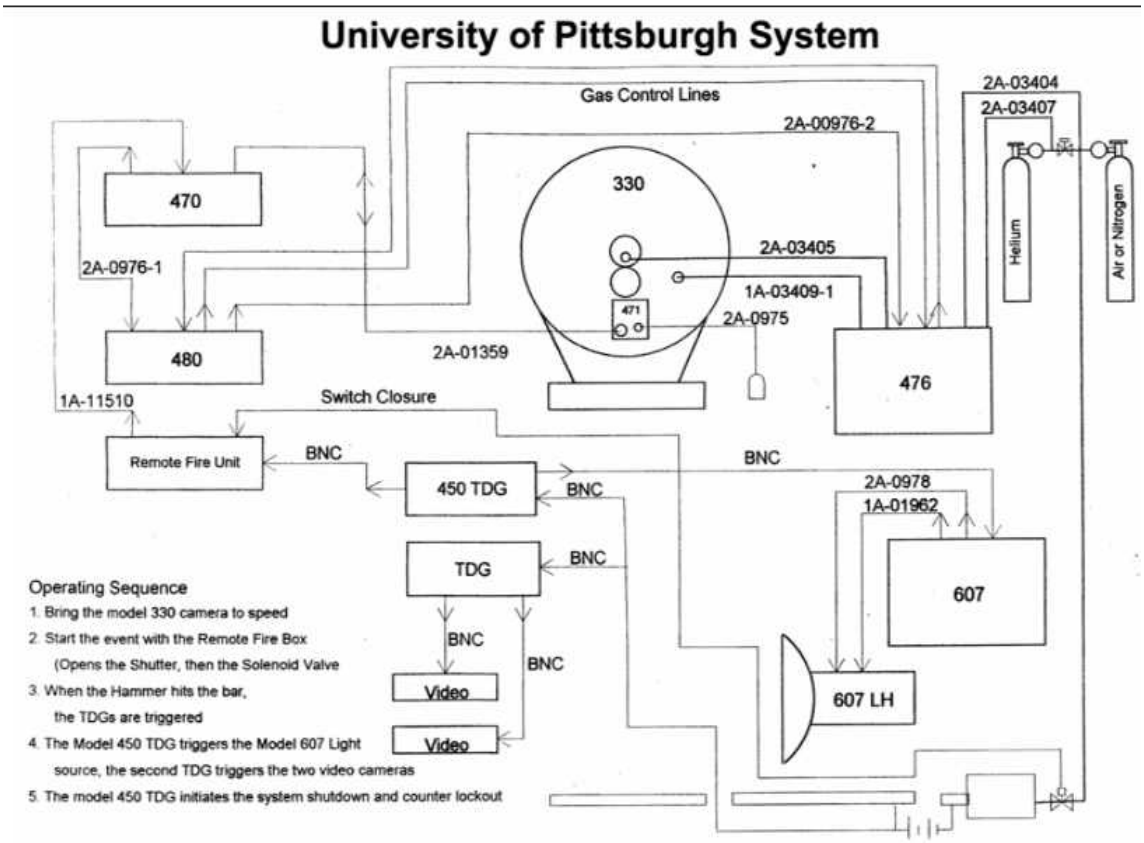

Figure 61. Integrated Operational Layout of the P-SHPB System

3.4 Theoretical Formulation and Data Reduction Methods

3.4.1 Review of Classical SHPB analysis for Composite Penetration Mechanics

Hopkinson [39] was the first to perform stress wave experiments thus, the bar became known as a Hopkinson bar. Kolsky [40] performed compressive research involving stress wave dynamics using a P-SHPB. Kolsky's split bar consisted of a pair of long axially aligned cylindrical bars of equal diameter. A test specimen was sandwiched between the bars. In the case of the perforation/penetration test, the specimen is loaded inside a specimen holder attached to the transmitter (output) bar. Upon generation of a uniaxial compression wave at the end of the incident bar, the wave continues down the bar's length to the bar-specimen interface. Part of the energy is reflected off the interface and is manifested as a returning tensile wave in the incident bar. Similarly, part of the energy is transmitted through the specimen into the transmitter bar and

remains as a compression wave. The difference in magnitude between the transmitted and reflected waves is the energy absorbed by the specimen because of inelastic behavior. Through an analysis of the wave, the specimen's mechanical response to high strain rate compressive loading can be evaluated. The original work of Kolsky has been modified and validated for other applications.

Figure 62 is a schematic diagram of the perforation assembly for the Hopkinson bar system. The figure shows the penetrator and specimen support that holds the composite plate. The fixture is sandwiched between the incident and transmitter bars as shown. The penetrator is attached to the end of the incident bar through its inner diameter. The sample holder fixture is attached to the transmitter bar with its open end facing the indenter. The space between the end of the fixture and the backside of the test plate allows for complete penetration or perforation beyond the thickness of the plate without reaching the end of the fixture. (In experiments performed near and beyond the perforation threshold, the penetrator could punch through and impact the end of the steel fixture and could result in damage to the indenter.) The collar prevents the indenting end from reaching the end of fixture. The effective length of the materials between the incident bar and the transmitter bar is given as Le = $L_1 + L + L_3$.

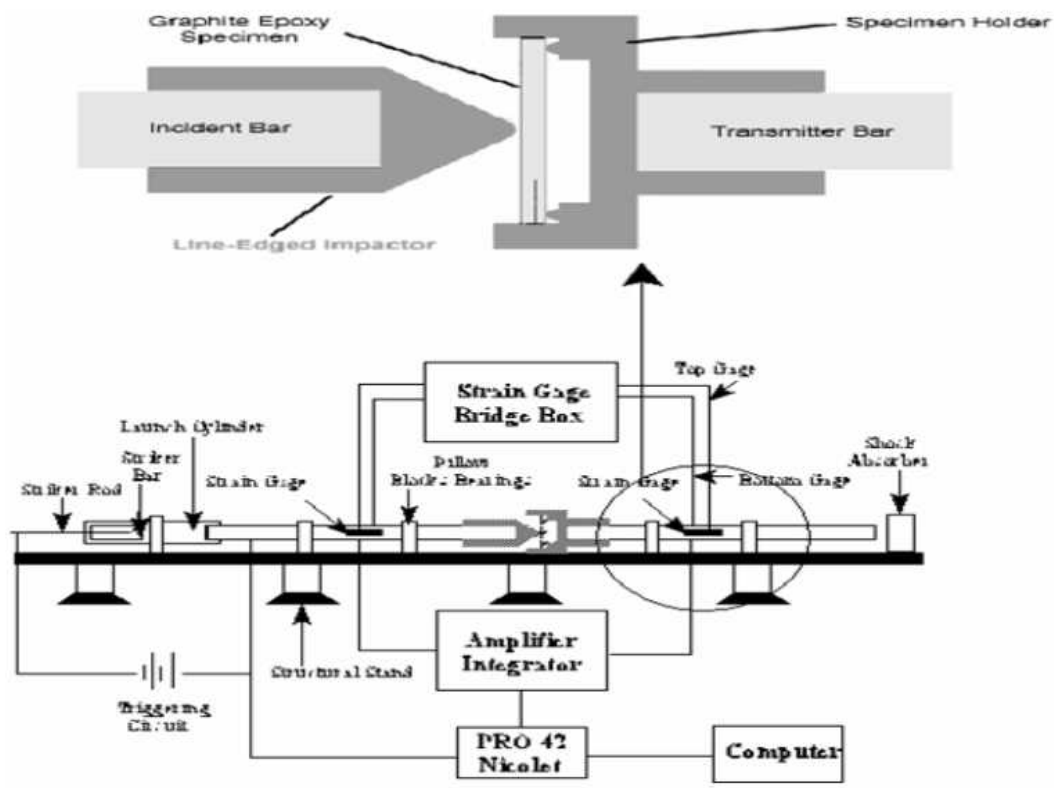

Figure 62. A Schematic Diagram of the P-SHPB System Showing (top) Perforation Sample Holder Fixture and (bottom) System Configuration and Instrumentation

For a transverse experiment in which the specimen is sandwiched between the bars, L_s represents the thickness of the specimen. In perforation experiments, however, the specimen is placed inside the fixture as shown Figure 61. Since the strain of the fixture material is much less than the strain in the specimen, the contribution of the fixture material (maraging steel) to the total specimen strain is negligible such that only the specimen length (L) is used for strain calculations.

Some important assumptions for the mathematical description of material deformation under dynamic impact are as follows (Zukas et al. [34], Bickle [41]):

1. The composite plate is elastic and its properties remain unchanged by the impact.
2. The state of the stress over the cross-sectional area is one-dimensional and uniaxial.
3. The wave is non dispersive.
4. The state of the stress at any instant is homogenous and in equilibrium over the entire composite plate.
5. Transverse strain, lateral inertia, and body forces are all negligible.
6. Sample strain is much greater than the total strain of the bar and the specimen fixture.

These assumptions were carefully investigated for the present set-up and found to be satisfied (Nwosu [37]). The validity of SHPB for application to the dynamic behavior of materials is well documented by others. Dynamic loading of the composite plates is provided by the longitudinal impact load $F_{0\,of}$ the striker, resulting in a uniaxial stress pulse transmitted to the incident bar as

$$\sigma(t) = \frac{F_0}{A} = (\rho c_0) V_p(t), \tag{15}$$

where $c_0 = dx/dt$ is the velocity of the wave pulse in the bar, $V_p(t)$ is the particle velocity, and ρ is the density of the striker bar material. Accurate measurements of the wave pulse and particle velocity in dynamic impact studies are important since the wave train is really the propagation of the disturbance or vibration of the particles. The amplitude of the incident wave pulse depends on the impact velocity (a function of the applied air pressure) and material properties of the striker. The measurement is expected to be accurate when measured at steady state conditions. Theoretically, such a steady (equilibrium) condition is satisfied by the continuity condition. The particle displacement is expressed as

$$u(t) = \int_0^t V_p(t)dt = \frac{c_0}{E_0}\int_0^t \sigma(t)dt\,. \tag{16}$$

Upon the arrival of a compressive incident wave at the specimen/incident bar interface, the wave is partially reflected (because of the impedance mismatch) and partially transmitted through the specimen. Thus, the net displacement at the surface is given as

$$U_1(t) = u_i - u_r = \frac{c_0}{E_0}\int_0^t [\sigma_i(t) - \sigma_r(t)]\,, \tag{17}$$

Where $c_0 = (E_0/\rho)^2$ and E_0 is the bar Young's modulus, and σ_i and σ_r are the incident and reflected stress pulses, respectively. Similarly, the net displacement at the specimen-transmitter bar interface is expressed as

$$U_2(t) = u_t(t) = \frac{c_0}{E_0}\int_0^t \sigma_t(t)dt\,. \tag{18}$$

Thus, from Equations (17) and (18), the net specimen displacement is given as:

$$U_1(t) - U_2(t) = u_n(t) = \frac{c_0}{E_0}\int_0^t [\sigma_i(t) - \sigma_r(r) - \sigma_t(t)]dt \tag{19}$$

Equation 20 represents the specimen displacement due to the interaction of compressive and tensile waves in the sample. The specimen's strain is ε_s (t)= $u_n(t)/L_e$), and since $\sigma(t) = E_0\varepsilon(t)$, the sample strain and strain rate using bars of the same cross section area can be expressed as:

$$\varepsilon_s(t) = \frac{c_0}{L_e}\int_0^t (\varepsilon_i(t) - \varepsilon_r(t) - \varepsilon_t(t))dt\,. \tag{20}$$

and

$$\frac{d\,\varepsilon_s(t)}{\partial t} = \frac{c_0}{L_e}(\varepsilon_i(t) - \varepsilon_r(t) - \varepsilon_t(t))\,, \tag{21}$$

respectively.

3.4.1.1 Stress, Particle Velocity, and Force Measurements

The particles in the incident bar will propagate to the right at a relative velocity of V_b in the longitudinal direction of the wave pulse. With a specimen of the cross sectional area, A_s, sandwiched between the incident and transmitter bars of the cross-section area, A_b, equilibrium at the interfaces is satisfied by the continuities of forces and velocities at the interfaces. Neglecting the specimen deflection in this case (correction of specimen deflection is considered separately), for equilibrium at the interfaces requires $\sum F = 0$ for each interface input bar-specimen (input), specimen-fixture (fixture), and fixture-output bar (output). This implies

$$\sum_{input} F = \sum_s F, \quad \sum_s F = \sum_f F\text{, and } \sum_f F = \sum_{output} F\,. \tag{22}$$

Equation 22 gives equilibrium of forces as

$$F_{input}(t) = \sum_i F = (\sigma_i + \sigma_r)A_b = F_s(t) = \sum_s F = (\sigma_t)A_b = F_{output}(t). \tag{23}$$

Similarly, continuity of velocities at the interfaces requires that

$$V_b = V_i - V_r = V_s, \tag{24}$$

Substituting Equation 3.1 into Equation 3.10, it can be shown that the particle velocity can be expressed as:

$$V_s = \frac{C_0}{E_0}(\sigma_i - \sigma_r). \tag{25}$$

The sample stresses at the incident bar/specimen and specimen/transmitter interfaces are

$$\begin{aligned} \sigma_{input}(t) &= \frac{F_{input}}{A_s} = \frac{A_b(\sigma_i(t) + \sigma_r(t))}{A_s} \\ \sigma_{output}(t) &= \frac{F_{output}}{A_s} = A_b \sigma_t(t), \end{aligned} \tag{26}$$

where A_s *is* the specimen cross-sectional area. Thus, the average sample stress is the mean of the stresses at the interfaces, i.e.,

$$\sigma_s(t) = \frac{1}{2}(\sigma_{input} + \sigma_{output}) = \frac{1}{2}\frac{A_b}{A_s}(\sigma_i + \sigma_r + \sigma_t). \tag{27}$$

Assuming uniform stress through a thin specimen, $\varepsilon_t(t) = \varepsilon_i(t) + \varepsilon_r(t)$ and $\sigma_t(t) = \sigma_i(t) + \sigma_r(t)$, Equation 27 gives

$$\sigma_s(t) = \frac{A_b}{A_s} E_0 \varepsilon_t(t), \tag{28}$$

and Equations (20) and (21) give the strain and strain rate as

$$\begin{aligned} \varepsilon_s(t) &\approx \frac{-2c_0}{L_e}\int_0^t \varepsilon_r(t)dt \\ \dot{\varepsilon}_s(t) &\approx \frac{-2c_0}{L_e}\varepsilon_r(t), \end{aligned} \tag{29}$$

respectively.

Equation 28 shows that stress is proportional to strain. The elastic Young's modulus, E_0, is applied when the magnitude of the stress is less than the yield stress of the material. In the general case of yielding, we have retained the dynamic modulus of elasticity as the ratio of ultimate yield stress to corresponding yield strain. Plastic deformation of a material subjected to

uniaxial stress occurs at a stress level above the yield stress of the material, while the rapture of the material occurs above its ultimate strength. Thus, when the stress-strain curve is composed of elastic and plastic portions, the elastic modulus is determined as the slope of the straight-line portion of the stress-strain curve in the limit of small strain interval.

3.4.1.2 Energy Measurements

The net energy released by the penetrator and carried by the propagating compressive wave to the composite plate is given by

$$E_R = \int_0^t F_i(t)\, du_n, \tag{30}$$

where $F_i(t) = A\,(\sigma_i(t) + \sigma_r(t))$ is the net compressive loading force and du_n is the net plate displacement. E_R can be obtained as the integrated area of the force-displacement curve over the duration of the wave. Assume that the net energy released by the penetrator is equal to the total expendable energy in the system (P-SHPB and composite plate) for penetration/perforation. Substituting Equation 19 into Equation 30, the net energy to be expended for the damage generation process plus minor losses by the fixture is given as

$$E_R = \left(\frac{Ac_0}{E_0}\right)\int_0^t [\,\sigma_i(t)^2 - \sigma_r(t)^2 - \sigma_t(t)^2\,]dt = \Delta E_{abs} + \Delta E_s, \tag{31}$$

Since the net energy lost by the penetrator is equal to the energy absorbed by the plate plus other losses, Equation 31 gives the total energy absorption curve, and is decomposed into energy absorbed by the plate (ΔE_{abs}) and the system strain energy release (ΔE_s). The numerical integration is carried out with all time shifted to zero and all three waves beginning at the same time and for the same time duration, t. The rest of the energy is dissipated in the formation of plastic deformation of the plate or lost in overcoming friction.

In terms of the energy of the longitudinal wave along the one-dimensional bar, Equation 31 can also be expressed as the net energy lost by the incident compressive wave, i.e., $E_A = E_i - E_r - E_t$, where $E = (Ac_0/E_0)\int\sigma^2 dt$ and can be written for incident (E_i), reflected (E_r), and transmitted (E_t) energies. Following energy balance, the energy absorbed by the composite plate and all competing processes is presented [42] as

$$E_A = (E_c + E_b + E_e) + (E_d + E_f), \tag{32}$$

where E_c is the energy expended by the penetrator during Hertzian contact, E_b is the energy due to bending, E_e is the energy associated with elastic stretching, E_d is the energy associated with permanent plate damage, and E_f is the energy lost by the penetrator due to friction. In the case of circular plate with a spherical penetrator with negligible membrane stretching, Equation 32 can be expressed as

$$E_A = P^2\left[\frac{3/2(1-\nu_r{}^2)R^2}{4\pi E_r L_s{}^2}\right] + P^{5/3}\left\{\frac{4}{5}\left[\frac{3\pi(k_1+k_2}{(R/2)^{1/2}}\right]^{2/3}\right\} + E_{fx}, \tag{33}$$

where, $k_1 = (1-\nu_s^2)/(\pi E_s)$ and $k_2 = (1-\nu_r^2)/(\pi E_z)$, E_s and ν_s are the Young's modulus and Poisson's ratio of the indenter, respectively, and E_r is the laminate modulus in the thickness direction, and ν_r is the laminate's Poisson's ratio, and R is the radius of the circular plate. The first term expresses the bending effect (E_b), the second term gives the Hertzian contact effect (E_c), and E_{fx} accounts for the energy losses. For the assumed point contact between the penetrator and the circular plate, the maximum deflection at the center of the circular plate due to the load P is given as:

$$\delta = \frac{3PR^2(1-\nu^2{}_r)}{4\pi E_r L^3{}_s} \tag{34}$$

In a typical perforation test, the penetrator emerges through the plate of thickness (L_s) to the maximum distance, $\delta = L_s + \chi$, where χ can be either the distance the penetrator travels beyond the plate during punch-through, or the height of the damage cone above the rear surface of the laminate. For a negligible plate deflection and energy losses, the total energy delivered by the penetrator for the process can be expressed as:

$$E_R = \frac{1}{2}m_b V_{pb}{}^2 = \int_0^{\delta} P(x)\ dx = \int_0^{L_s} P(x)dx + \int_{L_s}^{\delta} P(x)dx \tag{35}$$

where V_{pb} is the penetrator's critical penetration velocity or "penetration limit" velocity, m_b is the mass of the input bar, and $P(x)$ is the penetrator's point contact force exerted on the plate. The functional dependence of $P(x)$ on depth of penetration x can be represented by appropriate contact force model for the regions of interest. The second term in Equation 35 is the work done in the penetrator head traversing through a distance, $\chi = \delta - L_s$ above the plate.

To determine the critical (penetration limit) velocity for specimen perforation, one can use deterministic or probabilistic techniques. The complexity of the governing partial differential equations complicates the use of deterministic approach [34]. The probabilistic approach is based on the object's striking velocity and either its residual velocity or the resulting critical velocity is most commonly expressed as a V_{50}, that is, a striking velocity for which there exists a 50 percent probability of perforation of the barrier. Usually V_{50} is determined by averaging six projectile-striking velocities that include the three lowest velocities that resulted in complete penetration and the three highest velocities that resulted in a partial penetration [34]. In this research, perforation is defined as complete penetration of target so that light will pass through it. As expressed by Nwosu [36], a plot of striker impact velocity versus residual velocity, or a plot of crack length or crack height versus impact velocity can be used to estimate the threshold velocity required for incipient perforation. The critical velocity for perforation is then experimentally determined as the striker velocity at which the residual velocity or crack height length is equal to

zero. This satisfies that all the energy at the point of peroration is used for the perforation damage with zero residual energy.

The second term in Equation 32 can be seen as the residual energy after perforation. This has been modeled as the work done by an average contact force P_c over the duration of the perforation in moving a distance χ above the plate thickness and given as [36]

$$E_r = \frac{1}{2} m_b V_r = P_c \chi \tag{36}$$

Thus, the residual velocity is given by

$$V_r = \left(\frac{2}{m_b} P_c \chi \right)^{1/2} . \tag{37}$$

3.5 Experimental Design and Results

3.5.1 Experimental Considerations

All of the laminates were subjected to transversely applied compressive contact loads as supplied by the modified Hopkinson bar. The contact force was applied perpendicular to the plane of the panel. In the order of increased energy levels, damage can occur as minor matrix cracking, delamination, fiber breakage, penetration, and perforation (a combination of matrix cracking, fiber fracture, and delamination). The major experimental objectives in this phase of the project are to characterize the generation of damage during the entire penetration process involving indentation, penetration, and perforation in terms of energy expenditure and visible (surface) damage size.

The following data were measured for each composite plate: damage height, surface crack length, strain-time history, striker impact energy and velocity, penetrator velocity, length, and sample thickness. For the high-speed imaging, the following data were measured: camera speed, sequence of crack propagation on 80 frames, time delay, visible damage size, interframe, and interframe crack length.

Experiments and data analysis of the above data were designed to determine the relationship between the following:

- The feasibility of achieving penetration using Hopkinson bar apparatus.
- Incident stress and total energy absorption for a constant thickness.
- Effect of impact energy on energy absorption.
- Effect of impact energy on specimen deformation, strain rate, yields strength (penetration depth).

- Variation of stress with time.
- Contact force as a function of time.
- Displacement and particle velocity variation with time.
- Crack propagation (velocity) as a function of time and impact velocity from the high-speed camera.

The criteria for experimental validation of Hopkinson's pressure bar are as follows:

- The strain rate must exhibit a plateau for about 200 microseconds for valid data.
- A tensile strain release wave usually occurs between 250-300 microseconds. This is shown to be negative since it is the direct opposite of compressive wave stress.
- On the integration graph, the incident, reflected and transmitted waves are shifted to 0 so that data can be integrated from $0 \rightarrow t$.

The experiments were performed at ambient temperature and moisture conditions. The different experimental parameters are summarized in Table 17.

The penetrators (see Figure 63) were made out of maraging steel. The outer diameter is 38.10 mm and inner diameter hole of 25.4 mm drilled and recessed to allow the penetrator to sit properly on the incident bar when coupled to reduce mismatch effect between the incident bar and the penetrator. The conical end is 12.7mm long with the protruding end extending 0.20, 0.19, and 0.14-inch long respectively. The protruding section allows the specimen deformation to be achieved by not allowing the conical section to take part in the specimen failure response. The spherical- shaped end is 4.76 mm in diameter for this case. The total length of the penetrator is 72.64mm long. This geometry is typical for all the protruding spherical penetrators except for the spherical ends, which were 4.76, 5.56, and 6.35 mm, respectively.

3.5.2 Experimental Results

3.5.2.1 System Calibration

Striker and Penetrator Velocity Calibration Results: The objective is to develop a calibration curve and establish a correlation between the (compressor) impact pressure and striker delivered to the input bar and penetrator energy delivered to the specimen. The striker velocity just before impacting the incident bar was measured as a function of impact pressure using two infrared photo gate detectors.

Calibration: Two sets of two small flags constructed out of 25.4 mm wide strips of cardboard were attached: one set to the end of the striker bar and the second to the end of the incident bar. The strategic placement of the two infrared photo gate detectors along the SHPB system allowed for automatic data collection of the necessary time for the flags to pass through each gate with the first gate recording the time of the striker bar and the second capturing the incident bar's time. The capture times were automatically converted into velocities using computer software. All other response parameter measurements, excluding impact energy, were taken from the wave analysis.

Table 17. Experimental Parameters

Specimen Parameters	
Samples Diameter: 1.5 inches (38 mm)	
Composite sample type:	
a) Eight-layer satin weaved carbon fiber composite	
b) 8-, 12-, 16-, 24-layer plain carbon fiber composite	
c) 16-ply $[\pm 45/0/90]_{2S}$ graphite-epoxy laminated composite	
System Parameters	
Hopkinson Bar	
Young's modulus of maraging steel bar:	2.07×10^{11} Pa
Wave velocity in maraging steel bar:	5010 m/s
Bar length:	43.9 m
Density of maraging steel:	8000km/m^3
High Speed Camera	
Speed (Continuous Access):	100,000 to 1 million frames per second
Light Duration:	166 µs to 700 µs
Delay Time:	700–850 µs
Film Type:	T-Max 400 and 3200
Impact Parameters	
Penetrator:	1/4-inch diameter conical hemispherical-nosed maraging steel 3/16-, 1/4- and 7/32-inch protruding spherical-nosed
Striker bar length:	2 feet (0.61m) maraging steel
Ram displacement:	0.61 m to impact the incident bar
Compressed air pressure:	0–250 psi
Striker impact energy (from calibration):	$E_i = ap^x$
Striker impact velocity (from calibration)	$V_i = bp^y$
(where p is compressor pressure in MPa; 1 MPa=145 psi, and a, b, x, y are constants that depends on system set-up)	

Conical hemispherical-nosed Protruding spherical-nosed Protruding hemispherical-nosed

Figure 63. Different Types of Penetrators Used in Current Tests

Figure 64 depicts the calibration curves and the empirical equations showing nonlinear relationship between the striker and penetrator velocities and pressure.

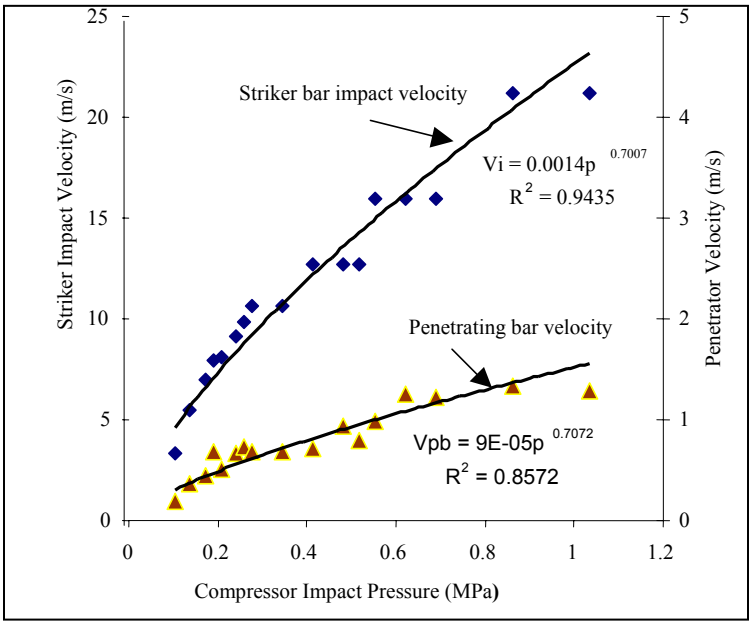

(a)

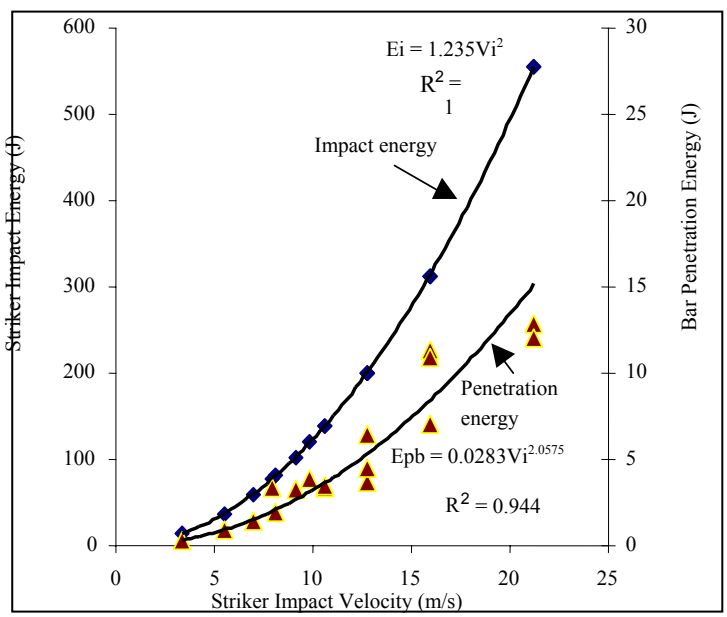

(b)

Figure 64 a) Variation of Striker Impact and Penetrator Velocities with Compressor Air Pressure (MPa), and b) Variation of Incident Bar Penetration Energy with Striker Velocity ($V_{pb}=0.0665V_i, R^2 = 0.92$, $E_{pb}=0.0271E_i, R^2=1.0$)

The penetrator attached to end of the incident bar penetrates the composite plate at an initial penetrator velocity, V_{pb}. The striker and the penetrating bar velocities are calibrated in terms of the compressor air pressure directly controlled by the experimenter. The data have been represented by a nonlinear curve fitting schemes that gave the following empirical equations:

$$V_{pb} = 9x10^{-5}\, p^{0.7072} \qquad (38)$$
$$V_i = 0.0014 p^{0.7007}.$$

The corresponding perforation and impact energies are determined from

$$E_{pb} = \frac{1}{2} m_{pb} V_{pb}^{\ 2} \qquad (39)$$
$$E_i = \frac{1}{2} m_{sb} V_i^{\ 2},$$

where m_{sb} is the mass of the 0.61-m striker bar equal to 2.47 kg, m_{pb} equal to 14.6 kg is the mass of the 3.66-m penetrating incident bar, the compressor pressure, p, is in Pa (1 MPa = 145 psi), velocity in m/s, and energy in joules. The above relationships provide us with a reliable impact pressure-impact energy calibration.

During calibration, the following effects and characteristics were observed for impact damage:

- Effects such as crack height and length depended on the pressure and thickness of the specimen.
- Lower thickness required lower pressures for significant damage.
- The strength of the specimen was apparent by the extent of the damage.
- The response parameters increased with an increase in pressure.
- The amplitude of the incident wave increased with an increase in pressure.

3.5.2.2 Characterization of the Wave Forms

Figure 65 shows typical incident, reflected, and transmitted stress pulses determined from the measured strain signal using appropriate system calibration. The incident wave reaches the strain gage located at 1.829 mm in 395 μs and 790 μs to the bar/specimen interface at 3.658 m. This represents a wave speed of 4630 m/s compared to the 5010 m/s theoretical value, a difference of less than 10 percent. It is noted that the theoretical wave speed is determined from the density and elastic modulus data supplied for the maraging steel Hopkinson bar material. Part of this incident wave is reflected back and travels the same time (395 μs) to reach the strain gage on the incident bar. Without a specimen, the transmitted wave will also begin its traverse time at the same time as the reflected wave and will reach the strain gage on the transmitter bar after 395 μs. The waveform is captured at a sample rate of 250,000 samples/sec at 68 J penetration limit

energy and 246 J above penetration energy. The figure shows more than two full reflections before the wave experiences any distortion. The wave is completely smooth at 246 J energy. This is because this energy is post-penetration limit energy with most of the residual energy returned to the system. In the case of partial penetration (with the penetrator head inside the specimen), Nwosu [33] has shown that the distortion of the wave will be more significant due to the global effect of the penetrator inside the specimen.

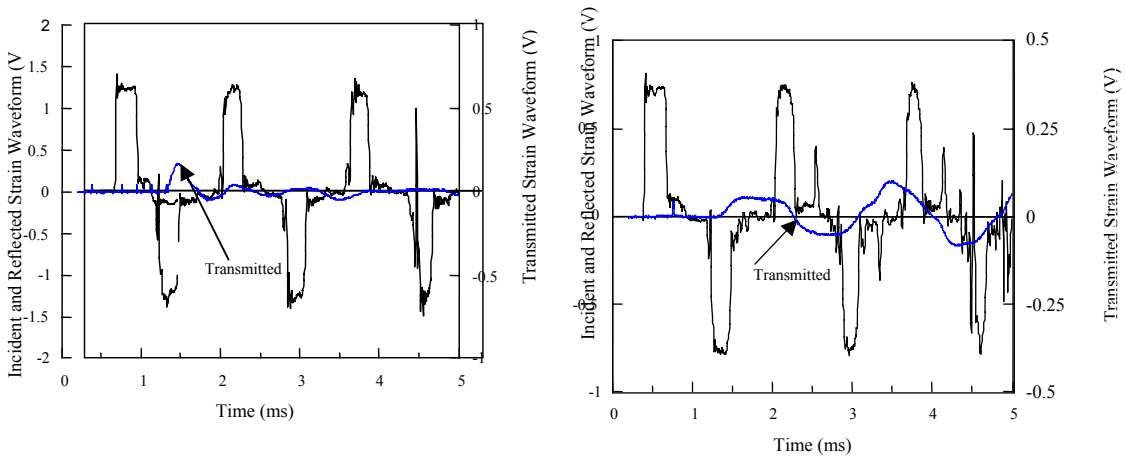

(a) (b)

Figure 65. Typical Strain Wave Pulses for a) 68 J (30 psi) and b) 246 J (75 psi)

The strain wave pulse provides information for complete characterization of the damage process. Figures 66 and 67 illustrate the time histories of force, particle velocity, energy absorption, and stress for woven carbon fiber penetrated with a conical hemispherical-nosed penetrator. The typical complete penetration process of carbon fiber composites generally involves five inter-dependent damage events: compression induced matrix cracking and fiber fracture, shear plug formation, plug separation, delamination, and perforation. This first stage is mainly compressive and corresponds to initial loading of the plate by the incident compressive stress as shown by the sharp rise in the force-time, energy absorbed-time curves. The penetrator velocity being greater than that of the laminate's flexure characterizes the compressive loading stage. The contact force increases as the plate is pushed or flexed forward with increasing particle velocity and decreases, as the plate is unloaded. Sudden decrease in the contact force may be indicative of incipient damage. A portion of the compressive pulse is reflected at the bar/specimen interface as a tensile wave. As the contact force increases to a critical value, allowing permanent deformation to occur, damage is initiated at the contact site depending on the target's mechanical properties and the stress level attained. Since the perforating velocity is greater than the laminate's forward velocity, it is conceivable that initial matrix cracking and penetration are dependent on the threshold kinetic energy at which these events occur. For all of the energies, the specimen rapidly reached a constant strain rate and particle velocity within the first few microseconds of the test and remained constant for more than 200 microseconds. Thus, there is more than enough time for the

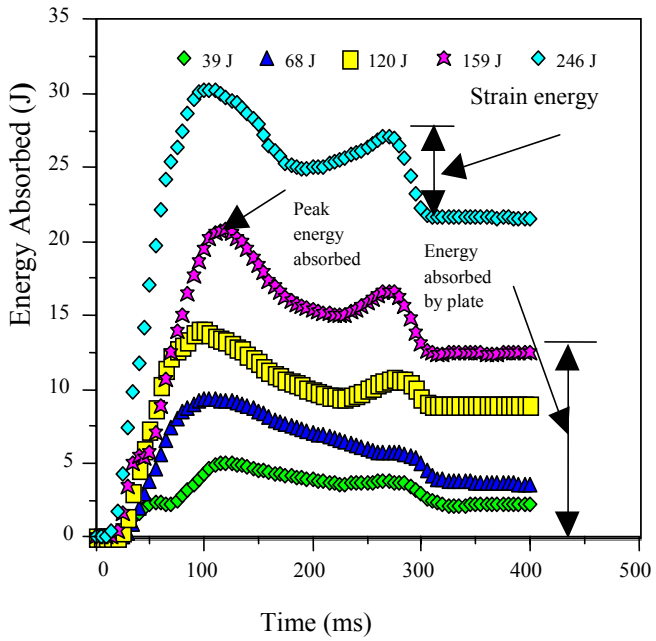

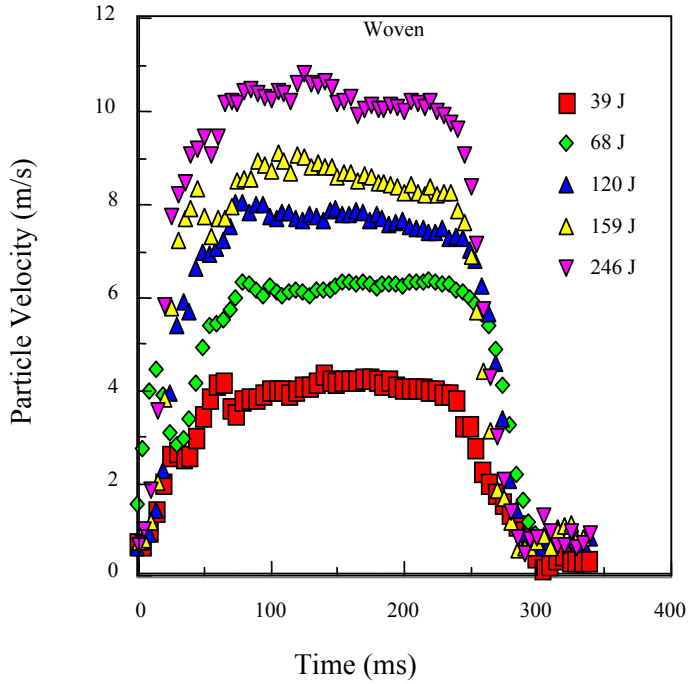

Figure 66. Time Variations of a) Total Energy Absorbed, and b) Particle Velocity for Different Striker Impact Energies

damage event to be completed and measured. The constant particle velocity clearly shows uniformity of the propagating wave, validating the assumption of uniform stress in the specimen.

3.5.2.3 Sample Responses to the High Strain Rate Perforation Damage

Figures 68–74 document the responses of the eight-layer satin woven composite plate to different impact and experimental input variables.

3.5.2.3.1 Energy Absorbed by the Composite Plate

The energy absorption-time curves in Figure 67 (a) show that the total energy released or delivered by the penetrator-incident bar system for damage initiation and propagation depends on the striker impact energy. The results clearly show that the energy retained by the composite plate is only slightly different at low energies. Ringing in the energy-absorbed curve is an indication of greater particle vibration and energy dissipation in the specimen. The higher the impact energy, the greater the load on the specimen will be and, therefore, the greater the vibration and propagation of the particles. The maximum energy delivered for the penetration process varies uniformly with incident (impact) energy. Hence, we define the peak energy, E_{peak}, as the net energy expended by the system (penetrator, fixture, and others (See Equation 3.21). Neglecting energy losses to the fixture, the peak energy is approximately the maximum energy available for the damage process (initiation and propagation). Some part of this energy will be lost to damage mechanisms such as vibration, friction, and plastic deformation, and the rest (E_{abs}) will be absorbed by the plate or returned to the penetrator. The energy absorbed by the plate is the peak energy minus the strain energy released (E_s) since the strain energy is E_p-$E_{abs.}$

A steady rise in energy-absorption mechanism is observed to be independent of the specimen thickness and the impact energy applied. Most of the energy is expended within the first 100 microseconds of loading depending on the striker impact energy as shown in Figure 66 a. This area is associated with initial elastic response. However, it takes about 150 microseconds for the specimen to reach the elastic yield point, as shown in Figure 67 a. Most of the damage is characterized by plastic deformation beyond the elastic region of damage. Beyond this point, the energy absorption continues in a uniform but non-linear fashion. There is a change in slope just before the peak energy level. Note that the specimen continues to strain even at the constant energy absorption level of the specimen. In Figure 67 b, the force-time history exhibits a sharp loading of the compressive force of the penetrator followed by the unloading region, all of which is completed with the first 100 microseconds. The initial compressive force is reflected in tension at the rear surface of the specimen after 200 microseconds period net zero force. As shown in the stress-time curve, the specimen continues to deform plastically even during this period. The magnitude of the tensile release force is shown by the arrow in Figure 67b to depend on the impact energy, as expected.

3.5.2.3.2 Strain Rate sensitivity

Figures 68 and 69 show the effects of strain rates and strain on sample response to damage. The strain rate is plotted on a logarithm scale to elucidate strain rate sensitivity of the materials responses. The plot shows that the yield stress increases with strain rate. A threshold strain rate is observed above which the specimen will begin to respond to the applied stress. These results appear to decompose the strain rate into two regions exhibiting elastic behavior below these values, and a region of incipient plastic deformation above this value. The first region of the

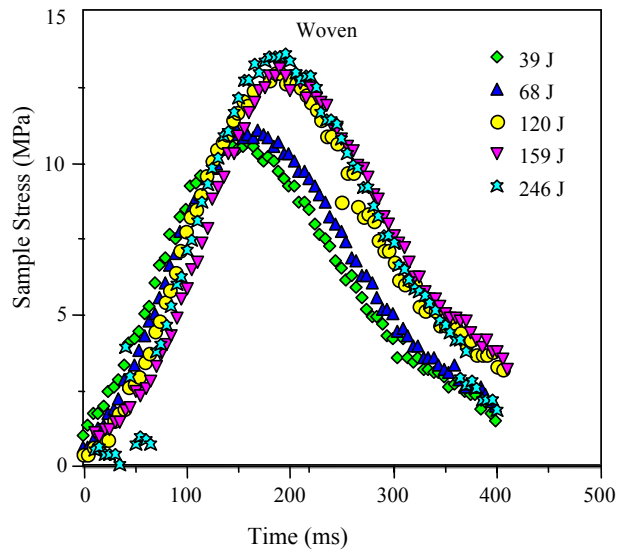

(a)

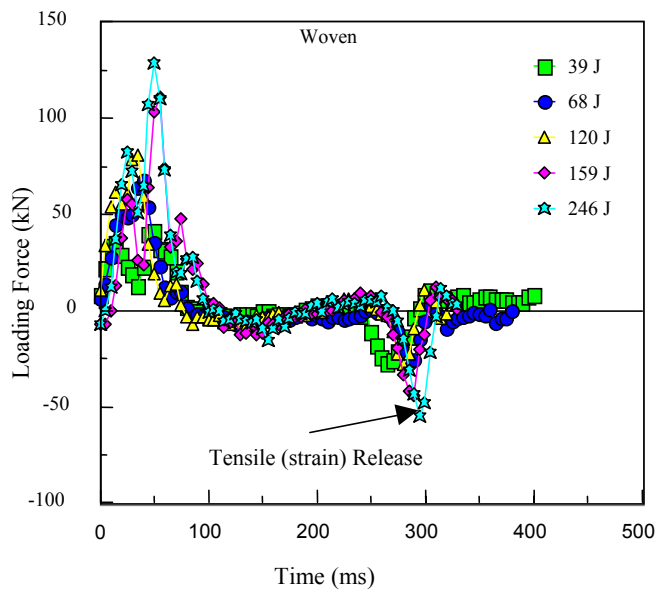

(b)

Figure 67. Time Variations of a) Sample Stress and b) Loading Force for Varying Striker Impact Energies

figure could also indicate minor inertia effects. This observation is in agreement with strain-rate-dependent theory original proposed by Malvern [43] which decomposes strain rates into an elastic and plastic portion and predicts that a material will reach a state of incipient plastic flow after a certain amount of elastic strain has been attained. Subsequently, the specimen begins to retain or dissipate the incident energy for minor damage events such as delamination when the strain rate is above this strain threshold value. As seen in Figure 68 a, the stress is strain rate sensitive up to

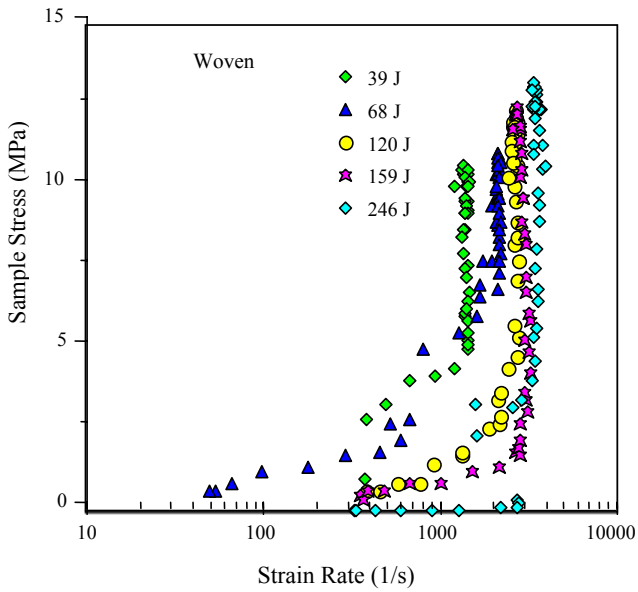

(a)

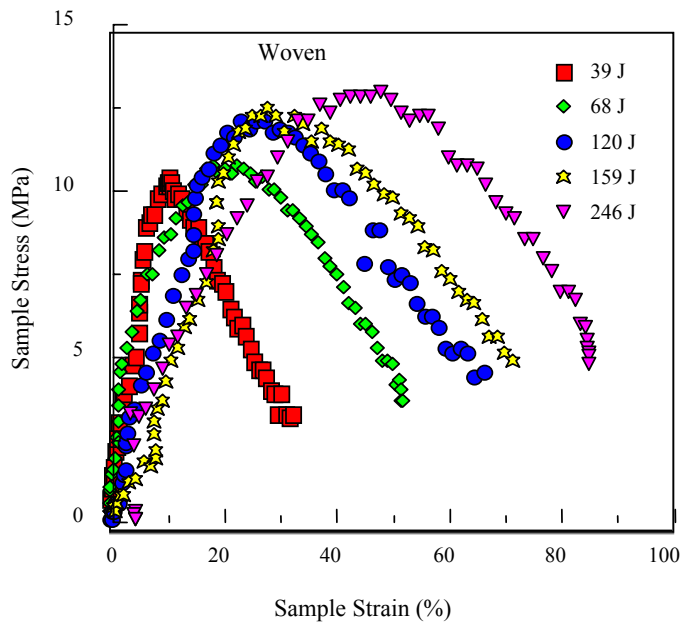

(b)

Figure 68. Variations of Sample Stress with a) Strain Rate, and b) Strain for Varying Striker Impact Energies

2200, 2600, 3000, and 3700 1/s for 68, 120, 159 and 246 J, respectively. There is a slight linear dependence of strain rate below these values. The stress-strain behaviors in Figure 68 b exhibit very high ductility with ultimate strength slightly dependent on energy.

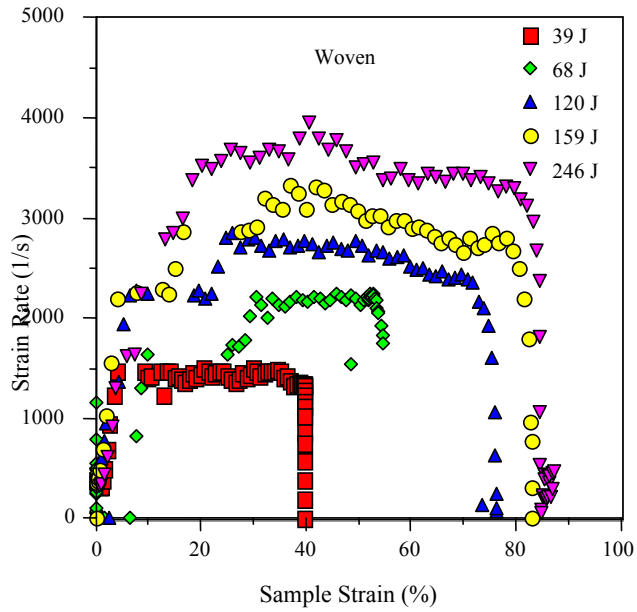

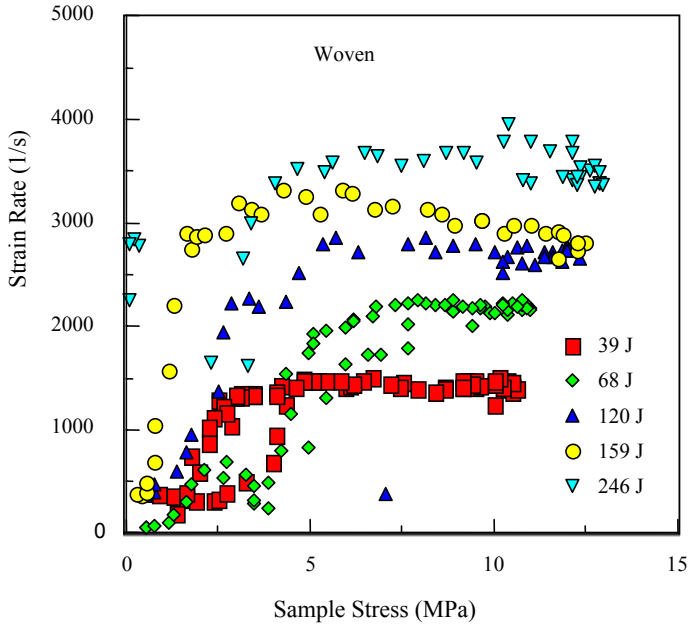

(b)

Figure 69. Variations of Strain Rate with a) Strain, and b) Sample Stress Using Conical Hemispherical Penetrator for Varying Striker Impact Energies

It is clear from the stress-strain curve that 39 J was enough to initiate surface cracks on this specimen. The failure mechanism is dominated by plastic deformation for all the energy levels. The specimen experienced perforation damage at energy 68 J. In this study, the ultimate failure

strength (maximum stress at failure) proved to be a more sensitive basis for surface damage development and characterization. The curves show that the material is of low modulus fiber.

3.5.2.3.3 Force and Energy Absorption Variations with Displacement

Figure 70 describes the variation of energy released with displacement or specimen deformation at varying energy levels covering the range from incipient surface crack to perforation and punch through. The curves show that the loading force and the energy absorption are strongly dependent on impact energy or incident stress level and displacement. The tensile release wave in the force displacement curve is released at the rear of the specimen, caused by the specimen being in tension specimen rear surface. Maximum displacement and tensile release are reached after about 300 s from the time the stress wave impacts the specimen. The value of the absorbed energy after this point is equal to the energy retained by the specimen. Thus, it provides a good estimate of strain energy to failure or the residual properties of the damage process. The net specimen displacement is taken as a measure of the specimen total deformation at any instant of time. The results clearly show that the absorbed energy depends on specimen deformation. As the specimen rear surface is approached, energy released drops to zero as all of the available energy has been dissipated.

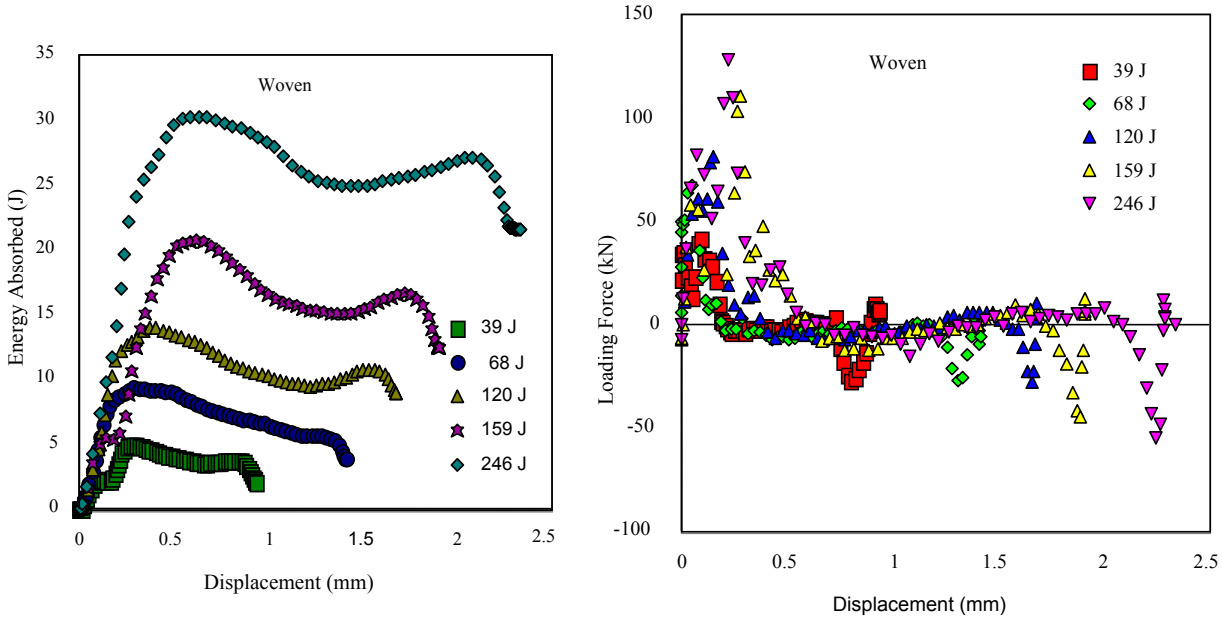

(a) (b)

Figure 70. Variations of (a) Total Energy Absorbed, and (b) Loading Force with Displacement for Varying Striker Impact Energies

Figures 71–74 display the summaries of the dependencies on different variables. Values of the peak energy absorption for the eight-layer satin weaved plates are determined for impact energies

varying from 39 J to 246 J. A surface crack was initiated at 39 J, perforation around 68 J, and punch through at 159 J.

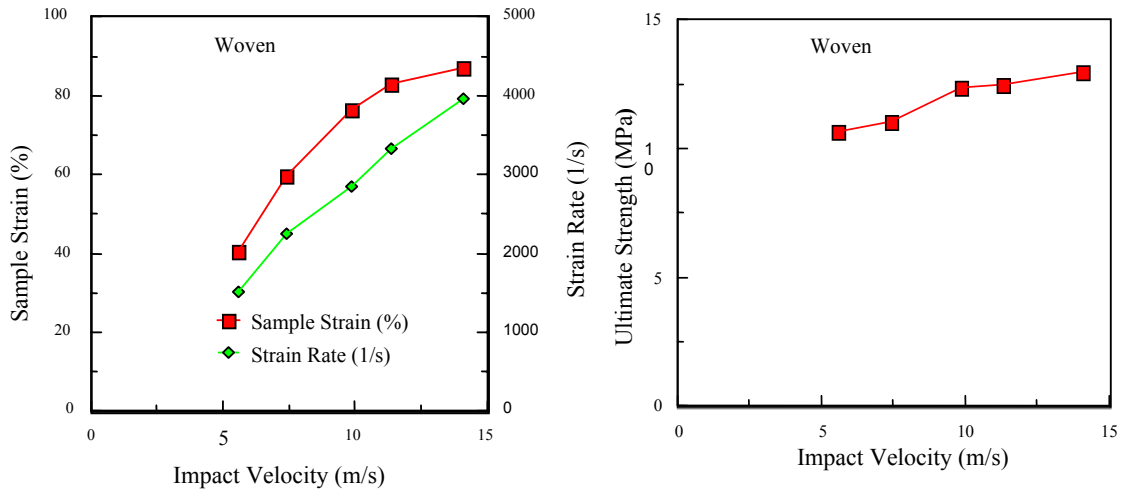

(a) (b)

Figure 71. Effects of Impact Velocity on a) Ultimate Strain, and b) Ultimate Strength

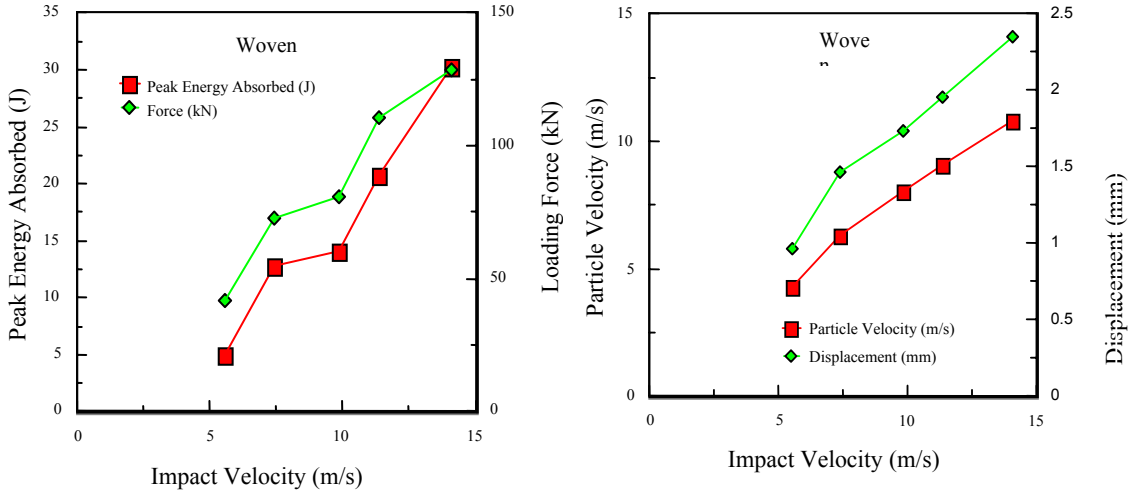

(a) (b)

Figure 72. Effects of Striker Impact Velocity on (a) Total Peak Energy Absorbed in Penetration/Perforation Event and (b) Peak Particle Velocity and Displacement

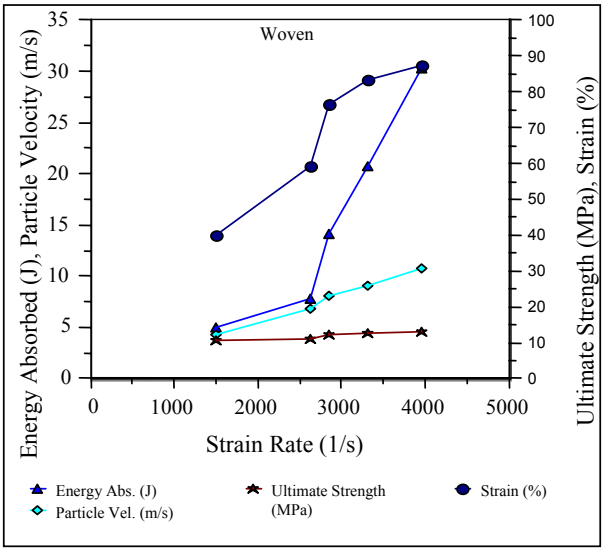

(a)

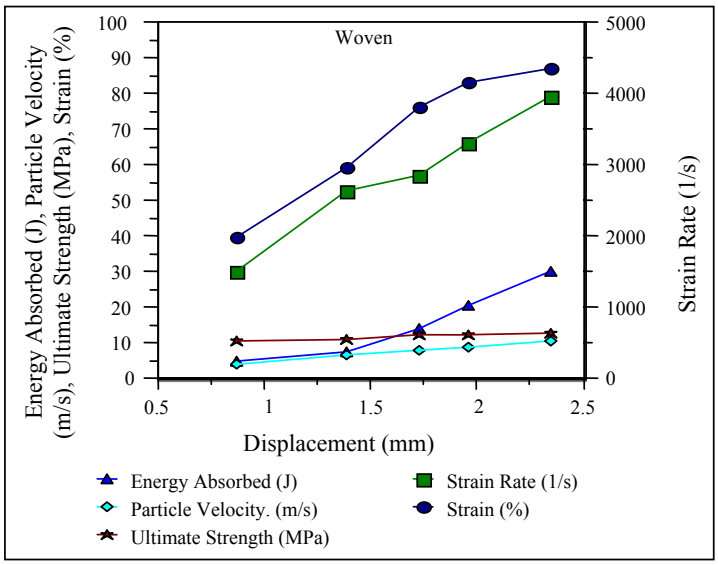

(b)

Figure 73. Effects of (a) Strain and (b) Displacement on Materials Responses

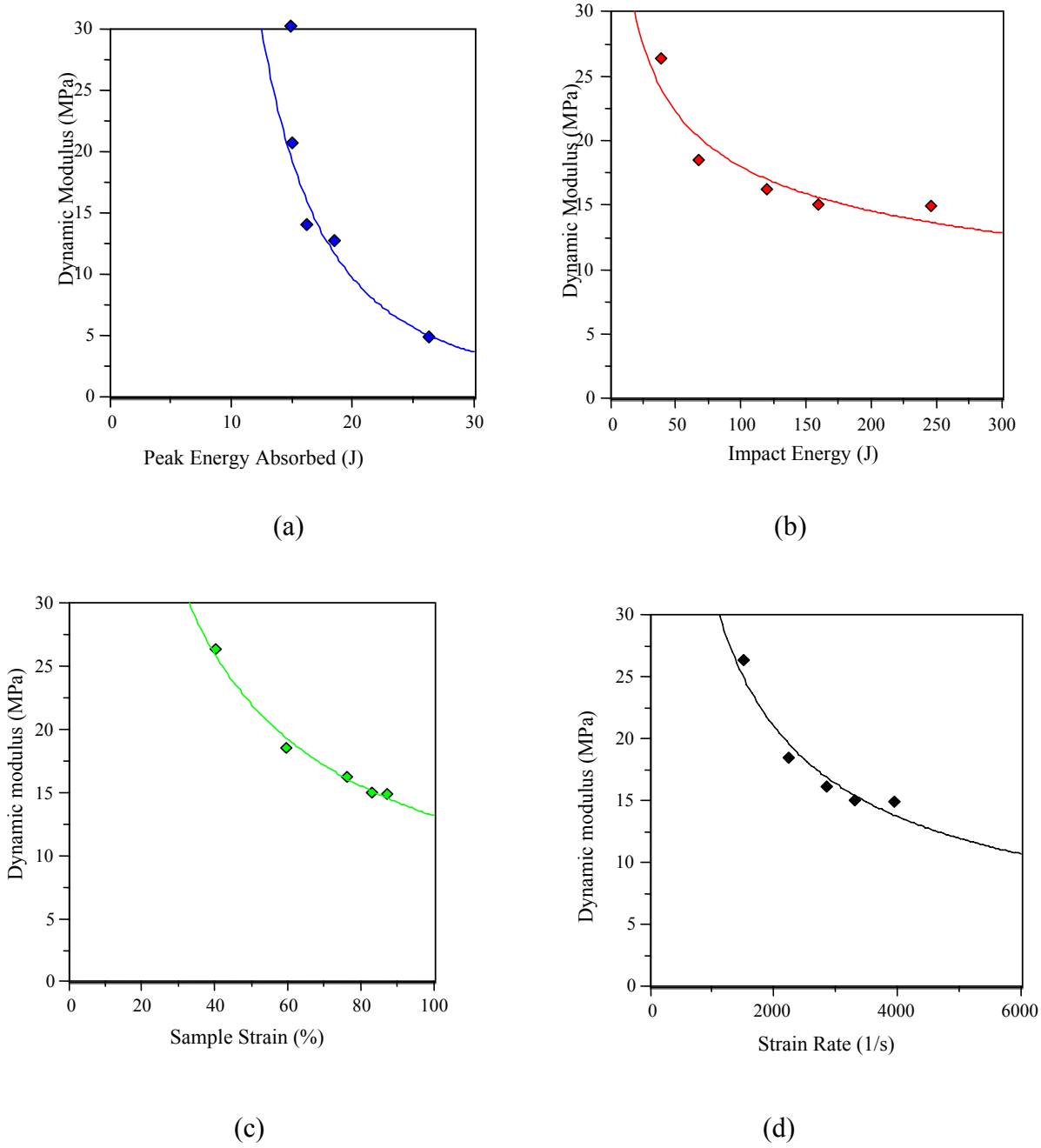

Figure 74. Effects of (a) Total Energy Absorbed in the Penetration/Perforation Event, (b) Impact Energy, (c) Strain, and (d) Strain Rate on Dynamic Modulus

3.5.2.4 Interaction and Effect of Incident Stress and Fiber Orientation on the Measurement of Energy Released

Factorial analysis is used here to investigate the effects and interactions of the controlled parameters. In these experimental studies, by conducting a factorial analysis, volumes of data can be reduced to information that is more meaningful in order to show the effects and interaction of the various parameters. The factorial experiment, designed by utilizing orthogonal arrays in the statistical experimental methods, investigated the effect and interaction of two levels of incident stress, and two levels of orientation on the measurement of energy absorbed. As shown in the Table 18, four possible combinations of the two factors exist. Thus, using the SHPB, the amount of energy absorbed by the graphite-epoxy samples was measured at the four different combinations of incident stress and orientation. Two runs were considered from the set of randomly conducted trials. The results were then tabulated and factorial analysis conducted.

Table 18. Factorial Analysis

Orientation = B			
Incident Stress =A	b_1	b_2	total = $b_1 + b_2$
a_1	a_1b_1	a_1b_2	a_1
a_2	$a_2\ b_1$	a_2b_2	a_2
total = $a_1 + a_2$	b_1	b_2	

In this 2^2 analysis, variation may be decomposed into the components of 1) variation due to factor A, 2) variation due to factor B, 3) variation due to the interaction of factors A and B, and 4) variation due to error.

An equation for total variation may be written as shown below, where the interaction is the mutual effect of incident stress and orientation in terms of the response scale (energy absorbed). Some preliminary calculations sped up the analysis of this experiment such that the total variation can be expressed as

$$SS_T = SS_A + SS_B + SS_{AxB} + SS_e. \tag{40}$$

The calculation of the interaction of factors A and B was done when the data was organized into the possible factor A and B combinations and summed for each combination as shown in Table 19. With respect to the determination of the penetration limit, two completely different sets of graphite-epoxy samples were perforated at different striker impact energies or impact pressures. After the wave-files were analyzed, the residual and impact velocities were calculated from Equation 37. Plots of the impact versus the residual velocities of the samples were generated so that the critical velocity could be illustrated graphically. The penetration limit was then determined from averaging the velocities corresponding to partial and complete penetration or from the value of its impact velocity for zero residual velocity or zero cracks height determined by graphical representation for each of the graphite-epoxy samples characterized by fiber orientation. All of the data analysis and graphical rendering in this case was done in Lotus® SmartSuite. Table 19 below shows the results of the factorial experiment.

Table 19. Results of Factorial Experiment

Orientation = B			
Incident Stress =A	b_1 40 psi	b_2 60 psi	total = $b_1 + b_2$
a_1= $+45_2/-45_2/0_2/90_2$	0.327087 0.274034	1.242620 1.374637	3.218378
a_2= $+45_2/-45_2/+45_2/-45_2$	0.318040 0.072321	0.981781 0.653502	2.025644
total = $a_1 + a_2$	0.99148	4.25254	5.24402

Table 20 shows the complete analysis of variance (ANOVA). It was found (by both the manual and computer application of ANOVA to the sample set) that there was no significant interaction between the two factors. The difference between the simple effects of A for the two levels of B is not significant. Thus, one can say that factors A and B do not interact. This result was also confirmed by the SigmaStat® application, as shown in Table 20.

Table 20. Analysis of Variance

Source	DF	SS	Mean Square	F
Treatments	ab-1=3	1.582		
A	a-1=1	0.1779	0.1779	7.554
B	b-1=1	1.3294	1.3294	56.453
AB	(a-1)(b-1)=1	0.07428	0,07428	3.155
Error	ab(r-1)=4	0.09419	0.0235	
Total	rab-1=7	1.6757		0.2394

DF = degree of freedom
SS = sum of squares
F = F-test, after Sir Ronald Fisher, a British statistical that invented the ANOVA

What was most interesting was to find whether the factors interacted and caused a significant response. SigmaStat® confirmed that there was no interaction between incident stress and fiber orientation. In addition, the computer application confirmed that the effect of the factor incident stress was significant and that the factor, fiber orientation was not significant. These results are clearly outlined in the SigmaStat® ANOVA (Table 21).

Table 21. Two–Way Analysis of Variance

Two–Way Analysis of Variance Data source: Data 1 in Notebook
Balanced Design
Dependent Variable: Energy
Normality Test: Passed (P > 0.200)
Equal Variance Test: Failed (P = <0.001)

Source of Variation	DF	SS	Mean Square	F	P
Orientation	1	0.178	0.178	7.552	0.051
Pressure	1	1.329	1.329	56.450	0.002
Orientation x Pressure	1	0.0743	0.0743	3.157	0.150
Residual	4	0.0942	0.0235		
Total	7	1.676	0.239		

- The difference in the mean values among the different levels of orientation is not great enough to exclude the possibility that the difference is just due to random sampling variability after allowing for the effects of differences in pressure. There is not a statistically significant difference (P = 0.051).
- The difference in the mean values among the different levels of pressure is greater than would be expected by chance after allowing for effects of differences in orientation. There is a statistically significant difference (P = 0.002).
- The effect of different levels of orientation does not depend on what level of pressure is present. There is not a statistically significant interaction between orientation and pressure. (P = 0.150)

This non-interaction of incident stress and fiber orientation within the penetration range led to two very powerful questions: Is there a relationship between orientation and penetration limit? Or is there a relationship between penetration limit and sample thickness?

3.5.3 Measurements of Penetration Limit Velocities

3.5.3.1 Penetration Limit Velocities of Laminated Composites

The Tables 22–27 lists the data recorded in the penetration limit determination experiment of the laminated composite of two layups of varying plies. The compressor pressure ranged from low pressure (low energy) for thin specimen to high pressure (high energy) for thicker specimen. Table 23 lists the data recorded in the penetration limit determination experiment of the 16 ply $[+45/-45/0/90]_{2S}$ samples upon impact with compressor pressures 90–115 psi. The test data (as shown in Tables 22–27) yielded the limit-velocity curves shown in Figure 75. The striker impact

velocity versus residual velocity curve shows the limiting value of residual velocity dependent on critical impact velocity.

Table 22. Penetration Test Data for 24-Ply Quasi-Isotropic Laminate $[+45/-45/0/90]_{3S}$

Sample id	Pressure	bulge	x-value	Peak Force	Velocity (r)	Pressure	Velocity (i)
	psi	mm	m	N	m/s	MPa	m/s
gep80	175	5.19	0.00209	52339.88	2.56	1.207	10.63
gep81	175	5.2	0.002075	42988.48	2.32	1.207	10.63
gep82	200	5.2	0.002075	57085.36	2.67	1.38	11.56
gep83	225	6.24	0.003115	56806.21	3.27	1.552	12.44
gep84	215	5.18	0.002055	58062.37	2.68	1.483	12.09
gep87	150	4.15	0.001025	49548.42	1.75	1.034	9.63
gep89	200	5.2	0.002075	57922.8	2.69	1.379	11.56
gep90	225	8.29	0.005165	60295.54	4.33	1.552	12.44
gep91	215	6.21	0.003085	56527.07	3.24	1.483	12.09
gep92	220	6.26	0.003135	56108.35	3.25	1.517	12.26
gep93	220	6.22	0.003095	55270.91	3.21	1.517	12.26
gep94	225	7.26	0.004135	57643.65	3.79	1.552	12.43
gep95	225	10.38	0.007255	58481.09	5.05	1.552	12.434
gep97	235	5.22	0.002095	53316.89	2.59	1.621	12.77
gep99	230	7.25	0.004125	56247.92	3.74	1.586	12.61

Table 23. Penetration Test Data for 8-Ply Quasi-Isotropic Laminate $[+45/-45/0/90]_S$

sample id	Pressure	Bulge	X-value	Peak Force	Velocity (r)	Pressure	Velocity (i)
	psi	mm	M	N	m/s	MPa	m/s
gep 114	25	0.52	0	8932.672	0	0.1724	2.442
gep 115	27.5	0.52	0	9211.818	0	0.1893	2.688
gep 116	30	1.04	0.00052	11305.41	0.595	0.2068	2.909
gep 117	30	1.03	0.00051	9630.537	0.544	0.2068	2.909
gep 120	32.5	2.04	0.00152	13399.01	1.107	0.2243	3.125
gep 121	32.5	2.1	0.00158	12561.57	1.093	0.2243	3.125
gep 123	35	4.17	0.00365	14376.02	1.778	0.2418	3.334
gep 124	35	4.15	0.00363	13817.73	1.738	0.2418	3.334
gep 125	40	4.16	0.00364	16330.04	1.892	0.2757	3.731

Table 24. Penetration Test Data for 16-Ply Quasi-Isotropic Laminate $[+45/-45/0/90]_{2S}$

Sample id	Pressure	Bulge	X-value	Peak Force	Velocity (r)	Pressure	Velocity (i)
	psi	mm		N	m/s	MPa	m/s
gep140	90	2.11	1E-005	27775.03	0.129	0.620	6.851
gep141	100	3.12	0.00102	34055.81	1.446	0.689	7.364
gep142	110	4.16	0.00206	33497.52	2.039	0.758	7.853
gep143	115	4.17	0.00207	33078.8	2.031	0.793	8.090

Table 25. Penetration Test Data for 16-Ply Laminate $[+45/-45]_{4S}$

sample id	Pressure	bulge	x-value	Peak Force	Velocity (r)	Pressure	velocity (i)
		m	m	N	m/s	MPa	m/s
gep 145	100	0.00315	0.00105	26379.3	1.2920	0.6896	7.3641
gep 146	110	0.0042	0.0021	31822.64	2.006	0.7586	7.853
gep 148	115	0.00832	0.00622	25262.71	3.077	0.7931	8.090
gep149	115	0.00833	0.00623	34195.39	3.583	0.7931	8.090
gep153	112.5	0.00521	0.00311	30287.34	2.382	0.7758	7.972
gep154	112.5	0.0052	0.0031	28193.75	2.295	0.7758	7.972
gep155	110	0.00418	0.00208	25123.14	1.774	0.7586	7.853
gep156	120	0.00835	0.00625	31124.78	3.424	0.8275	8.322
gep157	90	0.0021	0	32520.51	0	0.6206	6.851
gep158	60	0.0021	0	19679.79	0	0.4137	5.124
gep159	75	0.00211	1E-005	27635.45	0.1290	0.5172	6.028

Table 26. Penetration Test Data for 8-Ply Laminate $[+45/-45]_{2s}$

Sample id	Pressure	Bulge	X-value	Peak force	Velocity (r)	Pressure	Velocity (i)
		m	M	N	m/s	MPa	m/s
gep160	50	0.00209	0.00105	22750.4	1.199	0.3448	4.460
gep161	40	0.00105	1.00E-005	17446.63	0.1025	0.2758	3.731
gep162	45	0.00106	2.00E-005	19540.22	0.15349	0.3103	4.105
gep163	45	0.00105	1.00E-005	20098.51	0.1100	0.3103	4.105
gep164	50	0.00211	0.00107	22331.68	1.200	0.3448	4.460
gep165	55	0.00518	0.00414	23866.98	2.4402	0.3793	4.799
gep166	55	0.00517	0.00413	18284.06	2.1334	0.3793	4.799
gep167	55	0.00521	0.00417	22192.11	2.3615	0.3793	4.799
gep168	60	0.00523	0.00419	25123.14	2.5186	0.4137	5.124
gep169	52.5	0.00522	0.00418	18563.21	2.16254	0.3620	4.632
gep170	50	0.00211	0.00107	20517.23	1.1502	0.3448	4.460
gep172	51.25	0.00312	0.00208	19819.37	1.57629	0.3534	4.546
gep173	50	0.00206	0.00102	20377.66	1.119	0.3448	4.460
gep174	50	0.00207	0.00103	20796.38	1.1362	0.3448	4.460

Table 27. Penetration Test Data for 4-Ply Laminate [+45/-45]

Sample id	Pressure	Bulge	X-value	Peak Force	Velocity (r)	Pressure	Velocity (i)
45/45]s	4ply	M	m	N	m/s	MPa	M/s
ep187	25	0.00052	0	16330.04	0	0.1724	2.449
ep188	27.5	0.00052	0	16330.04	0	0.1896	2.684
ep190	32.5	0.00208	0.00156	16330.04	1.239	0.2240	3.125
ep191	32.5	0.00205	0.00153	16330.04	1.227	0.2241	3.125
ep192	35	0.00312	0.0026	16330.04	1.599	0.2413	3.334
ep193	35	0.00519	0.00467	16330.04	2.143	0.2413	3.334
ep194	35	0.00521	0.00469	16330.04	2.148	0.2413	3.334
ep195	30	0.00052	0	16330.04	0	0.2068	2.909
ep196	30	0.00052	0	16330.04	0	0.2068	2.909
ep197	30	0.00052	0	16330.04	0	0.2068	2.909
ep198	32.5	0.00312	0.0026	16330.04	1.599	0.2241	3.125
ep199	32.5	0.00104	0.00052	1116.584	0.187	0.2241	3.125
ep200	32.5	0.00207	0.00155	15353.03	1.197	0.2241	3.125
ep201	35	0.00521	0.00469	15353.03	2.083	0.2413	3.334
ep202	35	0.0052	0.00468	14515.59	2.023	0.2413	3.334
ep203	35	0.00418	0.00366	14515.59	1.789	0.2413	3.334
gep204	35	0.00418	0.00366	14515.59	1.789	0.2413	3.334
gep205	40	0.00418	0.00366	14655.17	1.797	0.2758	3.731
gep206	30	0.00106	0.00054	17167.48	0.747	0.2068	2.909
gep207	35	0.00413	0.00361	14376.02	1.768	0.2413	3.334
gep208	35	0.0052	0.00468	13259.44	1.933	0.2413	3.334

Figure 75 compares the rear surface damage patterns of satin woven composites with that of laminated composites. The experiment was conducted at varying striker impact energies using the conical hemispherical penetrator. The mode of perforation failure is localized with obliquely shaped cracks for the woven fiber. In the case of the laminated composite, the delamination propagates through the diameter of the specimen.

Figure 76 illustrates the behavior of the samples upon impact with varying striker impact energies (compressor pressures up 235 psi). The impact versus residual velocity curve shows a sharply defined jump in the penetration region. The cluster of data points at the 12-m/s impact velocity coordinate could be explained by a number of phenomena. These include, but are not entirely limited to, the fluctuation of compressor pressure at values higher than 200 psi, as well as characteristic [+45/-45/0/90] sample behavior at high impact energies.

The bar penetrating velocity (i.e., velocity of incident bar) is plotted against the impact energy. The result shows that threshold velocity (velocity limit which has to be exceeded before perforation) increases as the specimen thickness increases among others [33,34,44].

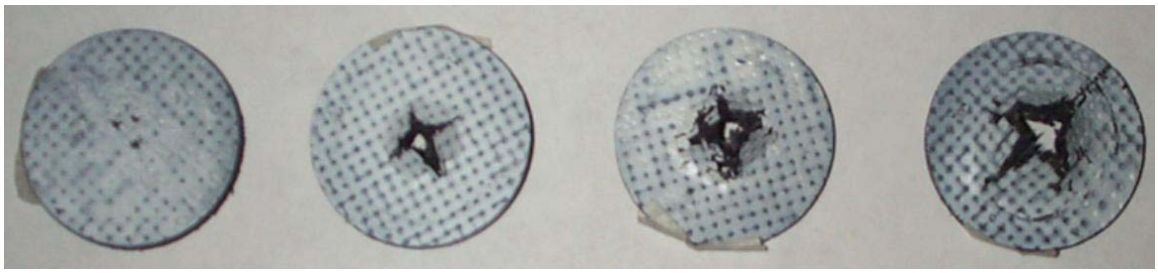

(a)

(b)

(c)

Figure 75. Photographs Showing Rear Surface Damage Pattern for a) 8-Layer Weaved Carbon Fiber at 39, 68, 120, and 159 J, b) 16-Ply $[\pm 45/0/90]_{2s}$ Graphite-Epoxy Laminates at 68, 80, 148, and 152 J Using c) 3/16-inch Conical Hemispherical Penetrator

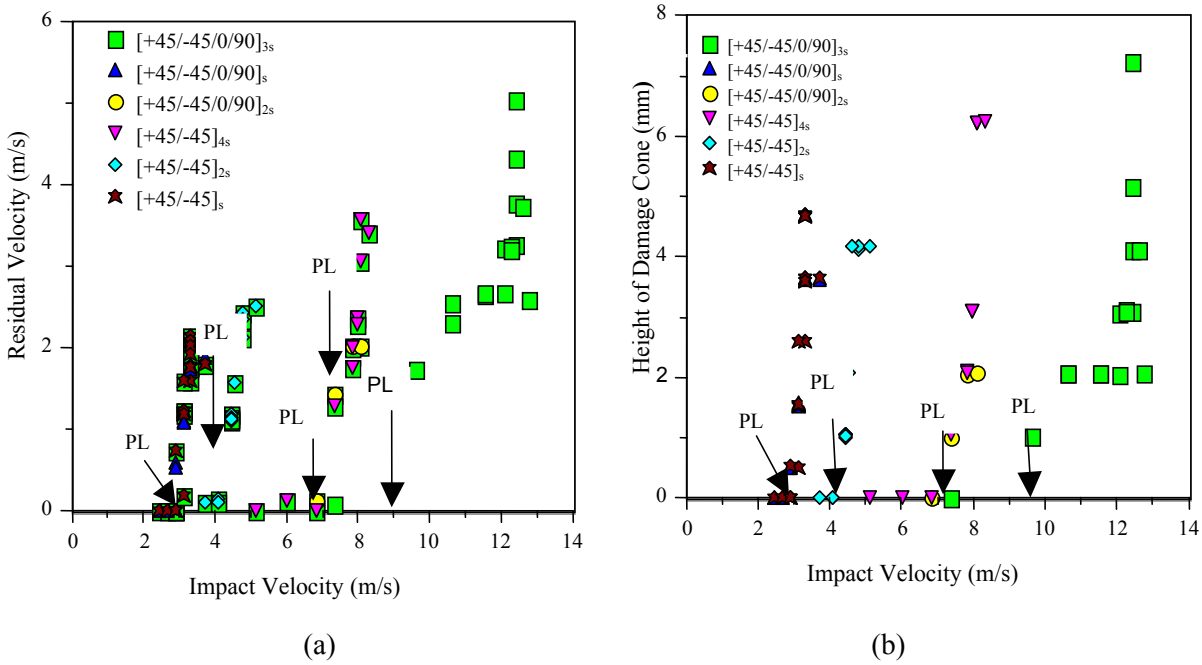

Figure 76. Variation of (a) Residual Velocity and (b) Specimen Damage Height With Striker Impact Velocity for [±45/0/90] and [±45] fiber Layups Using 1/4-inch Hemispherical-nosed Penetrator

Results indicated that the critical energy (energy corresponding to the threshold velocity) for (layer specimen) is 139 joules and crack length is 0.35 mm. The sudden rise seen on the result indicated that the specimen has been perforated, thereby depicting the penetration limit for this specimen. The crack length and height depends on the impact energy to a reasonable extent. Interestingly, after the penetration limit has been exceeded, the remaining residual energy (energy available after penetration limit) will result in almost no further local damage to the specimen.

The summary plot in Figure 77 clearly exemplifies a linear relationship between penetration limit and sample thickness. It is evident that the limit-velocity curves for all of the trials adequately represent the behavior of the graphite-epoxy samples, illustrating the very sharp boundary that is common to the penetration range.

The penetration limits of the [+45/-45] and [+45/-45/0/90] samples of different thickness were found by averaging, at most, six projectile-striking velocities that included the three lowest velocities that resulted in complete penetration and the three highest velocities that resulted in a partial penetration. Table 28 shows the result of these calculations.

Table 28. Summary of Penetrations velocities for laminated graphite/epoxy

Specimen Thickness (# of Plies)	Critical Striker Velocity	
	[±45/0/90]ns	[±45ns]
4	2.61 ± 0.21	3.02 ± 0.03
8	ND	4.59 ± 0.70
16	7.97 ± 0.65	7.8 ± 0.81
24	12.32 ± .08	ND

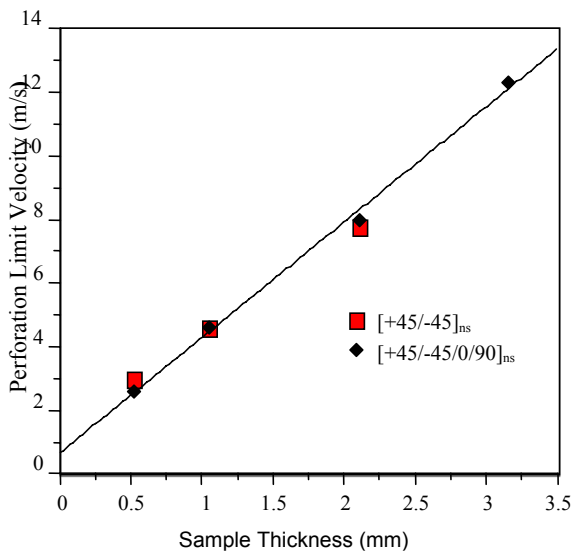

Figure 77. Relationship Between Critical Striker Velocity for Penetration of Laminated Graphite-Epoxy Composite Using 1/4-inch Hemispherical-nosed Penetrator

3.5.3.2 Determination of Penetration limit for Woven and Laminated Composites

The penetration limit for woven graphite epoxy was done following the same method described earlier for unidirectional laminates. Fig 78 shows the plot of crack length and crack height (residual displacement above perforation threshold) for different impact energies. The plot exhibits very good s- shaped curve typical of the penetration region phenomenon. The energies for perforation of the 12, 16, and 24-layer specimens are experimentally determined as indicated by the arrow in Figure 78. Thus, using Equation 39, the perforation or striker penetration limit velocities are calculated.

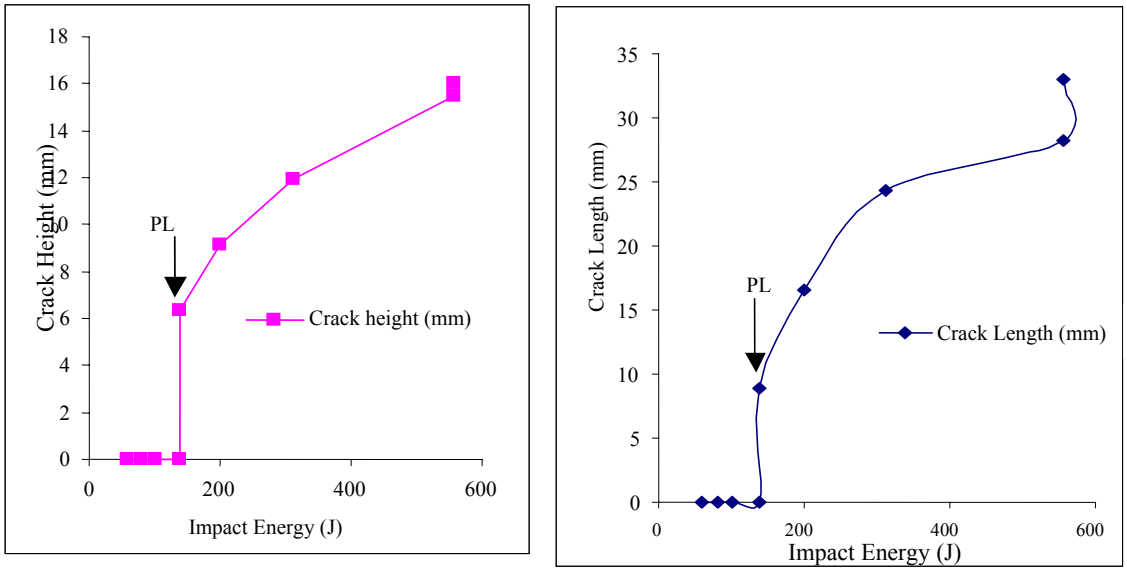

(a) (b)

Figure 78. Variation of (a) Crack Height and (b) Crack Length with Striker Impact Energy for Woven Graphite-Epoxy Composite Using 1/4-inch Spherical-Nose Penetrator

Figure 79 compares the effects of thickness on penetration limit velocity in generating surface crack, perforation and plugging or punch-through levels of damage modes using two penetrator geometries. Although the penetration limit velocity increases with thickness in general, it is clear that the two geometries have different effects on the specimen response at perforation damage mode. It is apparent that size rather than shape is a more significant factor in this case. For the same size, the protruding spherical-nosed penetrator has slightly higher penetration limit velocity than the protruding hemi-spherical-nosed penetrator (see Figure 79b and c). The results (Table 29-33 and Figure 79) indicate that the conical hemispherical penetrator requires a slightly higher energy level to perforate its target than the spherical penetrator does. The damage of the spherical penetrator is highly localized because of the penetrator shape. Thus, for the same thickness, the conical hemispherical will require higher energy to defeat its target, apparently because of the conical section of the penetrator. Once the target is defeated, it will cause a global damage to the target due to the effect of the increasing surface area. As the size of the penetrator is increased, as in Figure 79c, the penetration and perforation thresholds increase significantly through a more global destruction of the target.

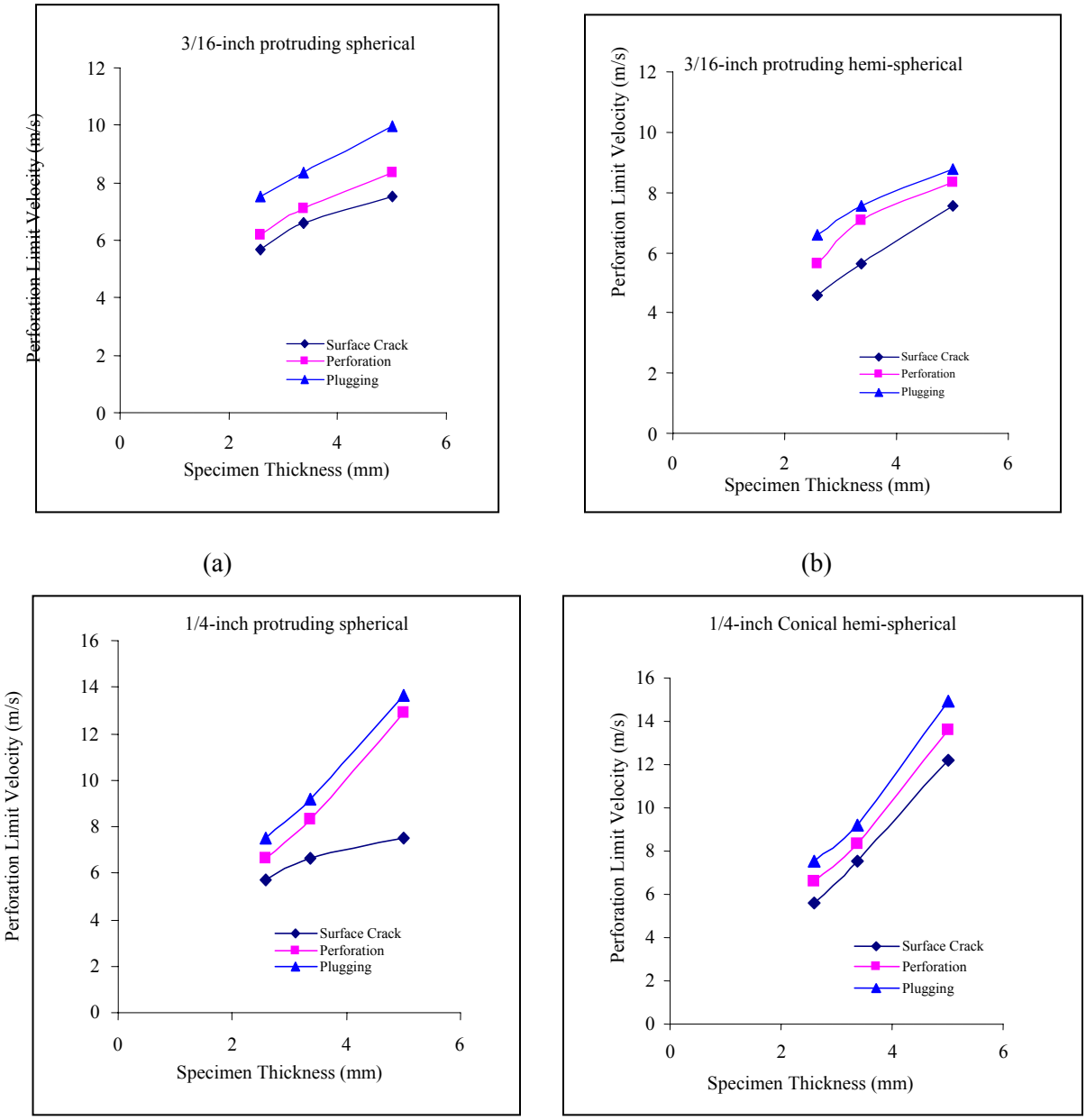

Figure 79. Variation of Striker Bar Penetration Limit Velocity With Sample Thickness for Three Penetrator Geometries (a and c) Protruding Spherical, b) Protruding Hemispherical, and d) Conical Hemispherical

Table 29. Damage Initiation Energy/Layer for Graphite-Epoxy Woven Specimen Using 3/16-inch Protruding Spherical Penetrator

Specimen	Surface Crack Initiation		Perforation		Plugging	
	Impact Energy (J)	Striker Impact Velocity (m/s)	Threshold Energy (J)	Threshold Velocity (m/s)	Threshold Energy (J)	Threshold Velocity (m/s)
12 layer	40	5.69	47	6.17	70	7.53
16 layer	54	6.61	62	7.09	86	8.34
24 layer	70	7.53	86	8.34	123	9.98
Energy (J)/layer for 12 layer	3.3		3.9		5.8	
Energy (J)/layer for 16 layer	3.4		3.9		5.4	
Energy (J)/layer for 24 layer	2.9		3.6		5.1	

Table 30. Damage Initiation Energy/Layer for Graphite-Epoxy Woven Specimen Using 7/32-inch Protruding Spherical Penetrator

Specimen	Surface Crack Initiation		Perforation		Plugging	
	Impact Energy (J)	Critical Striker Velocity (m/s)	Threshold Energy (J)	Threshold Velocity (m/s)	Threshold Energy (J)	Threshold Velocity (m/s)
12 layer	40	5.69	54	5.69	70	7.53
16 layer	54	6.61	78	7.95	86	8.34
24 layer	70	7.53	113	9.57	143	10.76
Energy (J)/layer for 12 layer	3.3		4.5		5.8	
Energy (J)/layer for 16 layer	3.4		4.9		5.4	
Energy (J)/layer for 24 layer	2.9		4.7		6.0	

Table 31. Damage Initiation Energy/Layer for Graphite-Epoxy Woven Specimen Using 1/4 -inch Protruding Spherical Penetrator

Specimen	Surface Crack Initiation		Perforation		Plugging	
	Impact Energy (J)	Critical Striker Velocity (m/s)	Threshold Energy (J)	Threshold Velocity (m/s)	Threshold Energy (J)	Threshold Velocity (m/s)
12 layer	40	5.69	54	6.61	70	7.53
16 layer	54	6.61	86	8.34	104	9.18
24 layer	70	7.53	206	12.92	229	13.62
Energy (J)/layer for 12 layer	3.3		4.5		5.8	
Energy (J)/layer for 16 layer	3.4		5.4		6.5	
Energy (J)/layer for 24 layer	2.9		8.6		9.5	

Table 32. Damage Initiation Energy/Layer for Graphite-Epoxy Woven Specimen Using 3/16 -inch Protruding Hemispherical Penetrator

Specimen	Surface Crack Initiation		Perforation		Plugging	
	Impact Energy (J)	Striker Impact Velocity (m/s)	Threshold Energy (J)	Threshold Velocity (m/s)	Threshold Energy (J)	Threshold Velocity (m/s)
12 layer	26	4.59	39	5.62	54	6.61
16 layer	39J	5.62	62	7.09	70	7.53
24 layer	70	7.53	86	8.34	95	8.78
Energy (J)/layer for 12 layer	2.1		3.3		4.5	
Energy (J)/layer for 16 layer	2.4		3.9		5.8	
Energy (J)/layer for 24 layer	2.9		3.6		4.0	

Table 33. Damage Initiation Energy/Layer for Graphite-Epoxy Woven Specimen Using 1/4 -inch Conical Hemispherical Penetrator

Specimen	Surface Crack Initiation		Perforation		Plugging	
	Impact Energy (J)	Striker Impact Velocity (m/s)	Threshold Energy (J)	Threshold Velocity (m/s)	Threshold Energy (J)	Threshold Velocity (m/s)
12 layer	39	5.62	54	6.61	70	7.53
16 layer	70	7.53	86	8.34	104	9.18
24 layer	184	12.21	229	13.62	275	14.92
Energy (J)/layer for 12 layer	3.3		4.5		5.8	
Energy (J)/layer for 16 layer	4.4		5.4		6.5	
Energy (J)/layer for 24 layer	7.6		9.5		11.5	

3.5.3.3 Strain Rate Sensitivity and Measurement Near Perforation Threshold (Penetration Limit) Energies for Woven Composites

Figures 80–86 show the results of experiments investigating the effects of penetrator geometry and size on the dynamic failure response of graphite-epoxy (plain woven) composites around the critical perforation energy. It is hypothesized that energy absorbed by a material will vary with the size and geometric shape of the penetrator due to the differences in the pressure distribution. Three different penetrator shapes and sizes described earlier, namely the protruding spherical, the conical hemispherical, and the protruding hemispherical, were used. At the same energy level, we predict that all of the penetrators would release nearly the same amount of impact energy to the specimen but that the level of damage caused by varying energy dissipation rates of each penetrator would vary. For example, we expect the damage caused by a smaller size penetrator, like the protruding hemispherical penetrator, to be localized. It was also hypothesized that the penetration limit for all the penetrators would increase as the diameter of the contact end of the penetrator increases.

Figure 80 displays the strain-rate time histories for 12-, 16-, and 24-layer specimens at the same striker impact energy of 68 J but varying penetrator sizes to see the effect of penetrator size on damage. The specimen reaches a plateau region of maximum strain rate and particle velocity within the first 100 microseconds after impact with the compressive stress wave. It remained constant for about 200 microseconds at which time the damage to the specimen must have been completed. This behavior also validates one of the assumptions made for the use of Hopkinson bar for high strain experiments. It is clear from the summary plot of the peak values that the strain decreases with thickness for all the penetrator sizes tested. The three penetrators have approximately the same effect for the 24-layer specimen. It appears, however, that the effect of size on peak strain rate is determined by the size of the penetrator nose relative to the specimen thickness. It was hypothesized that strain rate is inversely proportional to specimen thickness. The results show that the relationship in most cases is slightly nonlinear.

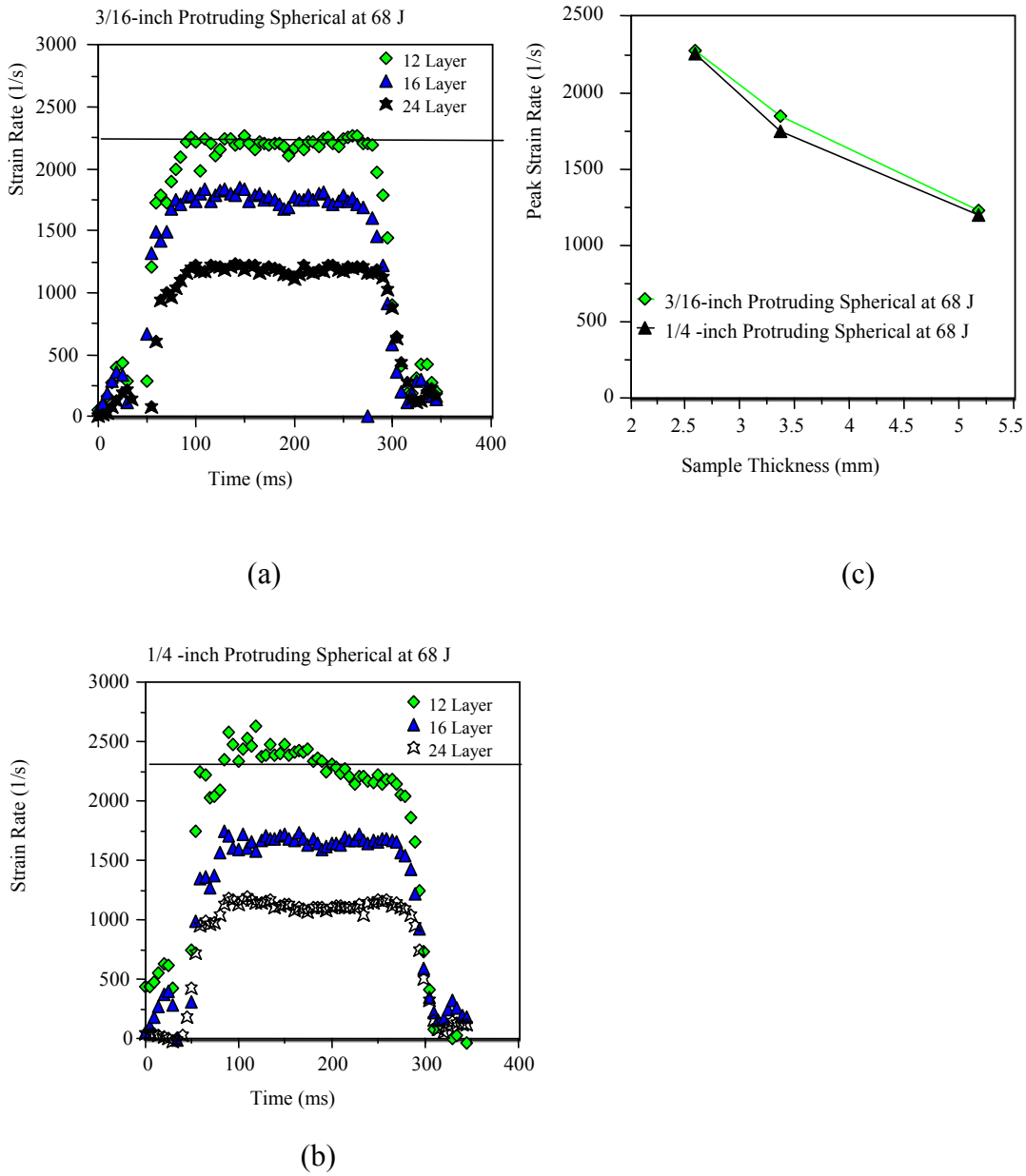

Figure 80. Strain Rate Time History Using a) 3/16-, b) 1/4- inch Protruding Spherical Penetrators at 68 J for 12-, 16- and 24-Layer Woven Sample, and c) Effect of Thickness on Strain Rate

The stress-strain curves for these specimens are shown in Figure 81 to exhibit behavior typical of composite materials with a well-defined region of plasticity for 16- and 24-layer specimens. The stress-strain rate results provide a good estimation of how much the specimen is strained at the onset of damage initiation. The closeness seen on the 24-layer specimen could be due to the greater thickness of the specimen and the effect of the conical section of the penetrator. To perforate the specimen, the tip of the penetrator has to be bigger than the specimen thickness

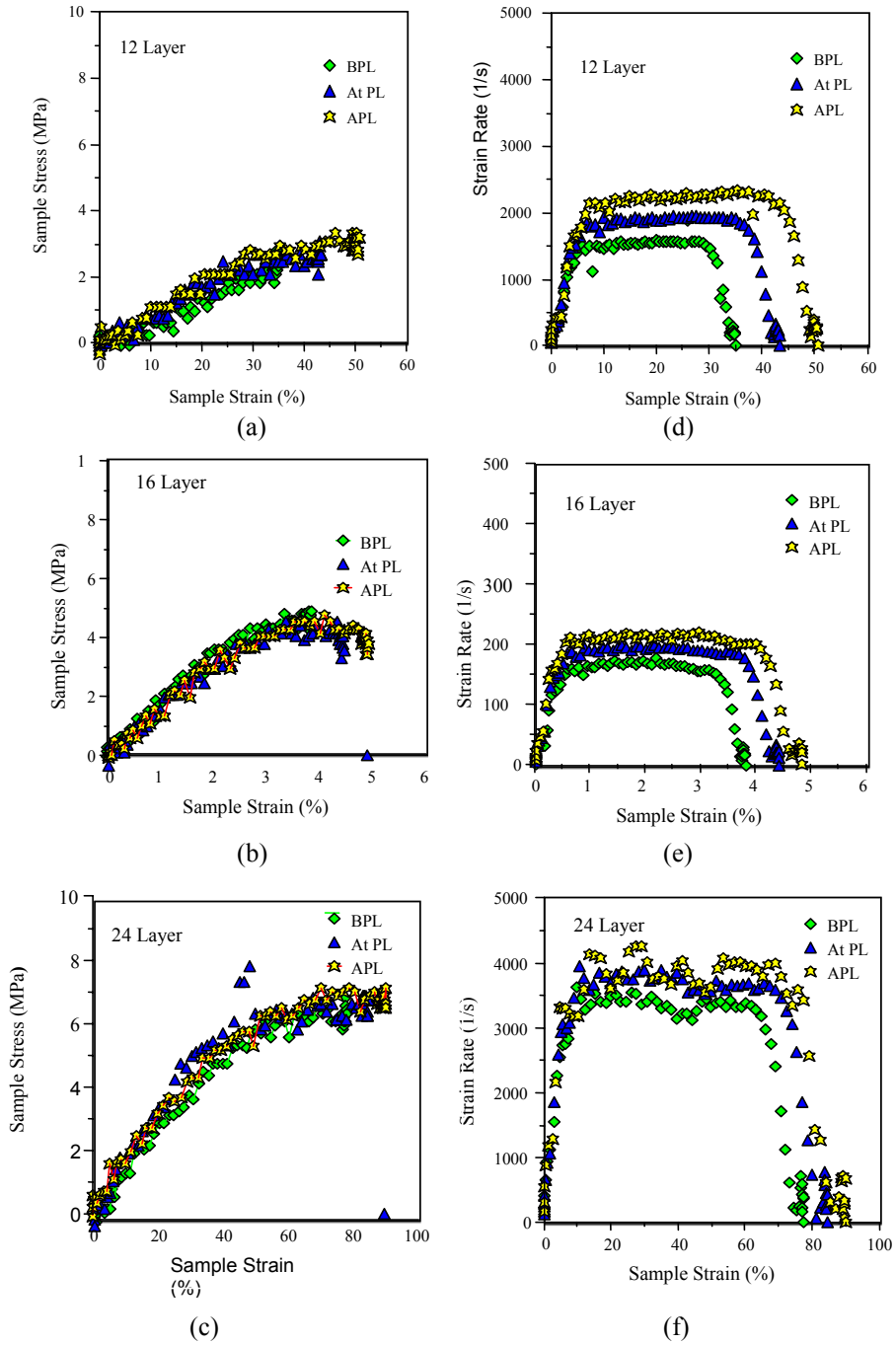

Figure 81. Variation of a-c) Sample Stress, and d-f) Strain Rate Using 1/4-inch Hemispherical-nosed Penetrator for Three-Sample Thicknesses

without the conical shape taking part in the deformation process. We can safely conclude that at the same impact energy, strain rate and particle velocity exhibit a high dependency on the sample thickness and impact energy. The result shows that at plastic region, the material continues to

strain after the load has been removed. The strain rates corresponding to 12-layer specimen below, at, and above penetration limit are at about 1500/s, 1800/s, and 2330/s, respectively. Strain rates corresponding to the 16-layer specimen below, at, and above penetration limit are 1700/s, 2000/s, and 2250/s, respectively. For the twenty-four layer specimens, the below, at, and above penetrations limit are: 3400/s, 3900/s, and 4100/s, respectively. Thus, for the same energy, the 12-layer specimen has higher strain rate than the 16-layer specimen, and the 16-layer specimen has higher strain rate than the 24-layer specimen. At the penetration limit, after the initial energy absorption by the specimen reaches its peak point, the specimen also undergoes a constant energy absorption region (plateau) for about 200 μs. Above the penetration limit, the sample response is similar that of a 16 layer specimen, with the exception that the thicker specimens require higher energy levels. As specimen thickness increases, the perforation resistance increases and the higher the impact energy required for the perforation. The specimen was found to have suffered some measure of irrecoverable damage at this point before tensile strain release energy occurring at the rear end of the specimen. In general, the specimen thickness has a greater influence on the nature of perforation resistance in the damage parameter around the critical energy using spherical protruding penetrator. The energy absorbed in the 12-layer specimen is much less than that absorbed by the 16-layer and 24-layer specimens. It took about 300 μs for the specimen to reach its maximum displacement from the time the wave reaches the specimen. The time for the strain release is independent of specimen thickness.

Figure 82 compares the energy absorption histories of 1/4-inch protruding spherical and 1/4-inch conical hemispherical penetrators for 12-, 16-, and 24-layer specimens at or near their penetration limit energies as indicated. The curves clearly show that for the same impact energy, the penetrators released different amounts of energy on the specimen as evidenced by the different energy absorbed peaks. In support of previous observations, we also note from Figure 81 (middle curves) that at the penetration limit damage level, the strain energy (drop in energy absorbed curve indicated as point B in Figure 82) is lower, with a corresponding higher specimen energy absorbed level. The peak energy absorption for the 1/4-inch conical hemispherical-nose is in most cases higher than that of the protruding spherical-nosed penetrator. Since the surface areas of these penetrator noses are the same, it appears that the shapes of the penetrator nose are the significant factor in this case. For the same incident axial stress wave of energy E_i, the net energy absorption in the penetration damage is given by E_i-E_r-E_t , where the reflected energy E_r depends on the impedance mis-match between the interfaces, and is measured by the amplitudes of the reflected compressive wave. Thus, it is conceivable that the conical shape allows smaller reflection of the incident wave than the spherical penetrator does. In addition, Figure 83 shows that for the same striker impact energy, the thicker 24-layer specimen absorbed the more energy than the 12- or 16- layer specimen did. Specimen energy absorption is strongly dependent on striker impact energy, specimen thickness, penetrator geometry, and size.

Figure 84 shows the variations of the peak values of energy, particle velocity, and ultimate strain with sample thickness and damage threshold- below penetration limit (BPL), at penetration limit (PL), and above penetration limit (APL), energies. The peak values of energy absorption in the penetration/perforation damage process (energy released by the penetrator-incident system), particle velocity, and ultimate strain all increase linearly with the striker (penetration) energy levels from below to above penetration energy for all specimen thicknesses.

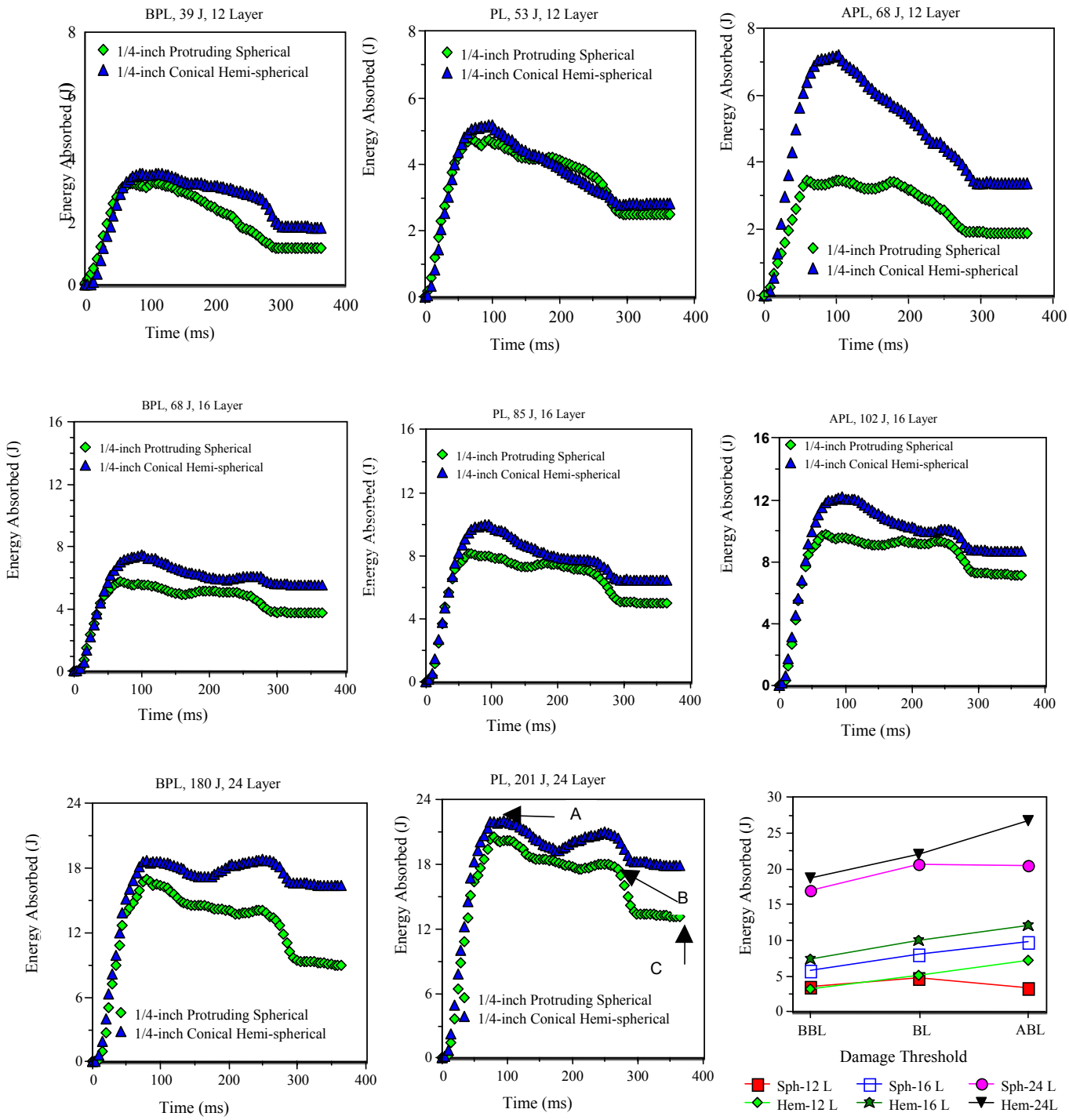

Figure 82. Comparison of Energy Absorption for 1/4-inch Protruding Spherical and 1/4-inch Hemispherical Penetrators for 12-, 16- and 24-Layer Specimen

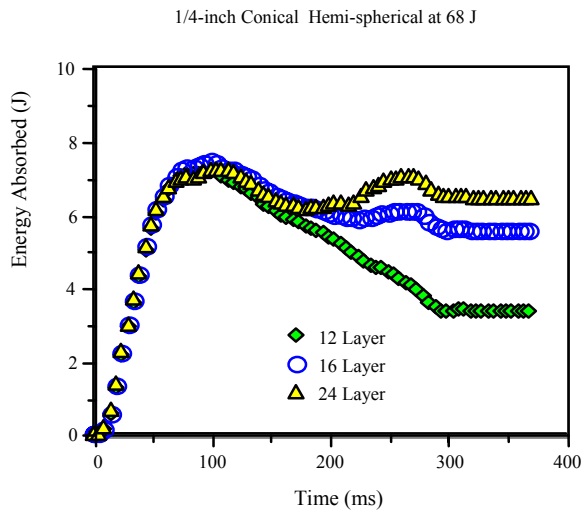

Figure 83. Effect of Specimen Thickness on Energy Absorption for 1/4-inch Hemispherical Penetrator at 68 J

Figures 85 and 86 take a further look at the effect of penetrator size and damage responses. The figures compare variations of various specimen failure response variables such as ultimate strain and energy released, strain rate, loading force, and particle velocity for 3/16-inch and 1/4-inch spherical penetrator sizes near damage threshold regions BPL, at PL and APL. The results show that a 3/16-inch protruding hemispherical penetrator does not absorb as much energy as the 1/4-inch protruding spherical penetrator. This is attributed to the differences in the shape of the penetrator nose, which creates a hole that enlarges as the specimen is impacted and continues to open at less energy once the crack has been opened by the tip of the penetrator. For the protruding hemispherical-nosed penetrator, the interaction between the specimen and the penetrator is constant because the protruding section of the penetrator does not take part in the damage process. Hence, no further energy absorption is needed to complete the deformation. One distinct feature of this penetrator is the gradual unloading which indicates that it takes a longer time for the crack to traverse the specimen due to the low energy level required by the penetrator for damage initiation. As the penetrator size increases, the energy absorption rate of the composite material increases as well. This is because the increase in the contact surface area of the projectile tends to distribute the impact energy over a wider area of the composite. Fiber stretching prior to perforation was also noticed during the experiment. Due to the large surface area, one would expect a lower stress on the sample for the same loading force. The plot of ultimate stress shows that this is not the case. The 1/4-inch penetrator still delivers greater ultimate stress than the 3/16-inch size, with the maximum occurring at the penetration limit for the 24-layer specimen. The difference is more significant in loading contact force and strain rate, and greater at the penetration limit than below or above.

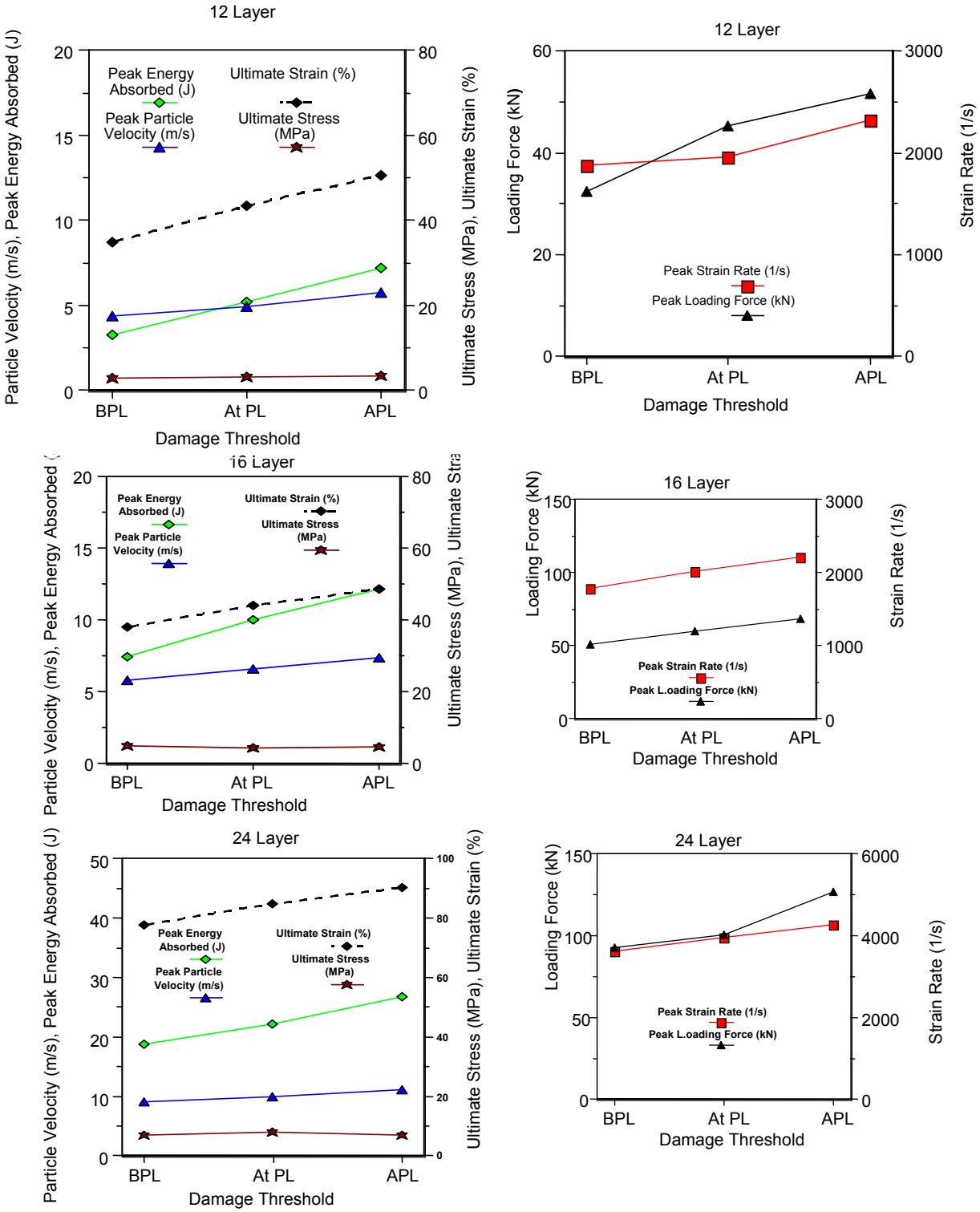

Figure 84. Variations of Particle Velocity, Energy Released, Ultimate Strain, Ultimate Stress, Strain Rate and Loading Force BPL, at PL and ABL

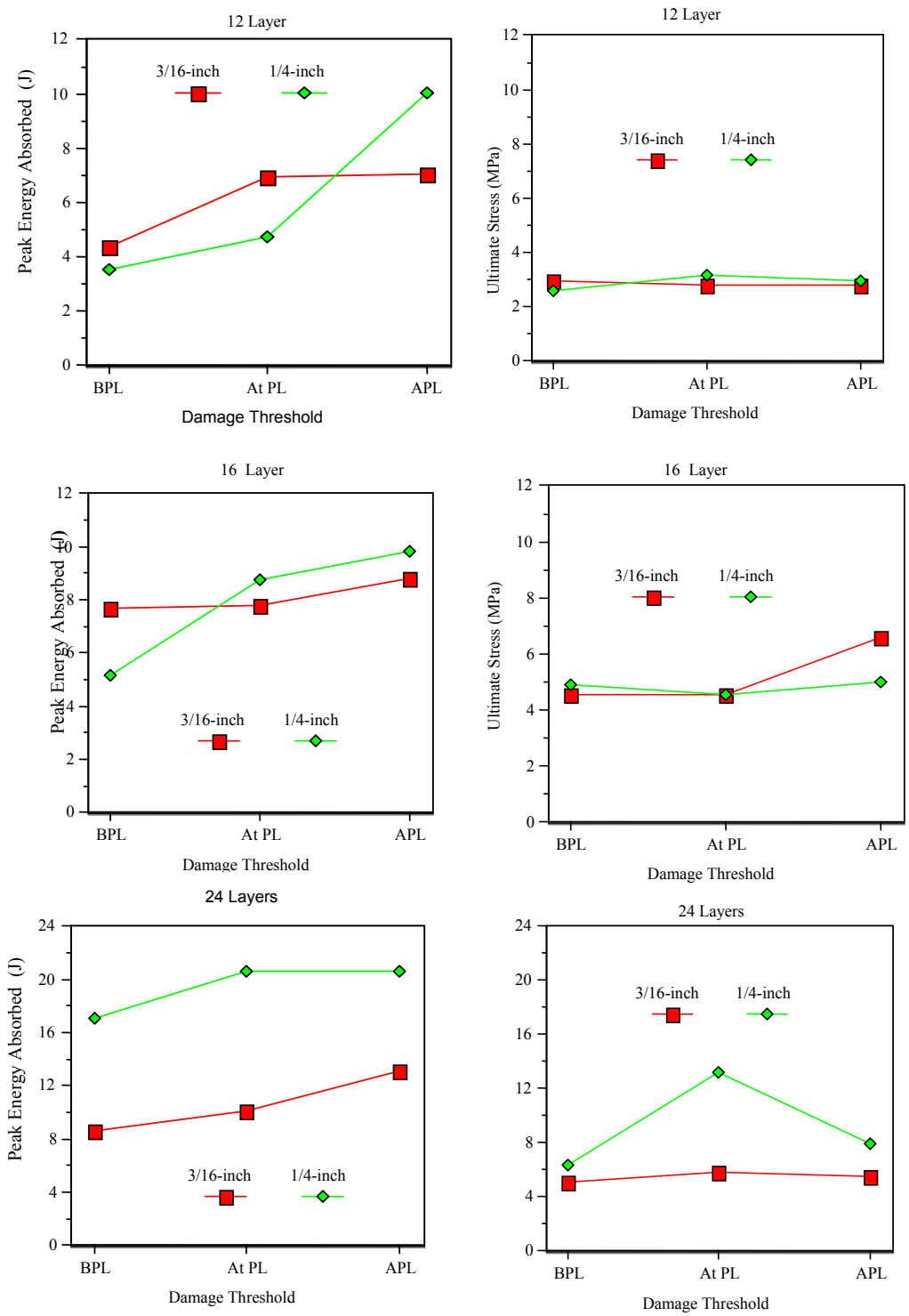

Figure 85. Effect of Penetrator Size: Comparison of Variations of Ultimate Strain and Energy Released, and Strain Rate for 3/16-inch and 1/4-inch Spherical Penetrators near BPL, at PL, and APL

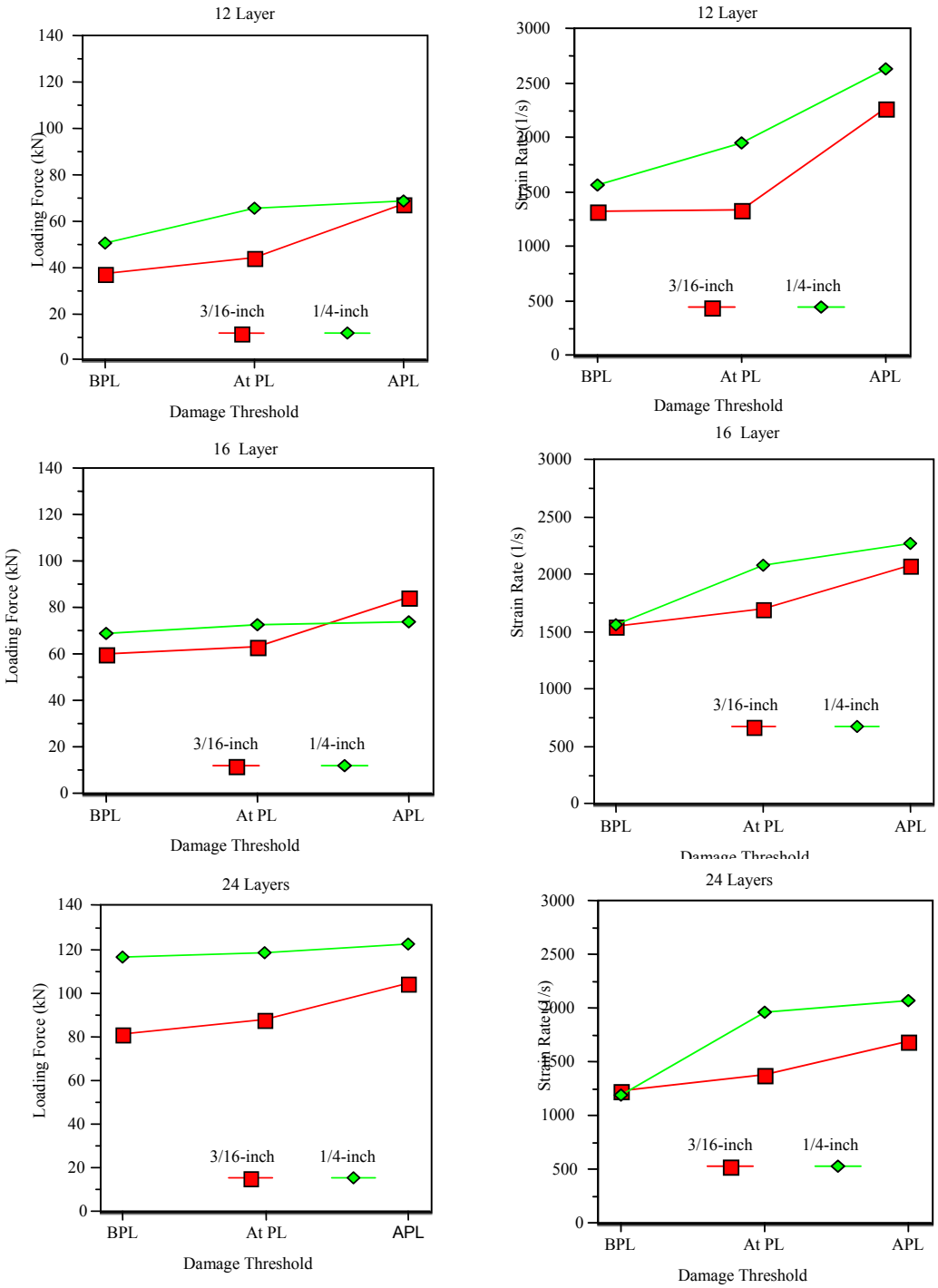

Figure 86. Effect of Penetrator Size: Comparison of Variation of Peak Loading Force and Strain Rate for 3/16- and 1/4-inch Spherical Penetrators near BBL, at PL, and APL

The significance of this observation of the perforation damage energy absorption shows in Figure 87 that the specimen absorbed its highest energy at the penetration limit. Figure 87 is a summary of specimen energy absorption versus striker impact energies curves for the three specimen thicknesses studied. Recall that the specimen energy absorption is measured as the last point on the total energy absorption curve (total peak energy absorption minus the strain energy) as illustrated by the arrow in Figure 87. This result is significant because it validates the definition of penetration limit as the threshold energy or velocity point above which the specimen is perforated at just enough energy with zero residual energy. Thus near this region, all of the energy released by the penetrator is absorbed and used up for the damage process. Beyond the perforation, resistance to damage is now low and, therefore, energy needed for continued damage would decrease. This is supported by the results and fully documented by Ojo [45]. The highest amount of energy is absorbed by the specimen at its penetration limit energy. It is clear from Figure 86 that the total energy absorption by the specimen (energy lost by the penetrator) and the fraction of energy absorbed in perforation peaks around the penetration limit in more than 88 percent of the cases tested. Similar behavior is observed using 1/4-inch penetrator on 16-layer and 24-layer plain-woven samples. Below the penetration limit, the system continuously absorbs energy to overcome initial resistance to penetration as indicated by a sharp rise up to the peak energy level.

Figure 88 compares the variations of strain rate with sample thickness for the 3/16-and 1/4-inch inch protruding spherical and 1/4-inch comical hemispherical penetrator sizes at energies near damage threshold regions - BPL, at PL, and ABL. The comparison is to further elucidate the effect of penetrator geometries. In almost all of the cases, the specimen penetrated with the 1/4-inch spherical-nosed penetrator suffered higher strain rate than those penetrated with the 3/16-inch nose, in agreement with previous observations. The strain rate versus thickness behavior for the spherical-nosed penetrators exhibits an initial increase and then maximum at about (3.34 mm) before starting to decrease. We note that the 3.34 mm corresponds to the thickness of the 16-layer specimen. This behavior is contrary to our predictions and is being investigated. Strain rate increases linearly with increases in energy level as shown in Figure 83 and decreases linearly with increases with thickness as in Figure 79d. Hence, the observed maximum behavior can be explained in terms of the interactions between the two variables (interaction effect of energy and thickness on strain rate) since the penetration limit energies are different for the different specimen thickness. At the same energy, strain rate is definitely inversely proportional to thickness as shown in Figure 80c. Thus, we can infer from this result that for the 3/16-inch protruding penetrator, the impact energy or damage threshold level is the dominant effect on strain rate at thickness less than 3.34 mm (16 layer) while thickness is a more significant effect at higher specimen thickness. In the case of 1/4-inch conical hemi-spherical in (Figure 88), below, at, and above penetration limits, the strain rate for the conical hemispherical penetrator increases with thickness with a change in slope at 3.34 mm also. This implies that with energy and thickness effects interacting, the energy or damage threshold level is so significant with the 1/4-inch conical penetrator that is cancels the effect of thickness. Other than the factorial interaction similar to the one reported earlier in Section 3.5.2.4 of this report, the other research question under further investigation is whether a theoretical threshold exists at which the decrease of strain rate with thickness will have a change in slope.

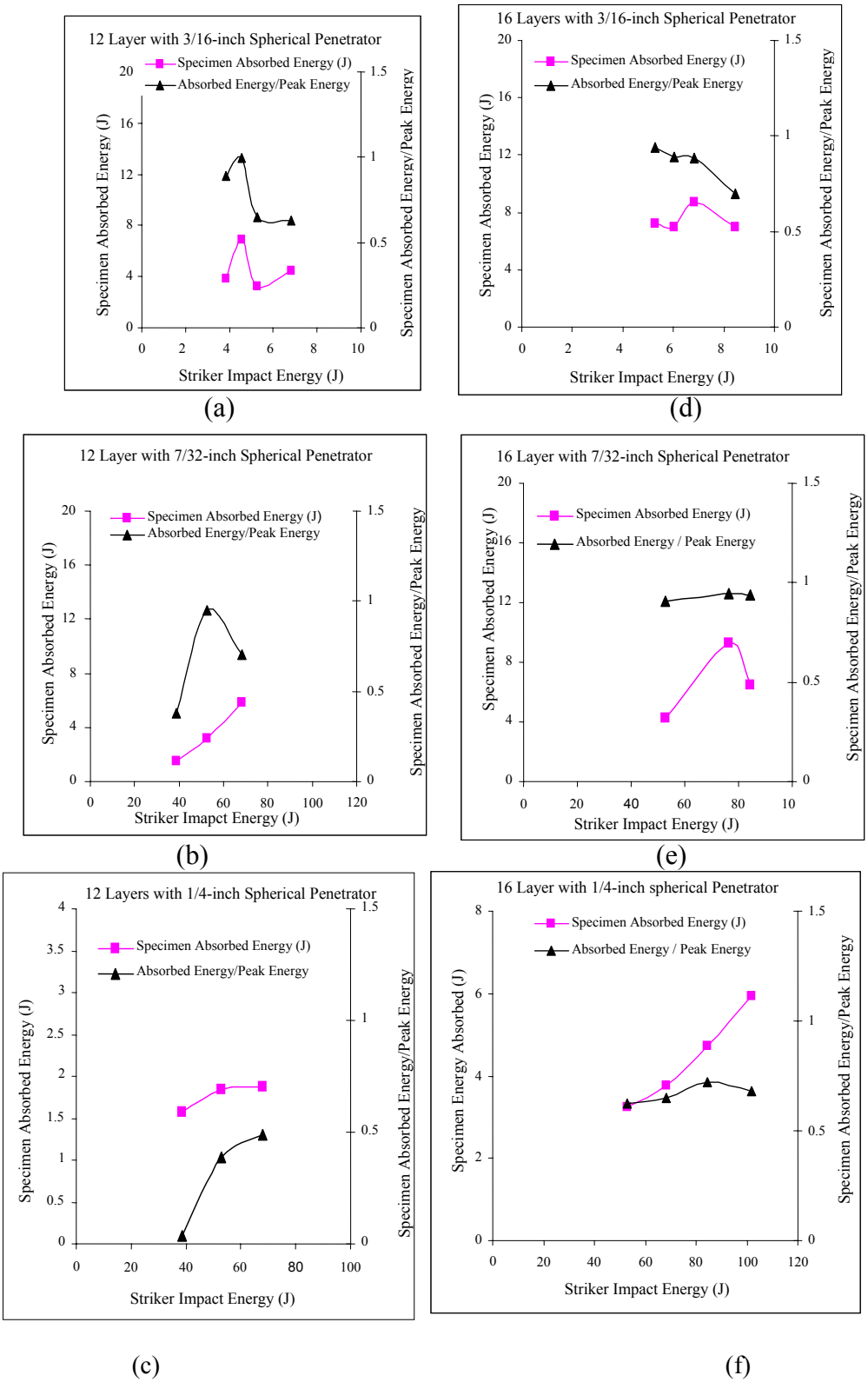

Figure 87. Variation of Energy Absorbed by Woven Composite Plate with Striker Impact Energy Penetrated with 3/16-, 7/52- and 1/4-inch Protruding Spherical Penetrators

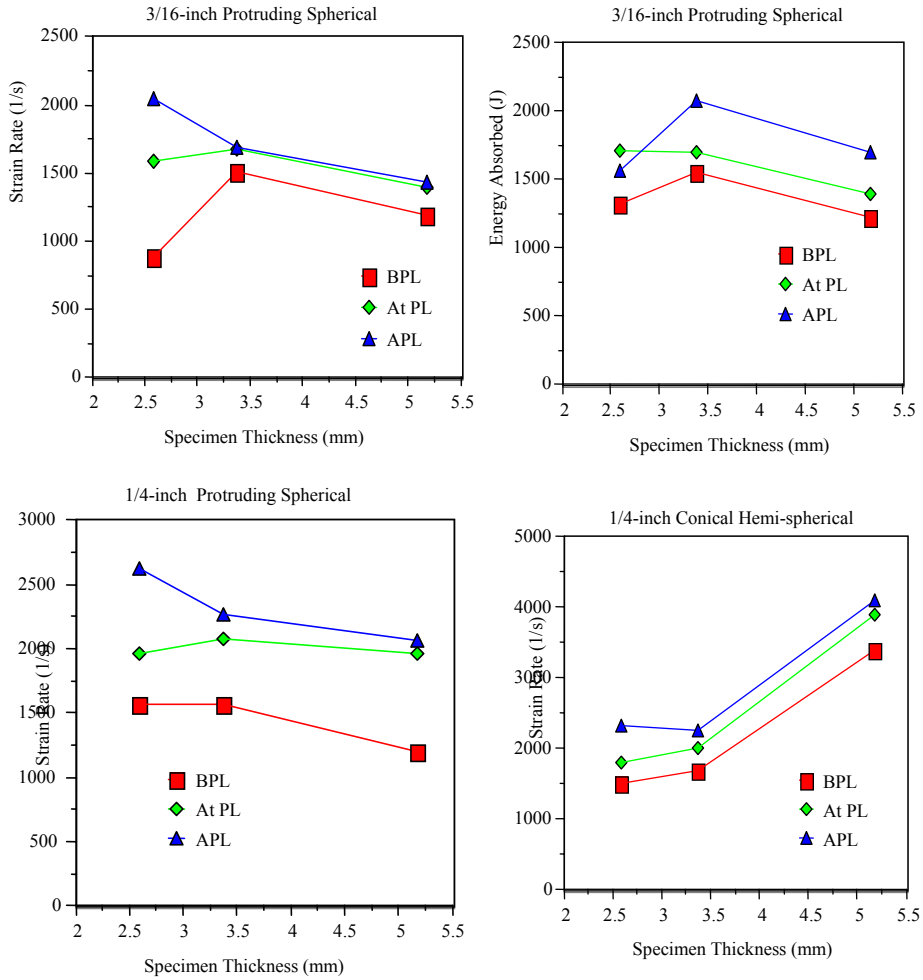

Figure 88. Effect of Penetrator Geometries: Comparison of Variations of Strain Rate with Sample Thickness for 3/16- and 1/4-inch Protruding Spherical and 1/4-inch Conical Hemispherical Penetrator Sizes in the Vicinity of Damage Threshold Regions (BPL, at PL, and APL)

Concluding this section, we note that the comparison of the effects of the penetrator geometry show clearly that the larger penetrator-nose delivered the higher energy to the specimen for the same striker impact energy. For all of the three thicknesses penetrated at the same impact energy, it can be seen from the result that more energy was absorbed using the 1/4-inch penetrator than for the 3/16-inch protruding spherical penetrator. Thus, for the same energy level, size of the nose contact area is more significant in energy delivery than the shape of the penetrator itself.

The results of the measurements around the penetration limit reveal some note worthy results. In a significant number of the cases investigated in these studies, it was observed that at the penetration limit, the tensile strain energy release (observed in the force-displacement curve

(Figure 67b or as a dip in the energy absorbed curve Figures 83 and 84) is lower than below or above the penetration limit. This is because below the penetration limit, the specimen absorbs most of the energy delivered with only some incipient damage characterized by indentation and penetration. At the penetration limit, most of the energy is used up in perforation with near zero residual energy. Thus, at penetration limit, the strain energy release is expected to be smaller than below penetration limit. Hence, the energy absorbed by specimen at the penetration limit is higher than at below penetration limit. The damage is characterized by perforation. These are shown to be the case in more that 85 percent of the cases. As shown in the force-displacement curve, some of the energy available for deformation is lost to the system as indicated by the tensile strain release wave. Thus, above the penetration limit, the damage to the specimen is characterized by post-perforation and plugging. Plugging here is defined as the stage where the conical section of the penetrator took part in the specimen damage. This behavior is typical for all specimen thicknesses studied regardless of the penetrator size, shape, or geometry. Figure 86 shows that on the average, strain rate and loading forces increase from below the penetration limit to above penetration limit with the 1/4-inch penetrator delivering more load and strain effects on the specimen than the 3/16-inch. The result shows that there is a significant difference between the effects of penetrator size on a specimen strain rate.

3.5.4 Crack Propagation and High Speed Imaging Data

3.5.4.1 Calibration and Magnification of the High Speed Camera

The correct crack extension and time of capture of a dynamic event is very crucial to the measurement of crack propagation. The speed at which the camera mirror must be rotated for event capturing purposes was achieved by running several experiments at the same impact energy while the speed of the camera is adjusted until a satisfactory picture is recorded on the films developed. In addition, the impact energy could be varied while maintaining a constant recording rate (speed of camera). Since the pictures are captured at magnifications different from the actual crack size, complete system calibration involves determination of the magnification factor defined as the ratio of the length actual specimen damage length to the damage measured on the picture developed ($F_f = L_a/L_f$), where L_f is the crack length from the film and L_a is the actual length of the crack on specimen. Placing a well-defined calibration mark on the specimen does this. The ratio of the actual length of this marking to the same length of the marking seen on the film gives the film magnification.

The back of an undamaged specimen was light painted white (for contrast) with a 25.4-mm mark at the center. Four fiber-optic cables were connected to the specimen holder overseeing the back of the specimen to better illuminate the specimen when the flash on the high-speed camera goes off. The picture taken was then developed, and the marked point was measured with the aid of a vernier caliper.

To determine the speed of the crack propagation, the specimen crack length was measured in each 35 mm frame with the aid of a magnifier. The value was multiplied by the magnification factor to get the actual length of crack. The film could also be digitized by a HP film digitizer and

printed on paper with certain printer magnification or resolution. This second magnification factor $F_p = L_f/L_n$ is also determined by determining the ratio of the actual length of marking on specimen to the same marking on the printer paper. The total crack length on each frame when divided by the total time to that frame gives the average crack speed as:

$$C_n = \frac{\Delta L_n}{T_n}, 1 \le n \le 80 \tag{41}$$

where, $\Delta L_n = F_f F_p L_p = F L_n$, is the total *crack* length in the nth film frame for the time $T_n = n\Delta T$ for an inter-frame time, ΔT, for the selected camera speed, and, $F = F_f F_p$

3.5.4.2 Experimental Results Using Dynamic Optical Imaging of High-Speed Digital Video Camera

The photographs in Figure 89 reveal the variation of a damage event as the function of impact energy for 1/4-inch protruding spherical-nosed and 1/4-inch conical hemispherical-nosed penetrators. Rear surface cracks on the woven specimen were first observed when the impact energy was 39 J. Since a surface crack is usually initiated before a perforation by the penetrator is achieved, the penetration limit will be higher than the surface crack initiation velocity when defined in terms of traverse velocity of the penetrator nose. Perforation was achieved at 68 J. It is conceivable that the punch-through threshold energy was exceeded for this specimen. It is part of ongoing research to investigate the nature of crack propagation around this region at a small increment of impact energy. Thus, the specimen requires a large amount of energy to sustain complete failure. For approximately the same damage threshold levels, the figure shows that the conical hemispherical-nosed penetrator appears to cause more pronounced damage than the protruding spherical-nosed penetrator does. This means that the spherical penetrator must deliver more energy than the spherical one of the same size. Note that this was also the conclusion from previous observations.

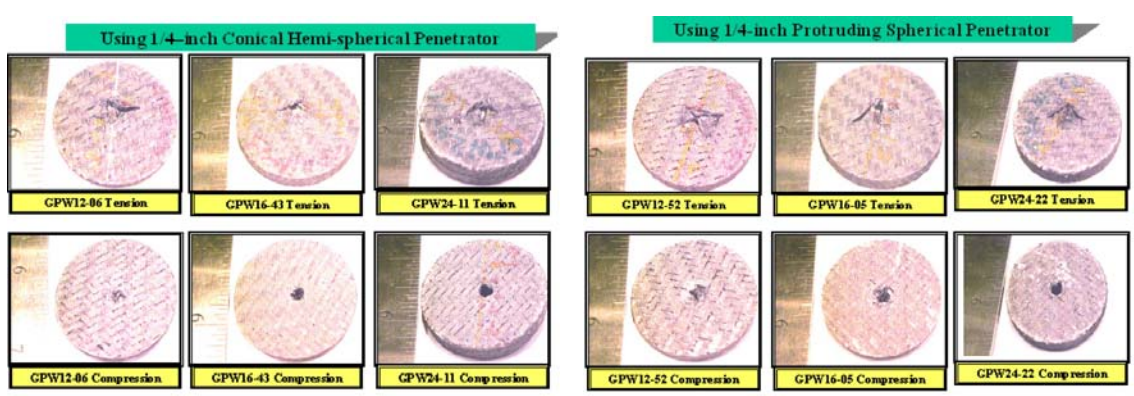

(a) (b)

Figure 89. Penetration of Graphite-Epoxy Woven Specimens Using 1/4-inch a) Conical Hemispherical-Nosed and b) Protruding Spherical-Nosed Penetrator

Figure 90 (a-c) displays the high-speed real-time measurement of the variation of crack extension at varying impact energies BPL, at PL, and above APL. The frames were magnified with an image magnifier and each crack measured with a vernier caliper. It is observed that the 40 frames of the crack slows down and mainly widens under the loading tensile load at the rear surface. The crack propagating speed is determined from the slope of a linear fit to the displacement-time curve of for the two 40-frame sets of images. The intercept is not zero because the crack had started propagating before the first camera frame.

W12-51a, Below PL, 60 J

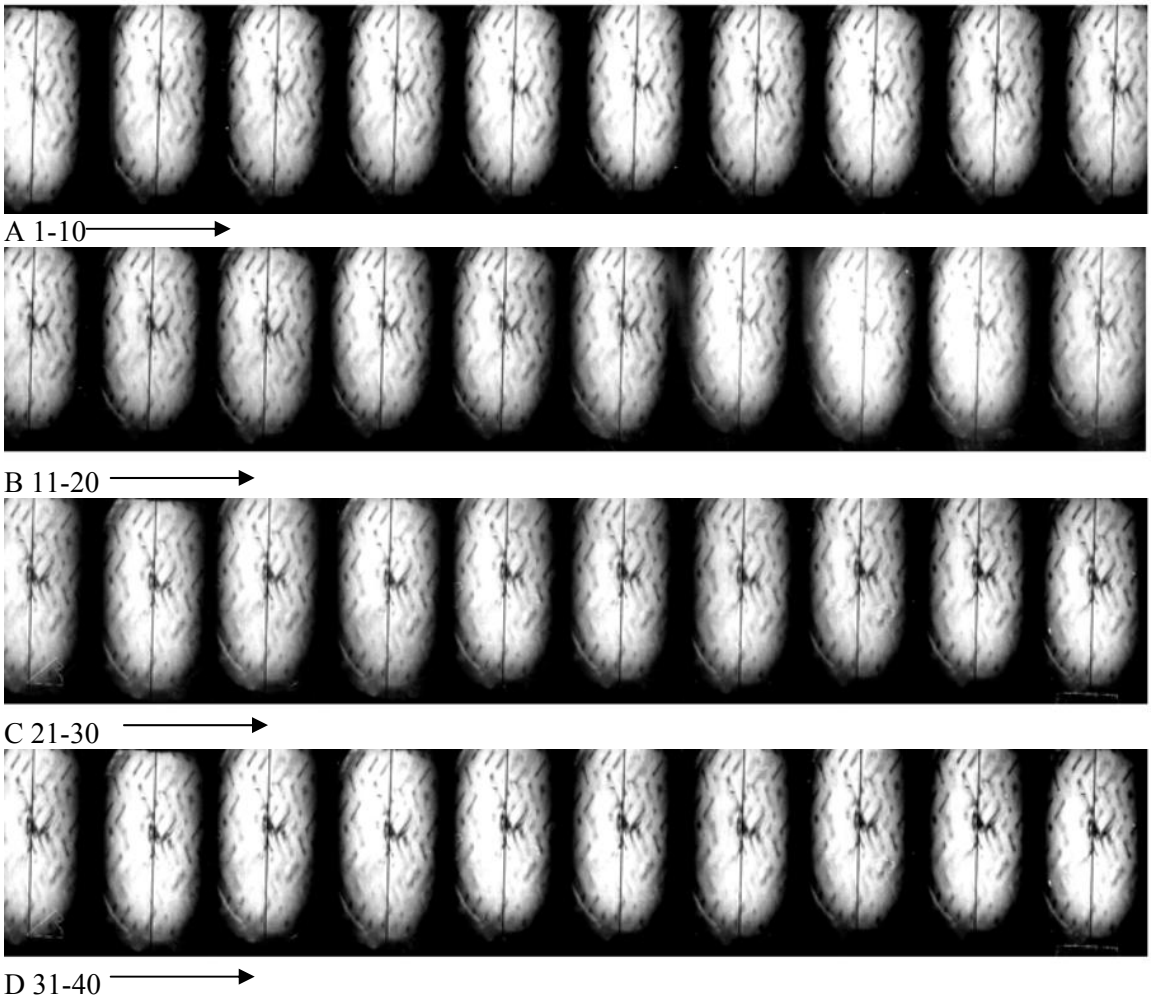

Figure 90. Crack Propagation for 12-Layered Woven Graphite-Epoxy Specimen BPL Velocity Using 1/4-Inch Spherical Penetrator

An observation of the rear (tension) side damage reveals complete fiber breakage with the fiber remaining attached to the specimen but pushed out obliquely to the rear side. Such shape in perforation mode failure has been shown [35] to occur at higher stress levels. Figures 90-96 show the crack extension for impact energies BPL, at PL, and above APL for 12-, 16-, and 24-layer specimens. The crack size is small at low speed, increases in the middle as more energy is pumped into the crack front by the compressive stress wave. Growths slow down toward the last few frames. It is also clear from the figures that cracks propagate more than they widens. It is worthy of note that in this woven specimen, the crack also appears crossed and propagates in both directions, although with one moving faster than the other. This is due to the woven nature of the specimen. It is conceivable that the cracks first initiate at the point of intersections of the weave, and move in both directions. The fact that the crack runs faster in one direction than the other means an uneven distribution of the strain intensity. It also shows that the point of intersection of the weave will also indicate the point of weaker or highest strain for the same energy, and will reveal a wave nature in the strain profile, as will be shown later.

W12-67a, Above PL, 60 J

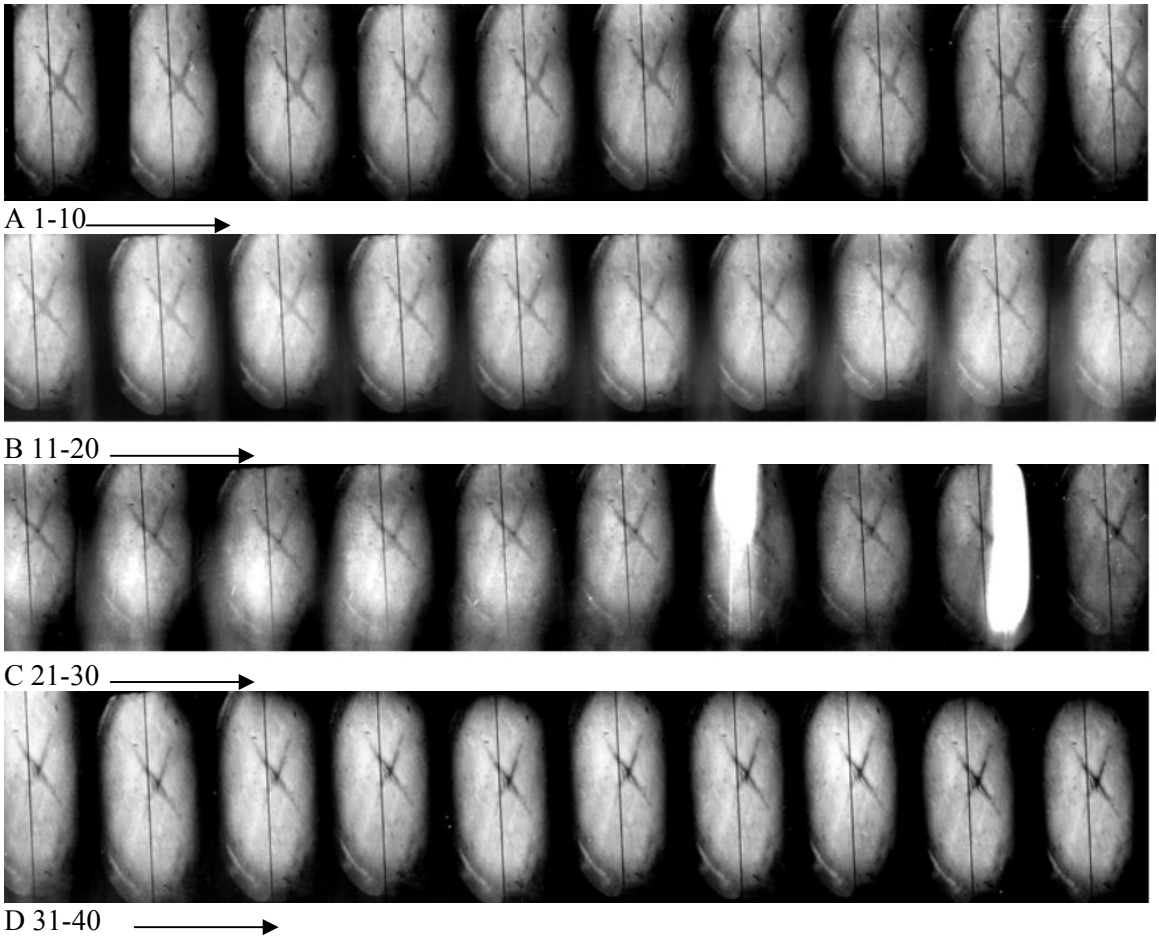

Figure 91. Crack propagation for 12-Layered Woven Graphite-Epoxy Specimen At Ballistic Limit Velocity Using 1/4-Inch Spherical Penetrator At 68 J Above BL Impact Energy

Figures 95 and 96 show that the thicker 24-layer specimen has only minor damage. The ability to capture even incipient damage shows the power of this technique. Plots of the crack length against extension time determined from a series of measurements like Figures 89-95 are shown in Figure 96 for the first 40 frames of record. The same calculations are done for the second 40-frame records to give 2 speeds of the same event.

W16-75ab BPL, 68 J

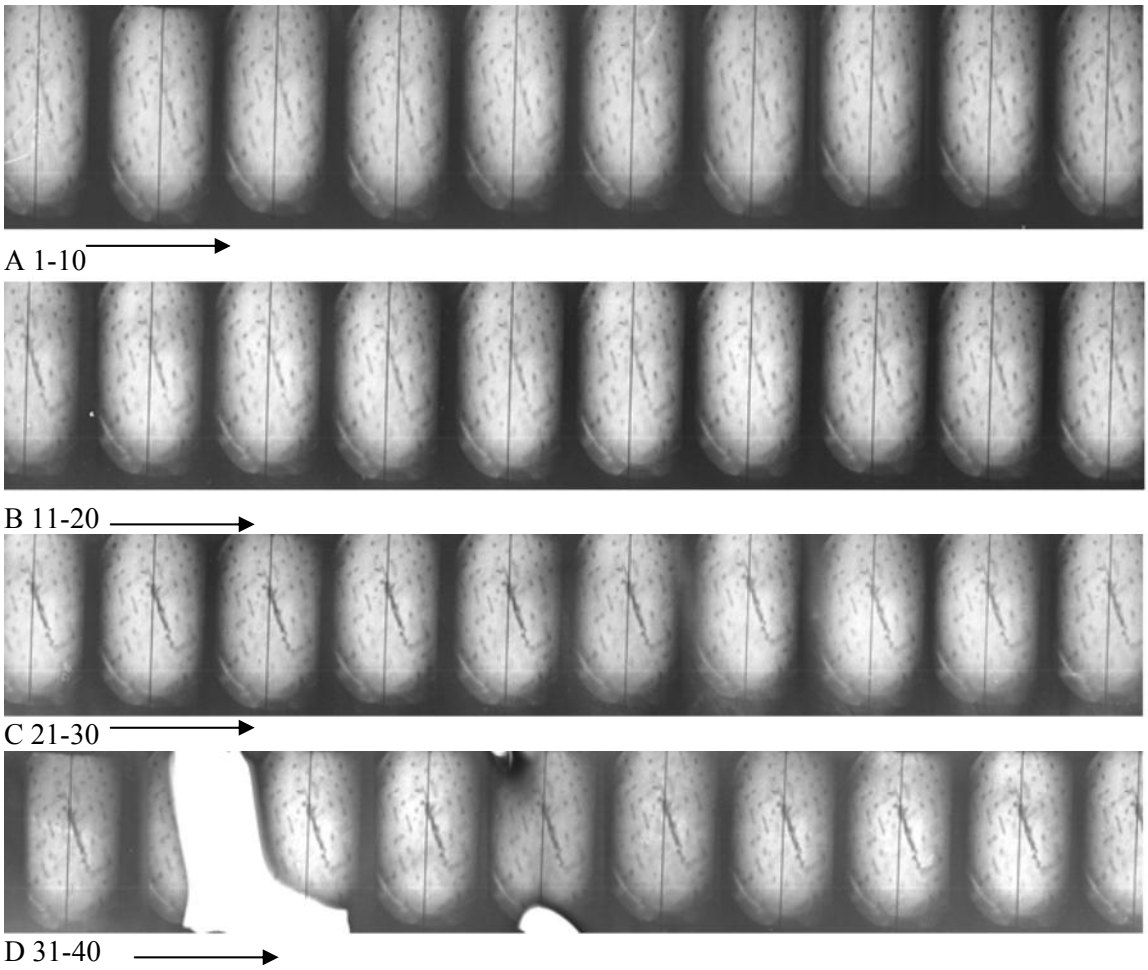

Figure 92. Crack Propagation for 16-Layered Woven Graphite-Epoxy Specimen BPL Velocity Using 1/4-Inch Spherical Penetrator at 68 J

W16-92a, PL, 76 J

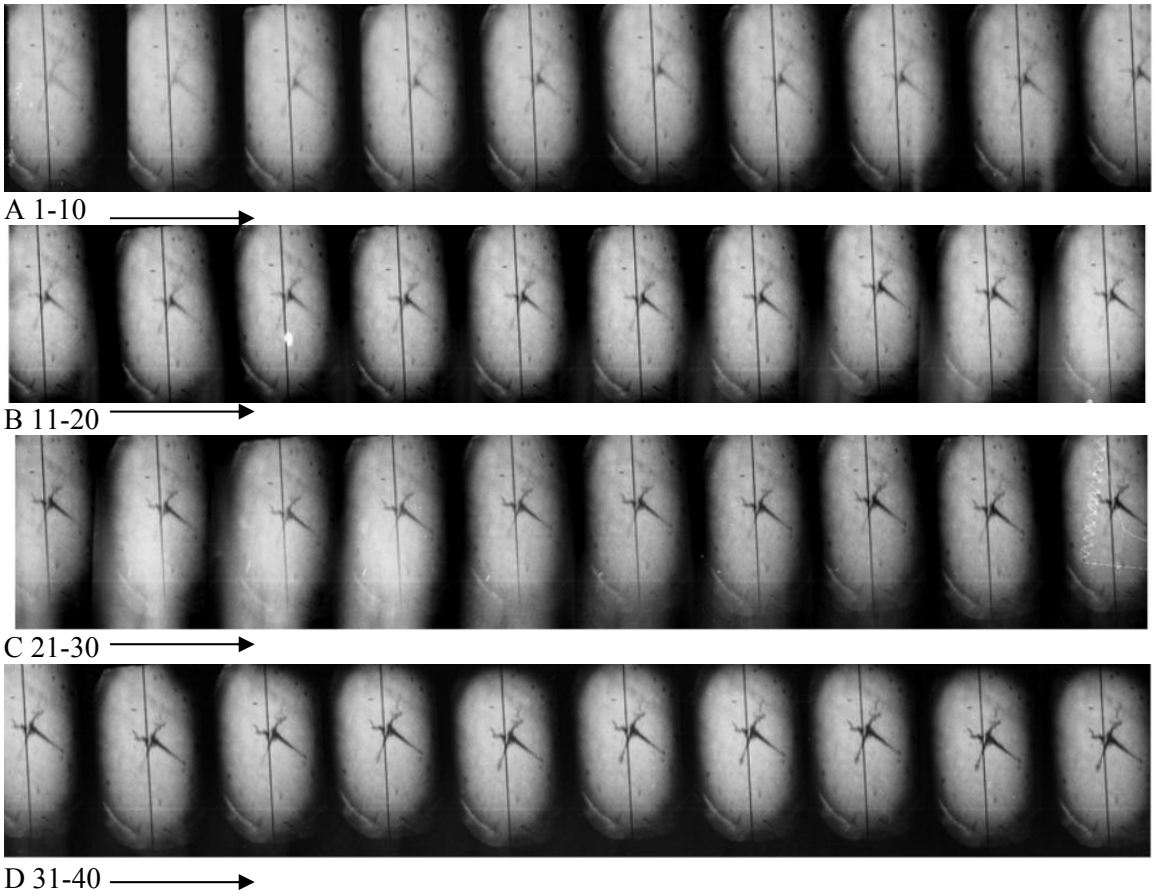

Figure 93. Crack Propagation for 16-Layered Woven Graphite-Epoxy Specimen at PL Velocity Using a 1/4-inch Spherical Penetrator at 76 J

W16-45ab, APL, 85 J

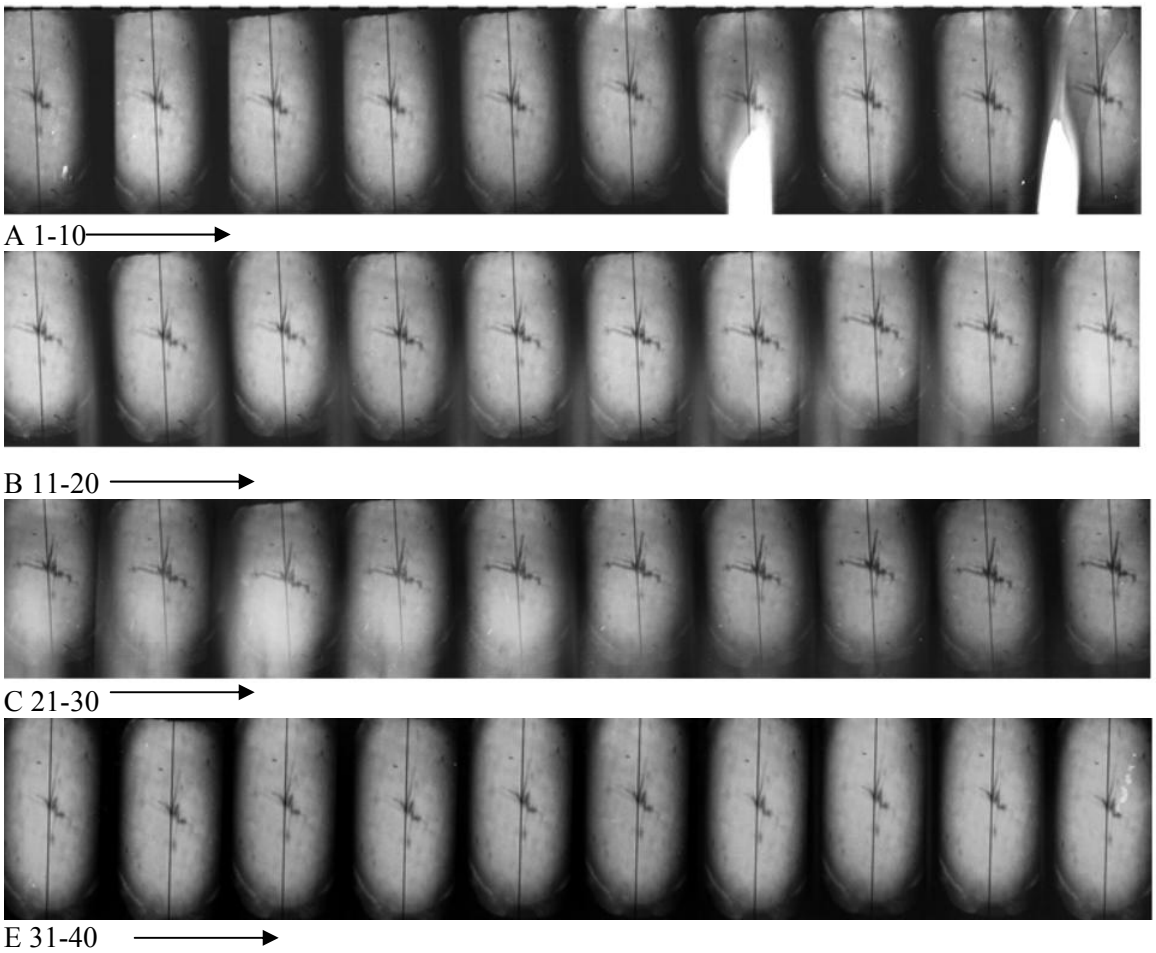

Figure 94. Crack Propagation for 16-Layered Woven Graphite-Epoxy Specimen APL Velocity Using a 1/4-inch Conical Hemispherical Penetrator at 85 J

GW24-41, BPL, 180 J

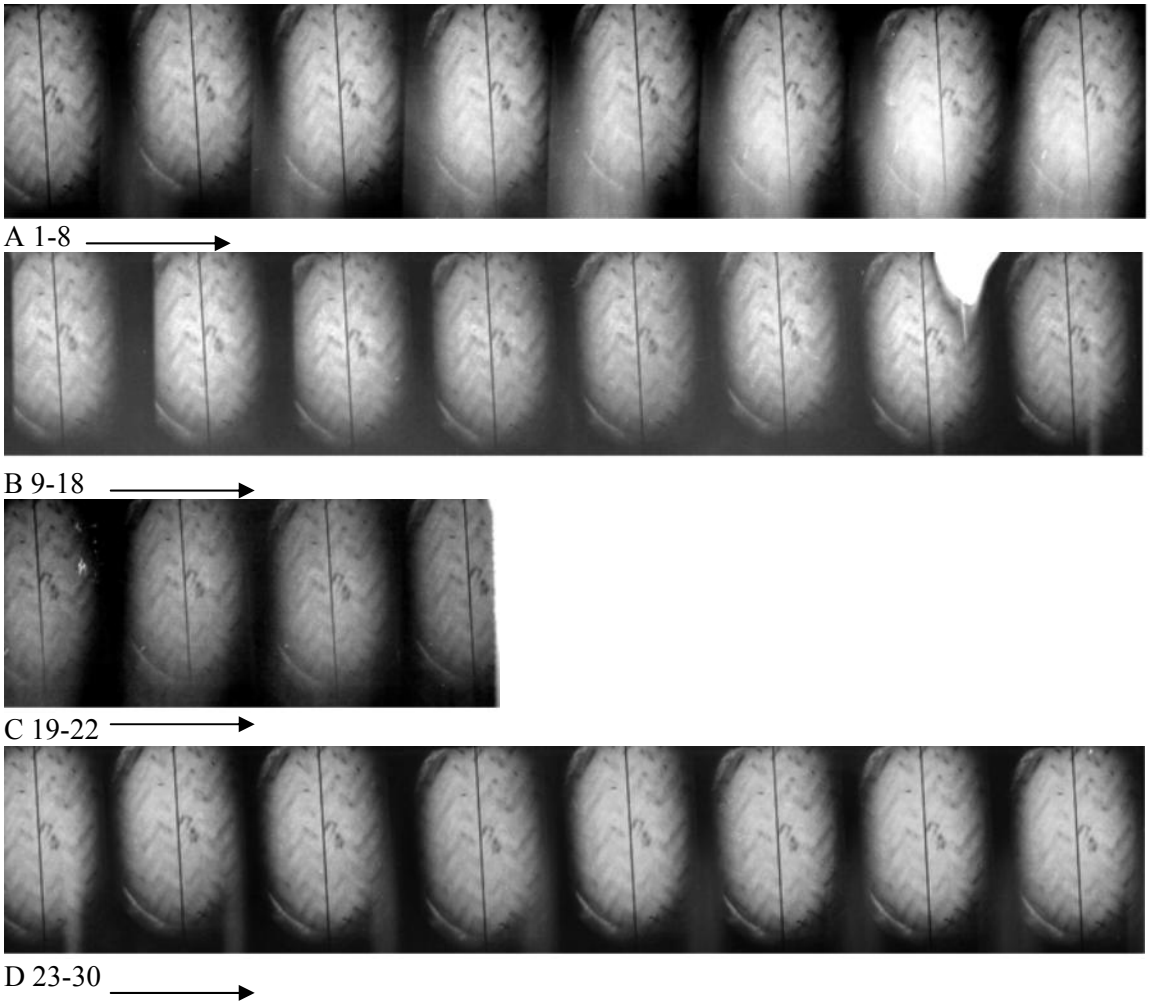

Figure 95. Crack Propagation for 24-Layered Woven Graphite-Epoxy Specimen BPL Velocity Using a 1/4-inch Conical Hemispherical Penetrator at 180 J

W24-09a, APL, 201 J

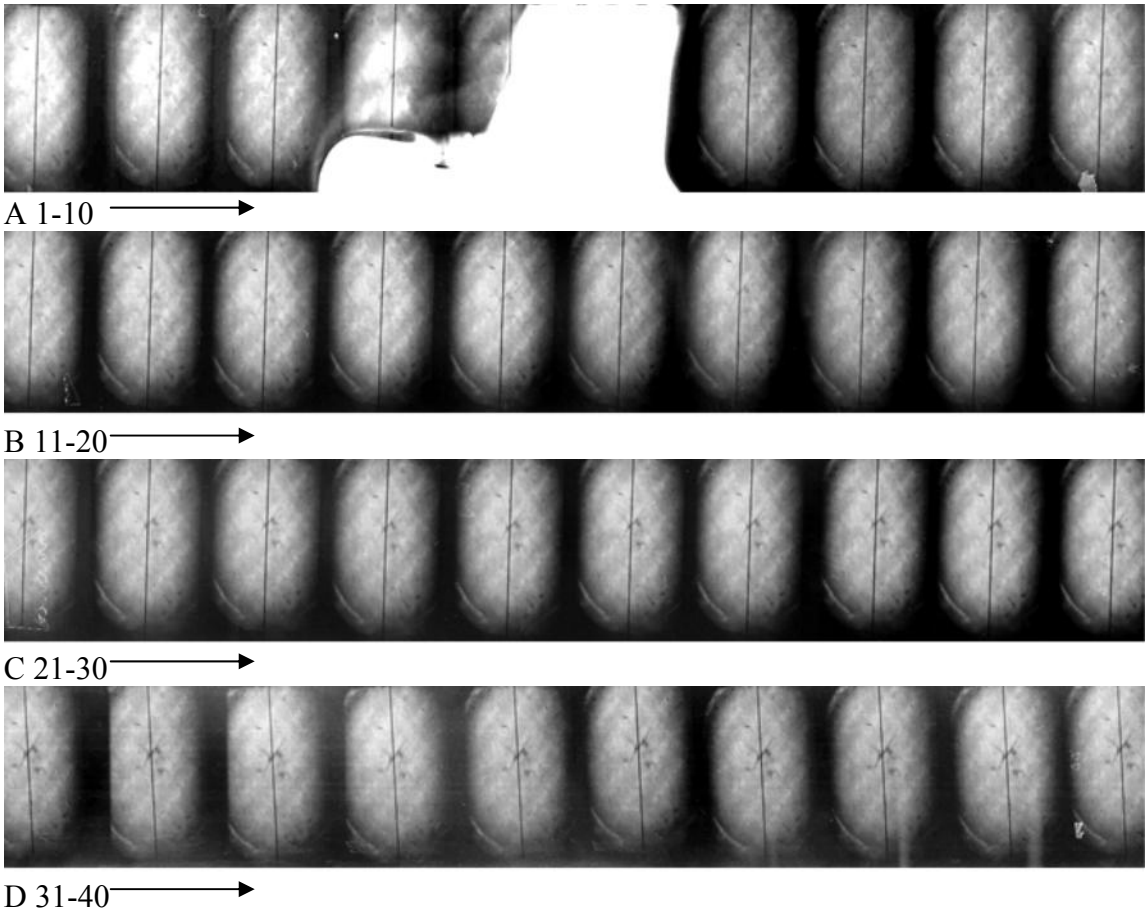

Figure 96. Crack Propagation for 24-Layered Woven Graphite-Epoxy Specimen APL Velocity Using a 1/4-inch Conical Hemi-Spherical Penetrator At 201 J

The results show a linear relation between crack length and time. This shows that the crack propagates uniformly across the plate once the initial resistance if overcome. The intercept in non-zero because the initial speed prior to the timing of the event is nonzero. The summary of the measurement is shown in Figure 97, showing the variation of the speed at different damage threshold levels and sample thickness. Figure 95 shows that at PL damage levels, the crack extension speed increases non-linearly with thickness.

For the 12-layer specimens, the speed increases as energy is increased, as should be expected. For the 16-layer specimens, the speed remains approximately constant for the three energy levels tested. In the case of the 24-layer specimens, no clear conclusion could be reached from the data. It is possible that the inconsistency in 24-layer specimens could be due to the fact that the energy levels selected for these runs were too close to the penetration limit or that the timing of the event did not allow for complete capture of the event. It is important that the energy levels selected for

measurement of crack speed must be reasonably above the penetration limit to overcome inertia effects. This allows some residual kinetic energy for crack propagation.

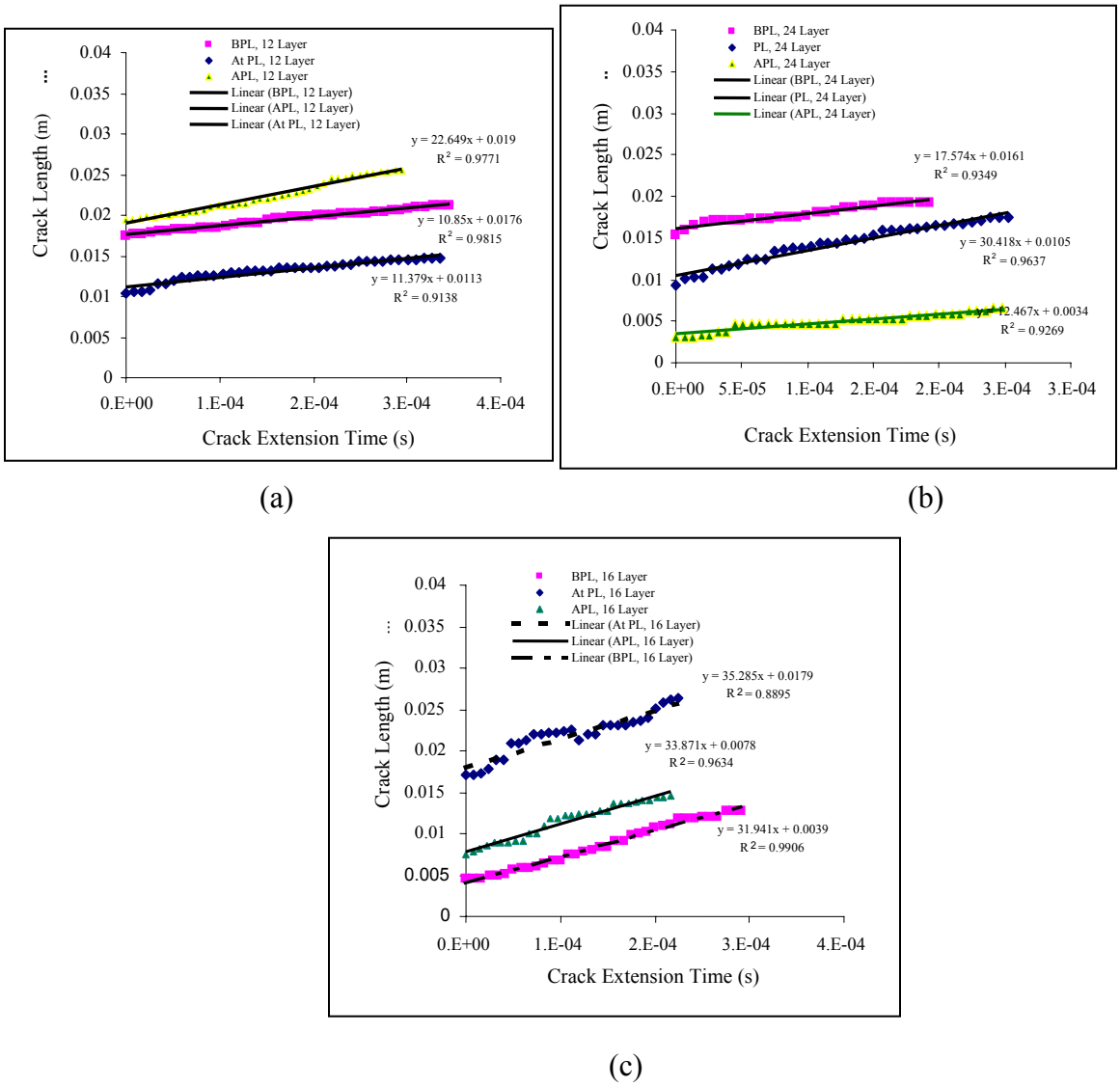

Figure 97. Variations of Crack Length With Crack Extension Time From the High-Speed Images Around the PL Energies for a) 12 Layer, b) 16 Layer and c) 24 Layer Specimens

One major concern in this experiment is that the crack speed is about a factor of 10 lower than the speed in laminated graphite epoxy. It is suspected that this could be due to the woven nature of the specimen that impedes the propagation of the crack or that the energy levels were not high enough or the timing was so low that we missed the developed crack. To explore the last conjecture, a high-speed CCD intensifier camera was used to explore the results. The experimental results are shown in Fig 98 and 99 and for the two-penetrators. The use of the high-speed digital intensifier is much easier than the rotating mirror camera. The measurements involve measuring the event at two pre-selected times. Two static shots: one before and other after the event are taken for characterization of the complete penetration failure. The event is time-delayed for 900μs delay plus a total of 260 μs event time. This allowed 800 μs for the wave to reach the specimen and extra 260 μs for damage process. The accurate establishment of this time is very critical, and is often complicated by such factors as cabling in the system and difficulties with the trigger circuitry.

BPL: 25 psi, 54 J

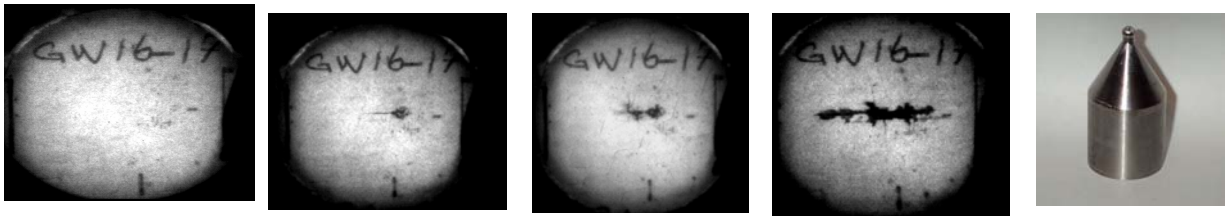

Before 160 μs 260 μs Static

At PL: 32.5 psi, 76 J

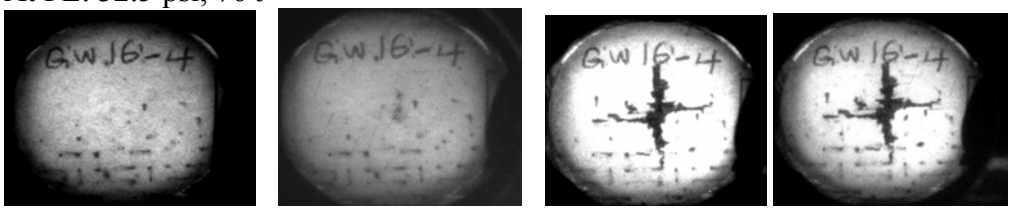

Before 160 μs 260 μs Static

APL: 35 psi, 84 J

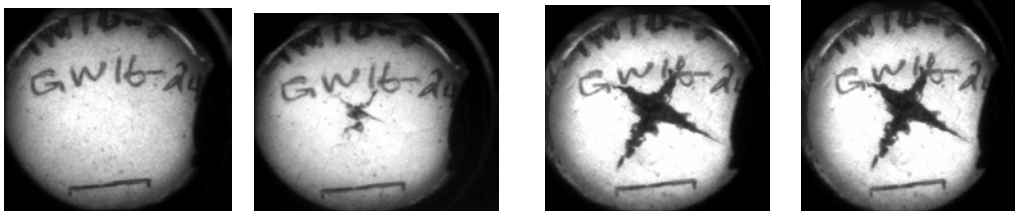

Before 160 μs 260 μs Static

Figure 98. Crack Propagations Using High-Speed Video CCD Camera and 1/4-inch Spherical-nosed Penetrator

A 10-mm calibration marker is placed on each sample for the measurement of the magnification factors. The results are shown in Figure 100, and clearly show that the crack average speed increases with energy levels for the two penetrators. This is significant because it verifies the earlier indication that the timing of the event will be such to capture well-developed cracks for the

accuracy of the measurements. The variation of crack speed with energy is shown in Figure 101. It is evident in the case of the spherical-nosed penetrator that the crack will start to propagate at about 54 J. The penetration limit velocity for this specimen is 76 J. Although the penetration energy is higher for the conical penetrator, the spherical penetrator induced greater crack speed than the conical hemispherical-nosed penetrator at the penetration energy. It thus appears that most of the energy for the conical penetrator goes into overcoming forward resistance caused by the conical section and not in propagating the crack. The spherical penetrator exhibits the expected s-curve that is typical of the limiting-velocity phenomenon. The perfect correlation and coefficient of determinant (r^2=1) shows with confidence the low variability of the results and the definite nonlinearity between crack speed and PL.

BPL: 25 psi, =54 J

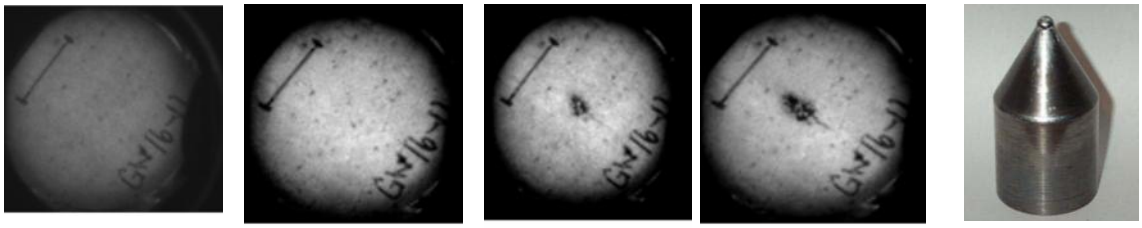

Before 160 μs 260 μs Static

At PL: 32.5 psi, =76 J

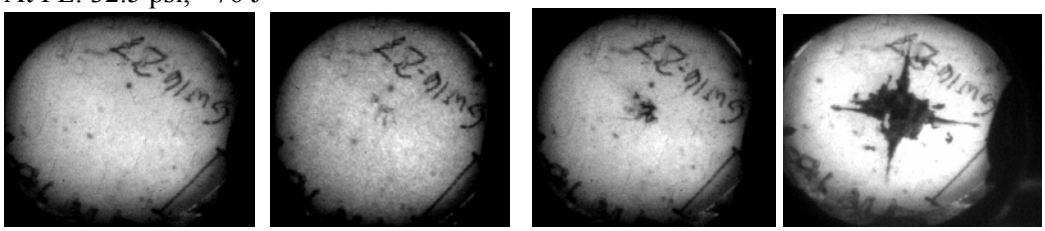

Before 160 μs 260 μs Static

APL: 35 psi = 84 J

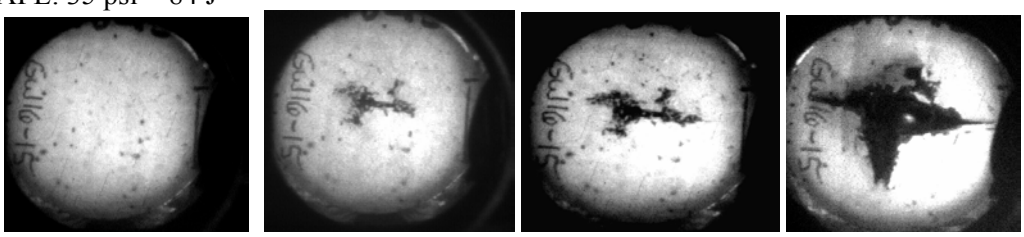

Before 160 μs 260 μs Static

Figure 99. Crack Propagations Using High-Speed Video CCD Camera and 1/4-inch Conical Hemispherical-Nosed Penetrator

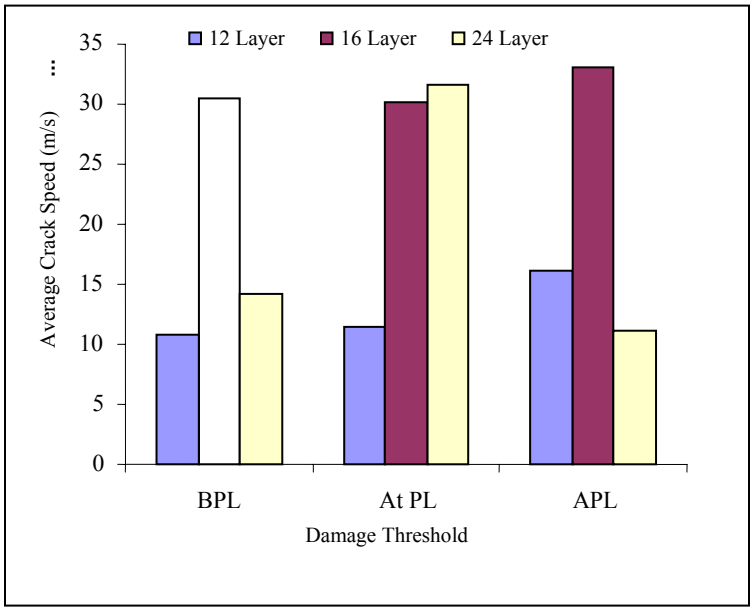

(a)

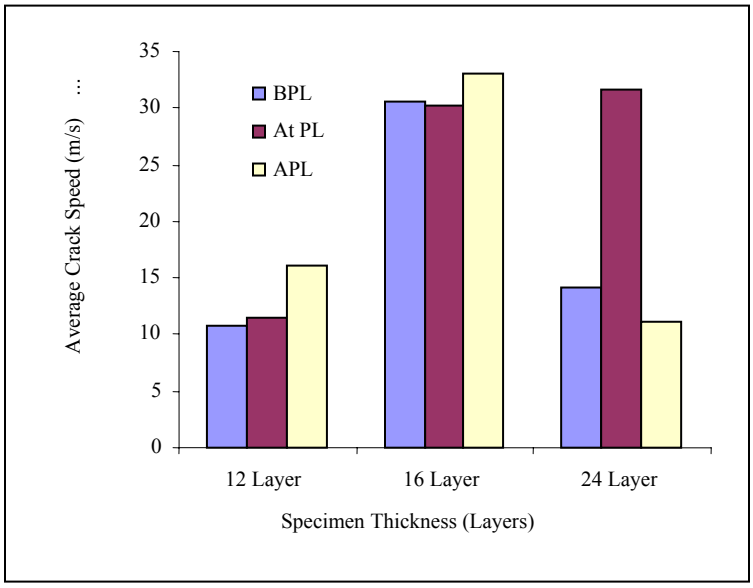

(b)

Figure 100. Variation of Crack Speed With a) Damage Energy Threshold, and b) Sample Thickness Measured with High-Speed Camera at 100 kFPS-12 kFPS (BPL=54 J, PL=76 J, and APL=84 J)

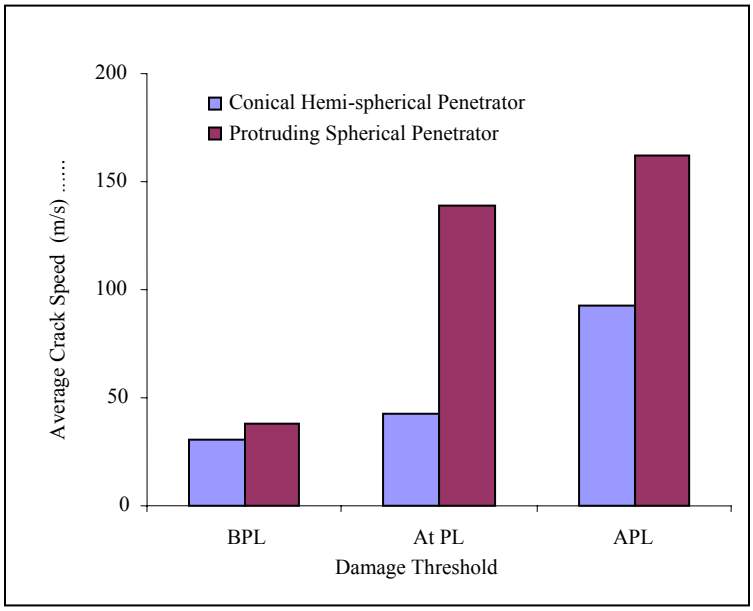

(a)

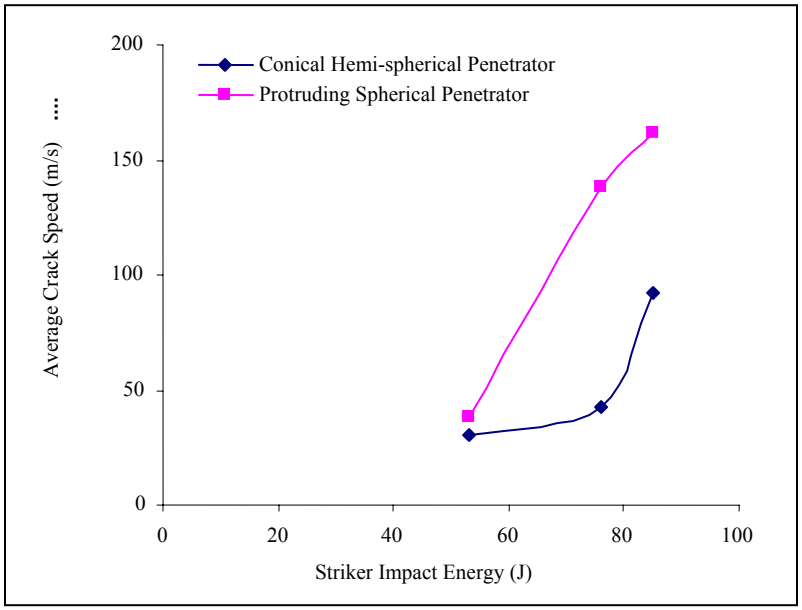

(b)

Figure 101. Comparison of Average Crack Speed Variation With a) Damage Threshold Levels Around the PL Energies, and b) Striker Impact Energies for Conical Hemispherical and Protruding Spherical Penetrators

3.6 Quantitative Analysis of Perforated Carbon-Epoxy Plates by Micro-Raman Spectroscopy

3.6.1 Introduction

As an alternative to SEM, a nonsubjective means of understanding and quantifying the surface damage shown in the previous section are presented in this section. One such method is based on coupling the micro-Raman spectroscopy (MRS) to our high speed materials testing system. Such integration is capable of measuring the residual dynamic fiber strain/stress relation and local stress intensity factor at the microscopic level. In contrast to SEM, the use of micro-Raman spectroscopy can probe micromechanical behavior to atomic levels with well-defined specificity.

In the last few years, the use of micro-Raman spectroscopy for characterization of composite materials has received some attention in the literature. Raman spectroscopy has been applied successfully in studies of the following: the effect of matrix cracking during the deformation of composite materials [46]; failure mechanisms of unidirectional carbon fiber-epoxy composite [47]; investigation of the micromechanics of two-dimensional carbon fiber/epoxy micro-composites [48]; micromechanical investigation of unidirectional carbon-epoxy [49]; stress concentration phenomena due to fiber failure resulting in fiber-fiber interaction in graphite-epoxy composites [50]; and load transfer in a short-fiber, high-modulus epoxy composite as a function of angle loading [51]. While the conclusions of the above studies were based on the analysis of the observed Raman spectra, the studies did not provide concrete correlation between the observed atomic vibrations to dynamics of fracture. This is significant because a more accurate understanding of the material behavior is needed to advance the search for new composite materials. While most of the recent Raman application focused mainly on fiber-reinforced composites, little work has been done on graphite-epoxy woven composites. We propose to cut through the specimen by previous techniques and measure the Raman spectra from the exposed fiber-matrix interface or fiber-fiber interface. The dominant failure mechanism in laminated composites is interlaminar delamination. To fully understand this mode and other modes of composite failures, the interfacial measurements characteristic of the fracture surface is very important. Chohan et al. [48] investigated interfacial measurement and fracture characteristics of composites using Raman spectroscopy and demonstrated that stress concentration exists in regions of fiber break, and regions in which inter fiber distance is very small. Micro-Raman spectroscopy has also been applied to evaluations of stress intensity factors and fracture toughness measurements [52]. Recent research has shown that this stress concentration in tension is different from that of compression [50]. The modes of fracture (mode I tearing, mode II shearing, and mode III twisting) can be differentiated by the energy levels of tension/compression, bending, and shearing/twisting. We believe the differences are due to variations in the materials atomic deformation, which can be studied by measuring the atomic vibration energy using the proposed system.

As part of the SOW for this project, the University of Pittsburgh proposes laser-based quantitative means of analyzing the surface damage to gain a better understanding of material residual dynamic structural properties and behavior at failure transition or interphase zones. The major task is to develop a quantitative means of profiling the residual strain and so characterize the

perforation deformation of composite materials at critical failure transition zones such as critical (penetration) limit velocity region.

In Raman phenomena, an incident light is scattered inelastically at a frequency higher (energy is gained) or lower than (energy is lost) the incoming photon source. Micro-Raman spectroscopy technique employs Raman spectroscopy with about 1 μm resolution. The energy lost or gained is equal to the Raman shift or vibration energy of the material. For the purpose of this investigation, we will define strain intensity as Raman shift in wave numbers. Materials, because of their unique atomic and molecular makeup, have unique vibration energies that can be identified and whose behaviors can be predicted. Laser Raman spectroscopy is a reliable technique for direct measurement of fiber stress at the microscopic level based mainly on the fact that Raman frequencies of the constituent fibers are stress-strain dependent. Heat, moisture absorption, dynamic impact, or a combination of these factors result in transformation of micro-mechanical properties of composite materials in the region of damage and beyond. The materials may be toughened due to changes in phase incorporation or grain distribution. Several authors have shown that the mechanical properties of fiber-reinforced composites are also controlled by fiber orientation, length, and the fiber-matrix interaction. This is due to the fact that the applied load is mainly carried by the fiber length and the interface, and the effective propagation of the strain on the fiber are affected by the number of fiber ends, the interface, and fiber-fiber interaction. In many crystalline or paracrystalline materials, the Raman peak position shifts linearly to lower wave numbers under tensile strains and to higher wave number under compressive strains.

3.6.2 Experimentation

The experimental setups that integrate all components of the system to micromechanical analysis require the samples (such as matrix resins or fibers pulled from damaged specimens) tested by the dynamic mechanical testing DMT system be transferred to the MRS system for micro-mechanical analysis. The degradation rate due to high rate loading in this case, for example, is known to depend on chemical and physical structures, local heating, nature of the material, duration of induced stress, types of additives and modifiers used, contaminants, and microbes. The basic system is configured with a true confocal microprobe for maximum spatial resolution. The system provides two interchangeable gratings for both high-resolution spectra and a fast overview function for wider wavelength ranges in one system. The appropriate holographic notch filter is incorporated into the system to enable acquisition of Raman spectra with conditions optimized for sensitivity and low frequency performance. The LabRam is delivered with a 17 mW 633 nm HeNe laser and additional lasers for other excitation wavelengths. The main excitation source for the spectrometer will be a medium-power argon laser capable of delivering wavelengths of 514.5 nm, 488.0 nm, and 532 nm, and a solid-state laser with temperature control and ventilation for high stability and extended operating life. For the fastest and easiest conversion from one laser to another, a specially designed prealigned plugin module is provided, housing the appropriate filter and mirror for each laser choice. To confirm the correct alignment of the laser, a very special feature has been incorporated. A low-power laser diode is mounted inside the spectrograph to back illuminate the entrance slit and an alignment confirmation can be initiated by computer keystroke. The complete stigmatic spectrograph, achromatic over a broad range (450 nm–1.05

microns), is equipped with two interchangeable gratings for variable spectral resolution. The 1800 g/mm grating provides a spectral resolution of ~2.5 cm^{-1} in three pixels using the standard HeNe laser and one optional argon laser. The second grating is chosen for a wide Raman spectroscopic overview in one scan or for recording laser fluorescence spectra over a broad wavelength range. The LabRam system is equipped with a rugged, compact, air-cooled CCD made by ISA. The CCD is an extremely sensitive ease-of-use detector and represents state-of-the-art technology in multichannel, two-dimensional detectors. It exhibits exceptionally low dark current as well as high sensitivity and high dynamic range. The sample (solid or liquid in a vial) is placed in the xyz plane of the microscope stage and can be easily adjusted. This macrosampling device mounts on the turret of the microscope via a standard microscope objective thread.

Thus, Raman spectroscopy is used in this experiment to measure the Raman spectra for selected specimens penetrated in the vicinity of penetration limit using conical hemispherical, spherical protruding, and hemispherical protruding. The window of the Raman machine was set at 1579.92 cm^{-1} to scan for the Raman signal of the graphite fiber in the specimens. Laser was used as the light source because it provides a narrow beam, high-intensity light source and blue-green excitation line. The data was also plotted using graphic computer software. The expectation of the shift (wavelength number) change is not linear with respect to strain. In tension, the strain increases the shift decrease such that

$$\Delta f \propto \frac{1}{\varepsilon} \tag{42}$$

where, Δf= Wavelength number (cm^{-1}), and ε = Strain (percent).

The Raman shift is determined for each woven graphite-epoxy specimen of varying thickness by taking the shift reading on the transverse side by cutting the samples along the x-axis.

3.6.3 Experimental Procedure

The experiment was designed to determine the variation of residual strain for both through-the-thickness compression (penetrator entrance side), tension (the exit side), and in the traverse direction (in-plane). Each specimen was marked along the diameter on the surface of the composite disk, as shown from the X-Y intersect point (Figure 102).

To establish the baseline for the real specimens, Raman spectra of undamaged specimens were obtained for each sample thickness. For the transverse side, a specimen holder was designed to hold the samples on the Raman machine. Samples were picked randomly and the reading of the shift and the intensity recorded on the log notebook. The outcome of this experiment meets the hypothesis expectation.

Location	Measured Distance
2	6
1	16
0	18
-1	24
-2	30

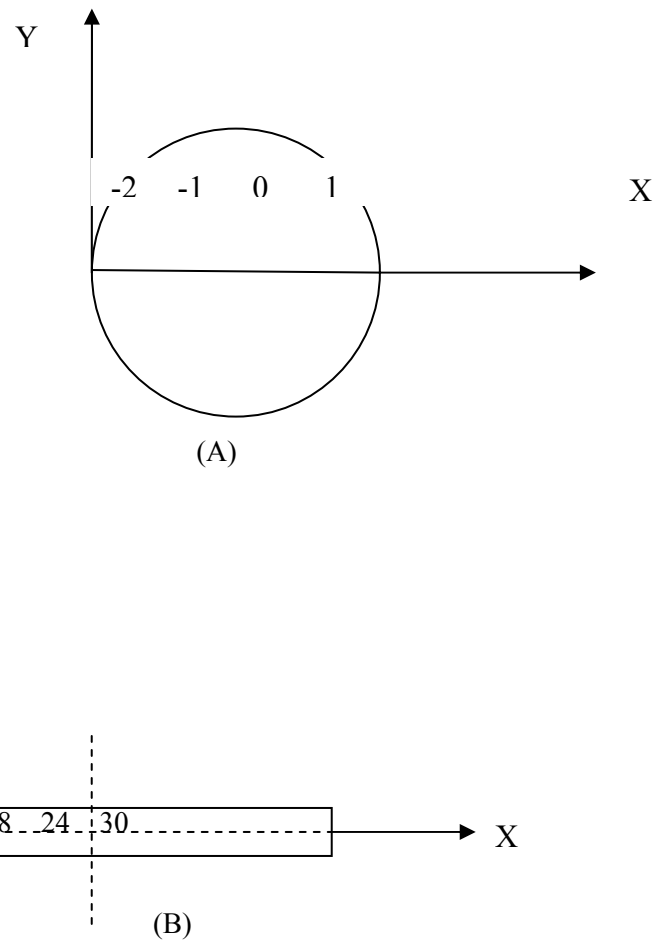

Figure 102. Experimental Configuration for Obtaining Strain Intensity Profile From the a) Surface, and b) Internal Traverse (In-plane) Surface of Damaged Specimen

3.6.4 Raman Experimental Results

Figures 103-106 show the Raman spectra with intensity plotted in arbitrary units (counts/s). The peak of the spectrum is proportional to the concentration of atomic species giving the Raman frequency. For this experiment, the shift from graphite is most dominant and resolved. The spectrum compares the spectrum of undamaged specimen with the compression side of a damaged specimen. Typical shift of graphite is at 1580 cm^{-1}. This was observed by our setup to be at 1605±5 cm^{-1}. The peak of the damaged specimen can be seen in Figure 102 to be shifted ±5 wave numbers to the left. The vertical line is to guide your eyes. Figure 104 also compares the tension side to the undamaged spectrum and shows that the peak is also shifted, but this time to the right. The complete strain intensify profile is shown in Figure 105. The data is obtained as previously described by scanning across the specimen surface around the damage zone, as in Figure 103. Comparison of these profiles shows a definite difference between strain distributions

in compression. The profile indicates a local minimum at the center of highest strain. Both minimum and maximum occur at the center, although in opposite directions. This corresponds to around the center, corresponding to the point of impact and, therefore, highest strain. There is also the presence of alternation of the smaller lows and highs. This may be due to alternate regions of intersections of woven fibers.

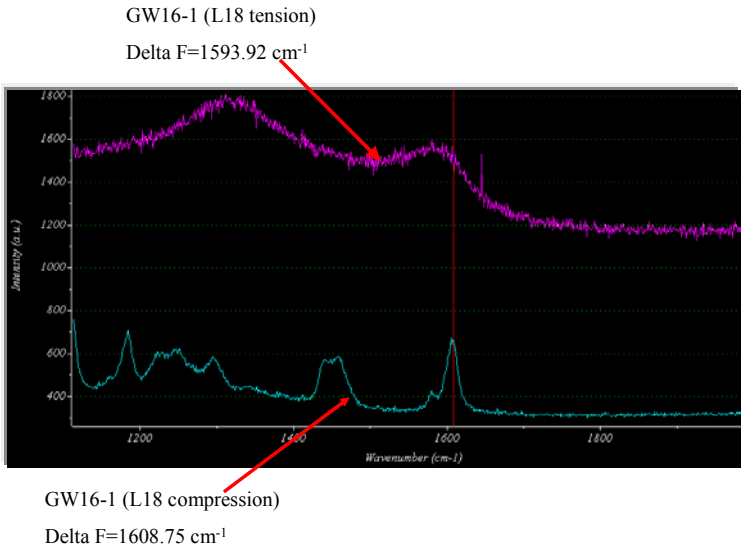

(A)

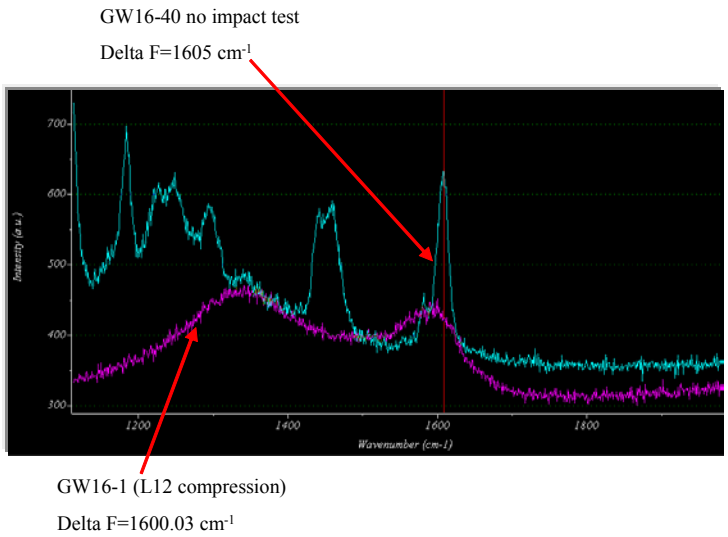

(B)

Figure 103. Comparison of Raman Spectrum for 16-Layer Sample a) Compression and Tension Sides at Center Location b) Compression Side Damage Compared to Undamaged Sample

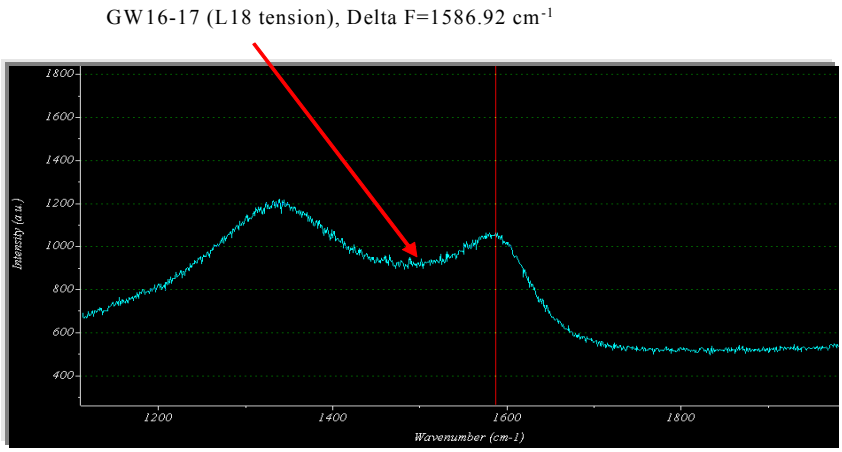

(A)

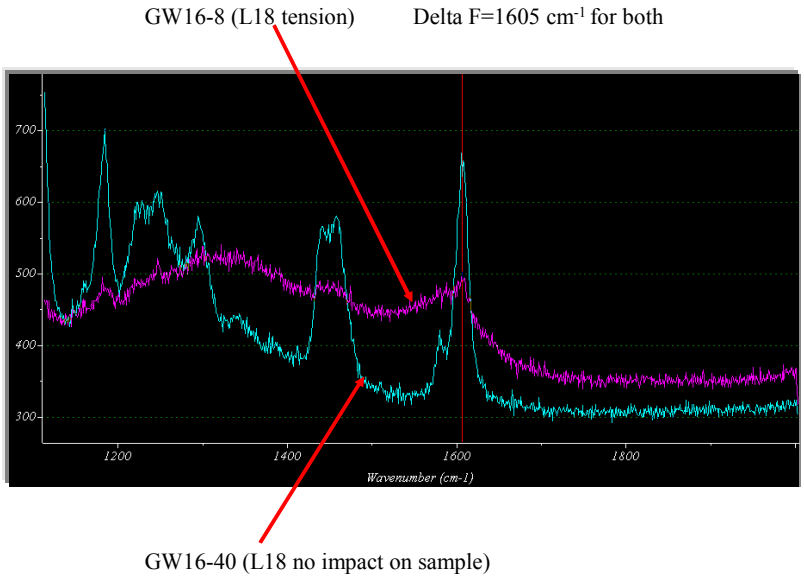

(B)

Figure 104. Comparison of Raman Spectrum of Undamaged and Damaged Samples for 16-Layer a) Tension Side at Center Location b) Tension Side Damage Compared to Undamaged Sample

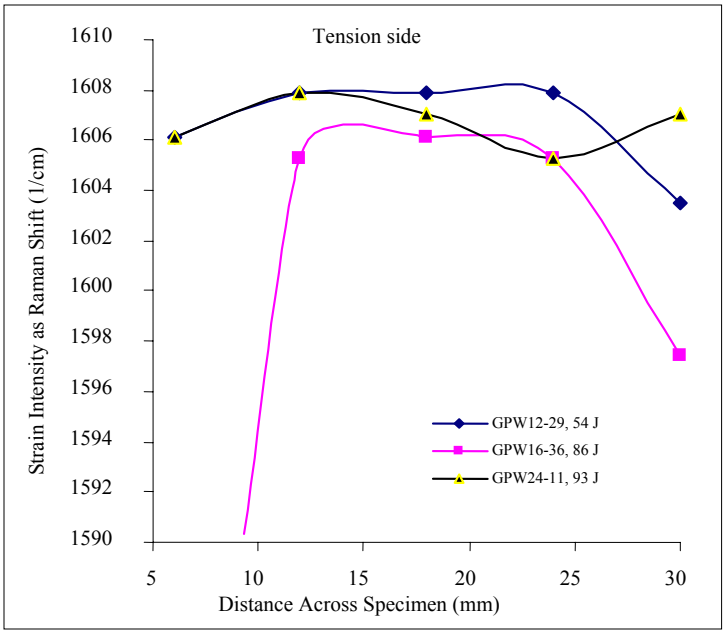

(A)

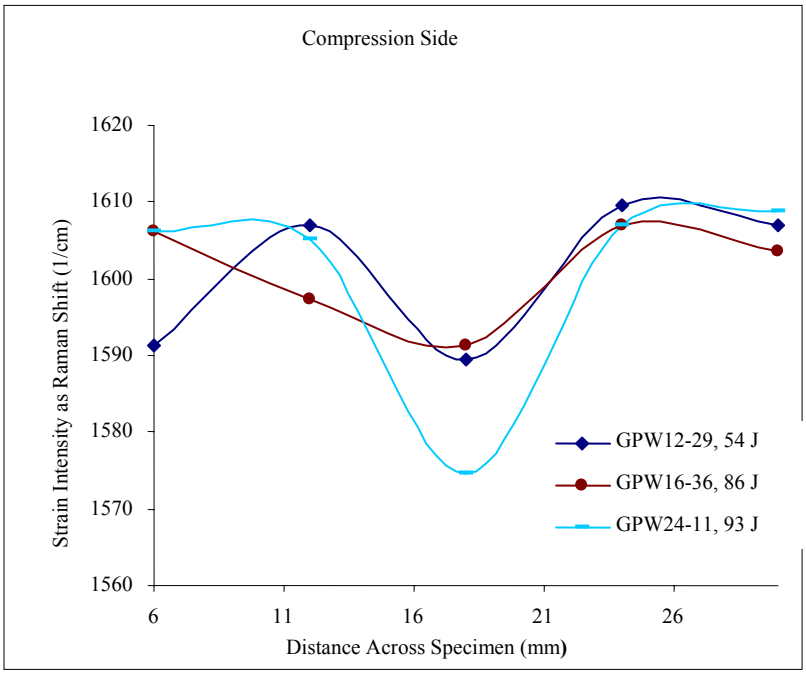

(B)

Figure 105. Strain Intensity Profile for 16-Layer Sample for a) Tension and b) Compression

Figure 106 compares the strain intensity profile for both hemispherical and spherical penetrator for varying strain rates. Again, the peak shows a minimum at the center. However, the hemispherical penetrator shows a no localized strain effect. The plot shows that when the shift decreases the strain increase, this can be seen very clearly with the specimens: GPW24-11,

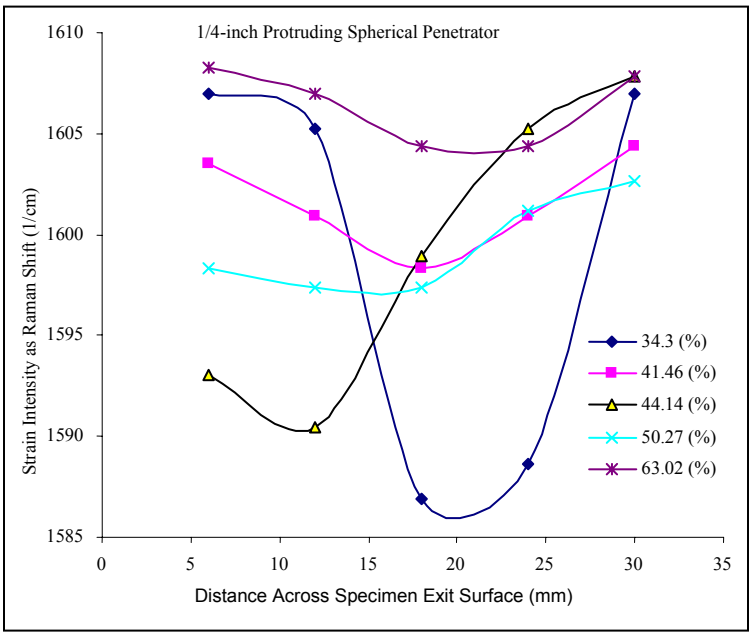

(a)

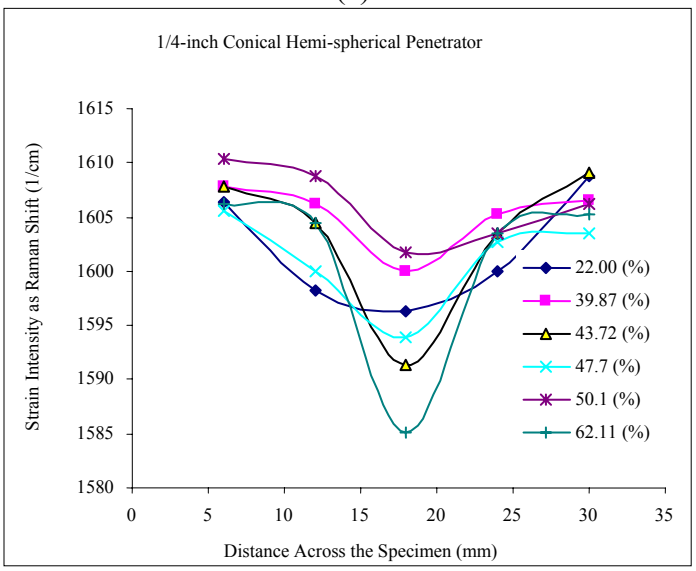

(b)

Figure 106. Strain Intensity Profile for a) Protruding Spherical, and b) Conical Hemispherical Penetrator at Varying Sample Strains (%)

GPW24-22, GPW24-43, GPW16-36, GPW16-43, and GPW12-29 in Figure 105. In addition, from the visional observation to the specimens, the highest damage is located at the center of the composite disks. This is about 18 mm from the reference frame and this match with the above outcome. Thus, the highest stress point occurs at the center point of impact of the specimen where perforation occurs. The highest strain is expected there as shown by these results. The most interesting is the sinusoidal shape of some of the plots. This suggests the way in which the layers and the matrix of the composite materials put together.

Figure 107 shows the comparison of average Raman shift peak induced by changes in strain intensity for compression and tension. The results show that carbon graphite/epoxy have positive wave number shift in compression compared to negative shift in tension, in agreement with typical published results [53]. This observation shows that compression induced strain can be measured and monitored using the Raman spectroscopy technique presented in this studies. This is important in the assessment of residual strength of aged aircraft structures.

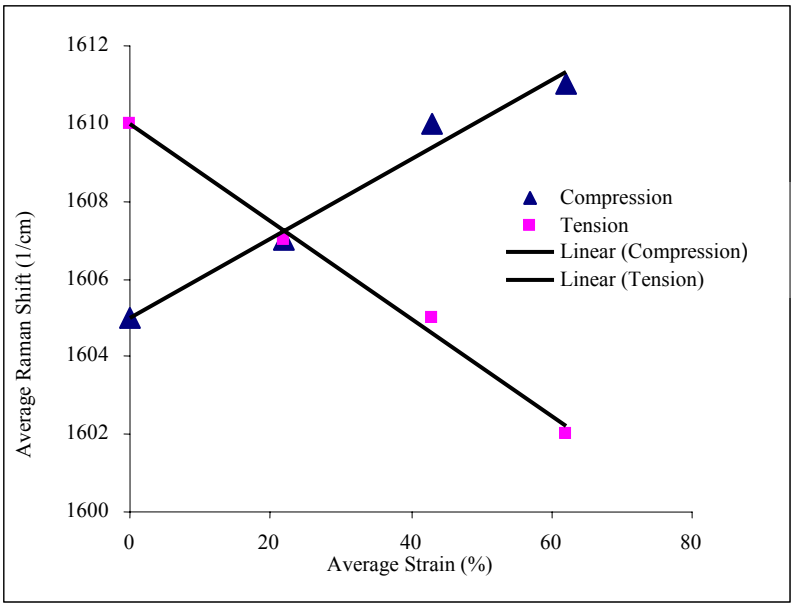

Figure 107. Variation of Strain Induced Raman Shift Averaged Over all the Locations with Sample Average Strain

3.7 Conclusions

The conclusions from these plots are as follows:

- Strain rate and ultimate strain and energy released increase nonlinearly, particle velocity and displacement increase linearly with impact energy, and ultimate strength depends slightly on impact energy. Within the threshold (penetration) energy for perforation, energy released increases linearly with impact energy.
- Energy released and strain rate are sensitive to increases in strain and increase nonlinearly; ultimate strength and particle velocity increase linearly with strain.
- Ultimate strength, particle velocity, strain rate, and strain increase linearly with displacement.
- Particle velocity, ultimate strength and ultimate strain increase linearly with strain rate, and energy released increases non-linearly with strain rate.
- The dynamic modulus (defined ultimate strength relative to the ultimate strain) seems to decrease non-linearly with impact velocity, energy released, strain rate and strain. Simple power law function of the form $y = ax^2$ was sufficient to predict the dependency.
- Incident stress and fiber orientation did not interact since physical principles suggest that such an interaction would affect the amount of energy released. The limit-velocity curves superbly showed the observed V_{50} PL velocities correlated within a 5 percent range with the calculated values.
- The respective PLs of the 24-ply, 16-ply and 4-ply [+45/-45/0/90] samples were 12.32 m/s, 7.97 m/s and 2.61 m/s; and 7.80 m/s, 4.59 m/s and 3.02 m/s respectively for the 16-ply, 8-ply and 4-ply [+45/-45] samples. Finally, there is a linear relationship between PL and sample thickness.
- Above the PL, the damage to the specimen is characterized by post-perforation and plugging.
- On the average, strain rate and loading forces increase with damage energy threshold levels, from BPL to APL, 1/4-inch penetrator delivered more load and strain effects on the specimen than the 3/16-inch penetrator of the same shape.
- The results show that there is a significant difference between the effects of penetrator size on a specimen strain rate. Specimen energy absorption is strongly dependent on thickness, penetrator geometry, and size.
- The results indicate that the conical hemispherical penetrator will defeat its target at a higher energy level than the spherical penetrator will. However, the damage of the spherical penetrator is highly localized because of the penetrator shape.
- As the size of the penetrator is increased, the penetration and perforation threshold energies increase significantly. The same energy level, the larger size penetrator-nose will deliver more energy to the target. The size of the nose contact area is more significant in energy delivery than the shape of the penetrator itself.
- Although the penetration energy is higher for the 1/4-inch conical penetrator, below, at, and above the penetration limit energies, the spherical penetrator-nose induced greater crack speed 40, 149, and 162 m/s, respectively, compared to 38, 42, and 90 m/s, respectively for the 1/4-inch conical hemi-spherical-nosed penetrator. It thus appears that most of the energy for the conical penetrator goes into overcoming forward resistance caused by the conical section and not in propagating the crack.
- Micro-Raman spectroscopy is a reliable quantitative means of characterizing residual strain in a damaged specimen. The strain intensity profile shows a definite difference between strain

distribution in compression and tension. Raman shift is shown to be inversely proportion to the strain in tension and proportional to strain in compression.

- While profiles indicate a local minimum at the center of highest strain. This corresponds to around the center, corresponding to the point of impact and therefore highest strain. There is also the presence of alternation of the smaller lows and highs.
- The results show that in woven specimens, the crack also appears crossed and propagates in both directions probably due to the woven nature of the specimen. It is conceivable that the cracks first initiate at the point of intersections of the weave, and move in both directions.
- It also shows that the point of intersection of the weave will also indicate the point of weaker or highest strain for the same energy and exhibits a wave nature in the strain profile.

3.8 Further Research and Recommendations

The research generated some questions that need further investigation.

1. There is a need to further investigate the crack propagation in woven graphite-epoxy at energies well above the threshold energy and with better timing of the event. The research using the rotating camera is inconclusive as far as thick specimen is concerned. This is important since there is no data available for crack propagation in woven specimen.
2. The success of integration and use of micro-Raman spectroscopy now expands our capabilities in penetration mechanics. However, further analysis of the transverse experiment is needed to completely characterize the residual strain distribution under the surface of the damaged specimen. There is also no known theoretical formulation for the observed phenomenon.
3. The integrative use of the rotating camera and the CCD intensifier clearly shows that the CCD intensifiers save a lot time and cost of running these experiments, and is more reliable than the rotating mirror camera. However, the system is not at its maximum since it is equipped with only a coupled CCD with two objective views. It will be better to extend this to Model 220-8 or 220-16 that has 8 –16 objective lenses. These will readily improve the accuracy of the results.

4. References

1. Sierakowski, R. L., "Strain Rate Effects in Composites," *Applied Mechanics Reviews,* Vol. 50, No. 11, Part 1, pp. 741-761, December 1997.
2. El-Habak, A. M. A., "Compressive Resistance of Unidirectional GFRP Under High Strain Rate of Loading," *Journal of Composite Technology and Research JCTRER,* 15(4), 311-317, (1993).
3. Montiel, D. M., and Williams, C. J., "A Method for Evaluating the High Strain Rate Compressive Properties of Composite Materials," In: G. C. Grimes, editor. *Composite Materials: Testing and Design (Tenth Volume) ASTM STP 1120.* Philadelphia: American Society for Testing and Materials, pp. 54-65 (1992).
4. Harding, J., "Effect of Strain Rate and Specimen Geometry on the Compressive Strength of Woven Glass-reinforced Epoxy Laminates," *Composites,* 24, pp. 323-332 (1993).
5. Powers, B. M., and Vinson, J. R., Wardle, M., and Scott, B., "High Strain Rate Effects on Two AS4 Graphite Fiber Polymer Matrix Composites," In: *Proceedings of the ASME Aerospace Division Board AD-48, High Strain Rate Effects on Polymer, Metal, and Ceramic Matrix Composites and Other Advanced Materials*, pp. 179-189, (1995).
6. Powers, B. M., and Vinson, J. R., "High Strain Rate Effects in Materials in Sandwich Construction," In: Allen HG, editor. *Sandwich Construction, 3rd Edition. England: Engineering Materials Advisory Services, Ltd.,* pp. 769-778, (1996).
7. Woldenbet, E., and Vinson, J. R., "Effect of Specimen Geometry in High Strain Rate Testing of Graphite/epoxy Composites," In *Proc. of 38th AIAA/ASME/ASCE/AHS/ASC. Struc. Dyn. and Matl. Conf.,* 2, pp. 927-934, (1997).
8. Waas, A. M., Takeda, N., Yuan, J., and Lee, S. H., "Static and Dynamic Compressive Behavior of Glass Fiber Reinforced Unidirectional Composites," In: Gibson RF and Newaz GM, editors. *Proceedings 12th Annual Technical American Society for Composites Conference,* Dearborn, MI, pp. 552-561, (1997).
9. Hsiao, H. M., Daniel, I. M., and Cordes, R. D., "Strain Rate Effects on the Transverse Compression and Shear Behavior of Unidirectional Composites," *Journal of Composite Materials,* 33, pp. 1620-1642, (1999).
10. Hosur, M. V., Vaidya, U. K., Abraham, A., Jadhav, N., and Jeelani, S., "Static and High Strain Rate Compression Response of Thick Section Twill Weave S2-Glass/Vinyl Ester Composites Manufactured by Affordable Liquid Molding Processes," *ASME Journal of Engineering Materials and Technology,* No. 4, pp. 468-475, (October 1999).
11. Vaidya, U. K., Jadhav, N. C., Hosur, M. V., Gillespie Jr., J. W., and Fink, B. K., "Influence Of Through-The-Thickness Stitching on the High Strain Rate Impact Response of Resin Infused S2-Glass/Epoxy Composites," *Proceedings of American Society for Composites 14th Technical Conference, Fairborn, OH,* pp. 141-151, (September 1999).
12. Weeks, C. A., and Sun, C. T., "Modeling Non-Linear Rate Dependent Behavior in Fiber-Reinforced Composites," *Composites Science and Technology,* Vol. 58, 603-611, (1998).
13. Ninan, L., and Sun, C. T., "High Strain Rate Characterization of Off-Axis Composites Using Split Hopkinson Pressure Bar," *Proceedings of American Society for Composites 13th Technical Conference, Baltimore, MD,* pp. 1732-1745, (September 1998).
14. Dee, A. T., Vinson, J. R., and Sankar, B. V., Effects of High Strain Rate Compression on the Mechanical Properties of A Uniweave AS4/3501-6 Composite Laminate With Through-Thickness Stitching," *AIAA/ASME/ASCE/AHS 38th SDM conf., Orlando, FL,* Paper No. AIAA-97-1048, pp. 945-954, (April 1997).

15. Huang, S. L., Richey, R. J., and Deska, E. W., "Cross Reinforcement in a GFRP Laminate," Paper presented at ASME, Winter Annual meeting, San Francisco, December 1978.
16. Mignery, L. A., Sun, C. T., and Tan, T. M., "The Use of Stitching to Suppress Delamination in Laminated Composites," *ASTM STP 876,* pp. 371-385, (1985).
17. Kang, T. J.; and Lee, S. H., "Effect of Stitching On The Mechanical And Impact Properties Of Woven Laminate Composite," *Journal of Composite Materials,* Vol. 28, No. 16, pp. 1574-1587, (1994)
18. Dransfield, K., Baillie, C., and Mai, Y., "Improving the Delamination Resistance of CFRP by Stitching -A Review*," Composite Science and Technology,* 50, 305-317, (1994).
19. Enboa, W., and Jyue, W., "Behavior of Stitched Laminates Under In-Plane Tensile and Transverse Impact Loading," *Journal of Composite Materials,* 29, pp. 2254-2279, 1995.
20. Reeder, J., "Stitching Vs. A Toughened Matrix: Compression Strength Effects," *Proceedings of the NASA Langley Research Center, USA; Mechanics of Textile Composites Conference;* pp. 99-130, (October 1995).
21. Hosur, M. V., Adya, M., Alexander, J., Vaidya, U. K., Jeelani, S., and Mayer, A., "Studies on Impact Damage Resistance Of Affordable Stitched Woven Carbon/Epoxy Composite Laminates," *Journal of Reinforced Plastics and Composites,* Vol. 22, No. 10, pp. 927-952.
22. Nemat-Nasser, S., Isaacs, J. B., and Starrett, J., "Hopkinson Techniques for Dynamic Recovery Experiments," *Proceedings of Royal Society of London,* A, pp. 371-391, (1991).
23. Li, Z., and Lambros, J., "Determination of the Dynamic Response of Brittle Composites by the Use of the Split Hopkinson Pressure Bar," *Composite Science and Technology,* Vol. 59, 1097-1107, (1996).
24. Li, Z., and Lambros, J., "Dynamic Thermomechanical Behavior of Fiber Reinforced Composites," *Composites-Part A,* Vol. 31, pp. 537-547, (2000).
25. Palmese, G. R., McCullogh, R. L., and Sottos, N. R., "Relationship Between Interphase Composition, Material Properties and Residual Thermal Properties in Composite Materials," *Journal of Adhesion,* Vol. 52 pp. 101-113, (1995).
26. Heslehurst, R. B., "Off-axis Transformation of the Composite Laminate Stiffness Properties", *Composite Structures,* Vol. 35, pp. 369-374, (1996).
27. Weeks, C. A., and Sun. C. T., "Modeling Non-Linear Rate Dependent Behavior in Fiber-Reinforced Composites", *Composites Science and Technology,* Vol. 58: pp. 603-611, (1998).
28. Ninan, L., and Sun, C. T., "High Strain Rate Characterization of Off-Axis Composites Using Split Hopkinson Pressure Bar," In: Vizzini AJ, editor. *Proceedings of American Society for Composites 13th Technical Conference, Baltimore, MD,* pp. 1732-1745, (1998).
29. Ninan, L., Tsai, J., and Sun, C. T., "Use of Split Hopkinson Pressure Bar for Testing Off-Axis Composites", *International Journal of Impact Engineering,* No. 25, pp. 291-313, (2001).
30. Woldesenbet, E., and Vinson, J. R., "Effect of Fiber Orientation on High Strain Rate Properties of Graphite/Epoxy Composites", *Proceedings of American Society for Composites 12th Technical Conference on Composite Materials, Ann Arbor, MI,* pp. 460-468, (1997).
31. Preissner, E., Woldesenbet, E., and Vinson, J. R., "Off-Axis Fiber Orientation on High Strain Rate Compression Testing of K-49/3501-6 Kevlar/Epoxy Composites", In: *Proceeding of ICCM-11, Gold Coad, Australia,* pp. 797-806, (1997).
32. Vinson, J. R., and Woldesenbet, E., "Fiber Orientation Effects on High Strain Rate Properties of Graphite/Epoxy Composites", *Journal of Composite Materials,* Vol. 35, No. 6, pp. 509-521, (2001).

33. Nwosu, S. N., and Czarnecki, G., " Dynamic Crack Propagation and Perforation of Laminated Composites," *Australian Composite Structures Society*, pp 1153-1161, (1997).
34. Zukas, J. A., Nicholas, T., Swift, H., Greszczuk, L. B., and Curran, D., *Impact Dynamics,* Kreiger Publishing Co., (1992).
35. Nwosu, S. N., "High Strain Perforation and Mixed Mode Delamination of Laminated Composites," *Wright Patterson AFB, Report # TR 6096,* October 1997.
36. Nwosu, S. N., "Dynamic Crack Propagation by High Speed Imaging," *Proceedings of the Fourth International Conference on Composites Engineering, Hawaii,* pp. 741-742, (August 1997).
37. Nwosu, S. N., "Hopkinson Bar Perforation of Laminated Graphite/Epoxy Composite," USAFORS Report WL-TR-96-3080, pp1-66, 1996.
38. Instructional Manual for Model 330 Cameras, Cordin Company, (1995).
39. Hopkinson, B., "The Effects of Momentary Stresses in Metals," *Proceedings of Royal Society London,* Vol. 74-A, pp. 498-506, (1905).
40. Kolsky, H., "Stress Waves in Solids," Oxford University Press, London, (1953).
41. Bickle, L. W., "An Introduction of the Use of Strain Gages for the Measurement of Propagating Strain Wave," Sandia Laboratories, Albuquerque, NM, (1970).
42. Shivakumar, E. W., and Illg, W., "Prediction of Impact Force and Duration Due to Low Velocity Impact on Circular Composite Laminate," *Transaction of ASME,* Vol. 52, pp. 674. (1984).
43. Malvern, L. E., "Behavior of Materials under Dynamic Loading," in *N.J. Huffingtyon, Jr, ed ASME,* NY (1965).
44. Meyers, M. A., "Dynamic Behavior of Materials," John Wiley, and Sons, Inc, New York (1994).
45. Ojo, O., "Effect of Penetrator Configuration and Size on the Dynamic Behavior of Composite Material Under High Strain Rate Loading," MS Thesis, University of Pittsburgh, (2003).
46. Bennett, J. A., and Young, R. J., "Micromechanical Aspects of Crack/Crack Interactions in an Aramid/Epoxy Composite," *Composites Science and Technology,* Vol. 57, No. 8, pp. 945-956, (1997).
47. Marston, C., Gabbitas, B., Adams, J., Nutt, S., Marshall, P., and Galiotis, C., "Failure Characteristics in Carbon/Epoxy Composite Tows," *Composites Part A,* Vol. 27, No. 12, pp. 1183-1194, (1996).
48. Chohan, V., and Galiotis, C., "Interfacial Measurements and Fracture Characteristics of 2D Microcomposites Using Remote Laser Raman Microscopy," *Composites Part,* Vol. 27, No. 9, 881-888, (1996).
49. Bucci, D.V., Koczak, M. J., and Schadler, L. S., "Micromechanical Investigations of Unidirectional Carbon/Carbon Composites via Micro-Raman Spectroscopy," *Carbon,* Vol. 35, No. 2, pp. 235-245, (1997).
50. Amer, M. S., and Schadler, L. S., "Stress Concentration Phenomenon in Graphite/Epoxy Composites: Tension/Compression Effects," *Composites Science and Technology,* Vol. 57, No 8, pp. 1129-1137, (1997).
51. Mehan, M. L., and Schadler, L. S., "Micromechanical Behavior of Short-Fiber Polymer Composites," *Composites Science and Technology,* Vol. 60, pp. 1013-1026, (2000).
52. Miyagawa, H., Sato, C., and Ikegami, K., "Fracture Toughness Evaluation for Multidirectional CFRP by the Raman Coating Method," *Composites Science and Technology,* Vol. 60, No. 16, pp. 2903-2915, (2000).

53. Bucci, D.V., Koczak, M. J., and Schadler, L. S., "Micro-Mechanical Investigation of Unidirectional Carbon Composites Via Micro-Raman Spectroscopy," *Carbon*, Vol. 35, No. 7, pp 1035-1038, (1997).

List of Acronyms

Acronym	Description
APL	above penetration limit
ANOVA	analysis of variance
BPL	below penetration limit
CCD	charge-coupled device
DMT	dynamic mechanical testing
FSW	forward swept wing
GPIB	general purpose interface bus
HiMAT	highly maneuverable aircraft technology
L/D	length to diameter
M.T.S	materials testing system
MRS	micro-Raman spectroscopy
PL	penetration limit
P-SHPB	penetrating split Hopkinson's pressure bar
rps	revolutions per second
SEM	scanning electron micrograph (or microscope or microscopy)
SHPB	split Hopkinson's pressure bar
SOW	statement of work
VARIM	vacuum-assisted resin infusion molding